Jens Gächter

Evaluation of Rotor Position Sensor Characteristics and Impact on Control Quality of Permanent Magnet Synchronous Machines

Doctoral Thesis

to achieve the university degree of

Doktor der technischen Wissenschaften (Dr. techn.)

submitted to

Graz University of Technology

Assessors

Assoc.Prof. Dipl.-Ing. Dr.techn. Mario Hirz

Institute of Automotive Engineering, Graz University of Technology

Prof. Dr.-Ing. Su Zhou

College of Automotive Engineering, Tongji University

Graz, July 2017

Acknowledgement

I would like to thank my supervisor Assoc.Prof. Dipl.-Ing. Dr.techn. Mario Hirz for his support, inputs and patience during this project. I'm also very thankful that Prof. Dr.-Ing. Su Zhou declared himself willing to take over the second assessment of this work. A lot of important support came from foreign institutes, which I do not take as granted. Therefore, a special thank goes to Ass.Prof. Dipl.-Ing. Dr.techn. Roland Seebacher and Ao.Univ.-Prof. Dipl.-Ing. Dr.techn. Herwig Friedl. I would also like to thank my project partners from MAGNA for the good cooperation and working partnership.

Fortunately I had important and well executed support from two close friends of mine, Wasi and Döme, which were participating in this work by finishing their masters thesis. This was a challenging, but mostly fulfilling experience and I enjoyed working with these guys. I'm also very thankful to the people of the Institute of Automotive Engineering (FTG), because I value the collegial attitude, the excellent working climate and the help I received from them within this project. Last of all, I would like to thank especially my family for their support all over the years and their motivation to finish this work.

Statutory Declaration

Ich erkläre an Eides statt, dass ich die vorliegende Arbeit selbstständig verfasst, andere als die angegebenen Quellen/Hilfsmittel nicht benutzt, und die den benutzten Quellen wörtlich und inhaltlich entnommenen Stellen als solche kenntlich gemacht habe.

Graz, am ....
(Unterschrift)

I declare that I have authored this thesis independently, that I have not used other than the declared sources / resources, and that I have explicitly marked all material which has been quoted either literally or by content from the used sources.

....
(date) (signature)

Abstract

This work deals with the evaluation of different rotor position measurement principles for controlling a permanent magnet synchronous machine. In order to meet average fleet consumption targets, vehicle powertrain components are getting progressively electrified. Especially for automotive applications, electric machines are used for different purposes, e.g. as traction machine in electric vehicles, in hybridization concepts as supplementation of the internal combustion engine or as actuator for different ancillary units.

Due to the demanding environment of such automotive applications, the first part of this work introduces a method to evaluate the robustness of rotor position sensors in terms of parameter variations, which is tested by a specifically designed test bench. The presented method allows to compare different measurement principles and sensor configurations with each other, since these investigated sensor concepts differ in terms of complexity regarding signal processing, system integration and costs.

The second emphasis of this work lies on investigations, how measured rotor position signals from different sensors influence the control of a permanent magnet synchronous machine. A system theory based description of a field-oriented control is introduced to analyze the impact of rotor position measurement errors regarding machine currents and torque. Additionally, the influence of these errors in terms of different control strategies, additive losses and efficiency and their impact on speed controlled applications is discussed. The presented methods and results are motivated by automotive applications, but not restricted in their conclusiveness and validness by this specific field of activity.

Kurzfassung

Die vorliegende Arbeit beschäftigt sich mit der Evaluierung verschiedener Rotorlagemessprinzipien, die zur Regelung einer permanenterregten Synchronmaschine eingesetzt werden. Im Zuge der Realisierung von Flottenverbrauchszielen werden Antriebsstrangkomponenten im Fahrzeug sukzessive elektrifiziert, wobei in automotiven Anwendungen elektrische Maschinen in unterschiedlichen Anwendungsbereichen zum Einsatz kommen, z.B. als Traktionsantrieb in Elektrofahrzeugen, bei Hybridisierungskonzepten als Ergänzung zu einer Verbrennungskraftmaschine oder als Aktuator von verschiedenen Nebenaggregaten.

Aufgrund der anspruchsvollen Umgebung, die der automotive Einsatzbereich bereitstellt, wird als erster Schwerpunkt in dieser Arbeit eine Methode erarbeitet, mit der die Robustheit von Rotorlagesensoren bezüglich verschiedener Parametereinflüsse mithilfe eines eigens dafür aufgebauten Prüfstandes untersucht werden kann. Dadurch können diverse Messprinzipien und Sensorkonfiguration gegenübergestellt und bewertet werden, da die Komplexität der Sensorik bezüglich Signalverarbeitung, Systemintegration und Kosten unter den verschiedenen Technologien stark unterschiedlich ausfallen kann.

Als zweiten Schwerpunkt wird bei dieser Arbeit darauf eingegangen, wie sich konkret gemessene Rotorlagefehler von verschiedenen Sensoren auf die Regelung einer permanenterregten Synchronmaschine auswirken. Dabei wird eine systemtheoretische Beschreibung der feldorientierten Regelung vorgestellt, die die Berechung des Einflusses von Rotorlagemessfehlern auf Maschinenströme und Drehmoment erlaubt. Weiters wird die Einwirkung dieser Messfehler auf verschiedene Betriebsstrategien, zusätzliche Verluste und den Wirkungsgrad, sowie deren Einfluss bei Einsatz geschwindigkeitsgeregelter Applikationen erläutert. Die vorgestellten Methoden und Ergebnisse sind von automotiven Einsatzzwecken motiviert, aber in ihrer Aussagekraft und Gültigkeit nicht auf dieses Betätigungsfeld beschränkt.

Contents

Abbreviations

AC	Alternate Current
AMR	Anisotropic Magnetoresistance
ANN	Artificial Neural Network
ANOVA	Analysis of Variance
ASIC	Application Specific Integrated Circuit
BB	Box-Behnken
BLDC	Brushless DC Machine
BSG	Belt-driven-Starter-Generator
CCC	Central Composite Circumscribed
CCF	Central Composite Faced
CCI	Central Composite Inscribed
CMFL	Constant Mutual Flux Linkage
CO_2	Carbon Dioxide
CSG	Crank-Starter-Generator
DC	Direct Current
DOE	Design Of Experiments
DUT	Device Under Test
EMF	Electromotive Force
FEM	Finite Element Method
FF	Full Factorial
FOC	Field-oriented Control
GMR	Giant Magnetoresistance
IM	Induction Machine
IMG	Integrated-Motor-Generator
IPMSM	Interior Permanent Magnet Synchronous Machine
LMC	Loss Minimizing Control
LTI	Linear Time Invariant
LUT	Look-Up Table
MAE	Mean Absolute Error
MAPE	Mean Absolute Percentage Error
MIMO	Multiple Input Multiple Output
MPC	Maximum Power Control
MTPA	Maximum Torque per Ampere
MTPV	Maximum Torque per Volt
PI	Proportional Integral
PMSM	Permanent Magnet Synchronous Machine

PT1	First Order Lag Element
PV	Prediction Variance
RBF	Radial Basis Functions
RMSE	Root Mean Squared Error
RSM	Response Surface Methodology
SMG	Separate-Motor-Generator
SPMSM	Surface Permanent Magnet Synchronous Machine
SVM	Space Vector Modulation
TIC	Theil's Inequality Coefficient
TMR	Tunnel Magnetoresistance
UPF	Unity Power Factor
UPV	Unscaled Prediction Variance
VCO	Voltage Controlled Oscillator
VR	Variable Reluctance
WF	Wound Field
ZDAC	Zero D-Axis Current

Symbols

Reference frames and notation

$\mathbf{f}^s_{abc}$	Three phase vector $\mathbf{f}$ in stationary abc-reference frame
$\mathbf{f}^s_{\alpha\beta}$	Complex vector $\mathbf{f}$ in stationary $\alpha\beta$-reference frame
$\mathbf{f}^r_{dq}$	Complex vector $\mathbf{f}$ in rotating dq-reference frame

Parameters and constants

Symbol	Description	Unit
A	Air gap area	m^2
B	Friction parameter	$\mathrm{kgm}^2/\mathrm{s}$
c_{fe}	Iron loss model fitting coefficient	-
c_{stray}	Stray loss model fitting coefficient	-
g	Air gap length	m
h_m	Magnet height	m
I_{max}	Rated stator current of electric machine	A
J	Inertia of electric machine	kgm^2
l_{core}	Flux path length within iron	m
L_a, L_b, L_c	Inductances of a-, b- and c-winding	H
L_d, L_q	Inductances in d- and q-axis	H
L_{ms}	Static average air gap inductance	H
L_δ	Stator inductance reluctance component	H
M_{max}	Torque of electric machine	Nm
N	Number of turns	-
n_{rated}	Rated speed of electric machine	rpm
p	Number of poles	-
P_{max}	Rated power of electric machine	kW
R_{c0}	Static iron resistance parameter	Ω
R_{c1}	Speed dependent iron resistance parameter	Ωs
R_s	Stator resistance	Ω
$T_{d,q}$	Time constant of stator transfer function in d- and q-axis	s
T_F	Speed filter time constant	s
T_G	Pre-filter time constant	s

T_{mech}	Mechanical time constant	s
$T_{Nd,q}$	Current PI-controller time constant	s
$T_{N\omega}$	Speed PI-controller time constant	s
T_t	Power electronic delay time	s
T_σ, T_Σ	Substitute time constants	s
U_{DC}	DC-link voltage	V
U_{max}	Rated stator voltage of electric machine	V
U_{ref}	Current control voltage command	V
$V_{R\omega}$	Speed PI-controller gain	$\mathrm{kgm^2/s}$
$V_{Rd,q}$	Current PI-controller gain	V/A
V_S	Gain of stator transfer function	$1/\Omega$
V_{inv}	Power electronic transfer function gain	-
α, β	Functions for analytic sensor error description	-
γ	Iron loss model fitting exponent	-
μ_{PM}	Permeability of magnet material	Vs/A
μ_0	Permeability of air	Vs/A
μ_{Fe}	Permeability of iron	Vs/A
Ψ_{PM}	Permanent magnet flux	Vs

Variables

a_k	Fourier coefficients of sensor error signal	$^\circ$
B	Magnetic flux density	T
d, q	Aligned d- and q-axis	-
$\bar{d}, \bar{q}$	Misaligned d- and q-axis	-
E_D, E_Q	Additional voltage terms	V
E_{ma}	Mean absolute sensor error	$^\circ$
E_{pp}	Peak-to-peak sensor error	$^\circ$
E_σ	Standard deviation of sensor error	$^\circ$
$E(\varepsilon)$	Residual expectation value	-
F_0	F-test value of regression model	-
F_{α,df_1,df_2}	F-distribution with confidence α and degrees of freedom df	-
$G_{d,q}(s)$	Stator dynamic transfer function	$1/\Omega$
$G_G(s)$	Speed control pre-filter transfer function	-
$G_{inv}(s)$	Approximated inverter power electronics transfer function	-
$G_{Rd,q}(s)$	Current controller transfer function in d- and q-axis	V/A
$G_{TL}(s)$	Tracking loop transfer function	-
$G_{T\theta}(s)$	Tracking loop position transfer function	-
$G_{T\omega}(s)$	Tracking loop speed transfer function	1/s
H_0	Null hypothesis	-
H_1	Alternative hypothesis	-
i_d, i_q	Machine currents in dq-reference frame	A

$i_{d,ref}, i_{q,ref}$	Control strategy reference currents for d- and q-axis	A
i_{dR}, i_{qR}	Equilibrium points of current control strategy	A
$\bar{i}_d, \bar{i}_q$	Misaligned d- and q-currents	A
i_{dc}, i_{qc}	Iron resistance currents	A
i_{d0}, i_{q0}	Machine currents with consideration of iron resistance	A
i_f	Short circuit current	A
i_α, i_β	Machine currents in $\alpha\beta$-reference frame	A
I_S	Stator current	A
k	Number of regression parameters	-
k_{DC}	Voltage offset	V
k_{AM}	Voltage scaling factor	-
k	Order of harmonic	-
k_1	Tracking loop control parameter	$1/s^2$
k_2	Tracking loop control parameter	$1/s$
L	Lagrangian	-
M_e	Electric machine torque	Nm
M_L	Load torque	Nm
M_{ref}	Reference torque	Nm
MS_E	Mean square error	-
MS_R	Mean square regression	-
n	Number of harmonic	-
n	Number of observations	-
n	Mechanical speed	rpm
p	Number of regression coefficients	-
P_{cu}	Copper losses	W
P_e	Electric machine power	kW
P_{el}	Electric input power of machine	kW
P_{fe}	Iron losses	W
$P_{fe,meas}$	Iron loss data from FEM simulation	W
P_{mech}	Mechanical output power of machine	kW
P_{stray}	Stray losses	W
P-Value	P-Value of statistical test	-
$\bar{P}$	Mean average power	W
R^2	Coefficient of determination	-
R^2_{adj}	Adjusted coefficient of determination	-
$R_0, \Delta R$	Static and magnetic field depending magneto-resistance	Ω
R_c	Iron resistance	Ω
$se(b_j)$	Standard error of regression coefficient b_j	-
$S_{\Delta\theta i_{d,q}}(s)$	Current disturbance transfer functions	rad/A
$S_{\Delta\theta M}(s)$	Torque disturbance transfer function	rad/Nm
$S_{\Delta\theta\omega}(s)$	Speed disturbance transfer function	$1/s$
SS_E	Error sum of squares	-
SS_R	Regression sum of squares	-

SS_T	Total sum of squares	-
t_0	t-test value of regression coefficient	-
$t_{\alpha/2,df}$	t-distribution with confidence α and degrees of freedom df	-
T	Measurement time interval	s
$T(j\omega)$	Closed current loop frequency response	-
$T_{id,q}(s)$	Closed loop current control transfer function	-
$T_\omega(s)$	Closed speed control transfer function	-
u_a, u_b, u_c	Phase voltages in stationary abc-reference frame	V
u_d, u_q	Machine voltages in dq-reference frame	V
u_{d0}, u_{q0}	Iron resistance voltages	V
$u_{dq,comp}$	Compensation voltages for d- and q-axis	V
u_{id}, u_{iq}	Current control voltages for d- and q-axis	V
u_α, u_β	Machine voltages in $\alpha\beta$-reference frame	V
$\bar{u}_d, \bar{u}_q$	Misaligned d- and q-voltages	V
U_{err}	Resolver error voltage	V
U_{exc}	Resolver excitation signal	V
U_{sin}, U_{cos}	Sine and cosine sensor output voltage	V
U^*_{sin}, U^*_{cos}	Normalized sine and cosine sensor output voltage	V
$\hat{U}$	Resolver output voltage amplitude	V
$\bar{U}_{sin}, \bar{U}_{cos}$	Arithmetic mean sine and cosine sensor output voltage	V
$Var(\varepsilon)$	Residual variance	-
w_i	Weighting coefficients	-
x_i	Regression parameter	-
x^*_i	Normalized regression parameter	-
y	Regression model	-
$\hat{y}$	Fitted regression model	-
$\hat{y}_{red}$	Reduced regression model	-
β	Current angle	°
β_j	Regression model coefficient	-
δ	Damping factor	1/s
Δn	Speed variation	rpm
$\Delta x, \Delta y, \Delta z$	Mechanical misalignment in x-, y-, z-direction	mm
ΔM	Torque ripple	%
ΔT	Temperature variation	°C
ΔV	Supply voltage variation	V
$\Delta\theta$	Rotor position error	rad
$\Delta\theta_m$	Mechanical sensor error	rad
$\Delta\varphi$	Tilt angle between sensor rotor and stator plane	°
$\Delta\omega$	Speed difference of aligned and misaligned reference frame	rad/s
$\Delta\omega_R$	Linearization equilibrium point for electric speed error	rad/s
$\Delta\theta_R$	Linearization equilibrium point for electric angle error	rad
ε	Regression model residual error	-
ε	Resolver-to-digital estimation error	rad

ε_i	Residuals	-
η	Efficiency	%
θ	Electrical rotor position	rad
θ_m	Mechanical rotor position	rad
$\bar{\theta}$	Measured rotor position	rad
$\hat{\theta}$	Estimated rotor position	rad
λ	Lagrangian multiplier	-
$\lambda_a, \lambda_b, \lambda_c$	Flux linkage in stationary *abc*-reference frame	Vs
$\hat{\mu}$	Estimation of expected value	-
ν	Welch-test degrees of freedom	-
σ^2	Variance of residuals	-
σ^2	Pooled variance for two-sample t-test	-
$\hat{\sigma}^2$	Estimation of residuals variance	-
φ	Phase error	rad
ϕ	Basis function	-
Ψ_0	Stator flux	Vs
ω	Electric angular frequency	rad/s
ω_m	Mechanical angular frequency	rad/s
ω_x	Resolver excitation frequency	rad/s
ω_0	Natural frequency	rad/s
$\bar{\omega}$	Misaligned rotor speed	rad/s

Vectors

$\mathbf{a}$	Vector of linear regression coefficients
$\mathbf{b}$	Least squares estimators of $\boldsymbol{\beta}$
$\mathbf{e}$	Vector of least square residuals
$\mathbf{f}$	System function
$\mathbf{g}$	Output function
$\mathbf{i}$	Current vector
$\mathbf{x}$	State vector
$\mathbf{x}_\mathbf{i}^*$	Observation point of regression model
$\mathbf{x}_R, \mathbf{u}_R$	Equilibrium points
$\mathbf{x}_s$	Stationary point
$\mathbf{u}$	Input vector
$\mathbf{u}$	Voltage vector
$\mathbf{y}$	Output vector
$\mathbf{y}$	Vector of observations
$\hat{\mathbf{y}}$	Fitted regression model
$\boldsymbol{\beta}$	Vector of regression coefficients
$\boldsymbol{\Delta\lambda}$	Flux linkage of reluctance inductance
$\boldsymbol{\varepsilon}$	Vector of residuals

$\boldsymbol{\lambda}$	Flux linkage vector

Matrices

$\mathbf{A}$	Dynamic matrix
$\mathbf{B}$	Input matrix
$\mathbf{B}$	Matrix of interaction and quadratic regression coefficients
$\mathbf{C}$	Output matrix
$\mathrm{Cov}(\mathbf{b})$	Variance-covariance matrix of model parameters $\mathbf{b}$
$\mathbf{D}$	Feedforward matrix
$\mathbf{E}$	Identity matrix
$\mathbf{G}(s)$	Transfer function matrix
$\mathbf{L}_{abc}$	Stator inductance matrix
$\mathbf{L}_{\alpha\beta}$	Stator inductance matrix in $\alpha\beta$-reference frame
$\mathbf{L}_{rlc}$	Rotor angle dependent stator inductance matrix
$\mathbf{M}$	Moment matrix
$\mathbf{R}$	Rotation matrix
$\mathbf{T}$	Transformation matrix
$\mathbf{X}$	Design or Model matrix
$\mathbf{X}^{+}$	Moore-Penrose pseudoinverse of $\mathbf{X}$

1. Introduction

The importance of electric machines as propulsion systems for electric or hybrid vehicles has increased recently, since utilization of such motors promises to be an effective method for reducing CO_2 emissions. Different electric motor types are available such as

- DC Machines
- Induction Machines
- Permanent Magnet Synchronous Machines
- Brushless DC Machines
- Switched Reluctance Machines
- Transverse Flux Machines.

All of these types provide advantages and disadvantages. Technical characteristics of the different technologies and a detailed comparison can be found in literature, e.g. [1], [2]. At the moment, three-phase electric machines such as Induction (IM) and Permanent Magnet Synchronous Machines (PMSM) seem to be the most interesting solutions for electric and hybrid vehicles. These machines are usually controlled via field-oriented control concept (FOC), which demands a rotor position, respectively rotor speed measurement. PMSM's, as depicted in Figure 1.1, are usually field-oriented controlled with a rotor position sensor, whereas for the IM a speed encoder is sufficient in general [3]. This work focuses on rotor position sensor error characteristics and its influence on the control of a PMSM, therefore no other machine types are considered further.

Figure 1.1.: Interior Permanent Magnet Synchronous Machine [4].

Note that the purpose of the present work is motivated by automotive sensors and applications, but the results and methods are not restricted to these specific applications.

1.1. Rotor Position Measurement for Electric Vehicle Applications

The rotor position information plays a key role in the field-oriented control concept. This is the state of the art method for controlling a three-phase electric machine within electric or hybrid vehicle propulsion systems. This concept allows a high dynamic control of three-phase electric machines, which is desired for vehicle traction applications. Due to the fact that certain coordinate transformation are necessary within the FOC, the rotor position of the electric machines must be measured. For this purpose, several rotor position sensor concepts are available. Figure 1.2 shows the basic control architecture of an electric drive within a vehicle powertrain.

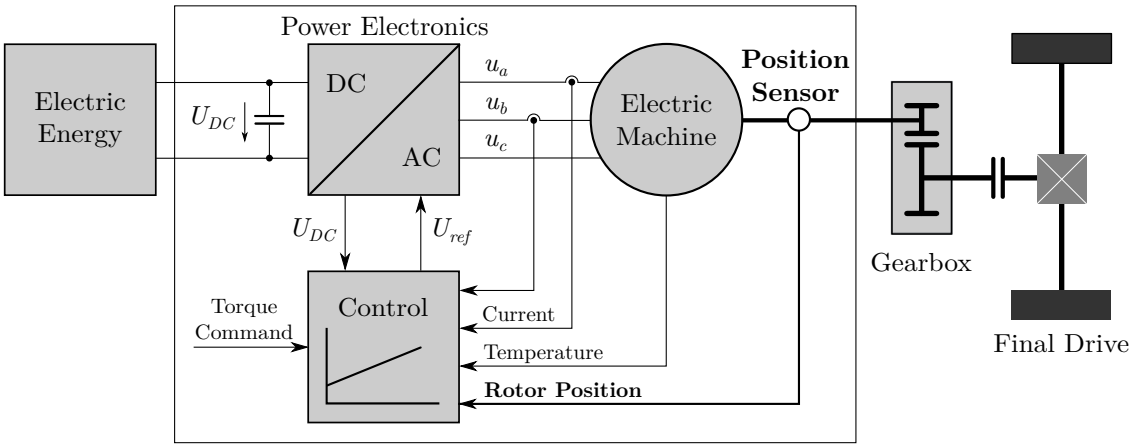

Figure 1.2.: Typical architecture of an electric vehicle [5].

For hybrid vehicles, different kinds of hybridization concepts have been developed. These concepts differ in different characteristics; e.g. in their power ratio between electric machine and internal combustion engine, such as Crank-Starter-Generator (CSG), Belt-driven-Starter-Generator (BSG), Integrated-Motor-Generator (IMG) and Separate-Motor-Generator(SMG) [6].

Besides electric and hybrid vehicles, electrification of conventional powertrains is another key technology to reduce emissions. Therefore, ancillary units like power steering, cooling units, fuel pumps, etc. are replaced by controlled electric actuators, for example PMSM's and Brushless DC (BLDC) machines [6]. Figure 1.3 shows the architecture of an exemplary electric power steering application, where PMSM is used to provide an additional torque, represented as an actuator connected to the steering wheel system.

Both machine types need the rotor position information for commutation purposes, but the requirements on BLDC types on rotor position measurement is drastically lower than for the PMSM type. In this work, only absolute rotor position sensors are considered, which are applied within field-oriented control of PMSM. Figure 1.4 shows the basic idea

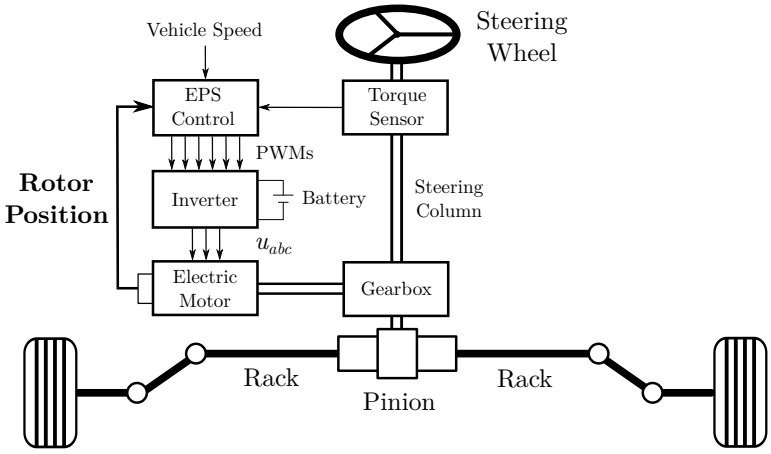

Figure 1.3.: Electric power steering as an exemplary application of a PMSM with rotor position sensor, adapted from [7].

behind this control method and the rotor position sensor's role in it.

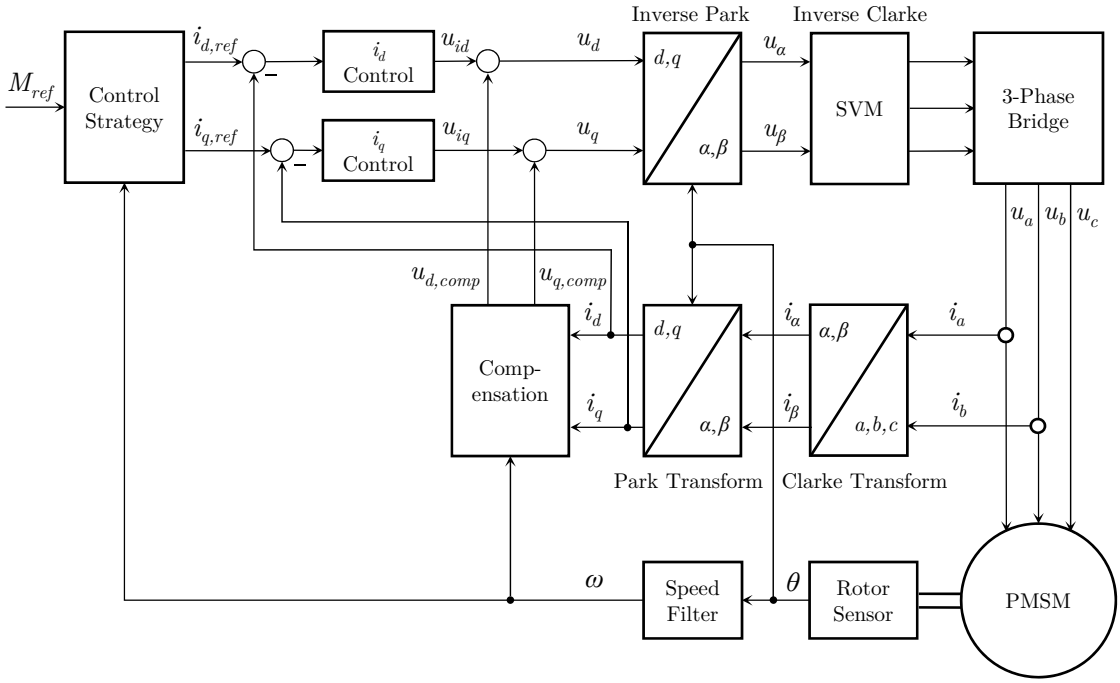

Figure 1.4.: Field-oriented control concept and rotor position sensor.

The rotor position information is used to perform a transformation from the stator reference frame to the rotor reference frame and vice versa, which is usually denoted in most common literature as Park and inverse Park transformation. A more detailed funda-

mental description of the field-oriented control concept in combination with permanent magnet synchronous machines is given in Section 4.2.3. Additionally, a speed information signal is derived by the rotor position measurement, which plays an important role for speed control applications. This topic is discussed in more detail in Section 4.12.

1.2. Thesis Contribution and Outline

The research issue of this work consists of two main goals: The first one represents the development of a method to evaluate different rotor position sensors regarding parameter robustness and assess their automotive usability under use of a specific test bench. The second one includes a mathematical description to investigate how different kinds of measured rotor position signals do interfere the field-orientated control of PMSM and to rate the sensor measurement error impact on various control quality aspects.

This work is subdivided into four chapters. In the introduction chapter the motivation is presented, why rotor position measurement plays an important role for automotive applications, respectively for electric drive engineering in general.

In Chapter 2, different sensor technologies, which are suitable for automotive applications, are introduced. Additionally, the necessary signal processing of these sensors and different error types are classified and discussed to provide better insights into various sensor error mechanisms.

Chapter 3 introduces a methodology to test different automotive rotor position sensors regarding their robustness of different parameter variations. For this purpose, a test bench was designed, which is used to vary different sensor parameters and to investigate their influence on measurement accuracy. This method provides information within the complete experimental space, but with a tractable amount of necessary measurements to rate and compare different sensor concepts with each other. This chapter deals with the evaluation of sensor error characteristics regarding parameter variations by use of the specific test bench, its mathematical and statistical description and benchmarking of different sensor types and configurations.

In Chapter 4, an analytic approach is presented to compute the sensor error contribution regarding torque, different control strategies and efficiency of the electric drive system. Additionally, the influence of rotor position measurement errors regarding speed control applications is investigated. This method allows a complete description of the dynamic system consisting of controller, electric machine and disturbance represented by the measured sensor error. This approach is applicable for the PMSM machine type within the complete speed range, which constitutes an enhancement of previous work in this field.

2. Automotive Rotor Position Sensors and Error Mechanisms

This chapter introduces different rotor position sensor technologies, which are utilized within automotive environments. These sensors provide conceivably different electrical interfaces; therefore various rotor position calculation methods are introduced. The focus lies on analogues sine, respectively cosine signals and modulated resolver signals. Additionally, the effect of different kinds of influences and distortions in these signals regarding the resulting sensor error is summarized at the end of this chapter.

2.1. State of the Art Automotive Rotor Position Sensors and Functional Principles

Several physical principles can be exploited to perform rotor position measurement. Figure 2.1 shows an overview of different rotor position sensor working principles with available interfaces and which of these types are further considered in this work.

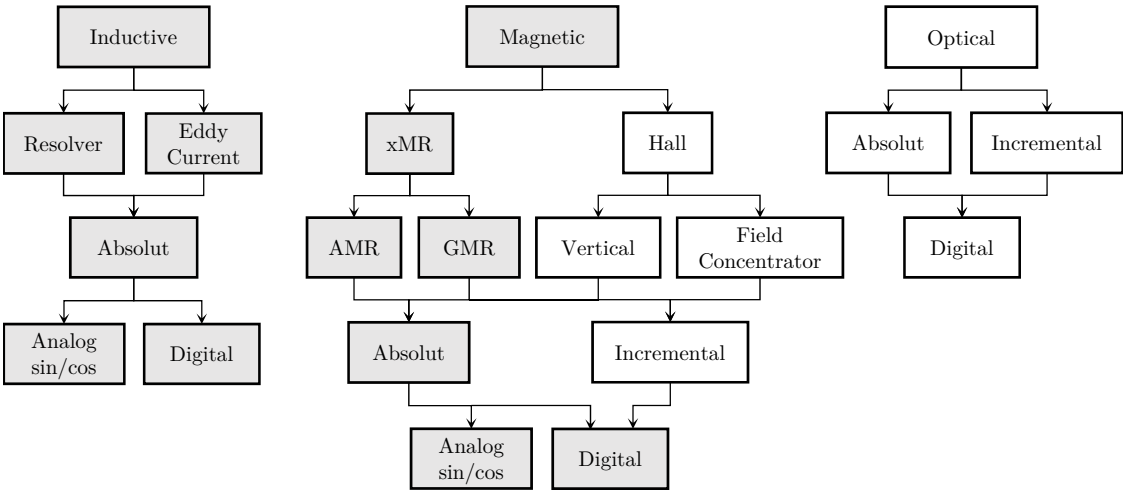

Figure 2.1.: Rotor position sensor overview according to [6]. Grey underlined sensor principles are investigated in this work.

For automotive applications, robustness of the sensors regarding temperature, dust, vibrations etc. is mandatory. Other technologies, for example optical sensors, are designed with very high accuracy and resolution, but are typically not used within automotive environments. This is caused due to their sensitivity to mechanical tolerances, insufficient robustness regarding harsh surroundings and high costs [6].

2.1.1. Resolver

A resolver is basically a rotating transformer and the most common used sensor type for this kind of application. It consists of a primary and two secondary windings, where the primary winding is located on the rotor and is excited by a frequency of a few kHz. The secondary windings are placed orthogonal to each other inside the stator and provide modulated sine and cosine signals according to the resolver rotor, respectively motor shaft position θ. As described in [8], this resolver technology is known as Wound Field (WF) resolver and has several disadvantages due to necessary rotor excitation, which increases the total axial length and complicates the manufacturing process. In contrast to the WF resolver, the Variable Reluctance (VR) resolver has both output and excitation windings on the stator. This technology has the benefits of a shorter axial length, easier integration, a more simple structure and better robustness regarding temperature and external field distortions. Therefore, this type of resolver is the preferred choice in automotive applications. Figure 2.2 shows the schematic principle of both resolver types.

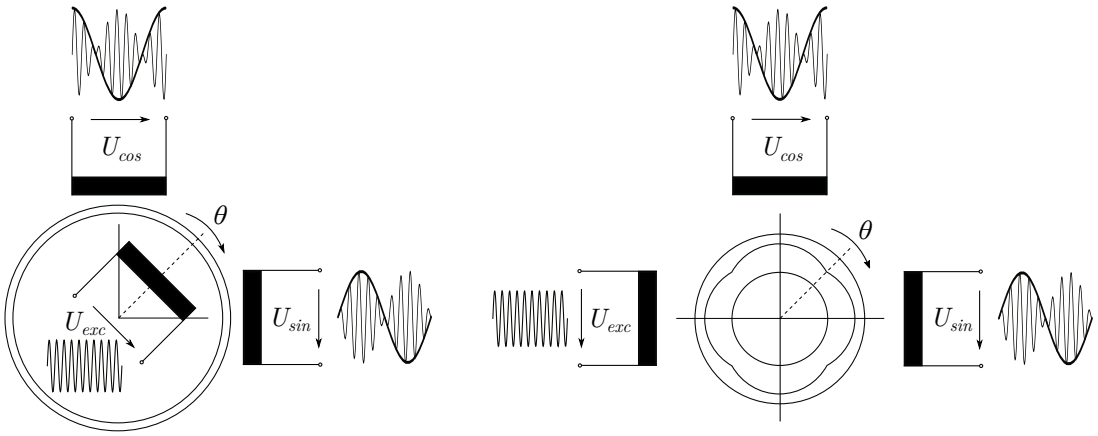

Figure 2.2.: Resolver principle: Wound Field (left) and Variable Reluctance (right) resolver.

The significant difference in their operating principle is, that the WF type is designed with a constant air-gap length and provides sinusoidal output voltages due to a sinusoidal distributed excitation winding. In contrary, the VR resolver has uniform distributed excitation coils and the sinusoidal output signals are a consequence of the sinusoidal air-

gap flux density established through a sinusoidal air-gap permeability, which is provided by the specific shaped rotor design. The pole number of the specific shaped rotor usually matches the pole number of the used electric machine. Figure 2.3 shows exemplary technical realizations of a WF and VR resolver.

Figure 2.3.: Technical realization of a Wound Field (left) [9] and Variable Reluctance resolver (right) [10].

Properties of the resolver can be summarized as:

- High Accuracy
- Elaborate signal processing
- High excitation currents
- Sensitive to mechanical tolerances and external electromagnetic fields
- High system costs
- Large installation space requirements

2.1.2. Magnetoresistive Sensors

In this subsection, sensor principles are introduced which interact with external magnetic fields like Hall-based and Magnetoresisitve (MR) sensors. Due to their advantages according accuracy, sensitivity and temperature stability, MR sensors replaced Hall-based sensors in automotive electric traction motor applications, therefore only the latter will be discussed. Magnetoresistive sensors can be subdivided into AMR (Anistropic Magnetoresisitve), GMR (Giant Magnetoresistive) and TMR (Tunnel Magnetoresistance) types, but only the first two are further considered in this work. This is caused by the fact, that no TMR example is part of further investigations, but the presented methods and characterization do not depend on the utilized physical principle. Origin of the magnetoresistance is - as for the Hall effect - the Lorentz force, where due to a magnetic field the current path is increased, which increases the effective resistance of the structure. The AMR effect was discovered 1857 by William Thomson and is a typical effect in ferromagnetic materials. It is described as a change in the scattering due to atomic

orbitals caused by magnetic fields. According to [11], the dependency of the resistance as a function of magnetization direction θ is described as:

$$R(\theta) = R_0 + \Delta R \cos^2\theta = R_0 \left(1 + \frac{\Delta R}{R} \cos^2\theta\right) \tag{2.1}$$

Due to the squared cosine term in equation 2.1, the AMR sensor shows two sine shaped curves over one full mechanical revolution. Figure 2.4 shows the basic principle of magnetoresistance of the material or structure resistance as a function of external magnetic fields.

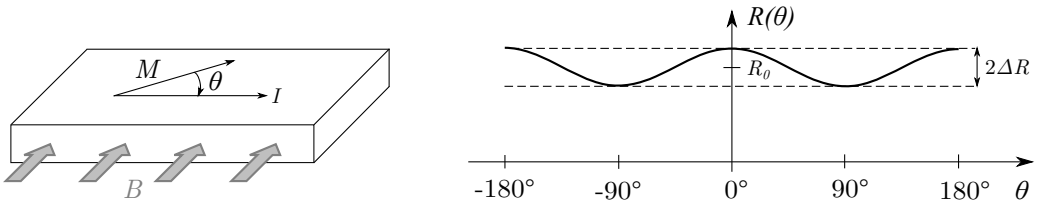

Figure 2.4.: Operating principle of a MR element. A magnetic field B, which is passing the MR sensor, is influencing the internal magnetization M of the sensing element and thereby modifying its resistance [11].

To minimize temperature influences, usually four resistors are combined to Wheatstone's bridges. By adding a second 45° shifted AMR bridge, the necessary cosine signal for rotor position calculation is generated. Both signals squared have to fulfil the $\sin^2\theta + \cos^2\theta = 1$ identity, which is used for self diagnosis purposes. Because of its high resistance and low magnetostriction, Permalloy ($Ni_{81}Fe_{19}$) is the most used material for AMR sensors.

The GMR effect is, like the AMR effect, obtainable by interaction with ferromagnetic materials. As described in [6], this technology uses multiple ferromagnetic alloys as sensing elements, which are separated by non-magnetic interlayers. At least 2 layers are necessary, which are separated by a non-magnetic intermediate layer. The change of resistance depends on the angle between the magnetic directions of superposed thin-films. With no external field, both layers are aligned anti-parallel. Under the influence of external magnetic fields, the magnetizations and their directions are influenced. The GMR layers have maximum resistance by anti-parallel aligned magnetizations and vice versa; therefore an external field has a decreased resistance as consequence. The sensitivity is comparable with AMR sensors, but with the benefit of an unambiguous 360° rotor position calculation over one mechanical revolution.

All of the magnetoresisitive sensor principles have in common, that a permanent magnet is required, which carries the rotor position information in it. Specified by the design of the AMR and GMR brigdes, the sensor senses different components of the magnet field, but mostly diametrically magnetized magnets are used for this purpose. These magnets

have to be mounted on the end of the shaft and to rotate near above the sensor chip surface. Therefore, these sensor types will be further indicated as end-of-shaft sensors in this work. Figure 2.5 shows a sensor, which operates with a diametrically magnetized permanent magnet and the resulting output voltages produced by the sensitive MR bridges.

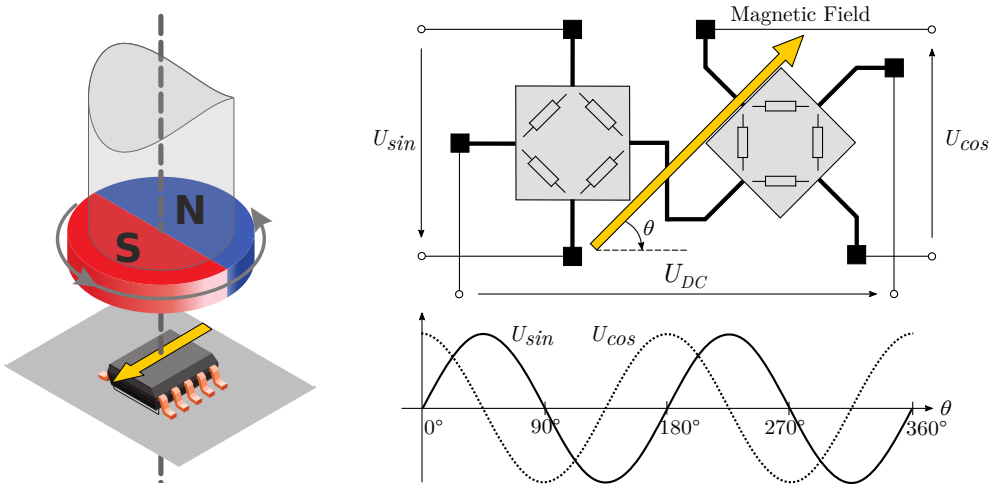

Figure 2.5.: MR sensor integration with sensitive bridges and output signals [12]

.

The necessity of such magnets implies, that these sensors are mainly used in end-of-shaft applications in contrast to eddy current sensors and resolvers. Properties of the xMR sensors can be summarized as:

- Less installation space requirements
- Low power consumption and simpler signal processing within application specific integrated circuit (ASIC) and different kind of interfaces
- Less sensitive regarding mechanical tolerances
- High accuracy only for end-of-shaft applications
- Sensitive regarding external electromagnetic fields

2.1.3. Eddy Current Sensors

Measuring the rotor position with eddy currents is a newer technology and is categorized as inductive angle sensor. These sensors consist of one excitation, two identical spatial phase shifted receiving coils, and a conductive rotor part. The excitation coil is driven with a periodic alternating current. An electromagnetic field is produced on the circumference of the excitation coil, which influences the impedance of receiving coils. Due to the winding scheme, the directly induced voltages from the excitation coils cancel each

other out. The induced voltages on the receiving coils are producing an eddy current flowing on the conductive rotor part, which depends on the conductive rotor part position and its shape. Figure 2.6 shows an exemplary design of an eddy current rotor position sensor with optimized shape of receiving coils and rotor part.

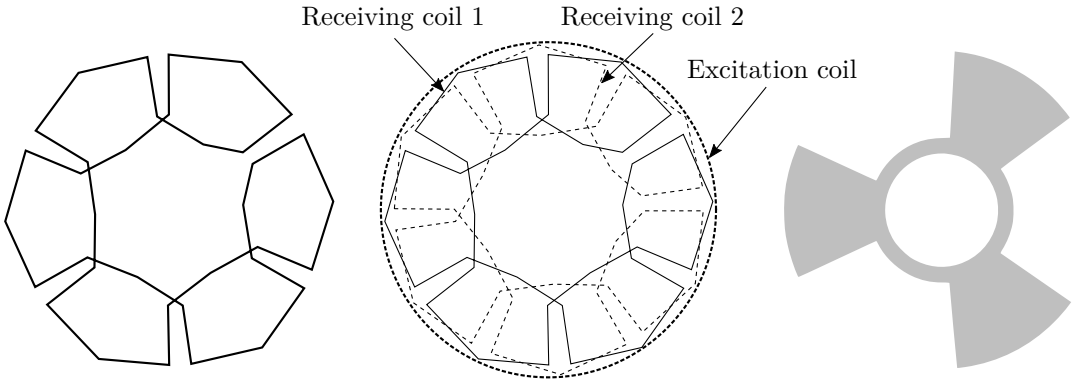

Figure 2.6.: Structure of a receiving coil (left), both receiving and excitation coils (middle) and optimized rotor shape design (right) [13]

As proposed in [13], the shaping of these rotor parts is mostly done by a combination of Finite Element Method (FEM) simulation and optimization algorithms. Due to the high frequency operation, eddy current sensors provide a better robustness against electromagnetic distortions. Figure 2.7 shows a technical realization of an eddy current sensor consisting of moon-shaped evaluation electronics and conductive rotor part.

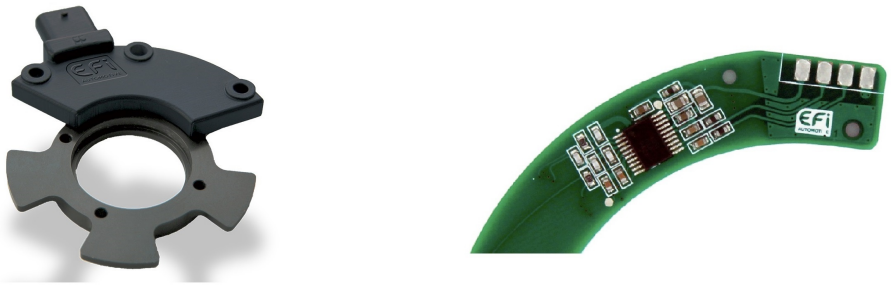

Figure 2.7.: Technical realization of an eddy current sensor (left) and evaluation electronics (right) [14].

Properties of the eddy current sensors can be summarized as:

- Flexible design of rotor shape and evaluation electronics
- Improved immunity to external magnetic fields due to high frequent eddy currents
- Integrated signal processing with different interfaces

- Installation space requirements comparable with resolver
- Lower accuracy compared to resolver and xMR sensors

2.2. Sensor Output Signals and Rotor Position Calculation

The three main types of discussed sensors provide analog signals (xMR and eddy current) or modulated sine and cosine signals (resolver). Both types differ in their state of the art rotor position angle calculation method.

2.2.1. Sine and Cosine Signals

Most rotor position sensors provide sine and cosine shaped output signals, where the angle of the rotor shaft θ is directly calculated with the output voltages U_{sin}, U_{cos} and the trigonometric identity

$$\theta = \arctan\left(\frac{U_{sin}}{U_{cos}}\right) \tag{2.2}$$

To receive continuous values for the rotor angle θ from 0 to 2π, a quadrant correction is necessary, which is realized as

$$\theta = \begin{cases} \arctan\left(\frac{U_{sin}}{U_{cos}}\right) & \text{if } U_{sin} \geq 0, U_{cos} \geq 0 \\ \arctan\left(\frac{U_{sin}}{U_{cos}}\right) + \pi & \text{if } U_{cos} \leq 0 \\ \arctan\left(\frac{U_{sin}}{U_{cos}}\right) + 2\pi & \text{if } U_{sin} < 0, U_{cos} > 0 \end{cases} \tag{2.3}$$

Figure 2.8, left, shows typical angle calculations results via sine and cosine output signals. Note that a DC offset compensation and amplitude normalization is performed before the rotor angle calculation, because this conforms to standard signal preprocessing within any application dealing with position sensors. A proposed method of normalizing sine and cosine signals include for example the removement of the DC component $\bar{U}_{sin,cos}$ and a normalization with the signal amplitudes $\hat{U}_{sin,cos}$, which can be written as

$$U^*_{sin,cos} = \frac{U_{sin,cos} - \bar{U}_{sin,cos}}{\hat{U}_{sin,cos}} \tag{2.4}$$

This normalization is important for maintaining stable rotor position measurement results, because sine and cosine signals might drift with temperature or contain additional noise. Applying a normalization in combination with filtering, both output signals establish a robust rotor angle position calculation. Figure 2.8, right, shows how a sensor harmonic distortion is added caused by a mechanical misalignment. This leads to an error in the computed rotor position. Note that the mechanical misalignment and the rotor position error is exaggerated for demonstration purposes, and not within a realistic order

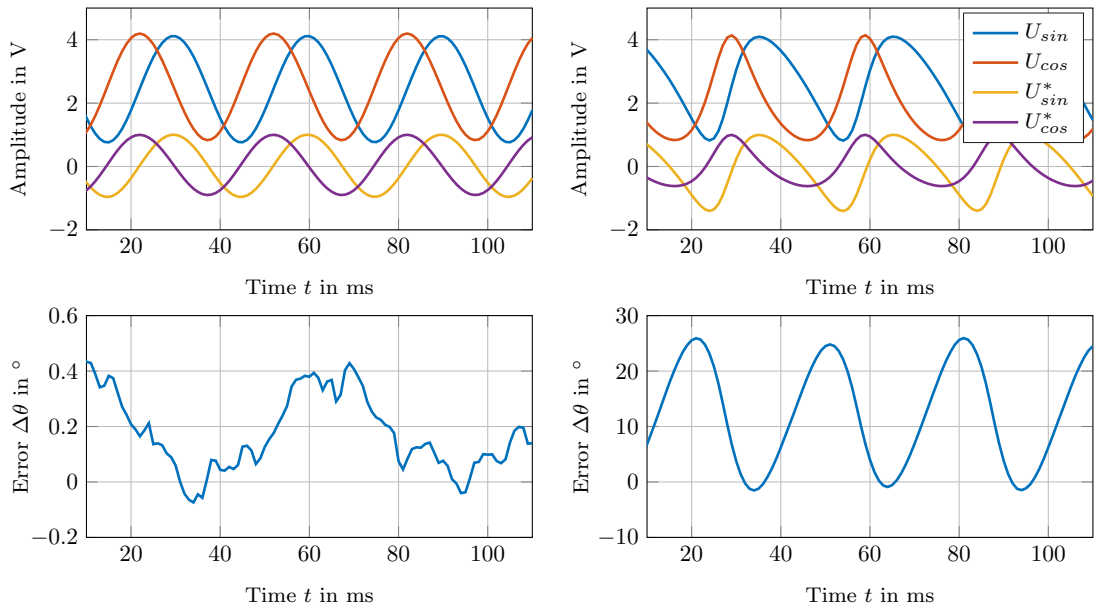

Figure 2.8.: Aligned (left) and strong misaligned (right) end-of-shaft sensor: corresponding sine and cosine signals and resulting rotor position error.

of magnitude for typical applications. In [15] and [16] methods are introduced, which improve the sensor output signal quality by an online optimization of correction terms regarding offset, harmonic distortion and quadrature phase shift. These approaches are not part of this work and not further investigated, because the focus of this work lies on a sensor behaviour description, without considering additional algorithms to improve the sensor's measurement performance.

2.2.2. Resolver Signals and Resolver-to-Digital Conversion

As described in 2.1.1, resolvers provide amplitude modulated signals. In a first step, these signals have to be demodulated to receive the envelope sine and cosine signals. For demodulated signals, Equation 2.2 could be directly applied, but in general a resolver is preprocessed with a resolver-to-digital conversion. This method, combined with a so-called tracking loop or angle tracking observer, allows better performance, accuracy and an additional smooth velocity calculation [17]. In addition to that, the division operation and arctangent function realization is non-trivial for embedded system implementations [18]. The basic structure of a resolver-to-digital conversion is shown in Figure 2.9.

The idea behind the angle tracking observer is to use a PI-controller within a closed phase loop, where the angle tracking observer is comparing the demodulated resolver output signals $\sin\theta$ and $\cos\theta$ with the estimation of the actual rotor position $\hat{\theta}$. The

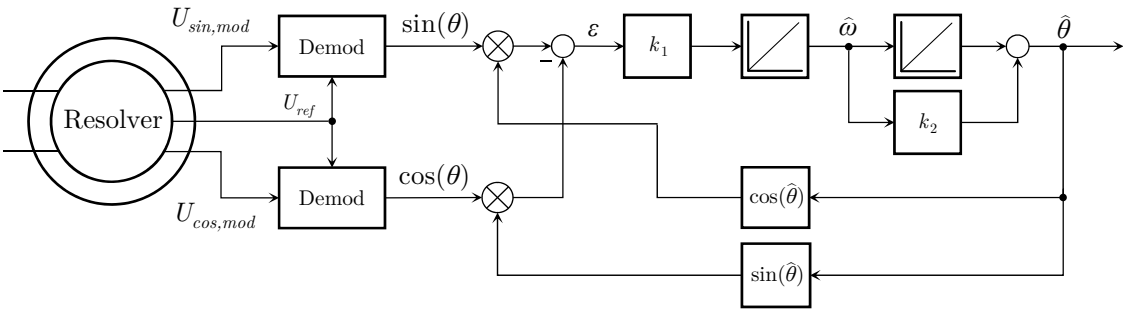

Figure 2.9.: Modulated sine and cosine signals within resolver tracking loop.

controller has the intention to minimize the deviation of the rotor position signals and position estimation $\hat{\theta}$. Utilization of the trigonometric identity

$$\varepsilon = \sin\theta\cos\hat{\theta} - \cos\theta\sin\hat{\theta} = \sin(\theta - \hat{\theta}) \tag{2.5}$$

and the sine approximation for small arguments

$$\sin(\theta - \hat{\theta}) \approx \theta - \hat{\theta}$$

leads to an error ε, which is minimized by the control loop and settles the rotor position error to zero. This means, that after a specific settling time, the real rotor position θ and the rotor position estimate $\hat{\theta}$ are matching each other. A benefit of this method is that an estimation of the rotor speed $\hat{\omega}$ - after an integration of the position error - is available too, which is beneficial for speed control applications. The transfer function of the closed loop system can be written as

$$G_{TL}(s) = \frac{\hat{\theta}(s)}{\theta(s)} = \frac{k_1(1 + k_2 s)}{s^2 + k_1 k_2 s + k_1}$$

The characteristic polynomial, which determines the dynamic behaviour, is defined by the coefficients k_1, k_2 and defines a general second-order system. Using the common abbreviations for these systems

$$k_1 = \omega_0^2$$
$$k_2 = \frac{2\delta}{\omega_0}$$

with damping factor δ and natural frequency ω_0 leads to

$$G_{TL}(s) = \frac{1 + s\frac{2\delta}{\omega_0}}{1 + s\frac{2\delta}{\omega_0} + s^2\frac{1}{\omega_0^2}}$$

Damping factor δ and natural frequency ω_0 are used to determine the dynamics of

the angle tracking observer in terms of overshoot and settling time for dynamic rotor position manoeuvres. Typical values for δ and ω_0 can be found in [18] and depend on the implemented application. Usually, a voltage controlled oscillator (VCO), fed by the speed signal $\hat{\omega}$, is used in combination with an up/down-counter to create a digital representation of the estimated rotor angle information $\hat{\theta}$.

2.3. Different Rotor Position Sensor Errors

In this section, a summary of different causes for rotor position errors is given. These errors are subdivided into different categories and approaches for analytic calculations of analogue output and resolver signals are presented. Methods will be introduced to show how different types of error influence the measurement results of analogue sensors and resolver types.

2.3.1. Sine and Cosine Signals

The output signals U_{sin} and U_{cos} may have different amplitudes and DC offset components. As described in the former section, offset ellimination and amplitude mismatch normalization is a standard procedure within the sensor's signal processing. For further investigations, the assumption is made, that this former signal conditioning is performed. Without these corrections, the rotor angle calculation sensitivity will be high and no stable measurements on the test bench or within a specific application are possible. Publications [19] and [20] describe, how the sine and cosine output signals from the rotor position sensor result in a wrong calculated position. The former describes the sensor error exact and the latter gives approximations for the calculated error. The variations of the sensors parameter takes direct effect on the shape to the sensor output signals, adds different harmonic content and thus additional errors in the rotor angle calculation occur. These errors can mainly be subdivided into:

1. DC Offset Error
2. Amplitude Mismatch Error
3. Harmonic Error
4. Quadrature Phase Shift Error

These different error types are caused due to non-ideal magnetization, shaft assembly variations, harmonic content, a DC bias or quadrature phase shift in the sensor signals. In adaption to [19], the basic idea to calculate the resulting rotor position error is to use the identity

$$\arctan(\alpha) + \arctan(\beta) = \arctan\left(\frac{\alpha + \beta}{1 - \alpha\beta}\right) \tag{2.6}$$

and setting $\alpha = \tan\theta$. Then the resulting angle error is calculated as

$$\Delta\theta = \theta - \bar{\theta} = -\arctan(\beta) \tag{2.7}$$

with the measured rotor position $\bar{\theta}$ and the function β, which has to be determined for the given case of specific sensor error.

2.3.2. Resolver Signals

Modulated resolver signals in combination with an angle track observer have the same error influences (except DC Offset Error), but additive errors can occur. According to [21], additional error types due to non-ideal resolver signals can be subdivided into:

5. Inductive Harmonics Error
6. Excitation Signal Distortion Error
7. Disturbance Signal Error

The calculation of these type of errors is based on considering a non-ideal angle tracking observation, which is used to drive the error signal ε to zero. By obtaining Figure 2.9, the error for the tracking loop results in

$$\varepsilon = \hat{U}\sin\theta\cos\hat{\theta}\sin\omega_x t - \hat{U}\cos\theta\sin\hat{\theta}\sin\omega_x t = \hat{U}\sin(\theta-\hat{\theta})\sin\omega_x t$$

with resolver excitation frequency ω_x, rotor shaft angle θ, estimated rotor position $\hat{\theta}$ and output signal amplitude $\hat{U}$. After demodulation, the remaining error signal ε

$$\varepsilon = \hat{U}\sin(\theta-\hat{\theta}) \stackrel{!}{=} 0$$

is driven to zero by the tracking loop which implies that $\theta = \hat{\theta}$. Due to the non-ideal resolver-to-digital conversion, an additional error voltage may occur and the tracking loop will track to a wrong estimated position

$$\varepsilon = \hat{U}\sin(\theta-\hat{\theta}) + U_{err} \stackrel{!}{=} 0$$

Note that only the sine signal is manipulated and the cosine signal is kept constant. In an actual parameter variation, the cosine signal will also be influenced, which adds more complexity to the resulting rotor angle error. The next sections give insight to a selection of signal manipulations and resulting errors due to the performed rotor position calculation.

2.4. Analytic Description of Different Sensor Errors

In the former section, several kinds of error mechanisms are distinguished into different categories. In this section, analytic approaches are introduced to describe the impact on the sensor measurement capability, if one of these errors is present. Analytic results and approximations are presented for analogue and resolver output signals. Note that these analytic calculations are not used further for sensor modelling and characterization. This chapter is a summary of different analytic error calculations to give an insight into mechanisms, how rotor position errors occur by various signal manipulations. The real, but usually unknown rotor position is indicated as θ, the measured rotor position as $\bar{\theta}$, and the difference - which represents the sensor error - as $\Delta\theta$.

2.4.1. DC Offset Errors

Different mean values of sine and cosine signals produces a DC offset error. The impact of a DC component on the sine component can be formulated as

$$\bar{\theta} = \arctan\left(\frac{U_{sin}}{U_{cos}}\right) = \arctan\left(\frac{\sin\theta + k_{DC}}{\cos\theta}\right)$$

with a DC offset of amplitude k_{DC} and ideal rotor shaft angle θ. By using Equation 2.6

$$\frac{\sin\theta + k_{DC}}{\cos\theta} \stackrel{!}{=} \frac{\alpha + \beta}{1 - \alpha\beta} = \frac{\tan\theta + \beta}{1 - \tan\theta\beta} \tag{2.8}$$

the function β and resulting sensor position error $\Delta\theta$ are calculated for this case as

$$\beta_{DC} = \frac{k_{DC}\cos\theta}{k_{DC}\sin\theta + 1} \Rightarrow \Delta\theta = -\arctan\left(\frac{k_{DC}\cos\theta}{k_{DC}\sin\theta + 1}\right)$$

Figure 2.10 shows, how the sensor error is developed by an additional DC offset in the sine signal for different values of k_{DC}. This kind of error is usually not discussed regarding resolver errors.

2.4.2. Amplitude Mismatch

In the ideal case, sine and cosine output signals have same amplitudes. Normalization of these two signals is usually done within the signal processing, which means that both signals are normalized to an amplitude of 1. If this is not the case, an additional error component will occur in the sensor position calculation. The amplitude imbalance is considered with a scaling factor $(1 + k_{AM})$ in the sine amplitude and is written as

$$\bar{\theta} = \arctan\left(\frac{U_{sin}}{U_{cos}}\right) = \arctan\left(\frac{(1 + k_{AM})\sin\theta}{\cos\theta}\right)$$

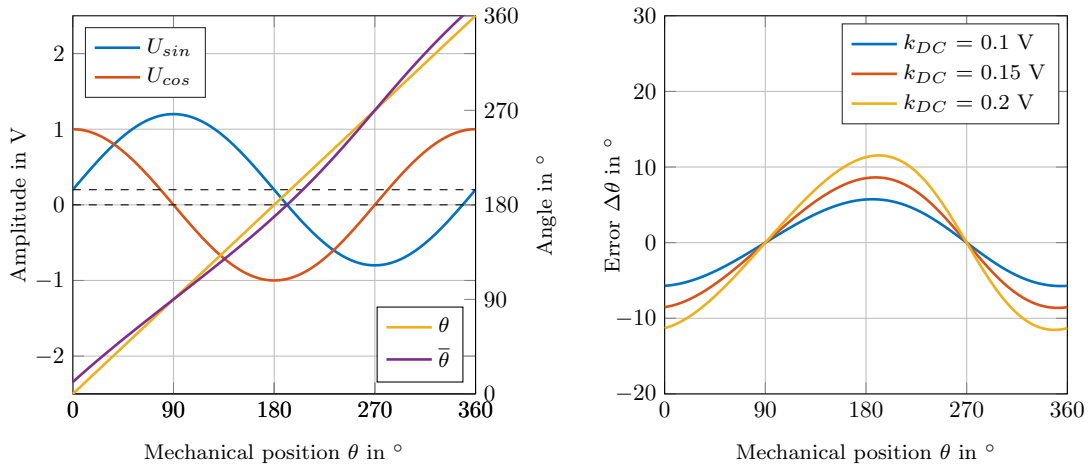

Figure 2.10.: DC Offset error in sine signal and resulting error for different values of k_{DC}.

Calculation of the searched function β and resulting sensor error in this case leads to

$$\beta_{AM} = \frac{-\sin\theta\cos\theta k_{AM}}{\cos^2\theta k_{AM} - k_{AM} - 1} \Rightarrow \Delta\theta = -\arctan\left(\frac{-\sin\theta\cos\theta k_{AM}}{\cos^2\theta k_{AM} - k_{AM} - 1}\right)$$

For resolver signals, calculation of amplitude imbalance is formulated as

$$U_{err} = U_{sin} - U_{cos} = \hat{U}\left((1+k_{AM})\sin\theta\cos\hat{\theta} - \cos\theta\sin\hat{\theta}\right)$$

$$U_{err} = \frac{1}{2}\hat{U}\left(-(k_{AM}+2)\sin(\underbrace{\theta-\hat{\theta}}_{\varepsilon}) - k_{AM}\sin(\theta+\hat{\theta})\right) \stackrel{!}{=} 0$$

Using $\varepsilon = \theta$ - $\hat{\theta}$ as position error yields to

$$\varepsilon = -\arcsin\left(\frac{k_{AM}}{k_{AM}+2}\sin(\theta+\hat{\theta})\right)$$

Assumption of small values for k_{AM}, using $\sin\varepsilon \approx \varepsilon$ and $\theta + \hat{\theta} \approx 2\theta$, gives the approximation

$$\varepsilon \approx -\frac{k_{AM}}{2}\sin(2\theta)$$

Figure 2.11 depicts the influence of an amplitude imbalance to the resulting sensor error for analogue output and resolver signals.

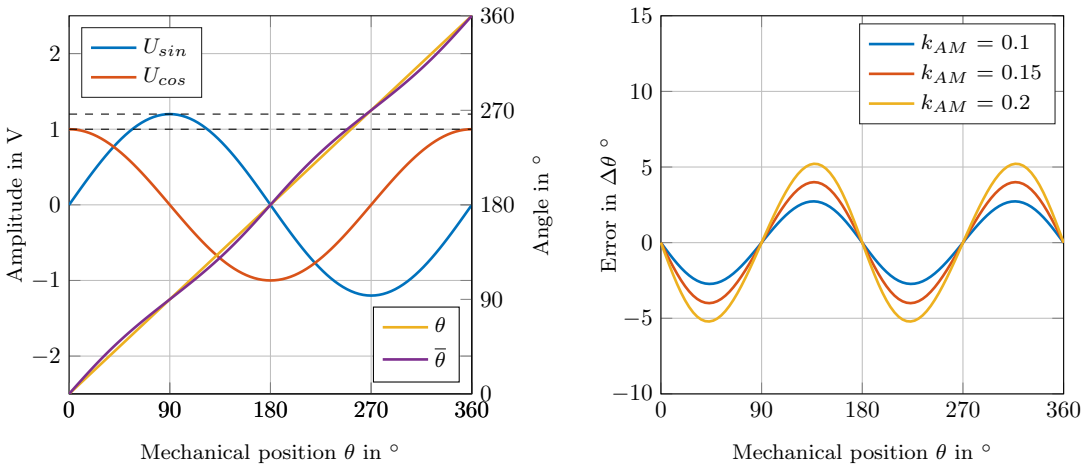

Figure 2.11.: Amplitude Mismatch error in sine signal and resulting error for different values of k_{AM}.

2.4.3. Harmonic Error

The sensor signals contain in general different kinds of harmonic components, which lead to additional position sensor errors. By defining n as the number of involved harmonic order and k_n as its amplitude, the resulting sensor error is calculated as

$$\bar{\theta} = \arctan\left(\frac{U_{sin}}{U_{cos}}\right) = \arctan\left(\frac{\sin\theta + k_n \sin(n\theta)}{\cos\theta}\right)$$

Repeated calculation of β leads to the sensor error

$$\beta_{HE} = \frac{k_n \cos\theta \sin(n\theta)}{k_n \sin\theta \sin(n\theta) + 1} \Rightarrow \Delta\theta = -\arctan\left(\frac{k_n \cos\theta \sin(n\theta)}{k_n \sin\theta \sin(n\theta) + 1}\right)$$

Considering resolver signals, additive harmonics yield to

$$U_{err} = U_{sin} - U_{cos} = \hat{U}\left(\sin\theta\cos\hat{\theta} + k_n \sin(n\theta)\cos\hat{\theta} - \cos\theta\sin\hat{\theta}\right)$$

$$U_{err} = \hat{U}\left(\sin(\underbrace{\theta - \hat{\theta}}_{\varepsilon}) + k_n \sin(n\theta)\cos\hat{\theta}\right) \stackrel{!}{=} 0$$

With $\varepsilon = \theta$ - $\hat{\theta}$, the remaining tracking loop error is written as

$$\varepsilon = -k_n \sin(n\theta)\cos\hat{\theta} \approx -k_n \sin(n\theta)\cos\theta$$

In this example, a third order harmonic is added ($n = 3$) with 3 different variations of its amplitude k_n. Figure 2.12 shows the influence of a harmonic distortion in the sine

signal regarding the calculated rotor position.

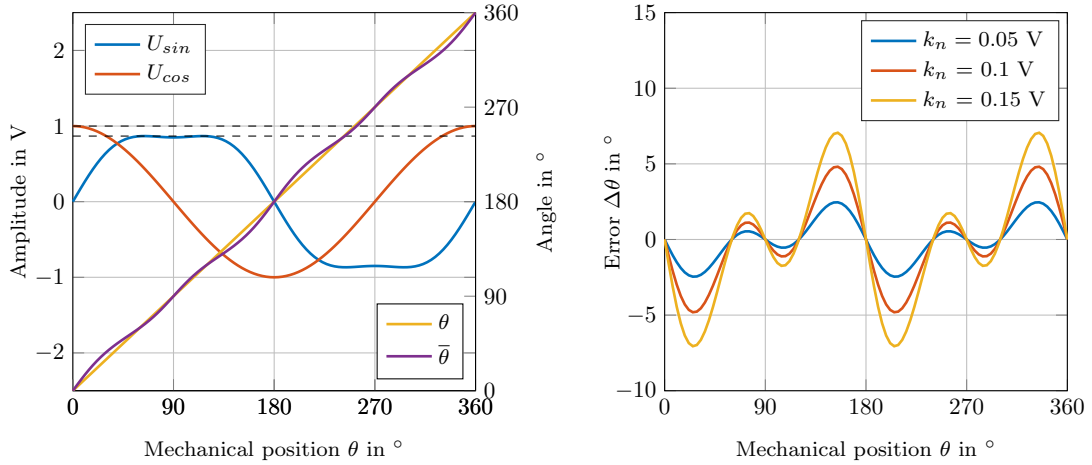

Figure 2.12.: Harmonic error in sine signal and resulting error for different values of k_n.

The results and characteristics match the sensor error discussed in [22], where linear Hall sensors are used to the detected the rotor permanent magnet edge field. These signals look like $\sin(\theta)$ and $\cos(\theta)$ signals and are used for rotor position determination, but they contain a signficant third order harmonic. An adaptive notch filter is used in the presented method to supress these harmonics and to improve the rotor position measurement results. In addition, a method is proposed in [21], how to calculate errors due to inductive harmonics concerning resolver signals.

2.4.4. Quadrature Phase Shift Error

The last kind of analytically analyzed error is caused by a violation of sine and cosine orthogonality and their ideal 90° phase shift. This error is described by an additional phase φ in the sine output signals argument

$$\bar{\theta} = \arctan\left(\frac{U_{sin}}{U_{cos}}\right) = \arctan\left(\frac{\sin(\theta+\varphi)}{\cos\theta}\right)$$

Coefficient comparison gives for this case

$$\beta_{QE} = \frac{-\cos\theta\tan\theta - \sin(\theta+\varphi)}{\tan\theta\sin(\theta+\varphi)+\cos(\theta)} \Rightarrow \Delta\theta = -\arctan\left(\frac{-\cos\theta\tan\theta - \sin(\theta+\varphi)}{\tan\theta\sin(\theta+\varphi)+\cos(\theta)}\right)$$

For resolver signals, the imperfect quadrature error can be described by using the appropriate addition theorem

$$U_{err} = U_{sin} - U_{cos} = \hat{U}\left(\sin(\theta+\varphi)\cos\hat{\theta} - \cos\theta\sin\hat{\theta}\right)$$

$$U_{err} = \hat{U}\left(\sin(\underbrace{\theta-\hat{\theta}}_{\varepsilon}) + \cos\theta\cos\hat{\theta}\varphi\right) \stackrel{!}{=} 0$$

For small values of φ and $\varepsilon = \theta$ - $\hat{\theta}$ the angle error yields to

$$\varepsilon \approx -\cos^2(\theta)\varphi = -\frac{\varphi}{2}(1+\cos 2\theta)$$

Figure 2.13 shows the impact of different phase shifts φ on the error signal, which is valid for analogue output and resolver signals.

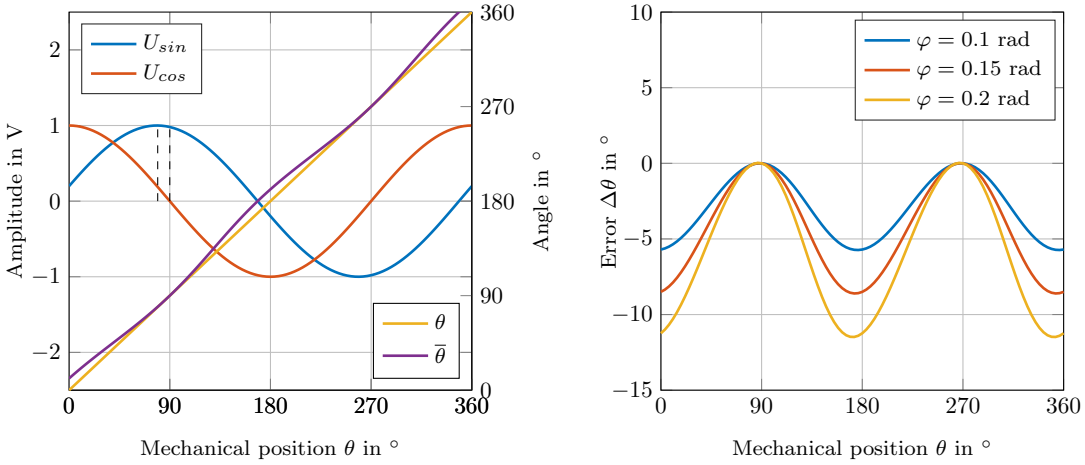

Figure 2.13.: Quadrature phase shift error in sine signal and resulting error for different values of φ.

2.4.5. Additional Errors

Several additional effects occur in resolvers, such as inductive harmonics, reference phase shift, excitation signal distortion and disturbance signals. In [21], these different kinds of errors are mathematically described and approximations are presented. These error types are not further considered in this work, because a lot of additional knowledge in terms of geometry, material, tolerances, reference signal etc. is necessary to describe these effects accurately. Additionally, the necessary signal processing in the resolver-to-digital conversion influences the rotor position accuracy. Therefore, analytic approaches are not

further considered due to the complexity of manipulating different sensor parameters and their effects on rotor position calculations.

2.5. Conclusion of Preliminary Considerations

This chapter has the aim to show, that there are plenty of different effects interfering the rotor position measurement capability of a sensor system. For simplicity, only one output signal is manipulated in the analytic calculations regarding the sensor error. If one sensor parameter is varied, a superimposition of all these error mechanism occur on both output signals. It is also utterly possible to describe how - for example - a temperature change or mechanical misalignment directly influences one or all of these mentioned error types. A potentially superimposition of all sensor parameter variations simultaneously complicates this task additionally. This means, an approach is desirable, which is not based on a mathematical or physical description of the involved process. The presented method in the next section has the aim to describe the complete sensor characteristics with its signal processing chain and to rate its performance regarding parameter variations by a holistic approach.

3. Evaluation of Rotor Position Sensor Error Characteristics

As shown in the previous section, analytic approaches can be used to describe the expected sensor error under the influence of different output signal manipulations. The aim of this chapter is to introduce a method, which describes the sensor performance as a function of several parameter variations, such as mechanical misalignment, mechanical speed, temperature drift or different supply voltage levels.

3.1. Comparison of Different Evaluation Approaches

The interactions of parameter variations with different kinds of error mechanisms, as described in Section 2.4, is challenging and complex. In the following three subsections different approaches are introduced, which can be utilized to analyze the sensors sensitivity regarding different parameter variations.

3.1.1. Analytic Method - Mathematical-Physical Approach

Analytic approaches for describing the sensors parameter dependencies are possible, as described for example in [23] and [24]. Based on Maxwell's Equation, the spatial magnetic field distribution can be calculated as a function of the magnet's mechanical misalignment. An advantage of this approach is that it allows to consider lots of different mechanical parameters, e.g. longitudinal shift, eccentricity of sensor with respect to the axis of rotation, angle between magnetization and tilt axis of magnet, angle of rotation of the shaft, azimuthal twist angle of the sensor surface, etc. [23]. Additionally, no test bench hardware or sensor samples are necessary, but this method yields to highly complicated expressions and mainly covers the dependency of mechanical parameters - temperature, rotational speed or supply voltage are difficult to consider. Detailed information about the geometry, materials and the internal sensor structure is also needed to perform the necessary calculations. Another big challenge of the analytic approach is to find and describe solutions of the electromagnetic interactions for all different kind of investigated sensor types, which is not necessary by applying numerical or physical methods.

3.1.2. Finite Element Method - Numerical Approach

Since analytic description of the introduced sensor systems can be very challenging or even impossible, numerical FEM methods are interesting and often used for sensor design and parameter studies. It allows to analyze complicated structures, taking non-linear material properties into account and to solve multiphysical coupled problems. For example, in [25] and [26], a FEM-based analysis of a mechanically misaligned Hall-based rotor position sensor is performed. In general, the special shapes of VR-resolver rotors or eddy current sensor flywheels are mostly simulated in combination with an FEM and optimization software [27], to produce high quality output signals for precise rotor angle computation. A drawback of this analysis is, that it needs detailed specific information about all investigated sensor technologies regarding geometry, packaging and involved materials. It allows to consider nearly any kind of mechanical parameter variations, but can be computational intense if 3D-simulations are necessary. Additionally, the implemented signal processing and rotor position calculation algorithms are not considered and it is difficult to take environmental influences, like temperature and aging, into account.

3.1.3. Design of Experiments - Experimental Approach

Many of the above mentioned drawbacks of analytic and FEM-based methods can be avoided, if an experimental approach is utilized to evaluate the sensor's parameter sensitivity. A common approach is to perform defined experiments according to the process that has to be modelled, and to use the measured results for a mathematical description in form of a so-called meta model. This method is called Design of Experiments (DOE). A big benefit of this method is, that all sensors can be described with the same approach; no detailed or maybe impossible analytic description or computational intense FEM analysis with a lot of necessary packaging information is necessary. It also considers the complete additional sensor signal processing chain automatically and enables the most realistic and accurate representation of a specific sensor in combination with additional signal processing. The biggest drawback of this method is that a specific test bench is necessary, which allows to perform different kinds of experiments with the necessary parameter variations. Additionally, the total number of parameters that can be investigated is usually small compared to the other two methods and the usability of this method is limited by the implemented functionality and possibilities of the test bench. Therefore, it is important to determine a parameter set, which contains influential parameters and to provide a generous experimental space by the test bench.

The DOE approach was identified as the most promising solution to fulfil the task of this work and is therefore considered exclusively for the evaluation of different rotor position technologies.

3.2. Test Bench Concept and Implementation of DOE Functionality

To perform several experiments with a DOE approach, a test bench was designed, which has the functionality to variate different parameters and to compare the measured rotor position from the device under test (DUT) with a reference sensor unit. Figure 3.1 shows the concept of the test bench, which was used to perform experiments that are treated in the present thesis.

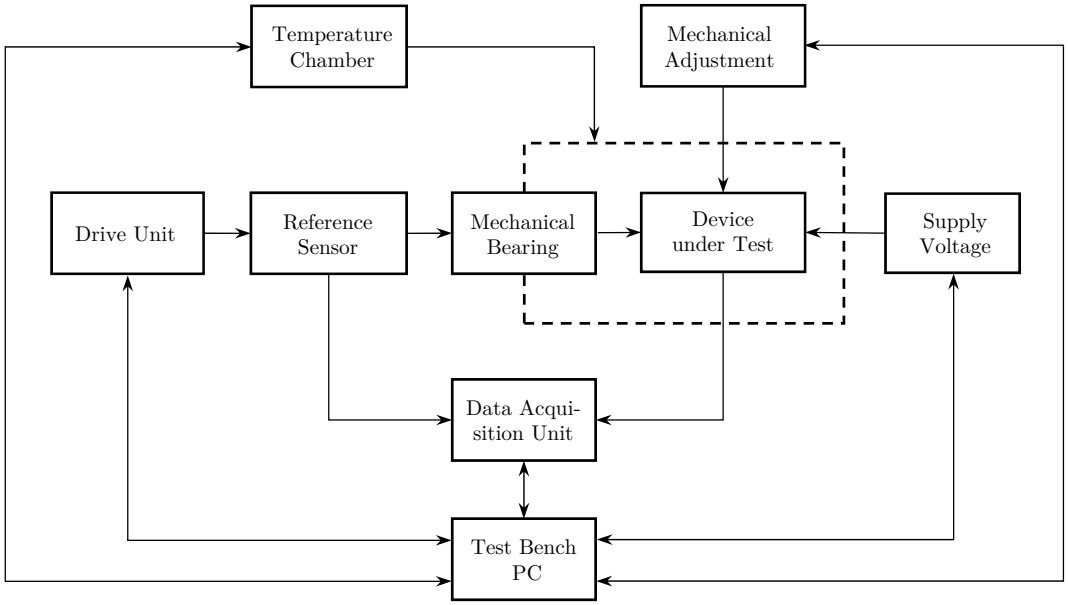

Figure 3.1.: Test bench concept overview.

The possible parameters variations of this test bench include:

- Mechanical misalignment in Δx-, Δy- and Δz-direction
- Tilt angle $\Delta\varphi$ between sensor rotor and stator plane
- Speed variations Δn
- Temperature changes ΔT within the typical automotive range
- Supply voltage variations ΔV

and describe typical parameter variations, which are present in automotive applications. With manipulation of these sensor parameters, the deviation of reference unit and measured rotor position of the DUT over one mechanical period is calculated (see Figure 2.8).

3.3. Performance Criterion

To rate the sensor's measurement accuracy, a performance criterion, respectively index for every parameter variation has to be defined. This performance index should represent the sensor's capability of measurement accuracy at the investigated operating point within one mechanical period. Considering the measured rotor position $\Delta\theta(t)$, different options to rate the sensor's position measurement error can be defined such as:

- Peak-to-peak value: $E_{pp} = \max[\Delta\theta(t)] - \min[\Delta\theta(t)]$
- Mean absolute value: $E_{ma} = \frac{1}{T}\int_{t_0}^{t_0+T} |\Delta\theta(t)|dt$
- Standard deviation: $E_{\sigma} = \sqrt{\frac{1}{T}\int_{t_0}^{t_0+T}(\Delta\theta(t) - \hat{\mu})^2}$ with $\hat{\mu} = \frac{1}{T}\int_{t_0}^{t_0+T}\Delta\theta(t)dt$ [28]

where the last one is used in [11]. Thereby the assumption of a normal distributed sensor error is made, and the distribution is fitted with a Gaussian bell curve. Figure 3.2, left, shows a typical error signal over one mechanical period with the above mentioned performance criteria. On the right, the histogram with a kernel smoothing function for a probability density estimate is plotted. It shows, that the assumption of a normal distributed sensor error is not necessary fulfilled.

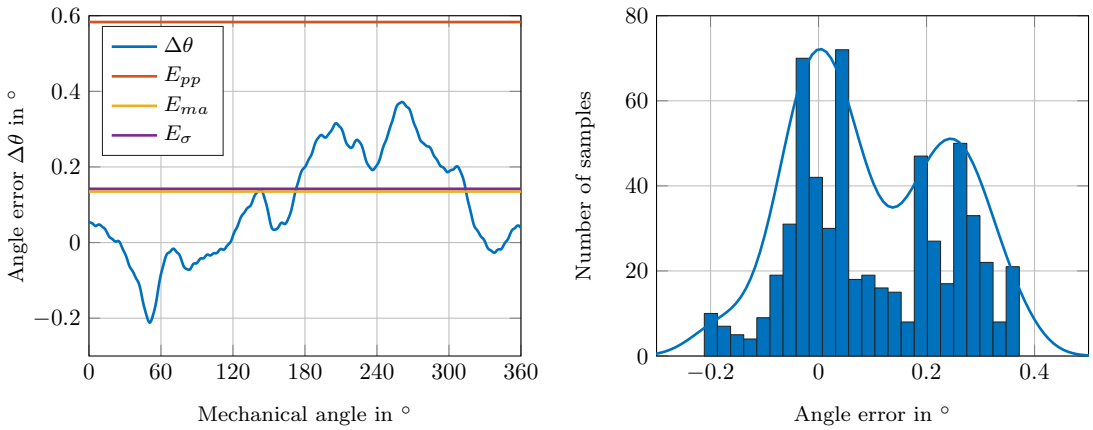

Figure 3.2.: Angle error of an aligned end-of-shaft sensor and error histogramm over one mechanical period.

Note that obtaining the histogram only represents an optical method to categorize distributions. For statistical purposes usually a Kolmogorov-Smirnov test is used [29]. Therefore, the sensor performance in the specific operating point is rated by its peak-to-peak value E_{pp}, calculated with the sensor error function $\Delta\theta(t)$ over one mechanical period. The peak-to-peak value is a worst-case consideration in contrast to the other options, which both have an averaging property in terms of error rating.

3.4. Response Surface Modelling

As described in the previous section, a test bench was designed [30] to perform parameter variations of the sensor's specified operating point and rate its performance by the peak-to-peak error. With the Response Surface Methodology (RSM) it is possible to develop an approximating model for the true response of the sensor behavior [31]. This method was introduced by Box and Willson and is beneficial, when the true response surface of the process is based on very complicated or unknown physical mechanisms. With the measured or observed data from the process it is possible to calculate an empirical model, which is an approximation of the obtained physical processes. Objectives and typical applications of RSM include following three categories:

- Mapping a response surface over a particular region of interest
- Optimization of the response
- Selection of operating conditions to achieve specifications

where the first one is the major aim in this work. In the next section, the mathematical basics of response surface calculation is introduced.

3.4.1. Basics and LSQ Estimation

The empirical model is intended to describe the relationship of the parameter variations, such as mechanical misalignment, temperature, rotational speed and supply voltage to the sensors peak-to-peak error. This can be formulated as a linear function

$$y = \beta_0 + \beta_1 x_1 + \beta_2 x_2 + \ldots + \beta_k x_k + \varepsilon = \sum_{j=1}^{k} \beta_j x_j + \varepsilon \tag{3.1}$$

which is called a multiple linear regression model with k regressor variables. For example, x_1 represents a tilt angle in degree and x_2 a misalingment in mm. The parameters β_j for $j = 0, 1, \ldots, k$ are called the regression coefficients. This model describes a hyperplane in the k-dimensional space of the regressor variables [31]. The parameters β_j represent the expected change in the response y per unit change in x_j by keeping the other remaining independent variables constant. The model y is called a linear regression model where the coefficients β_j have to be determined. This is done in the sense of a least squares model fitting approach, where the method of least squares is typically used to estimate the regression coefficients β_j [31]. For this approach some assumptions have to be made:

- $n > k$ observations y_1, $y_2, \ldots, y_n$ on the response variable y are availabe
- Expectation value of the residuals $E(\varepsilon) = 0$
- Variance of the residuals $\mathrm{Var}(\varepsilon) = \sigma^2$
- Residuals ε_i are uncorrelated random variables

In matrix notation, Equation 3.1 can be written for n observations as

$$\mathbf{y} = \mathbf{X}\boldsymbol{\beta} + \boldsymbol{\varepsilon} \tag{3.2}$$

with

$$\mathbf{y} = \begin{bmatrix} y_1 \\ y_2 \\ \vdots \\ y_n \end{bmatrix}, \ \mathbf{X} = \begin{bmatrix} 1 & x_{11} & x_{12} & \cdots & x_{1k} \\ 1 & x_{21} & x_{22} & \cdots & x_{2k} \\ \vdots & \vdots & \vdots & & \vdots \\ 1 & x_{n1} & x_{n2} & \cdots & x_{nk} \end{bmatrix}, \ \boldsymbol{\beta} = \begin{bmatrix} \beta_0 \\ \beta_1 \\ \vdots \\ \beta_k \end{bmatrix} \text{ and } \boldsymbol{\varepsilon} = \begin{bmatrix} \varepsilon_1 \\ \varepsilon_2 \\ \vdots \\ \varepsilon_n \end{bmatrix} \tag{3.3}$$

In this system of equations, $\mathbf{y}$ is a $n \times 1$ vector of observations, $\mathbf{X}$ is the so called Design matrix with dimension $n \times p$, $\boldsymbol{\beta}$ is a $p \times 1$ vector containing the regression coefficients and $\boldsymbol{\varepsilon}$ represents a $n \times 1$ vector of random errors. The basic idea of regression methods is to estimate a vector $\mathbf{b}$, that minimizes the residuals sum of squares. This can be formulated as

$$\begin{aligned} L &= \sum_{i=1}^{n} \varepsilon_i^2 = \boldsymbol{\varepsilon}^T\boldsymbol{\varepsilon} = (\mathbf{y} - \mathbf{X}\boldsymbol{\beta})^T(\mathbf{y} - \mathbf{X}\boldsymbol{\beta}) \\ L &= \mathbf{y}^T\mathbf{y} - \boldsymbol{\beta}^T\mathbf{X}^T\mathbf{y} - \mathbf{y}^T\mathbf{X}\boldsymbol{\beta} + \boldsymbol{\beta}^T\mathbf{X}'\mathbf{X}\boldsymbol{\beta} \\ L &= \mathbf{y}^T\mathbf{y} - 2\boldsymbol{\beta}^T\mathbf{X}^T\mathbf{y} + \boldsymbol{\beta}^T\mathbf{X}^T\mathbf{X}\boldsymbol{\beta} \end{aligned}$$

because $\mathbf{y}^T\mathbf{X}\boldsymbol{\beta}$ is a scalar and can be transposed, which yields to $\boldsymbol{\beta}^T\mathbf{X}^T\mathbf{y}$. The demand on the least squares estimators is

$$\left.\frac{\partial L}{\partial \boldsymbol{\beta}}\right|_{\mathbf{b}} = -2\mathbf{X}^T\mathbf{y} + 2\mathbf{X}^T\mathbf{X}\mathbf{b} = \mathbf{0}$$

and yields to

$$2\mathbf{X}^T\mathbf{X}\mathbf{b} = \mathbf{X}^T\mathbf{y}$$

This equation has to be solved for the vector $\mathbf{b}$, the least squares estimators of $\boldsymbol{\beta}$

$$\mathbf{b} = (\mathbf{X}^T\mathbf{X})^{-1}\mathbf{X}\mathbf{y} \tag{3.4}$$

where $\mathbf{X}^T\mathbf{X}$ is the so-called Moment matrix and $(\mathbf{X}^T\mathbf{X})^{-1}\mathbf{X}$ the Moore-Penrose pseudoinverse $\mathbf{X}^+$ of $\mathbf{X}$. This formalism is used to calculate a first order response surface model based on k observations fulfilling the least-squares error property. The fitted regression model can be written as

$$\hat{\mathbf{y}} = \mathbf{X}\mathbf{b}$$

This means, that the model describes a hyperplane as a function of the design variables x_i. Due to the presumed non-linear behavior of the sensor outside its "sweet spot", this approach will not be sufficient to describe the sensors peak-to-peak error behaviour in its parameter space. Therefore, Equation 3.1 will be extended with interaction and

quadratic terms [5]. This leads to

$$\begin{aligned} y &= \beta_0 + \beta_1 x_1 + \beta_2 x_2 + \ldots + \beta_k x_k \\ &\quad + \beta_{12} x_{12} + \beta_{13} x_{13} + \ldots + \beta_{k-1,k} x_{k-1,k} \\ &\quad + \beta_{11} x_1^2 + \beta_{22} x_2^2 + \ldots + \beta_{kk} x_k^2 + \varepsilon \\ y &= \beta_0 + \sum_{i=1}^{k} \beta_i x_i + \sum_{i=1}^{k-1} \sum_{j=i+1}^{k} \beta_{ij} x_i x_j + \sum_{i=1}^{k} \beta_{ii} x_i^2 + \varepsilon \end{aligned} \tag{3.5}$$

where interactions between the different parameters and quadratic effects are considered. The benefit of above matrix notation is, that it can be easily adopted for higher order models by extending the Design matrix $\mathbf{X}$ with appropriate interaction and quadratic columns. This extended version of the Design matrix $\mathbf{X}$ is called Model matrix and has following structure

$$\mathbf{X} = \begin{bmatrix} 1 & x_{11} & \cdots & x_{1k} & x_{11}x_{12} & \cdots & x_{1,k-1}x_{1k} & x_{11}^2 & \cdots & x_{1k}^2 \\ 1 & x_{21} & \cdots & x_{2k} & x_{21}x_{22} & \cdots & x_{2,k-1}x_{2k} & x_{21}^2 & \cdots & x_{2k}^2 \\ \vdots & \vdots & \cdots & \vdots & \vdots & \cdots & \vdots & \vdots & \cdots & \vdots \\ 1 & x_{2n1} & \cdots & x_{nk} & x_{n1}x_{n2} & \cdots & x_{n,k-1}x_{nk} & x_{n1}^2 & \cdots & x_{nk}^2 \end{bmatrix}$$

Due to this extension, the total number of coefficients increases, which means the number of regressors p changes to

$$p = 1 + 2k + \frac{k(k-1)}{2} = \frac{(k+1)(k+2)}{2}$$

with additional $2k$ quadratic and $\frac{k(k-1)}{2}$ interaction coefficients. Note that a second order response surface model is still a linear model, because the fitted regression model $\hat{y}$ is a linear function of the regression coefficients $\mathbf{b}$. With this scheme, the Model matrix can be extended to arbitrary polynomial order, but a reasonable choice is important due to numerical stability of the Moment matrix and its inversion for calculating the pseudoinverse as in Equation 3.4. Higher order models than quadratic are rarely used in Response Surface Methodology, because of the low additional benefit of considering higher order terms. With this derivations, the basic mathematics are defined, the last open point includes the design and structure of the Design-, respectively Model matrix $\mathbf{X}$, which will be discussed in the next section.

3.4.2. Designs for Quadratic Models

The value of the peak-to-peak error over one mechanical period is used as objective criterion, with which the DOE approach works to generate a quadratic RSM of the DUT behavior for visualization of the sensor error. To compute a second order response surface, there are two properties, which the experiment has to fulfill [31]:

- Availability of at least three levels of each design variable
- Measurement of at least $p = 1 + 2k + \frac{k(k-1)}{2}$ distinct design points

Three levelled design implies, that the factors of the experiment are varied in a minimal, middle and maximal value. There are many possible design strategies for executing such experiments. The most popular of the three leveled versions are [31],[32]

- Central Composite: Circumscribed (CCC), Inscribed (CCI), Face Centered (CCF)
- Box-Behnken (BB)
- Full Factorial (FF)
- Optimal Designs: D-, G-, A-Optimality

The number of experiment runs can be minimized compared to a Full Factorial design by using reduced designs, like Box-Behnken and Central Composite. Figure 3.3 shows an overview of the most popular experiment designs, which are used for response surface modelling.

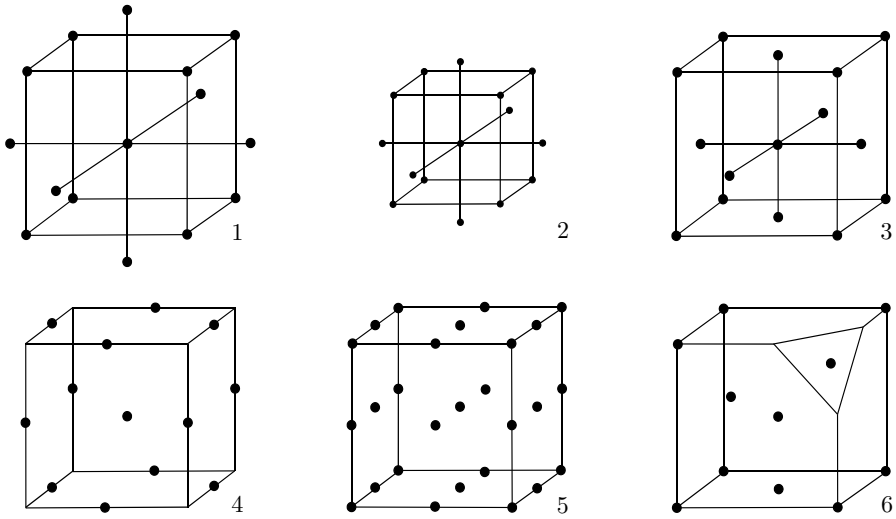

Figure 3.3.: Central Composite Circumscribed (1), Central Composite Inscribed (2), Central Composite Faced (3), Box-Behnken (4), Full Factorial (5) and Optimal Design (6).

In this case, a Full Factorial design in 3 levels and 7 factors demands $3^7 = 2187$ measurements. This is very time consuming and requires an unnecessary big amount value of measurements, compared to 35 model constants, which have to be determined in this specific case. Therefore, reduced test plans are the preferred choice for calculating response surfaces. The CCC design has the best properties with respect to the prediction variance and variance of the model coefficients, but it can not always be applied in this form, because the required measurement distance of lies outside the experimental space

[31]. That means, that if the response surface model should be examined for a typical position sensor within a temperature range from -40 °C up to +160 °C degrees, the experiment space is spreading from -67 °C up to 269 °C, which lies outside the allowed temperature range and most likely would destroy the device under test. Because of that reason, the CCC design is mostly adapted to Face Centered (CCF) or Inscribed (CCI) versions, which have no points outside the predefined experiment space. Optimal design plans are computationally created to optimize the Moment matrix $\mathbf{X}^T\mathbf{X}$ due to several objectives. This leads to an optimization of the determinant of the Moment matrix (D-Optimal), the trace of the inverse of the Moment matrix (A-Optimal), a maximum of the prediction variance (G-Optimal) or to a reduction of necessary test runs [33]. Optimal design is not further investigated in this work, since the number of test runs is not a significant restriction and computation of these designs is elaborate [34],[35].

A big benefit of the DOE approach is, that a physical modelling of the investigated process, which can be challenging and time intense, is unnecessary. It should be possible to compare different sensor principles error characteristics with a low number of measurements and variations of additional effects. Therefore, the DOE approach suggests itself as the preferred choice, because it leads to a sensor error model without the need of a mathematical description regarding the involved physical principles and effects.

3.4.3. Example and Data Acquisition for DOE

In this section, the method for evaluating rotor position sensors due to their error characteristic is applied, using the above mentioned approaches. The aim of this example is to introduce the capability of this method, to characterize the dependency of the sensor's measurement accuracy as a function of varied parameters with a mathematical description in form of a meta model. Figure 3.4 shows the integration of this exemplary end-of-shaft sensor into the test bench and different appropriate candidates of usable magnets.

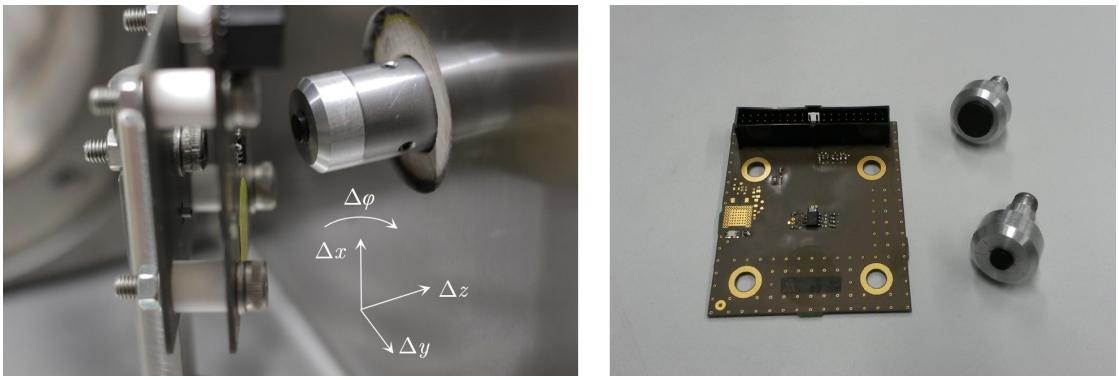

Figure 3.4.: End-of-shaft AMR sensor with inserted magnet; test bench configuration (left) and different kind of investigated magnets (right).

The device under test in this case is an Analog Devices ADA4571 AMR sensor [36] with a diametrically magnetized magnet, fabricated by Schramberg [37]. The sensor is aligned along the shaft axis with a 2 mm longitudinal distance from chip to magnet. The dependency of five parameters on the sensor peak-to-peak error can be investigated and modelled via quadratic response surface model. It has be to ensured, that the experiment space provides an appropriate size and that the functionality of the sensor inside this observation space is guaranteed. As mentioned in the previous section, the quadratic model requires a three levelled design, and the parameters are varied at following minimal, middle and maximum levels:

- $x_1 \mathrel{\hat{=}}$ Tilt angle $\Delta\varphi$: [-1, 0, +1] °
- $x_2 \mathrel{\hat{=}}$ Misalignment in x-direction Δx : [-1, 0, +1] mm
- $x_3 \mathrel{\hat{=}}$ Misalignment in y-direction Δy : [-1, 0, +1] mm
- $x_4 \mathrel{\hat{=}}$ Misalignment in z-direction Δz : [-1, 0, +1] mm
- $x_5 \mathrel{\hat{=}}$ Mechanical speed Δn : [200, 6100, 12000] rpm

These values represent an exemplary design space for this sensor type and have to be adjusted separately for every investigated sensor. Since no strict mechanical boundaries are present, unlike as for the resolver, the design space can be defined generously regarding mechanical parameters. Due to the low dependency on temperature and supply voltage, these two factors are neglected for this exemplary study, which is displayed later in Figure 3.23. In Figure 3.4, the coordinate system within the test bench is depicted. The calculation of the model coefficients with Equation 3.4 needs an inversion of the moment matrix, which can cause numerical problems, if the parameter range is too large. Therefore, a normalization of the varied parameters within -1 to +1 is recommended for RSM calculations, which is done by

$$x_i^* = \frac{x_i - \frac{x_{i,max}+x_{i,min}}{2}}{\frac{x_{i,max}+x_{i,min}}{2}}$$

After performing the experiment on the test bench, the measured data is available and the regression model $\hat{y}$ is calculated. The result of the regression in this exemplary Central Composite Inscribed (CCI) experimental design is written as

$$\begin{aligned}\hat{y} = {} & 0.3822 - 0.0020x_1 - 0.1274x_2 - 0.0369x_3 + 0.1280x_4 + 0.0429x_5 + \\ & 0.3242x_1x_2 + 0.0370x_1x_3 - 0.0678x_1x_4 - 0.0224x_1x_5 - 0.1828x_2x_3 - 0.0050x_2x_4 + \\ & 0.0454x_2x_5 - 0.1537x_3x_4 + 0.1408x_3x_5 - 0.1324x_4x_5 + \\ & 0.0602x_1^2 + 1.0465x_2^2 + 1.1408x_3^2 + 0.0687x_4^2 + 0.1163x_5^2 \end{aligned} \tag{3.6}$$

or as a quadratic function in matrix notation

$$\hat{y} = b_0 + \mathbf{x^T a} + \mathbf{x^T B x} \tag{3.7}$$
$$= b_0 + \mathbf{x^T} \begin{bmatrix} b_1 \\ b_2 \\ b_3 \\ b_4 \\ b_5 \end{bmatrix} + \mathbf{x^T} \begin{bmatrix} b_{11} & b_{12}/2 & b_{13}/2 & b_{14}/2 & b_{15}/2 \\ & b_{22} & b_{23}/2 & b_{24}/2 & b_{25}/2 \\ & & b_{33} & b_{34}/2 & b_{35}/2 \\ & & & b_{44} & b_{45}/2 \\ \text{sym.} & & & & b_{55} \end{bmatrix} \mathbf{x}$$

leads in this specific case to the following model

$$\hat{y} = 0.3822 + \mathbf{x^T} \begin{bmatrix} -0.002 \\ -0.1274 \\ -0.0369 \\ 0.1280 \\ 0.0429 \end{bmatrix} + \mathbf{x^T} \begin{bmatrix} 0.0602 & 0.1621 & 0.0185 & -0.0339 & -0.0112 \\ 0.1621 & 1.0465 & -0.0914 & -0.0025 & 0.0227 \\ 0.0185 & -0.0914 & 1.1408 & -0.0769 & 0.0704 \\ -0.0339 & -0.0025 & -0.0769 & 0.0687 & -0.0662 \\ -0.0112 & 0.0227 & 0.0704 & -0.0662 & 0.1163 \end{bmatrix} \mathbf{x}$$

where Figure 3.5 depicts the results of the main effect characteristics in the design origin, which is usually defined by the sensor supplier.

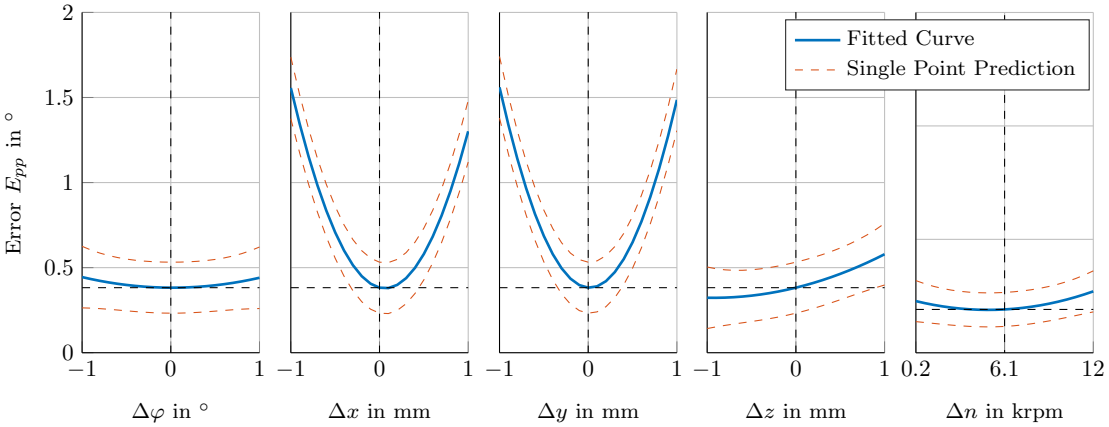

Figure 3.5.: Prediction plot of the end-of-shaft sensor example at the design origin $\mathbf{x_0^*}$.

The varied parameters in this exemplary design contains the tilt-angle $\Delta\varphi$, Δx-, Δy-, Δz- misalignments and speed variation Δn. The blue line in Figure 3.5 shows the sensor peak-to-peak error characteristics by varying the parameters from the center point of the design. This means, that the sensors peak-to-peak error in the design origin $\mathbf{x_0^*}$

$$\mathbf{x_0^*} = (\Delta\varphi = 0\ °, \Delta x = 0\ \text{mm}, \Delta y = 0\ \text{mm}, \Delta z = 0\ \text{mm}, \Delta n = 6100\ \text{rpm})$$

is expected to be 0.382 °. Note that Figure 3.5 shows the main effect plot and how the sensor error behaves, if one parameter is varied and the others are kept constant. The

response surface model represents a fifth dimensional full quadratic model, which means, if the error is obtained at a different test point $\mathbf{x}_1^*$, all curves are updated and change their characteristics. This includes, that these prediction plots are only valid at a specific observation point. Computation of this prediction plot for a different observation point $\mathbf{x}_1^*$

$$\mathbf{x}_1^* = (\Delta\varphi = 0.5\ °, \Delta x = 0.25\ \text{mm}, \Delta y = -0.75\ \text{mm}, \Delta z = 0.6\ \text{mm}, \Delta n = 10200\ \text{rpm})$$

leads to an expected peak-to-peak error of 1.267 ° and sensor error characteristics as depicted in Figure 3.6.

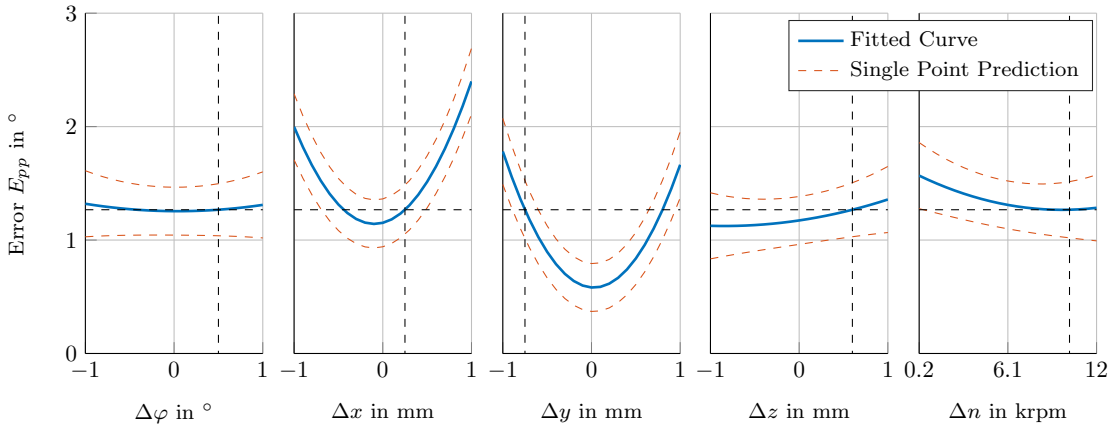

Figure 3.6.: Prediction plot of the end-of-shaft sensor example at a different observation point $\mathbf{x}_1^*$.

The second order model describes a surface of fifth order that can not be visualized intuitively. One possibility for visualization is to use three-dimensional plots to show the characteristics by keeping the other parameters constant. In this context, Figure 3.7 shows multidimensional surface plots of the sensor error behavior. The red lines in Figure 3.5, respectively 3.6, and the grey surfaces in 3.7 show the corresponding single point prediction intervals. Computations of these intervals is discussed in more detail in Section 3.4.9.

3.4.4. Statistical Evaluations

It is not sufficient to calculate the response surface model as described in the previous section, if different kind of control mechanisms have to be utilized. To rate the response surface quality, the model output and measurement results for the design points are plotted against each other. Figure 3.8 shows the results of the full quadratic model - which means that no model reduction has been applied yet (see Subsection 3.4.6) - and performed measurements in the design points.

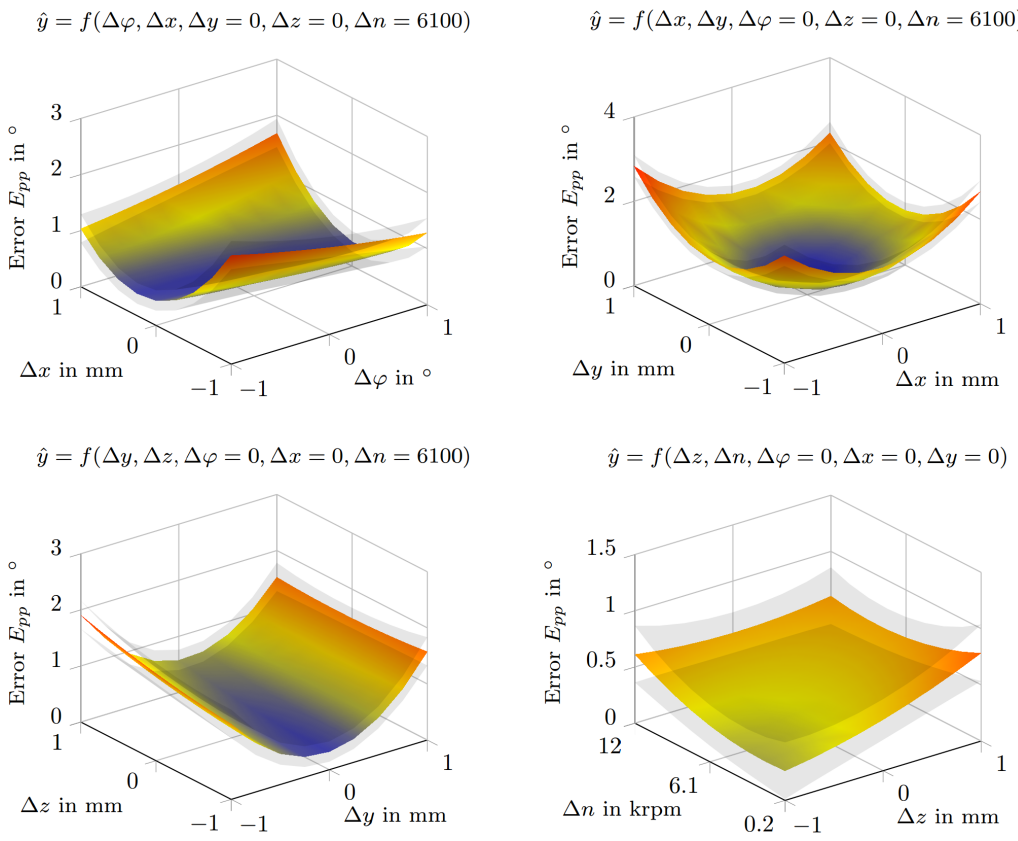

Figure 3.7.: Prediction surface plots of the exemplary sensor by varying each 2 parameters and keeping the others in the design origin. Grey surfaces portray the single point prediction intervals.

It shows, that the quadratic model is capable of representing the real sensor behaviour, which is determined by the small difference of measurement $\mathbf{y}$ and regression model $\hat{\mathbf{y}}$ output compared to the expected sensor error values. This difference is indicated by the so-called residuals $\mathbf{e}$, which are described as the remaining difference between measurement results and regression model. Calculation of the residuals is done by

$$\mathbf{e} = \mathbf{y} - \hat{\mathbf{y}} = \mathbf{y} - \mathbf{X}\mathbf{b}$$

The quality of the model compared to the performed measurements can be rated by different indicators, such as:

- Root Mean Squared (RMSE) and Mean Absolute Error (MAE)
- (Adjusted) Coefficient of Determination R^2 and R^2_{adj}

Calculation of these indicators is related with different kinds of sum of squares values. These sum of squares values are separated into:

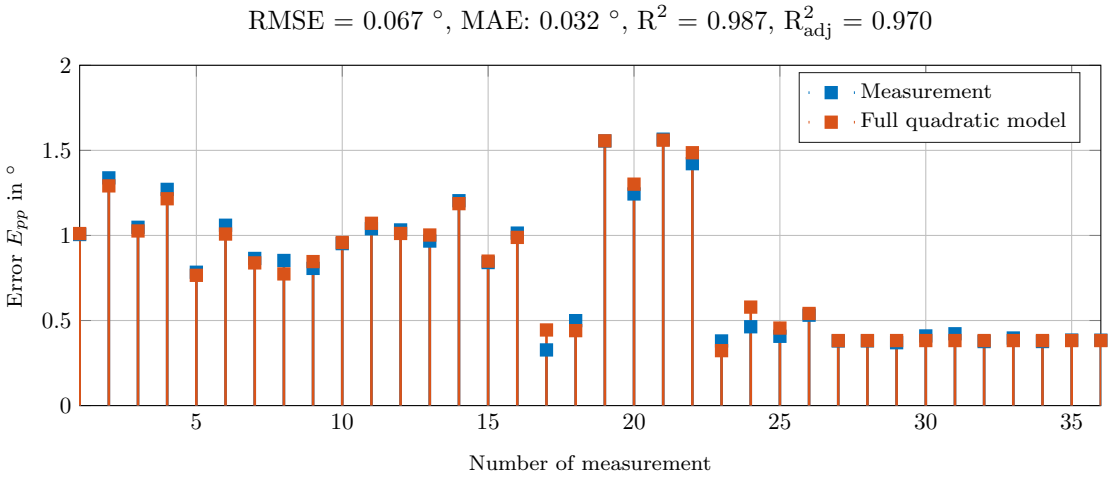

Figure 3.8.: Comparison of measurement and full quadratic model at the design points of the exemplary CCI design.

- Regression sum of squares SS_R
- Error sum of squares SS_E
- Total sum of squares SS_T

The basic idea includes the partitioning of the total sum of squares [31]

$$SS_T = \sum_{i=1}^{n}(y_i - \bar{y})^2 = SS_R + SS_E$$

into a regression and error sum of squares, which plays a key role by the significance of the regression test. This test method is called Analysis of Variance (ANOVA) and is used to rate how the model quality is changing, if variables are added or removed to the model [32]. The error sum of squares from the residuals $\mathbf{e}$ is calculated as followed

$$\begin{aligned} SS_E &= \mathbf{e}^T\mathbf{e} = (\mathbf{yXb})^T(\mathbf{yXb}) \\ &= \mathbf{y}^T\mathbf{y} - 2\mathbf{b}^T\mathbf{X}^T\mathbf{y} + \mathbf{b}^T\mathbf{X}^T\mathbf{Xb} \\ &= \mathbf{y}^T\mathbf{y} - \mathbf{b}^T\mathbf{X}^T\mathbf{y} \end{aligned} \tag{3.8}$$

$$SS_R = \mathbf{b}^T\mathbf{X}^T\mathbf{y} - \frac{\left(\sum_{i=1}^{n} y_i\right)^2}{n} \tag{3.9}$$

$$SS_T = \mathbf{y}^T\mathbf{y} - \frac{\left(\sum_{i=1}^{n} y_i\right)^2}{n} \tag{3.10}$$

and MAE and RMSE are defined as

$$\text{MAE} = \frac{1}{n}\sum_{i=1}^{n}|e_i|$$

$$\text{RMSE} = \sqrt{\frac{SS_E}{n-p}}$$

These indicators rate the residuals as an absolute or averaged error quantity. In this specific example, the average absolute deviation between model and measurements results in 0.032 ° and 0.067 ° for the root mean squared error, which represents the good model consistency shown in Figure 3.8. The quadratic response model has therefore the capability to map the sensors behaviour within the performed measurements determined by the chosen design.

The Coefficients of Determination R^2 and R^2_{adj} are normalized performance criteria to rate the model quality and are defined as

$$R^2 = \frac{SS_R}{SS_T} = 1 - \frac{SS_E}{SS_T} \tag{3.11}$$

$$R^2_{\text{adj}} = 1 - \frac{SS_E/(n-p)}{SS_T/(n-1)} = 1 - \frac{n-1}{n-p}(1-R^2) \tag{3.12}$$

Both coefficients measure the amount of reduction in the variability of y obtained by using the regressors $x_1, x_2, \ldots, x_k$ in the model [31]. For the value of R^2, $0 \leq R^2 \leq 1$ has to be fullfilled and it is interpreted as an indicator, how much of the response in y is explained by the model. A value of $R^2 = 1$ accords to a perfect match of model and measurement, where the residuals and therefore the error sum of squares are zero. A disadvantage of this indicator is, that the value of R^2 is always increasing, when additional terms are added to the regression model. These additional terms can be statistically insignificant and unnecessary, but it has not the desired consequences regarding R^2. Therefore, the adjusted coefficient of determination R^2_{adj} is defined, which takes also the number of model parameters p into account. This coefficient can be interpreted as a kind of "price-performance" ratio and will not always increase by adding variables to the model. With the applied CCI design, which consists of $n = 36$ and $p = 21$ model coefficients, the values of R^2 and R^2_{adj} for the full quadratic model of the exemplary end-of-shaft sensor are calculated as

$$R^2 = 1 - \frac{SS_E}{SS_T} = 1 - \frac{0.0676}{5.3273} = 0.9873$$

$$R^2_{\text{adj}} = 1 - \frac{SS_E/(n-p)}{SS_T/(n-1)} = 1 - \frac{0.0676/(36-21)}{5.3273/(36-1)} = 0.9704$$

This means, that the model explains 98.73 % respectively 97.04 % of the rotor position peak-to-peak error regarding parameter variations. A high deviation of R^2 and R^2_{adj} can

be an indicator for non-significant terms within the model. If a simple linear model with no interaction and quadratic terms is used to characterize this exemplary sensor, the model explanation of R^2 is only 4.03 %. Adding interaction terms only increases the Coefficient of Determination up to 7.94 %, which is unusable for this purpose. That means, linear and interaction models have no explanatory power and therefore a second-order response model approach is absolutely mandatory for describing the sensors characteristics properly.

As mentioned in [31], the least squares method is an unbiased estimator of the parameters $\boldsymbol{\beta}$ in the multiple linear regression model. This property is shown by calculation of the expected value of $\mathbf{b}$

$$\begin{aligned} E(\mathbf{b}) &= E[(\mathbf{X}^T\mathbf{X})^{-1}\mathbf{X}^T\mathbf{y}] \\ &= E[(\mathbf{X}^T\mathbf{X})^{-1}\mathbf{X}^T(\mathbf{X}\boldsymbol{\beta}+\boldsymbol{\varepsilon})] \\ &= E[(\mathbf{X}^T\mathbf{X})^{-1}\mathbf{X}^T\mathbf{X}\boldsymbol{\beta} + (\mathbf{X}^T\mathbf{X})^{-1}\mathbf{X}^T\boldsymbol{\varepsilon}] = \boldsymbol{\beta} \end{aligned}$$

because of the assumption $E(\boldsymbol{\varepsilon}) = \mathbf{0}$ and $(\mathbf{X}^T\mathbf{X})^{-1}\mathbf{X}^T\mathbf{X} = \mathbf{I}$. Another important quantity in regression analysis is the variance-covariance matrix of the parameter vector $\mathbf{b}$. This matrix consists of the covariances elements between b_i and b_j and the variances b_{jj} in the main diagonal and is calculated as [38]

$$\begin{aligned} \mathrm{Cov}(\mathbf{b}) &= \mathrm{Cov}\left((\mathbf{X}^T\mathbf{X})^{-1}\mathbf{X}^T\mathbf{y}\right) \\ &= (\mathbf{X}^T\mathbf{X})^{-1}\mathbf{X}^T\mathrm{Cov}(\mathbf{y})\left((\mathbf{X}^T\mathbf{X})^{-1}\mathbf{X}^T\right)^T \\ &= \sigma^2(\mathbf{X}^T\mathbf{X})^{-1}\mathbf{X}^T\mathbf{X}(\mathbf{X}^T\mathbf{X})^{-1} = \sigma^2(\mathbf{X}^T\mathbf{X})^{-1} \end{aligned} \tag{3.13}$$

The variance-covariance matrix plays an important role by the calculation of confidence intervals for the model parameters $\mathbf{b}$ and confidence, respectively prediction bounds, of the response surface model.

Another important test in regression analysis is done by a hypothesis test, which is formulated as

$$\begin{aligned} H_0 &: \beta_1 = \beta_2 = \ldots = \beta_k = 0 \\ H_1 &: \beta_j \neq 0 \text{ for at least one } j \end{aligned}$$

This test uses the assumption of normally and independent distributed residuals ε_i with mean zero and variance σ^2, which means that the observations y_i are also normally and independent distributed with mean $\beta_0 + \sum_{j=1}^{k}\beta_j x_{ij}$ and variance σ^2. If the hypothesis H_0 is rejected, the acceptance that at least one of the regressor variables $x_1, x_2, \ldots, x_k$ contributes significantly to the model is implied. By assuming a true null hypothesis H_0, which means all coefficients β_k are zero, the values for SS_R/σ^2 and SS_E/σ^2 are following a χ^2_k, respectively χ^2_{n-k-1} distribution with corresponding degrees of freedom [31]. The test procedure is done by computing the F-statistics F_0 via mean squared values MS_R

and MS_E

$$F_0 = \frac{SS_R/k}{SS_E/(n-k-1)} = \frac{MS_R}{MS_E}$$

It is rejected, if F_0 exceeds $F_{\alpha,k,n-k-1}$. An alternative way in hypothesis tests is to calculate the P-value and to reject the null hypothesis H_0, if its value is less than α. The P-value is defined as the probability, under the assumption of hypothesis, of obtaining a result equal to or more extreme, than what was actually observed. The smaller the P-value, the larger the significance. Calculation of the P-value is mentioned in Section 3.4.5, where the critical value of the t-statistcs has to be replaced by the critical value of the F-statistics. For the presented example, calculation of these values leads to

$$F_0 = \frac{SS_R/k}{SS_E/(n-k-1)} = \frac{5.260/20}{0.068/(36-20-1)} = 58.367 \Rightarrow P\text{-value} = 9.054 \cdot 10^{-11}$$

The critical value F_{crit} on a confidence level $\alpha = 0.05$ is $F_{0.05,20,15} = 2.328$ and leads therefore to a rejection of the null hypothesis. The alternative formulation via P-value gives a quantity of $9.054 \cdot 10^{-11}$ and is categorized usually as highly significant for P-value smaller than 0.001 [39]. This method is part of the ANOVA and can be executed in different variations, for example in partial groups of coefficients or to measure the progress in model quality from linear to quadratic models. Here in this case, the test is used to rate the statistical significance of the whole model.

3.4.5. Tests on Individual Regression Coefficients

Several statistical tests can be applied to the model coefficients, for example it is interesting to know, if inclusion of additional variables increases the quality of the model. In contrast, it is beneficial regarding the model quality, if nonsignificant coefficients are deleted. As proposed in [31], the significance of individual regression coefficients β_j is also rated by a hypothesis test. This test requires the assumption of normally and independent distributed residuals ε_i with mean zero and variance σ^2, which means that the observations y_i are also normally and independent distributed with mean $\beta_0 + \sum_{j=1}^{k} \beta_j x_{ij}$ and variance σ^2. This test is formulated as

$$H_0 : \beta_j = 0$$
$$H_1 : \beta_j \neq 0$$

If $H_0 : \beta_j = 0$ is not rejected, then this indicates, that x_j can be deleted from the model. To justify this, a test quantity has to be calculated, the so-called t-test statistics for the hypothesis t_0

$$t_0 = \frac{b_j}{\sqrt{\hat{\sigma}^2 C_{jj}}} \tag{3.14}$$

with the estimation of the residuals variance $\hat{\sigma}^2$ and the diagonal elements of the inverse moment matrix C_{jj}

$$\hat{\sigma}^2 = \frac{SS_E}{n-p}$$
$$C_{jj} = \text{diag}\left((\mathbf{X^T X})^{-1}\right)$$

The $\sqrt{\hat{\sigma}^2 C_{jj}}$ term is an important quantity in regression analysis and is called the standard error $se(\beta_j)$ of the regression coefficient β_j. The standard error is also calculated as the square root of the diagonal elements from the variance-covariance matrix $\text{Cov}(\mathbf{b})$ in Equation 3.13. Further, Equation 3.14 can be written as

$$t_0 = \frac{b_j}{se(b_j)}$$

Due to the fact, that the test statistics under H_0 follows a t-distribution with $n-k-1$ degrees of freedom on a confidence level α, the null hypothesis $H_0 : \beta_j = 0$ is rejected if $|t_0| \geq t_{\alpha/2,n-k-1}$. An alternative formulation includes the usage of the P-Value, where the cumulative distribution function of Student's t-distribution is used [31], [40]. If the P-Value is smaller than the confidence limit α, the hypothesis is rejected and coefficients contribute significantly to the model.

$$\begin{aligned} P\text{-Value} &= P(|t_0| \geq |t_{crit}|) \\ &= P(t_0 \geq |t_{crit}|) + P(t \leq -|t_{crit}|) \\ &= 2\ P(t_0 \geq |t_{crit}|) \\ &= 2\ (1 - P(t_0 \leq |t_{crit}|)) \end{aligned} \tag{3.15}$$

For the end-of-shaft sensor example, the critical value for the t-statistics on a confidence level $\alpha = 0.05$ is $t_{crit} = t_{0.025,25} = 2.0595$, which leads to following test statistics

$$\text{For } H_0 : \beta_1 = 0 \Rightarrow t_0 = \frac{b_1}{se(b_1)} = \frac{-0.002}{0.0274} = -0.0731 \quad \Rightarrow P\text{-Value} = 0.9427$$
$$\text{For } H_0 : \beta_2 = 0 \Rightarrow t_0 = \frac{b_2}{se(b_2)} = \frac{-0.1274}{0.0274} = -4.6475 \quad \Rightarrow P\text{-Value} = 3.1582 \cdot 10^{-4}$$

This can be concluded as $\beta_2 \neq 0$, which implies that the parameter x-misalignment x_2 contributes significantly to the model, whereas it is not the case for the tilt angle x_1. With the assumption of normally and independent distributed ε_i with mean zero and variance σ^2, it is possible to calculate confidence intervals for the individual regression coefficients. The least squares estimator $\mathbf{b}$ is normally distributed with mean vector $\boldsymbol{\beta}$ and covariance matrix $\sigma^2(\mathbf{X}^T\mathbf{X})^{-1}$ and each of the statistics

$$\frac{b_j - \beta_j}{se(b_j)},\ j = 0, 1, \ldots, k$$

follows a t-statistics with $n-p$ degrees of freedom [31]. A $100(1-\alpha)\%$ confidence interval for the regression coefficients β_j is then constructed as

$$b_j - t_{\alpha/2,n-p} se(b_j) \leq \beta_j \leq b_j + t_{\alpha/2,n-p} se(b_j) \tag{3.16}$$

In this example, the 95% confidence interval for β_1 is

$$-0.0604 \leq -0.002 \leq 0.0564$$

and for β_2

$$-0.1858 \leq -0.1274 \leq -0.0689$$

In contrary to β_2, the interval for β_1 overlays 0 and is therefore not significantly different from 0. The introduced t-test is applied to test coefficients due to their model significance and is used furthermore to reduce the full quadratic model, where successively coefficients are removed to increase the model quality.

3.4.6. Model Reduction

Model reduction is an important procedure in response surface methodology, because it is necessary to remove all components, which do not contribute statistically significant to the model. Two different approaches are introduced, where the first one removes coefficients by using t-tests as long the adjusted Coefficient of Determination R^2_{adj} increases. The first time, R^2_{adj} decreases, the retrieval of coefficients is stopped. Figure 3.9 shows the development of R^2 and R^2_{adj} with proceeded retrieval of coefficients, which is represented by y_{red1} in Equation 3.17.

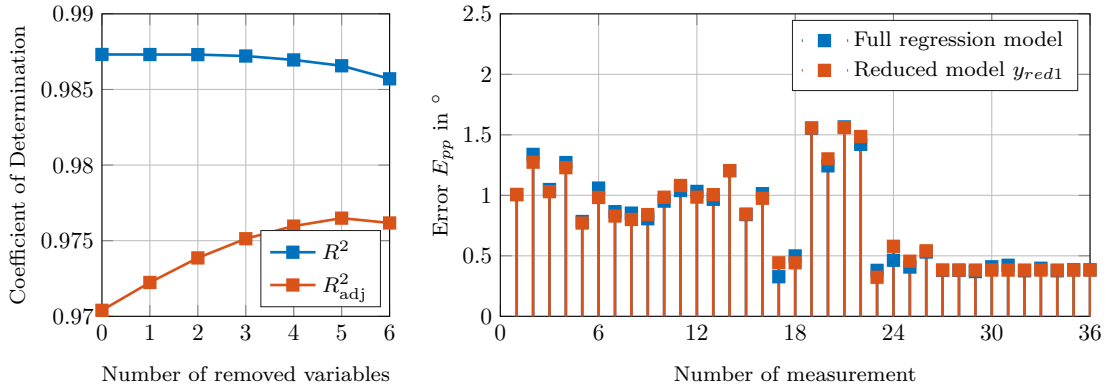

Figure 3.9.: Model reduction of exemplary experiment to maximize R^2_{adj}. After removing the six least significant coefficients, R^2_{adj} is decreasing.

The mathematical model from Equation 3.6 degenerates with this first introduced model

reduction strategy into

$$\begin{aligned}\hat{y}_{red1} = {} & 0.3822 - 0.1274x_2 - 0.0369x_3 + 0.1280x_4 + 0.0429x_5 \\ & + 0.3242x_1x_2 - 0.0678x_1x_4 - 0.1828x_2x_3 - 0.1537x_3x_4 + 0.1408x_3x_5 - 0.1324x_4x_5 \\ & + 0.0602x_1^2 + 1.0465x_2^2 + 1.1408x_3^2 + 0.0687x_4^2 + 0.1163x_5^2 \end{aligned} \tag{3.17}$$

Figure 3.9, left, shows how R^2_{adj} increases with further elimination of model coefficients. After six removed coefficients, R^2_{adj} decreases the first time and the model reduction process is stopped by then. Figure 3.9, right, shows the design results from full and reduced model plotted against each other. Another justification for the reduced model is shown in Figure 3.10, where the prediction plots of full and reduced model are depicted.

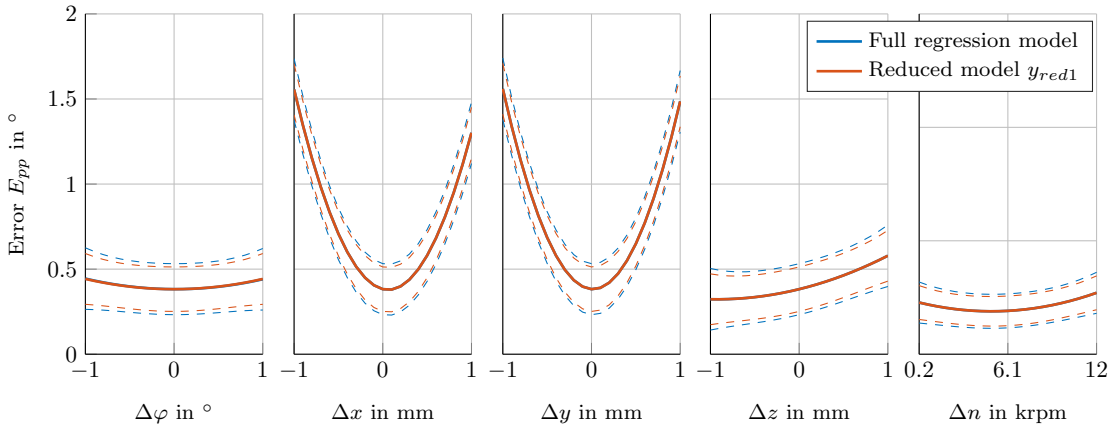

Figure 3.10.: Prediction plot comparison of full and reduced model by maximizing R^2_{adj}.

The second method starts with the interaction terms and tests them with above introduced method. Afterwards the quadratic effects are tested and removed if possible. Testing the linear effects is done in the last step, but it is important that only coefficients, which are not involved in any significant interaction terms, are allowed for elimination [31]. Note that the coefficient elimination has to be performed successively, which means that with every removed coefficient the regression model, the t-statistics, P-Values and Coefficient of Determinations have to be calculated renewed. The second method of model reduction is more strict: coefficients are always removed, if their P-value exceeds the confidence niveau. This leads to following quadratic model

$$\begin{aligned}\hat{y}_{red2} = {} & 0.4037 - 0.0020x_1 - 0.1274x_2 - 0.0369x_3 + 0.1280x_4 + 0.0429x_5 \\ & + 0.3242x_1x_2 - 0.1828x_2x_3 - 0.1537x_3x_4 + 0.1408x_3x_5 - 0.1324x_4x_5 \\ & + 1.0465x_2^2 + 1.1408x_3^2 + 0.1163x_5^2 \end{aligned} \tag{3.18}$$

where the resulting main effects of the full and reduced model are shown in Figure 3.11.

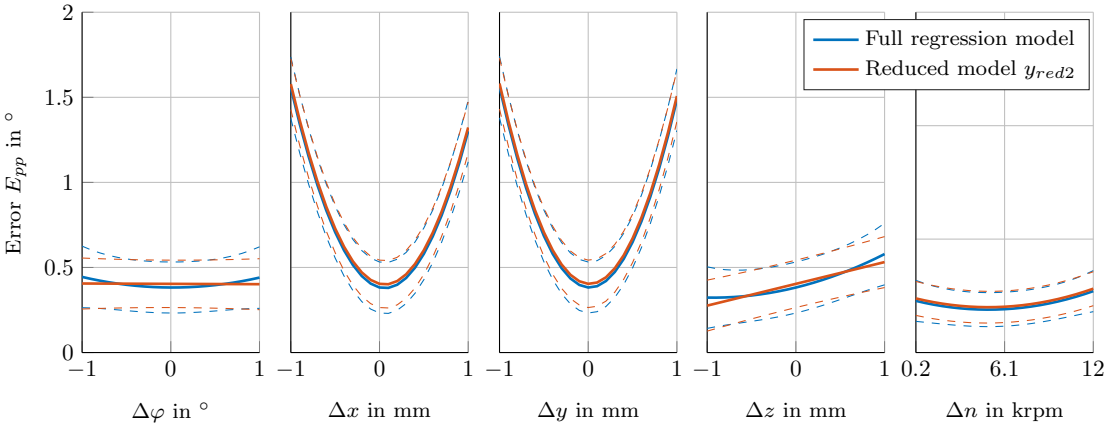

Figure 3.11.: Prediction plot comparison of full and reduced model with second method. The quadratic effects in x_1 (tilt angle $\Delta\varphi$) and x_4 (distance Δz) are classified as random and not statistically relevant.

The reduced number of coefficients results in a smaller standard error, which has direct influence on the width of the prediction bounds and therefore on the prediction quality of the model. Due to the fact, that all regressors are present in at least one of the interaction terms, none of them is allowed to be deleted in the linear case, although they are classified as non-significant by the performed t-test. Above equation and prediction plot show, that the quadratic main effects in x_1 and x_4 are removed in this case, because the performed t-test classified them as not statistically relevant. In this way, all following investigations and evaluations have to be done with the reduced models.

3.4.7. Residual Analysis

As suggested in [32], the residuals have to be investigated in more detail and different visual control methods have to be applied, such as:

- Predicted vs. actual
- Residual vs. run order
- Residual vs. predicted
- Full-Normal

These different plots are helpful to detect outliers, to rate the consistency between measurement and model or to assess the assumption of normal distributed residuals. Figure 3.12 shows these different kinds of plots.

The predicted vs. actual plot depicts the model prediction compared to measurement results; for a perfect model fit all points would lie on the straight line. With this plot type,

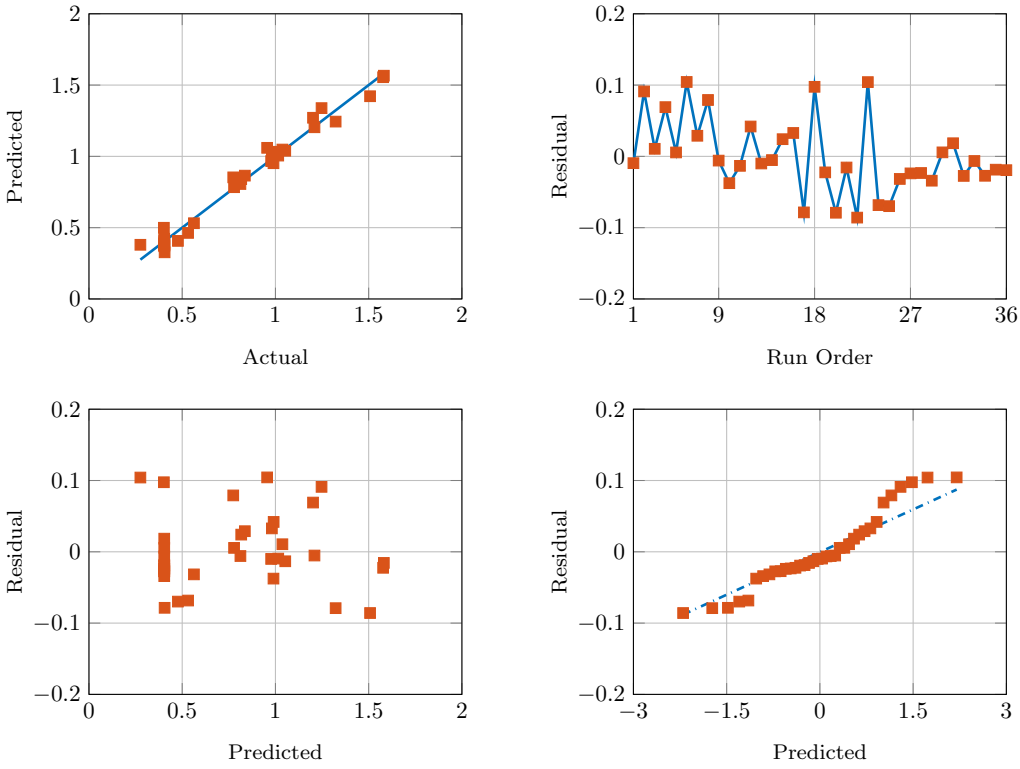

Figure 3.12.: Predicted vs. actual (top left), residual vs. run order (top right), residual vs. predicted (bottom left) and Full-Normal plot (bottom right).

detection of outliers is possible. The important property of Homoscedasticity can also be obtained, in case that the variance of the residuals is constant and does not depend on the predictor value. The residual vs. run order plot shows, in which experiment high deviations of model and measurement occur. It is used to detect possible wrong settings within the experiments [32]. Usually, the model prediction performance is better for middle output values compared to the smaller and higher quantities, which is examined with the residual vs. predicted plot. No trend or correlation should be apparent and the points should be randomly scattered. The assumption of normally distributed and uncorrelated residuals is important in regression analysis and is verified with the Full-Normal plot. This plot rates, how accurate the residuals follow a normal distribution, which is observed by how accurate the residuals lie on the straight line. Systematic errors, e.g. offset or scale factor errors, do not follow a normal distribution within the experiment and are recognized with this type of plot. No conspicuousness regarding the residuals is apparent here by obtaining this four plots, which indicates a good consistency of the calculated model.

3.4.8. Model Validation

Figure 3.8 shows, how the model represents the physical process at the design points, where the experiment is performed. The design points are - depending on the choice of experimental design as shown in Figure 3.3 - always on corners, edges, axis and center points within the investigated design space. A validation should be performed, where the model quality is verified at randomly sampled points within the experimental space to justify the model validity. Figure 3.13 depicts the result of this model validation.

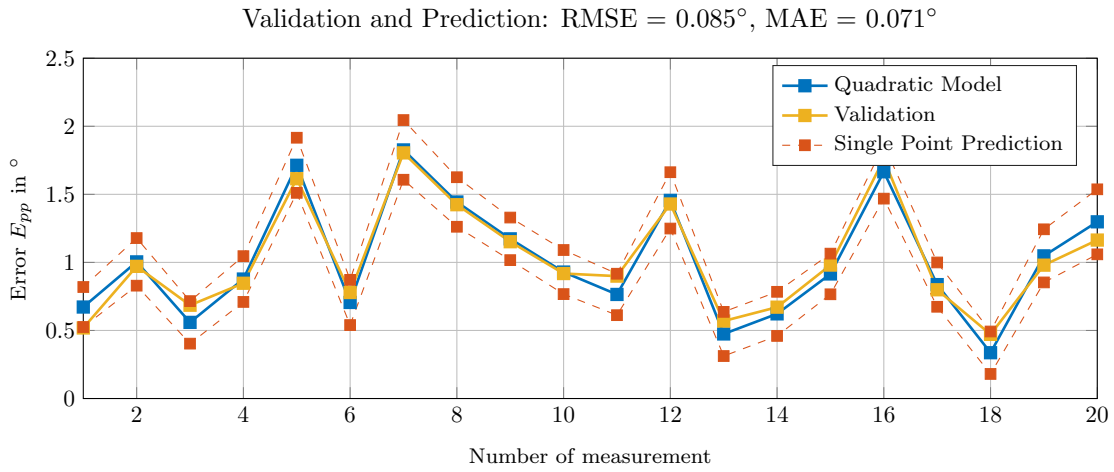

Figure 3.13.: Validation results with 20 randomly sampled points within experimental design space, comparison of measurements and full quadratic model with single prediction interval.

As a performance index, MAE and RMSE are applied for this purpose. In this example, the validation shows a mean absolute error of 0.071 °. This means, that the average deviation of model and real sensor measurement is expected to be approximately 0.07 °, which accords to a good sensor error prediction capability. Additionally, the sensor error model prediction results match the measurements accurate and lie very reliable within the single point confidence intervals.

3.4.9. Confidence and Prediction Bounds

As showed in Section 3.4.5, Equation 3.16 is used to calculate confidence bounds for the regression coefficients β_j. It is also possible, to define intervals for the mean response or for new observations of the regression model. The intervals of the mean response are used as confidence bounds, whereas the intervals on new observations are used as prediction bounds. These bounds are further subdivided into non-simultaneous and simultaneous bounds, where the first takes into account only individual predictor values and the latter

all predictor values. As shown in [31], for a vector

$$\mathbf{x}_0 = \begin{bmatrix} 1 \\ x_{01} \\ x_{02} \\ \vdots \\ x_{0k} \end{bmatrix}$$

the mean response of the fitted model at this point is given as

$$\mu_{y|\mathbf{x}_0} = \beta_0 + \beta_1 x_{01} + \beta_2 x_{02} + \ldots + \beta_k x_{0k} = \mathbf{x}_0^T \boldsymbol{\beta}$$

The estimation of the mean response for y, due to the fact that the used coefficients $\mathbf{b}$ are an estimation for the least squares coefficients $\boldsymbol{\beta}$, is

$$\hat{y}(\mathbf{x}_0) = \mathbf{x}_0^T \mathbf{b}$$

and with the variance of the mean response

$$\mathrm{Var}[\hat{y}(\mathbf{x}_0)] = \sigma^2 \mathbf{x}_0^T (\mathbf{X}^T \mathbf{X})^{-1} \mathbf{x}_0 \tag{3.19}$$

a $100(1-\alpha)\%$ confidence interval on the mean response at the point $\mathbf{x}_0$ is calculated as

$$\begin{aligned} &\hat{y}(\mathbf{x}_0) - t_{\alpha/2,n-p} \sqrt{\hat{\sigma}^2 \mathbf{x}_0^T (\mathbf{X}^T \mathbf{X})^{-1} \mathbf{x}_0} \\ &\quad \leq \mu_{y|\mathbf{x}_0} \leq \hat{y}(\mathbf{x}_0) + t_{\alpha/2,n-p} \sqrt{\hat{\sigma}^2 \mathbf{x}_0^T (\mathbf{X}^T \mathbf{X})^{-1} \mathbf{x}_0} \end{aligned} \tag{3.20}$$

This is called a non-simultaneous or single point confidence bound for the function at a single predictor value. If the regression model is used to predict future observations on the response y, a point estimation for a future observation y_0 at the point $\mathbf{x}_0$ is computed by

$$\begin{aligned} &\hat{y}(\mathbf{x}_0) - t_{\alpha/2,n-p} \sqrt{\hat{\sigma}^2 (1 + \mathbf{x}_0^T (\mathbf{X}^T \mathbf{X})^{-1} \mathbf{x}_0)} \\ &\quad \leq y_0 \leq \hat{y}(\mathbf{x}_0) + t_{\alpha/2,n-p} \sqrt{\hat{\sigma}^2 (1 + \mathbf{x}_0^T (\mathbf{X}^T \mathbf{X})^{-1} \mathbf{x}_0)} \end{aligned} \tag{3.21}$$

which is annotated as non-simultaneous or single point prediction bound for a new observation at the predictor value $\mathbf{x}_0$. Due to the additional variability of observations of the predicted mean value, an additional $\hat{\sigma}^2$ occurs under the root by the interval calculations; therefore prediction intervals are always wider as confidence intervals. For simultaneous prediction bounds, which are appropriate for the whole regression function over its entire range by considering the complete variability of model, the t-statistics has to be replaced by an F-statistics as shown in [40]. The simultaneous confidence bounds

for the function and all predictor values are given as

$$\hat{y}(\mathbf{x}_0) - \sqrt{pF_{1-\alpha,p,n-p}}\sqrt{\hat{\sigma}^2\mathbf{x}_0^T(\mathbf{X}^T\mathbf{X})^{-1}\mathbf{x}_0} \leq \mu_{y|\mathbf{x}_0} \leq \hat{y}(\mathbf{x}_0) + \sqrt{pF_{1-\alpha,p,n-p}}\sqrt{\hat{\sigma}^2\mathbf{x}_0^T(\mathbf{X}^T\mathbf{X})^{-1}\mathbf{x}_0} \tag{3.22}$$

and accordingly for the simultaneous prediction interval for a new observation y_0

$$\hat{y}(\mathbf{x}_0) - \sqrt{pF_{1-\alpha,p,n-p}}\sqrt{\hat{\sigma}^2(1+\mathbf{x}_0^T(\mathbf{X}^T\mathbf{X})^{-1}\mathbf{x}_0)} \leq y_0 \leq \hat{y}(\mathbf{x}_0) + \sqrt{pF_{1-\alpha,p,n-p}}\sqrt{\hat{\sigma}^2(1+\mathbf{x}_0^T(\mathbf{X}^T\mathbf{X})^{-1}\mathbf{x}_0)} \tag{3.23}$$

Figure 3.14 shows the resulting confidence intervals evaluated with all four methods. The first one considers the expectations on the mean of a new observation; these intervals are the tightest. For a comparison between model and responses as implemented in the model validation, the single point prediction intervals are the most appropriate. Therefore, this kind of bounds are used in former results and represent the default ones used in this work.

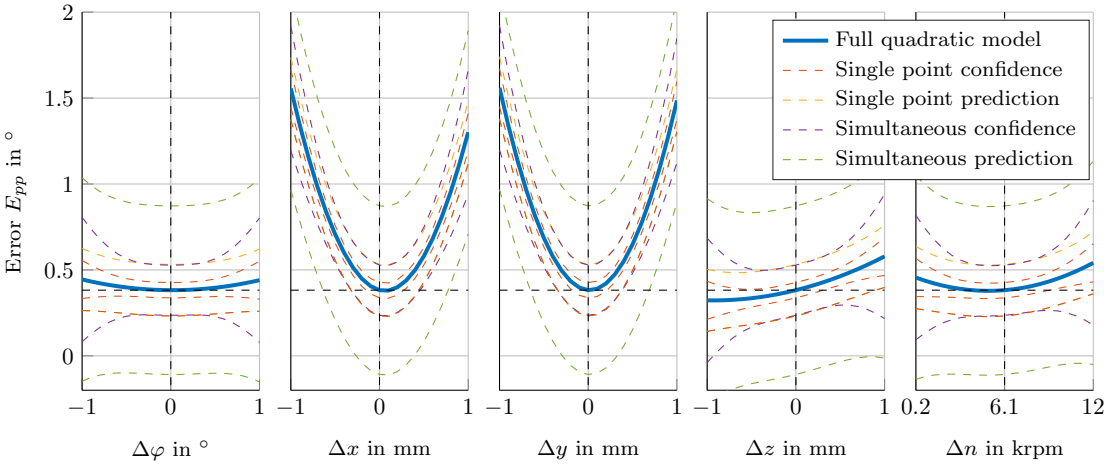

Figure 3.14.: Prediction plot with different confidence bound calculation methods.

Due to the consideration of the whole model variability, the bounds for simultaneous confidence and prediction intervals are wider (see Equations 3.20-3.23), especially for the prediction case. These intervals accord to a strong requirement due to the considered variability of all parameters to the response surface model and are therefore not considered further [40]. The dependency of different designs and the resulting confidence and prediction intervals is strongly influenced by Equation 3.19, which is called the prediction variance (PV). By analyzing the structure of the Moment matrix, properties for the prediction variance are obtained, which directly determine the shape of these confidence and prediction intervals. Due to the decreased number of model parameters p

by performing a model reduction, the degrees of freedom $n - p$ increase and therefore the residual error $\hat{\sigma}$ decreases. This explains the tighter confidence bounds in Figure 3.10, which is another benefit of reduced models. Additional influences on the width and shape of the confidence bounds are the number of observations n and the choice of the used design. By performing a design consecutively twice, the number of observations n increases, which results in a lower residual error and gives statistically more confident results. Figure 3.15 shows a comparison of an once and a twice executed CCI design and their resulting confidence bounds.

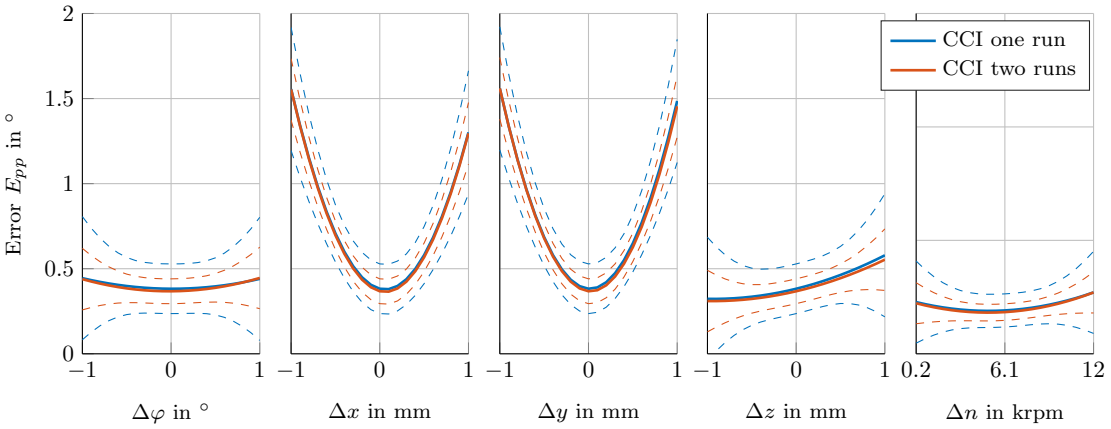

Figure 3.15.: Prediction plots with one and two consecutive performed CCI test runs.

The shape of the confidence bounds is mainly determined by the inverse of the moment matrix $(\mathbf{X}^T\mathbf{X})^{-1}$, which is called the Information matrix. The structure of this matrix is a consequence of the chosen experimental design, means that this choice directly influences the shape and size of the confidence intervals. This property of different kinds of experimental designs is summarized by the concept of spherical prediction variance [31].

3.4.10. Comparison of Different Design Approaches

As mentioned in Section 3.4.2, different choices due to the used experiments are possible. Usually, the choice of the design is the first task by performing a DOE and is not changed afterwards. This case - the process with the test bench and investigated sensors - allows to compare different designs with each other and to give suggestions for recommended designs for this specific application. Figure 3.16 shows a main effect comparison of different designs, where all models have been reduced by t-tests.

All designs are capable of representing the parameter dependencies of the sensor error as a function of the investigated parameters. The CCI and BB give very similar results (especially for unreduced models), whereas CCF and FF designs differ in their representation of z-direction dependency. The quadratic effects of tilt angle $\Delta\varphi$ and rotor

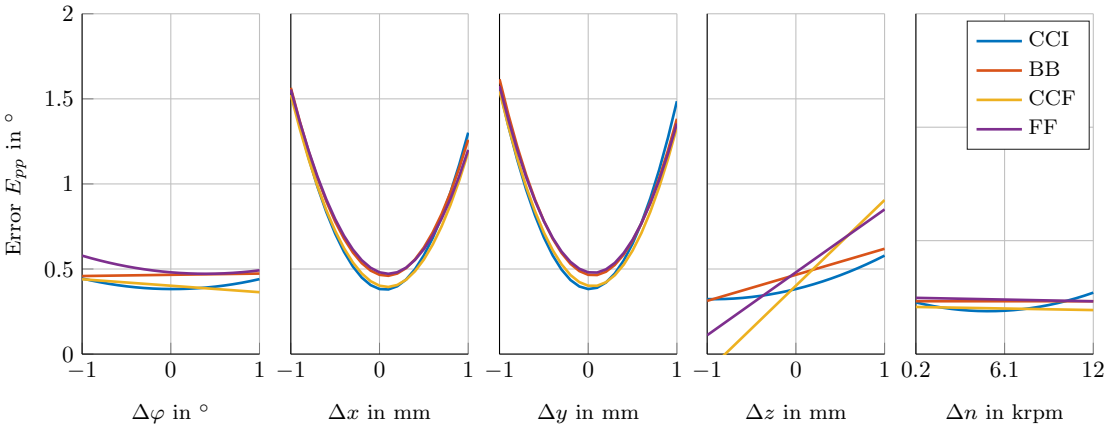

Figure 3.16.: Comparison of different reduced design results.

shaft speed Δn are still present in the reduced CCI, but not for the reduced BB design, where these effects are removed and classified as not significant. To rate and compare the different designs, the performed validation in Section 3.4.8 is used to find statistical significant differences in the design candidates. Figure 3.17 shows the validation results of different designs with MAE as performance criterion.

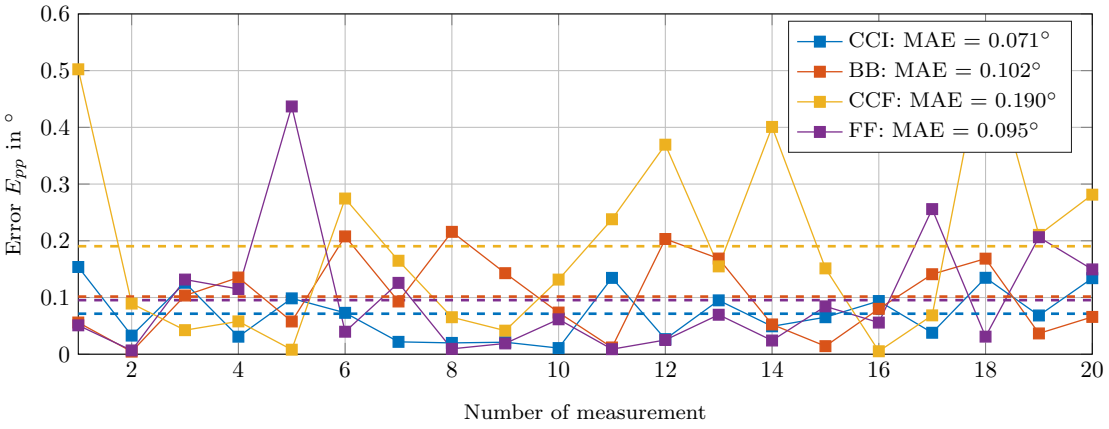

Figure 3.17.: Comparison of different design results.

There are different kind of performance criteria, which can be applied to evaluate the prediction quality of a response surface model, such as MAE, RMSE, Mean Absolute Percentage Error (MAPE) or Theil's Inequality Coefficient (TIC) [41]. The first two

were introduced in the former subsections, the other two are defined as

$$\text{MAPE} = \frac{1}{n}\sum_{i=1}^{n}\left|\frac{y_i - \hat{y}_i}{\hat{y}_i}\right| \cdot 100$$

$$\text{TIC} = \frac{\sqrt{\frac{1}{n}\sum_{i=1}^{n}(y_i - \hat{y}_i)^2}}{\sqrt{\frac{1}{n}\sum_{i=1}^{n} y_i^2} + \sqrt{\frac{1}{n}\sum_{i=1}^{n} \hat{y}_i{}^2}}$$

The MAPE is very similar to the MAE criterion, but due to its normalization of observation amplitudes, it is better suitable for comparing different validation results of different value ranges. TIC is mainly based on the RMSE, with the difference that its weighted by a RMSE of the observations y_i and predictors $\hat{y}$ and it must be within 0 and 1, where 0 means a perfect fit [41]. In this example, for rating the design quality, MAE is used, but it also correlates good with the other performance indices. Table 3.1 shows the validation results by applying different performance criteria and Figure 3.17 depicts the absolute values from regression model and validation measurement deviations of different designs, where the validation result of the twice executed CCI is not shown for better clarity.

Table 3.1.: Performance criteria for different experiments for prediction quality rating.

Design	**CCI**	**BB**	**CCF**	**FF**	**CCI 2x**
MAE	0.0714	0.1016	0.1904	0.0954	0.1101
RMS	0.0847	0.1210	0.2473	0.1402	0.1426
MAPE	9.0417	10.3408	25.4606	10.1499	9.9992
TIC	0.0386	0.0497	0.1104	0.0512	0.0617

All designs have quite similar MAE errors, except the CCF design gives the worst results in this specific comparison. To find a statistical significance difference between the performed experiments, the validation results of each design is grouped and a two-sample t-test is performed to compare the different designs. The CCI design performs best in the model validation. Therefore the CCI is compared with the other four to find a statistical difference in the results. The idea of the two-sample t-test is to proof, if two samples have the same expectation value μ_1 and μ_2 under the assumption of variance homogeneity [42]

$$H_0 : \mu_1 - \mu_2 = 0$$
$$H_1 : \mu_1 - \mu_2 \neq 0$$

The t-test statistics is calculated as

$$t = \frac{\mu_1 - \mu_2}{\sigma\sqrt{\frac{1}{n_1} + \frac{1}{n_2}}} = \sqrt{\frac{n_1 n_2}{n_1 + n_2}}\frac{\mu_1 - \mu_2}{\sigma}$$

with expectation values μ_1, μ_2 and sample numbers n_1, n_2 from the compared sample probes. The value σ^2 is the so-called pooled variance of the sample variances σ_1^2 and σ_2^2 and calculated as

$$\sigma^2 = \frac{(n_1 - 1)\sigma_1^2 + (n_2 - 1)\sigma_2^2}{n_1 + n_2 - 2}$$

The null hypothesis will be rejected if

$$|t| > t_{1-\alpha/2,df}$$

with a t-statistics consisting of $df = n_1 + n_2 - 2$ degrees of freedom, which leads to a critical t-value $t_{crit} = 2.0244$. Obtaining the results in Table 3.2 shows, that all t-test values - except for the CCF - are smaller than the critical t-Value.

Table 3.2.: CCI Design comparison and t-tests with all performed experiments.

Design	**CCI**	**BB**	**CCF**	**FF**	**CCI 2x**
MAE	0.0714	0.1016	0.1904	0.0954	0.1101
t	-	1.6463	3.1572	0.9283	1.6618
P-Value	-	0.1080	0.0031	0.3591	0.1048

This means that the CCF design is the only design, which is statistically significant worse than the CCI design. Caused by its minimal MAE value, the CCI design operates in this test as benchmark. All other candidates can not be statistically classified as worse as the CCI and are therefore also usable on investigations regarding these sensor types.

Since the assumption of samples with same variances is not fulfilled in this considerations, the t-test is usually replaced by Welch's t-test or unequal variances t-test. The t-test statistics in this specific case is formulated as an approximation and defined as [43]

$$t = \frac{\mu_1 - \mu_2}{\sqrt{\frac{\sigma_1^2}{n_1} + \frac{\sigma_2^2}{n_2}}}$$

where former degrees of freedom $df = n_1 + n_2 - 2$ are adjusted with

$$\nu \approx \frac{\left(\frac{\sigma_1^2}{n_1} + \frac{\sigma_2^2}{n_2}\right)^2}{\frac{\left(\frac{\sigma_1^2}{n_1}\right)^2}{n_1 - 1} + \frac{\left(\frac{\sigma_2^2}{n_2}\right)^2}{n_2 - 1}}$$

The null hypothesis is rejected in the same manner as for the two-sample t-test with modified degrees of freedom if

$$|t| > t_{1-\alpha/2,\nu}$$

In this case, the critical test value t_{crit} and degrees of freedom ν are not constant as in the two-sample t-test before and depend on the performed test. Table 3.3 summarizes

the Welch-test results regarding the comparative study of the different designs.

Table 3.3.: CCI Design comparison and Welch-test results with all performed experiments.

Design	**CCI**	**BB**	**CCF**	**FF**	**CCI 2x**
MAE	0.0714	0.1016	0.1904	0.0954	0.1101
t	-	1.6463	3.1572	0.9283	1.6618
t_{crit}	-	2.0326	2.0731	2.0548	2.0483
ν	-	33.8592	22.1511	26.1959	28.0331
P-Value	-	0.1090	0.0045	0.3617	0.1077

The Welch-test leads to the same t-test statistics as the two-sample t-test, but caused by the modified computation of critical test value and degrees of freedom, these quantities and P-Values slightly change. But the conclusion of the former two-sample t-test, that the CCF is the only design that is statistically significant worse than the CCI, stays valid by the performed Welch test. Therefore, the inhomogeneous variances of the validation samples do not interfere the results of the performed design benchmark.

Another factor, which is strongly influenced by the design choice, is the (scaled) prediction variance (SPV) and therefore the prediction and confidence intervals of the regression model [31]. Figure 3.18 shows a comparison of simultaneous confidence intervals of a CCI and BB design and their notable different shaped bounds.

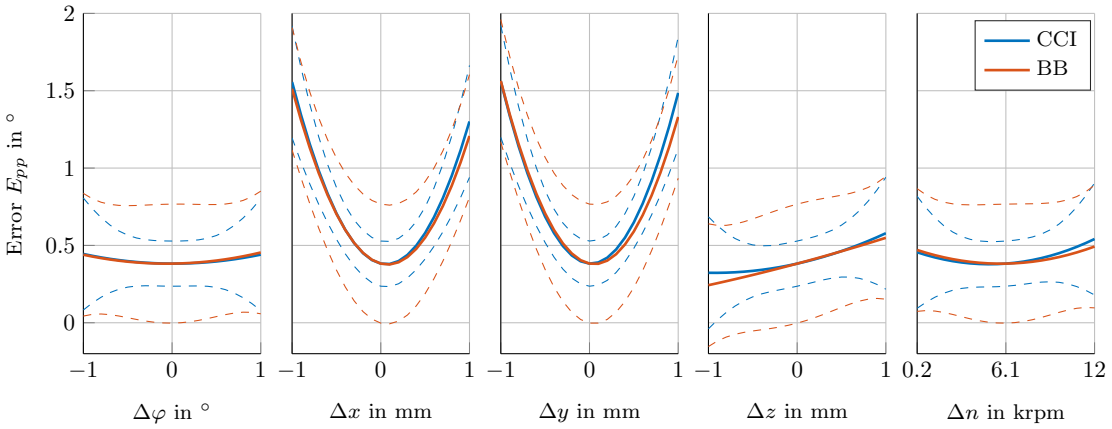

Figure 3.18.: Comparison of different reduced design results.

The SPV is defined as

$$\mathrm{SPV}(\mathbf{x}) = n\mathbf{x}^{(m)T}(\mathbf{X}^T\mathbf{X})^{-1}\mathbf{x}^{(m)} = \mathbf{x}^{(m)T}\left(\frac{\mathbf{X}^T\mathbf{X}}{n}\right)^{-1}\mathbf{x}^{(m)} = \mathbf{x}^{(m)T}\mathbf{M}^{-1}\mathbf{x}^{(m)} \tag{3.24}$$

with the scaled Moment matrix $\mathbf{M}$, the number of observations n and the observed point $\mathbf{x}^{(m)}$ expanded to corresponding model space. The unscaled version without the penalty term n is called the unscaled prediction variance UPV

$$\text{UPV} = \text{Var}[\hat{y}(\mathbf{x})]/\sigma^2 = \mathbf{x}^{(m)T}(\mathbf{X}^T\mathbf{X})^{-1}\mathbf{x}^{(m)} \tag{3.25}$$

The term on the right side plays an important role in calculation of confidence and prediction intervals as mentioned in Section 3.4.9, only scaled by the square root of the residuals RMSE and t-, respectively F-statistics. Due to their higher exemplary power, the simultaneous confidence intervals are depicted in this example, but the following statements are valid for all confidence and prediction bounds. Analyzing Equation 3.25 shows, that the UPV results in a quartic function of the regressors $x_1, \ldots, x_5$ and depends strongly on the choice of $\mathbf{X}$ and therefore on the choice of the used design. The number of center runs is an important aspect in fitting second-order models, because additional center runs are used to reduce the prediction variance in the design origin. Figure 3.19 on the top depicts the unscaled prediction variances of the applied default CCI and BB designs, which means that they consist of five variables and five, respectively six center runs.

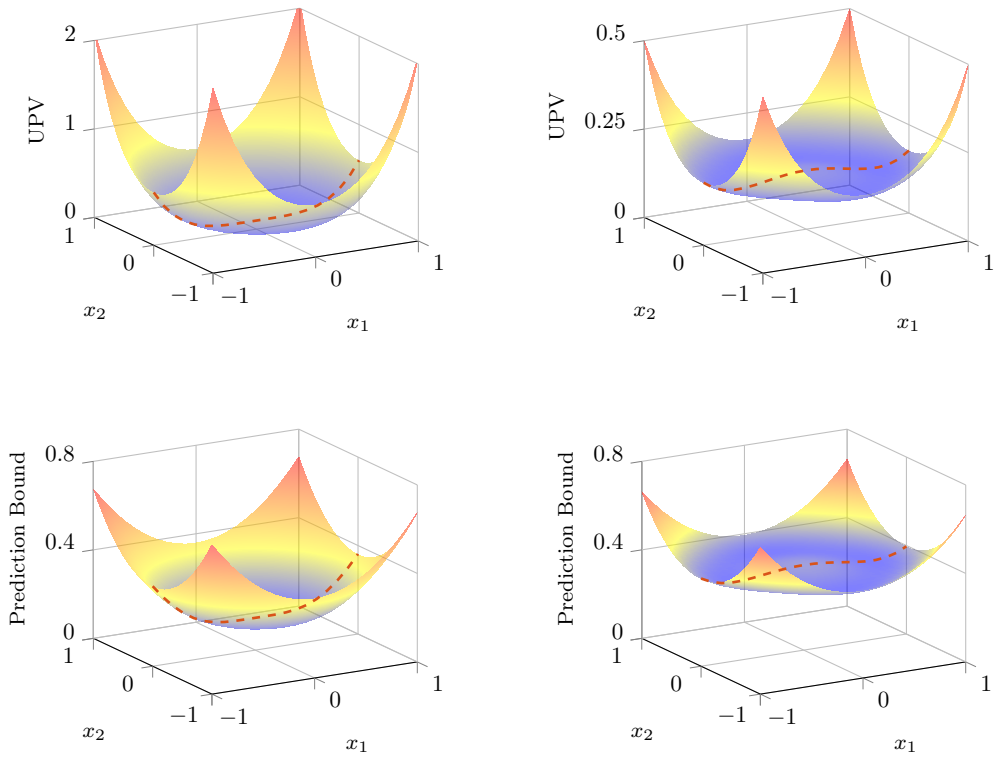

Figure 3.19.: UPV comparison of CCI (top left) and BB design (top right) with calculated prediction bounds for CCI (bottom left) and BB (bottom right). The red dashed lines correspond with the prediction bounds in Figure 3.18.

The red dashed line shows the UPV along factor x_1 by keeping x_2 constant. By scaling the unscaled prediction variance as in Equation 3.22, the simultaneous confidence intervals can be computed. These intervals are displayed in Figure 3.19 on the bottom. The red dashed line shows the simultaneous confidence interval again for varying x_1 by keeping x_2 constant. Adding these intervals to the quadratic model corresponds with the confidence bounds plotted in Figure 3.18. It shows, that the CCI has a better confidence, respectively prediction property near the design origin, at the corners and edges both designs perform nearly equal. The best design regarding the prediction variance is the CCC design [31], but this version can not be applied in this application as mentioned in Section 3.4.2. Further information regarding prediction variance and variance dispersion graphs can be found in [44].

As shown in Equation 3.24, the inverse of the Moment matrix is the key to compare different designs with each other in terms of variance properties. Optimal designs have the aim to optimize different variance aspects of the design, such as [33]

- The determinant of the Moment matrix (D-optimal)
- Minimization of the maximum prediction variance (G-optimal)
- Minimizing the trace of the inverse of the Information matrix (A-optimal)

A lot more different optimal designs were developed, but computation of these designs usually leads to non-trivial optimization problems and are therefore not further investigated in this work. This section has the aim to show, that the choice of design not only impacts the number of runs and the characteristics of the response surface model, it also influences the confidence and prediction quality of the computed model.

3.5. Results and Comparison of Different Sensor Technologies and Sensor Configurations

This section presents exemplary results, if the introduced DOE method is applied for different sensor technologies and sensor configurations. Note that the investigated sensors have different pole numbers p, for the end-of-shaft applies $p = 2$, the eddy current $p = 4$ and the resolver $p = 10$. In this comparison, the mechanical error of the sensors are plotted and the relation between mechanical and electrical angle error is given by

$$\theta = \theta_m \, p$$

which produces a scaling of the mechanical angle error direct proportional with the pole number. Due to the high number of poles, the resolver is the most accurate position sensor by considering the mechanical angle error. For controlling electric machines, the electrical angle is usually the quantity of interest, but in this case the mechanical angle error is depicted for a better comparison. Figure 3.20 shows a comparison of the main three investigated sensor technologies in this work.

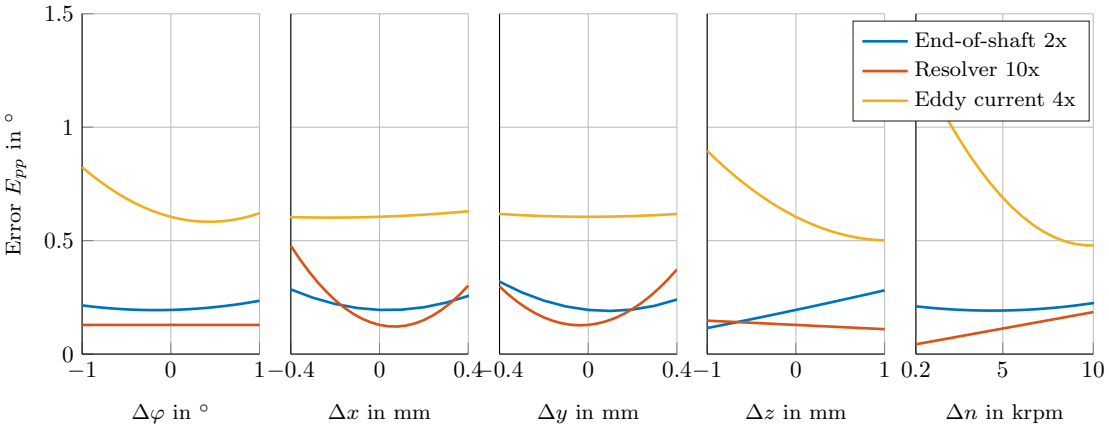

Figure 3.20.: Comparison of different sensor principles. All experiments performed with a Box-Behnken design.

Mind that these sensors have different experimental spaces, especially the resolver has an electrical speed limit due to the necessary signal processing and limited mechanical misalignment, which leads to smaller parameter variations in this benchmark. In the sense of a better overview, the confidence or prediction bounds are not depicted. The benchmark shows, that the eddy current sample has not the accuracy of the other two technologies, but a high robustness against planar misalignment. The decrease of error due to higher speeds is caused by an internal switch of the rotor position calculation algorithm. Regarding the improved sensor output signal quality at higher speeds, no detailed information is provided by the sensor supplier. The error speed dependency of the resolver is caused by the resolver-to-digital conversion [45] and its induced jitter at higher speeds. The plot also shows, that resolvers are highly sensitive regarding mechanical misalignment, especially in lateral direction. This is a disadvantage of resolvers, which requires a precise placement within the application to reach their specified accuracy. Another usage of the presented method is the comparison of different sensor configurations. For example, the investigated end-of-shaft sensors have to be equipped with a rotating diametrically magnetized magnet, as showed in Figure 3.4. Sensor manufacturers mostly give specifications about the field strength and geometry of the applied magnet, but a plurality of different magnets is available. This method can be deployed to test different sensor magnet combinations and to find the best magnet-sensor configuration, as shown in Figure 3.21.

It shows, that Magnet B [46] has a slightly better accuracy of rotor position measurement ability compared with Magnet A in the sensors ”sweet” spot, but it has a significantly stronger parameter dependency compared to Magnet A. Similar investigations are performed with eddy current sensor types. The rotating flywheel must consist of a conductive material and is produced of different metals, such as steel or aluminium. Aluminium has approximately a third of the specific density of steel and is non-ferromagnetic, which

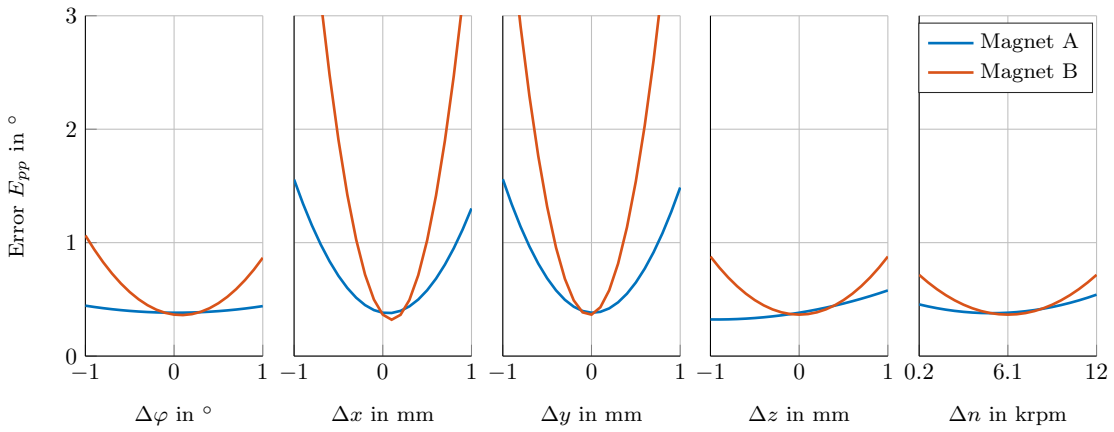

Figure 3.21.: Comparison of different magnet and end-of-shaft sensor combinations. All measurements performed with a CCI design.

can be beneficial for specific applications. Figure 3.22 shows a comparison of an eddy current sensor equipped with different target wheels, respectively target wheel materials.

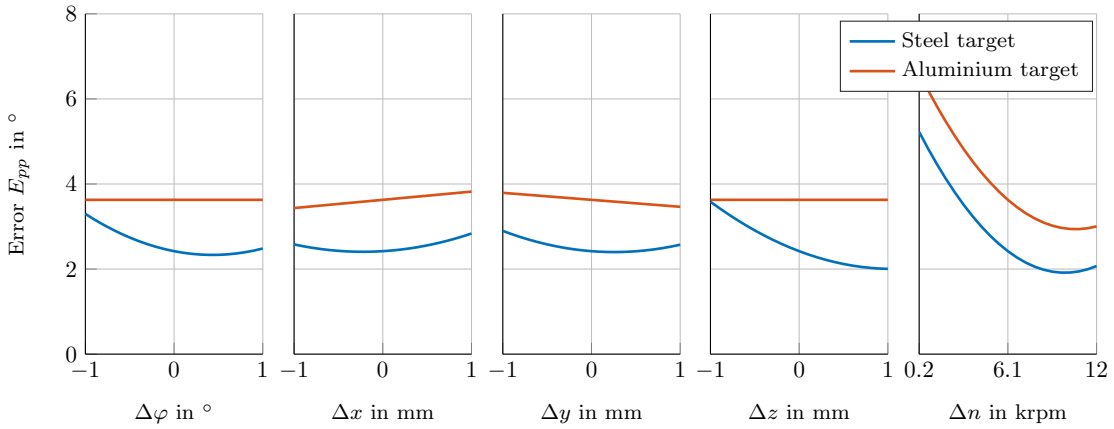

Figure 3.22.: Comparison of different targets and eddy current sensor combinations. All measurements performed with a Box-Behnken design.

As mentioned in the beginning of this section, measurements were performed on a specific test bench, which supports the functionality to vary different parameters. Additional interesting parameters are temperature and supply voltage. These two variables have not been considered yet for better clarity and oversight of the proposed method. Additionally, they usually have a small influence on the sensors measurement performance and were neglected in the former sections. Increasing the number of variables from five to seven makes the usage of reduced test plans necessary, because due to the high number of test

runs, applying a Full Factorial design is not worthwhile in this case anymore. Figure 3.23 shows the results of a Box-Behnken design measurement cycle of an end-of-shaft sensor with all seven parameter variations, which are possible to vary with the engaged test bench.

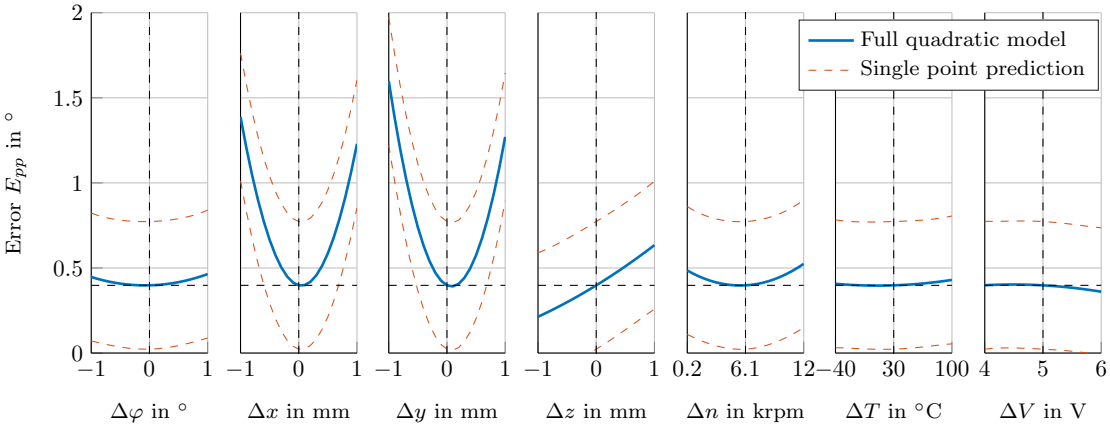

Figure 3.23.: Box-Behnken design for the exemplary end-of-shaft sensor error characteristics with seven varied parameters.

Compared with Figure 3.18, the same characteristics for the first five parameters are apparent and in addition the weak dependency of this specific sensor in terms of temperature and supply voltage is shown. After a model reduction, these two factors will be eliminated due their non present statistical significance. This justifies to neglect these two factors in the demonstration examples, because they increase the model complexity, wide the confidence and prediction bounds and provide no additional model explanation.

3.5.1. Calculation of Stationary Points

In the proposed method, second-order quadratic models are used to characterize the sensor behaviour in terms of parameter variations. Usually, manufacturers specify the geometrical placement of their sensors. But possible degrees of freedom can occur, for example in the z-distance for end-of-shaft and eddy current sensors. If the sensor characteristics are shaped like as the Magnet B type in Figure 3.21, the stationary point for the minimal sensor error is determined by differentiating Equation 3.7

$$\frac{\partial \hat{y}}{\partial \mathbf{x}} = \mathbf{a} + 2\mathbf{B}\mathbf{x} = \mathbf{0}$$

where the stationary point $\mathbf{x}_s$ is calculated as

$$\mathbf{x}_s = -\frac{1}{2}\mathbf{B}^{-1}\mathbf{a}$$

Calculation of stationary points of quadratic functions is only an indicator for a maximum, minimum or a saddle point. In this application, only minima are interesting. The condition for an existing minima is a positive definite matrix **B**. One criterion of a positive definite matrix is, that all eigenvalues of **B** are positive. This is the case for the given example and equations above can be used to calculate an "optimal" operating point of the investigated sensor, under consideration of all interaction terms (see Figure 3.5 and 3.6). In general, the stationary point lies outside the investigated experimental space or the positive definiteness is not satisfied, like as for the Magnet A curves in Figure 3.21. An operating point of minimal error for the second-order model is still present somewhere within the experimental space. This means, the restrictions of the parameter space have to be considered for calculating the point of minimal sensor error, which leads to a quadratic problem with inequality restrictions. Solving such problems is significant more difficult and in practice a numerical solver is used to solve problems in the form of

$$\begin{aligned} \text{minimize} \quad & \frac{1}{2}\mathbf{x}^T\mathbf{B}\mathbf{x} + \mathbf{x}^T\mathbf{a} \\ \text{subject to} \quad & \mathbf{A}\mathbf{x} \leq \mathbf{b} \end{aligned}$$

by considering inequality constraints in **A** and **b**. The exemplary results of the optimal z-distance for Magnet A leads by using a numerical solver (e.g. MATLAB Optimization Toolbox [47]) to z_{optA} = -1 mm, which is on the lower bound of the investigated experimental space. The minimal error for Magnet B is quite near the design origin and gives z_{optB} = -0.054 mm, which can also be calculated analytically in this case. This shows, that the regression model can be applied to find optimal operating points of the investigated sensors, which can differ with the sensor configuration. As mentioned in [31], confidence regions for the stationary points can be calculated too, but computation of these regions is not further discussed in this work.

3.6. Alternative Sensor Model Approaches

In this work, quadratic regression models were introduced to map the different sensor error characteristics as a function of the investigated parameters. But other methods are available for designing meta models, such as Splines, Kriging, Radial Basis Functions (RBF) or Artificial Neural Networks (ANN) [32]. These more sophisticated models provide benefits, if the sensor behaviour can not be described by quadratic models sufficiently. Equations 3.2 and 3.3 are used to calculate the coefficients of the linear regression model, where **X** represents a so-called monomial basis. This basis can be accomplished with different approaches, for example with N linear combination of functions ϕ, which

are defined by the radial distance $r = ||\mathbf{x} - \mathbf{x}_i||$

$$\mathbf{y} = \mathbf{f}(\mathbf{x}) = \sum_{i}^{N} w_i \phi(||\mathbf{x} - \mathbf{x}_i||)$$

The function $\phi(||\mathbf{x} - \mathbf{x}_i||)$ is therefore called a radial basis function and different commonly used types, such as gaussian, multiquadratic, inverse multiquadratic, polyharmonic spline or thin plate splines are established as basic approach. This leads to following equations

$$\begin{bmatrix} \phi(r_{11}) & \phi(r_{12}) & \cdots & \phi(r_{1N}) \\ \phi_(r_{21}) & \phi_(r_{22}) & \cdots & \phi(r_{2N}) \\ \vdots & \vdots & & \vdots \\ \phi_(r_{N1}) & \phi_(r_{N2}) & \cdots & \phi(r_{NN}) \end{bmatrix} \begin{bmatrix} w_0 \\ w_1 \\ \vdots \\ w_N \end{bmatrix} = \begin{bmatrix} f(\mathbf{x}_1) \\ f(\mathbf{x}_2) \\ \vdots \\ f(\mathbf{x}_N) \end{bmatrix} \tag{3.26}$$

where calculation of the weighting coefficients w_i in a least squares sense is performed via pseudoinverse matrix as in Equation 3.4. The RBF can be interpreted as a single layer ANN with the radial basis function taking over the role of the activating functions. The ANN consists of neurons and different layers, which are combined with weighting factors and activation functions, but the theory behind this specific surface fitting method is not carried out here further [32], [48]. Computation of the RBF is performed in MATLAB, where a multiquadratic basis function is used. In the present example, the computation of the ANN is done in MATLAB utilizing the Neural Network Toolbox [49] by implementing a default net structure of 5 inputs, 10 neurons in the hidden layer and a single output. Figure 3.24 shows a comparison of all three methods applied for the exemplary eddy current sensor measurement data.

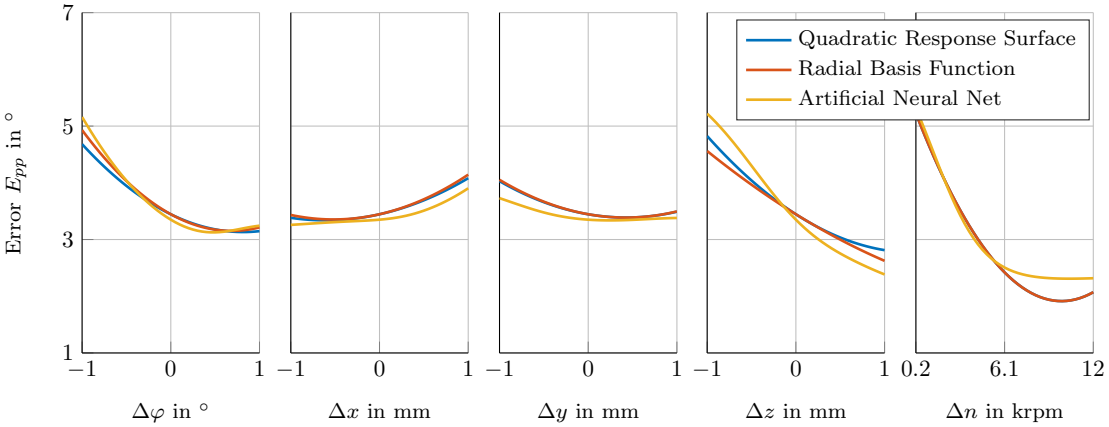

Figure 3.24.: Comparison of sensor error characteristics by utilizing a Quadratic Response Surface Model, Artificial Neural Net and Radial Basis Function.

The results show, that all three methods are capable of representing the sensor parameter characteristics, whereas the RBF and the quadratic RSM show very similar results. Due to this fact, the speed of the observation point in this example is shifted from 6100 to 3000 rpm to illustrate the different results. The Coefficient of Determination R^2, calculated as in Equation 3.11, gives for the RSM 0.9564 and 0.9692 for the ANN in this example. This coefficient results in 1 for the RBF, because the grid points are identical with the measurement points, where the RBF produces an exact interpolation of the measuremed data. The RBF and ANN provide advantages, if the sensor error characteristic behaves inconvenient and is difficult to fit via quadratic regression models, which is not the case within the investigated sensor examples. A big benefit of the quadratic RSM is its simplicity and the powerful statistic analysis methods. In addition the effects of experimental factors show their interactions on the response, which is not the case for the other two methods. It can be concluded, that for this specific application the more sophisticated methods do not provide a quantifiable benefit and are therefore not considered further. They should be kept in mind as alternative methods, if more demanding sensor error characteristics have to be modelled and the quadratic regression model fails. More comparative studies between RSM and ANN models are worked out in [50] and [51].

3.7. Construction of Parametrizable Look-Up Tables

The proposed DOE method delivers reliable results to describe the sensors peak-to-peak error behaviour under several parameter variations. A desirable extension is to model the real sensor error characteristic over one mechanical period under consideration of the same parameter variations. This is done by performing a Full Factorial design with the test bench and storing the measured sensor error over one mechanical period in a look-up table (LUT), as shown in Figure 3.25.

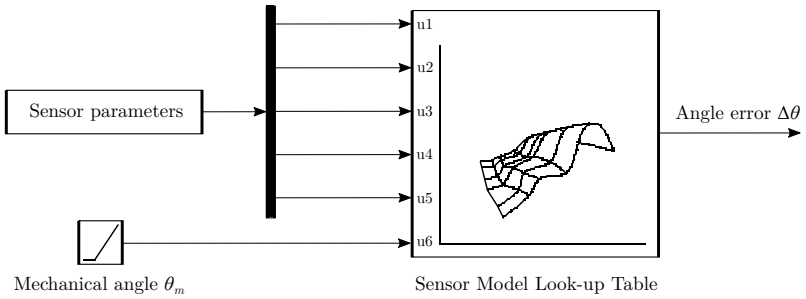

Figure 3.25.: Look-up table representing the sensor behavior on the test bench.

Considering the additional mechanical angle information, the look-up table consists of six dimensions in this case. Additionally to the points defined by the experiment, several

randomly distributed validation measurements are performed to compare the model and sensor output. Between measured Full Factorial design points, common interpolation techniques as linear and cubic spline interpolation are used [52]. Figure 3.26 shows for three exemplary end-of-shaft sensor validation points, how the look-up table represents the real sensor behaviour on the test bench.

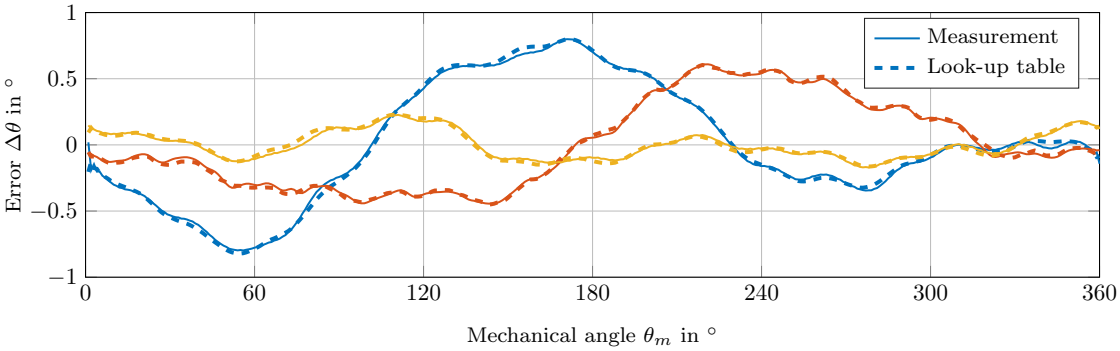

Figure 3.26.: Validation of look-up table with three random validation points from an exemplary end-of-shaft sensor.

Due to the high number of necessary measurements required by the Full Factorial design, only five parameters are considered, which means that $3^5 = 243$ measurements are necessary to fill the look-up table. This method provides the capability to represent a variety of different sensors angle error characteristics over one mechanical period in different operating points. To show the applicability of this method, Figure 3.27 depicts the representation of an eddy current sensor equipped with steel target and its validation measurements.

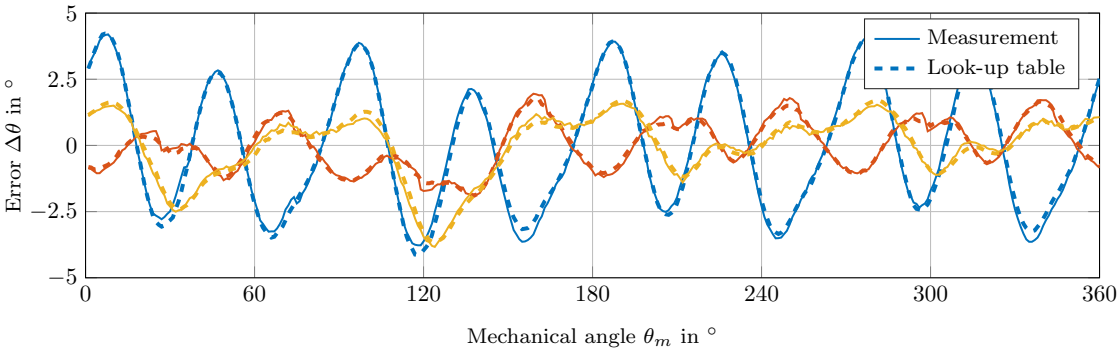

Figure 3.27.: Validation of look-up table with three random validation points from the exemplary eddy current sensor.

The information of the complete sensor error characteristics over one mechanical period is not necessary to rate and compare different sensor systems with each other. The reason

behind this approach is, that these curves of angle errors can be integrated into system simulations (e.g. MATLAB Simulink), which are used to examine electric machines with their appropriate control algorithms. This method allows to integrate the measured look-up tables in such simulations and to investigate the sensor's parameter dependency with its impact on the control quality of electric drives. In the next chapter, a method will be introduced, which takes usage of this measured sensor error data and describes the rotor position sensor error influence on the electric machine's control quality.

3.8. Conclusion

The aim of the proposed DOE method is to evaluate different sensor systems regarding their parameter variation robustness. It can be applied to compare and rate different sensor principles, types or configurations with each other. For instance, eddy current rotor position sensors are a quite new technology and their suitability for automotive applications is interesting. After defining a reasonable experimental space, this sensors are integrated into the test bench and their characteristics can be compared with existing state of the art solutions like resolvers. The comparison of the different technologies shows that the resolver sample provided the most accurate rotor position information, but if the packaging situation allows it, end-of-shaft technology can be a very interesting alternative. The method also shows, that the sensor configuration - for example different magnet types and materials - has a big influence on sensor measurement performance.

The approach with the quadratic RSM leads to a reliable and accurate representation of the investigated sensor behaviour and represents the preferred approach for this task. Different statistical methods are applied to delete insignificant model coefficients and to rate the model quality. Additionally, a method is introduced to evaluate how the different experimental designs can be compared in terms of their characterization ability. Computation of stationary points can be interesting, if the so-called sweet spot of the sensor is unknown or a certain degree of freedom - for example in sensor placement - is present. Designing of parametrizable look-up-tables is interesting for providing the complete rotor sensor error signal over one mechanical period as a function of the investigated parameter variations. Instead of just rating the peak-to-peak error, this method allows to combine the measured sensor error directly with system simulations and to obtain their influence on the control of the electric machine.

The DOE method has its limits, which are determined by the parameter variation capability of the test bench. The qudratic RSM models are basically only valid within the investigated design space, because new physical effects can occur outside the tested parameter space or certain discontinuities influence the system behaviour drastically [32]. Therefore, it is not recommended to use or extrapolate these models outside the tested parameter settings.

4. Impact of Rotor Position Sensor Error on Control Quality

In the previous section, a method was introduced to evaluate the characteristics of different sensor technologies in terms of parameter variations and their impact on the sensor's peak-to-peak error. With multidimensional look-up-tables, it is possible to map the sensors behaviour on the test bench into system simulations. In contrast to the RSM approach, these look-up-tables can be used to reproduce the sensor error signals over one mechanical period. This chapter has the aim, to combine the measured error signals with the field-oriented control to obtain their influence in terms of control quality. An analytic approach will be presented, which describes the complete system of electric machine, control unit and rotor position error as linear time invariant systems. This method provides a mathematical description of the involved process and calculation of output responses for any given input signal. Most control system design methods are based on this formulation, which allows stability analysis, closed loop signal calculations and parameter studies. A description of the influence from rotor position errors in terms of torque or efficiency are suitable quantities to rate the performance of the whole system, instead of an isolated consideration regarding the sensor error behaviour. The introduced method provides torque and efficiency calculation for nearly any kind of measured rotor position error, as depicted in Figure 4.1.

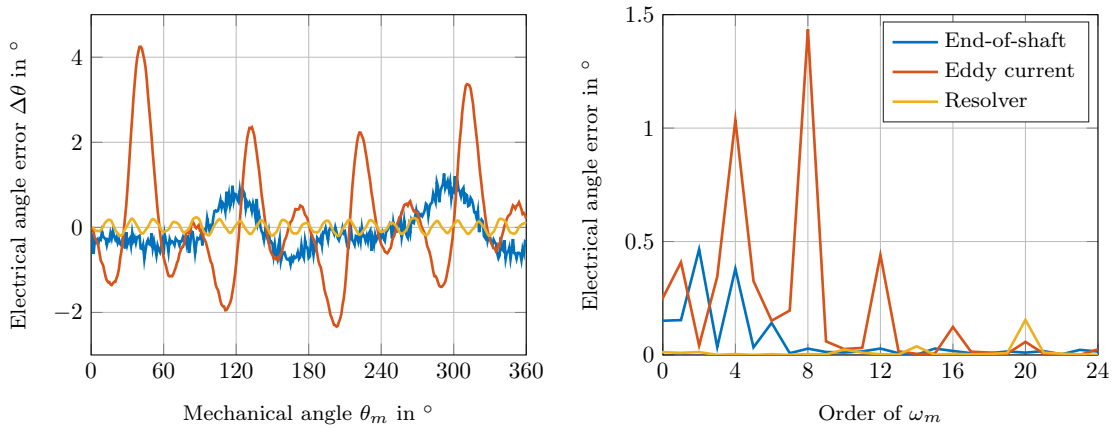

Figure 4.1.: Measured position sensor error signals over one mechanical period for different sensor technologies in time and frequency domain.

It shows, that the rotor position error shape varies strongly with different sensor technologies in terms of amplitude, pole number and harmonic content. For example, the eddy current sensor is characterized by dominant 4^{th}, 8^{th} and 12^{th} harmonics, induced by its pole pair number of four. The exemplary end-of-shaft sensor - which is a different type as the one in Chapter 3 - is more accurate, consisting mainly of a 2^{nd} and a 4^{th} harmonic. The most accurate type in this comparison is the resolver, whose error signal is essentially composed by a 20^{th} order harmonic, also determined by its pole number of ten. In combination with the former mentioned look-up tables, which allow to obtain the sensors parameter sensitivity regarding its measurement error, the influence on control quality of the electric drive can be evaluated by use of simulations. This chapter introduces a method to describe the sensor's effect on the control quality of the electric drive with an analytic approach, which gives deeper insights into involved mechanisms and parameter dependencies compared to straightforward simulation studies.

4.1. Motivation

Several publications have been published, which deal with the influence of rotor position measurement errors on control quality of electric drives. These errors influence the torque output of the electric machine; therefore the torque quality is one of the most important quantities for electric drives. In [53], the distortion of the electric machine's torque is investigated for surface- (SPMSM) and interior permanent magnet synchronous machines (IPMSM) for different operating regions in context of electric vehicle traction applications. Other examples, like [54] and [55], deal with the same problem and describe how rotor position errors take affect on the current control angle and resulting torque ripple. Consequences of present torque ripples within an electric vehicle's powertrain like excitation of resonant frequencies and its impact on drivability and comfort are discussed in [56] and [57]. In [58], several measured rotor position error signals are combined with a FEM simulation and their impact on torque, power and efficiency is discussed. All of them have in common that they only consider the torque equation of an IPMSM [59]

$$M_e = \frac{3}{2} p\big(\Psi_{PM} i_q + (L_d - L_q) i_d i_q\big) \tag{4.1}$$

and not the complete dynamics of the field-oriented control structure. In Sworowski's work [60], a method is introduced, which considers the closed loop dynamics of current control, but it assumes ideal decoupled voltage equations and only provides usable results for the SPMSM machine type. For this type, above torque equation simplifies to

$$M_e = \frac{3}{2} p \Psi_{PM} i_q \tag{4.2}$$

due to the missing magnetic saliency and no additional reluctance torque. This method is investigated in more detail in Section 4.3.1. Here, a motivation is presented, why consideration of current control and electric machine dynamics is necessary to provide

reliable results in torque ripple calculation caused by present rotor position measurement errors. Figure 4.2 shows the simulation model of a field-oriented control of a PMSM in the rotating *dq*-reference frame and sensor error $\Delta\theta$. More detailed information about each block will be given in the subsequent chapters. Results, which are produced by this implemented simulation model, are notated as simulation results in this work.

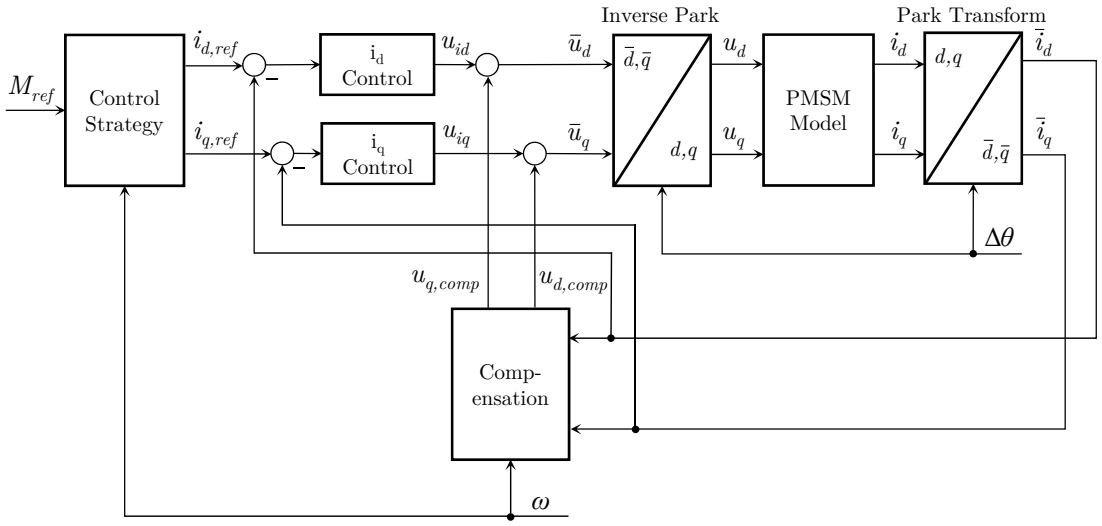

Figure 4.2.: Simulation model for field-oriented control and rotor position sensor error.

Operating points of electric machines are determined by torque demand and electrical speed ω. The control strategy block calculates the necessary *d*- and *q*- components of stator current I_s, and Park's transformation is used to transform the currents into the rotating *dq*-reference frame. Since the controlled machine is already investigated in this frame, only deviations of this transformation - caused by the rotor position error $\Delta\theta$ - have to be considered. The compensation block decouples the non-linear couplings between *d*- and *q*- voltage equations for a beneficial current control design and is discussed later in more detail. The sensor error changes the orientation of stator voltages $u_{d,q}$ and machine currents $i_{d,q}$. The PI-current controllers are forcing the currents $\bar{i}_d = i_{d,ref}$ and $\bar{i}_q = i_{q,ref}$, which means that the machine currents i_d and i_q do not match the desired control strategy current commands $i_{dq,ref}$. By utilizing Equation 4.1 the resulting torque distortion - the so-called torque ripple - can be calculated. Figure 4.3 shows, how torque ripples are produced by rotor position errors for constant torque operating points of a SPMSM and IPMSM machine type.

Usually, the alignment of the current vector I_s is controlled perpendicular to the iso-torque lines of the machine to maintain a maximum torque for a given stator current amplitude. This strategy is called Maximum Torque per Ampere (MTPA) and is discussed in Section 4.10.1. Grey lines represent the iso-torque lines calculated with Equation 4.2, respectively 4.1, which are resulting in straight lines for the SPMSM and hyperbolas for the IPMSM type. The torque deviation ΔM is a consequence of distorted stator

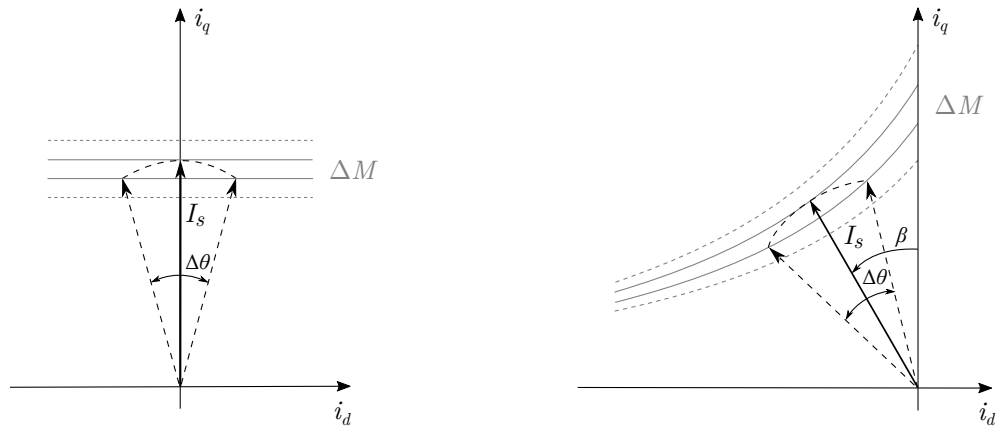

Figure 4.3.: Torque ripple incursion of SPMSM (left) and IPMSM (right) machine type with grey iso-torque lines, current angle β and rotor sensor error $\Delta\theta$.

current components i_d and i_q, caused by an additional current control angle β through the present rotor position error $\Delta\theta$. This is the approach, that most of the previous mentioned publications follow. It will be called "static method" in this work. If the simulation results are compared with these static calculations, a significant deviation between static and simulated torque ripple occurs, which is depicted in Figure 4.4.

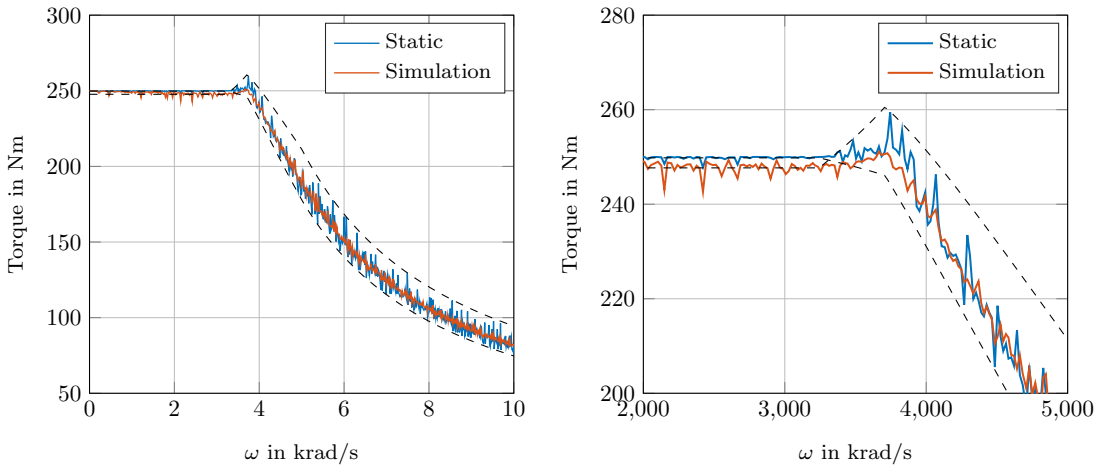

Figure 4.4.: Static torque ripple calculation compared with simulation results of a PMSM torque speed characteristic and eddy current sensor error. Transition from base speed to field weakening region in more detail on the right.

The static method gives nearly no torque ripple in base speed, whereas in field-weakening operation the torque ripple rises to considerable higher values. In contrast, the simulation shows, that also in constant torque speed significant torque ripples occur, but not

as significant as with the static method in field-weakening range. The reason for this deviation is, that the static calculations do not represent the complete dynamic system satisfiable. In high speed operation, the current controller has not the necessary bandwidth to produce these high torque ripples as predicted by the static calculation. The torque ripple ΔM, which is defined in this work as

$$\Delta M = \frac{\max[M_e(t)] - \min[M_e(t)]}{M_{ref}} \cdot 100\% \tag{4.3}$$

with the desired torque set point M_{ref}, is simulated for different operating points of the machine in the torque-speed-plane and depicted as surface plots. These so-called torque ripple maps are simulated with different current control bandwidths - in this case for the standard optimum modulus control setting, doubled and quadrupled control gains. Figure 4.5 shows, that with increasing control bandwidth the torque ripple map of the simulation is converging into the one calculated by the static approach.

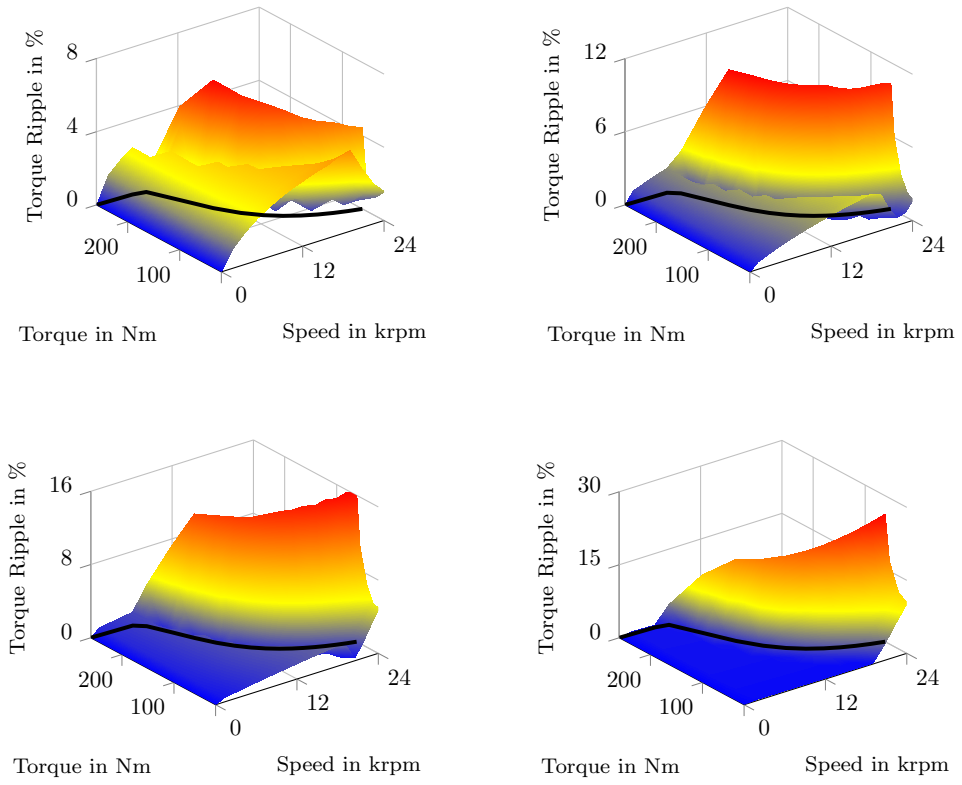

Figure 4.5.: Simulations for optimum modulus (top left), doubled (top right), quadrupled (bottom left) control bandwidth and static results (bottom right).

This means, that the static result corresponds to a current controller with a very high bandwidth, which is not the case for a reasonable designed controller. The motivation

here is to find a mathematical description of the whole system, which considers the dynamics of controller and machine to calculate these torque ripple maps via disturbance transfer functions and without simulations. The contribution from rotor position errors regarding torque quality can be described analytically and effects on efficiency or control parameter sensitivity are possible to investigate. This approach allows also to investigate different control algorithms and to analyze their impact in terms of rotor position errors. The above mentioned current control design is discussed more detailed in Section 4.2.4.

Table 4.1 shows the electric machine parameters for the IPMSM type, which are used in this work for simulation and analytic computation.

Table 4.1.: Parameters of exemplary IPMSM machine.

Parameter	**Value**	**Parameter**	**Value**
Motor Power P_{max}	160 kW	Stator Resistance R_s	20 mΩ
Rated Speed n_{rated}	5950 rpm	Flux Ψ_{PM}	0.0396 Wb
Rated Torque M_{max}	260 Nm	Rated Current I_{max}	523 A
L_d Inductance	0.1724 mH	Rated Voltage U_{max}	420 V
L_q Inductance	0.3168 mH	Number of Pole-pairs p	5
L_δ Inductance	0.048 mH	Inertia J	0.0175 kgm^2

For considerations regarding the SPMSM, the d-axis inductance L_d of the IPMSM is used for representing L_s for this machine type, because no unambiguous machine parameters were available. This implies, that the maximum output torque, output power and rated speed have to be adopted for this machine type. Table 4.2 shows the parameter set used for SPMSM considerations.

Table 4.2.: Parameters of exemplary SPMSM machine.

Parameter	**Value**	**Parameter**	**Value**
Motor Power P_{max}	130 kW	Stator Resistance R_s	20 mΩ
Rated Speed n_{rated}	8000 rpm	Flux Ψ_{PM}	0.0396 Wb
Rated Torque M_{max}	155 Nm	Rated Current I_{max}	523 A
L_s Inductance	0.1724 mH	Rated Voltage U_{max}	420 V
Number of Pole-pairs p	5	Inertia J	0.0175 kgm^2

4.2. Fundamentals of Field-oriented Control and PMSM Dynamics

The torque production of an electric machine is basically given as the vector product of flux and current vector [3], [59]. If this two quantities are spatial orthogonal, the developed torque of the machine is maximized. By obtaining a separately excited DC machine, the orthogonality of this two quantities is naturally given through the basic working principle of brush and commutator. Therefore, from a control point of view, separately excited DC motors have beneficial properties, because flux and current vector are completely decomposed and can be controlled independently. The situation is more complicated for AC machines, due to more present degrees of freedom. The distribution of flux and current is strongly coupled, relative from stator to rotor and determined by two currents (one is redundant) and the electric speed of the machine [61]. The basic idea is to perform a coordinate transformation, which allows a separate control of flux and torque with two independent current components. This transformation from the stator field-oriented scheme into the so-called rotor field-oriented scheme and vice versa is the basic operation in field-oriented control, and allows a separation of flux and torque regulation as like as with the separately excited DC machine. The fundamentals of the field-oriented control were described by F. Blaschke [62] and K. Hasse [63]. Following derivations in terms of coordinate transformations and dynamics of the electric machine are adapted from Kwang Hee Nam [3].

4.2.1. Change of Coordinates

In adaption to [3], the transformation from one reference frame into the other and vice versa is done by Clarke's and Park's transformation. The first describes how a three-phase vector is transformed into a complex pointer consisting of real and imaginary part and the latter is responsible for the transformation from the stationary into the rotating (synchronous) reference frame. A vector $\mathbf{f} = [f_a, f_b, f_c]^T$ can be written as a complex pointer with the relation

$$\mathbf{f^s} = f_\alpha^s + j f_\beta^s = \frac{2}{3}\left[f_a + e^{j\frac{2\pi}{3}} f_b + e^{j\frac{4\pi}{3}} f_c\right] \tag{4.4}$$

$$= \frac{2}{3}(f_a - \frac{1}{2}f_b - \frac{1}{2}f_c) + j\frac{2}{3}(\frac{\sqrt{3}}{2}f_b - \frac{\sqrt{3}}{2}f_c) \tag{4.5}$$

or in matrix formalism

$$\begin{bmatrix} f_\alpha^s \\ f_\beta^s \\ f_0^s \end{bmatrix} = \frac{2}{3}\begin{bmatrix} 1 & -\frac{1}{2} & -\frac{1}{2} \\ 0 & \frac{\sqrt{3}}{2} & -\frac{\sqrt{3}}{2} \\ \frac{1}{\sqrt{2}} & \frac{1}{\sqrt{2}} & \frac{1}{\sqrt{2}} \end{bmatrix}\begin{bmatrix} f_a \\ f_b \\ f_c \end{bmatrix} \tag{4.6}$$

with $f_0^s = 0$ in a balanced system. This matrix maps a vector from the stationary three-phase *abc*-frame into the stationary orthognal $\alpha\beta$-frame. In a next step, this vector is transformed into the rotating $\alpha\beta$-frame, which is performed via rotation matrix $\mathbf{R}(\theta)$

$$\mathbf{R}(\theta) = \begin{bmatrix} \cos\theta & \sin\theta & 0 \\ -\sin\theta & \cos\theta & 0 \\ 0 & 0 & 1 \end{bmatrix}$$

where θ represents the angle between the two participating coordinate systems. The complete transformation from the stationary *abc*-frame into the rotating *dq*-frame follows consequently with the transformation matrix $\mathbf{T}(\theta)$ as

$$\mathbf{T}(\theta) = \begin{bmatrix} \cos\theta & \sin\theta & 0 \\ -\sin\theta & \cos\theta & 0 \\ 0 & 0 & 1 \end{bmatrix} \frac{2}{3} \begin{bmatrix} 1 & -\frac{1}{2} & -\frac{1}{2} \\ 0 & \frac{\sqrt{3}}{2} & -\frac{\sqrt{3}}{2} \\ \frac{1}{\sqrt{2}} & \frac{1}{\sqrt{2}} & \frac{1}{\sqrt{2}} \end{bmatrix} \tag{4.7}$$

The inverse transformation $\mathbf{T}^{-1}$, which is also needed, follows as

$$\mathbf{T}^{-1}(\theta) = \begin{bmatrix} 1 & 0 & \frac{1}{\sqrt{2}} \\ -\frac{1}{2} & \frac{\sqrt{3}}{2} & \frac{1}{\sqrt{2}} \\ -\frac{1}{2} & -\frac{\sqrt{3}}{2} & \frac{1}{\sqrt{2}} \end{bmatrix} \begin{bmatrix} \cos\theta & -\sin\theta & 0 \\ \sin\theta & \cos\theta & 0 \\ 0 & 0 & 1 \end{bmatrix} \tag{4.8}$$

which means that

$$\mathbf{T}^{-1}(\theta) = \frac{3}{2}\mathbf{T}(\theta)$$

applies. The mapping of an exemplary current vector I_{abc} from the stationary *abc*-frame into the stationary $\alpha\beta$ and into the rotating *dq*-frame is depicted in Figure 4.6.

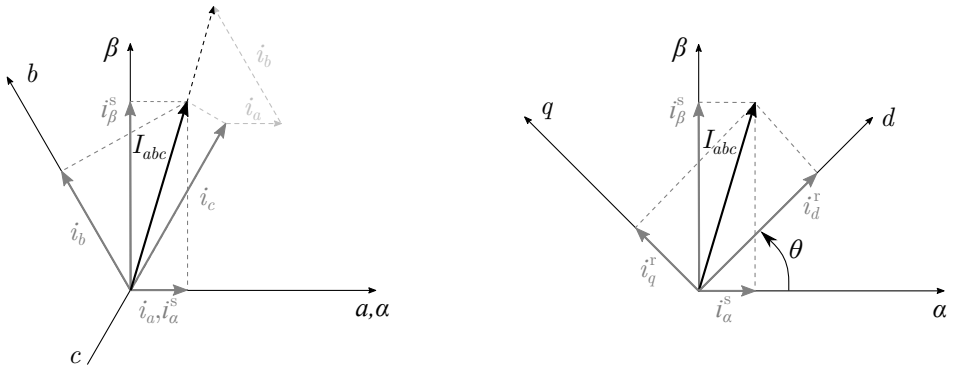

Figure 4.6.: Mapping of a three-phase vector I_{abc} into $i^s_{\alpha,\beta}$ in the stationary $\alpha\beta$-frame and $i^r_{d,q}$ into the rotating *dq*-frame.

The geometrical addition of i_a, i_b and i_c in the left picture results in a $\frac{3}{2}$-times longer

vector in the $\alpha\beta$-frame. This explains the $\frac{2}{3}$ factor in Equation 4.6.

4.2.2. Dynamics of Permanent Magnet Synchronous Machines

In this section, the dynamic system equations of the PMSM are derived. Due to the fact that later a more generalized model of the PMSM dynamic model is used, the derivation of the model dynamics is carried out here completely. For the mathematical description, common assumptions such as [64]

- Saturation effects are not considered and magnetization of iron is treated as linear
- Stator consists of a symmetric three-phase winding, which can be transformed into a rotating two-phase winding
- The three-phase electric system is symmetric and contains no zero component
- Current displacement (skin effect) and iron losses are neglected
- Temperature effects regarding windings and permanent magnets are not considered

are made. First it has to be mentioned, that PMSM can be subdivided into two main types: Surface mounted and interior permanent magnet synchronous machines, short SPMSM and IPMSM. For the first, the magnets are mounted on the rotor surface and for the second the magnets are buried in the cavities of the rotor core. These two types can be further subdivided into surface magnet and inset magnet, respectively interior magnet and flux concentrating types [3]. SPMSM's have the problem of fixating the magnets with bands or glue and their power density and speed range is smaller compared to the IPMSM type. Due to the non-symmetric magnetic structure, IPMSM produce an additional reluctance torque, which increases the power density considerable. Within vehicle applications, mostly IPMSM's are used. Drawbacks of this type is for example the effort-full cooling and their more complicated control strategies. Note that the SPMSM is a special case of the IPMSM, therefore the derivation of the PMSM dynamics will be done for the IPMSM and will be reduced for the SPMSM machine type afterwards. Figure 4.7 shows the cross-section of a SPMSM and the resulting flux paths.

For the dynamic model, machine parameters have to be known such as the inductances in d- and q-axis, denoted as L_d and L_q. As shown in Equations 4.1 and 4.2, these parameters play an important role in torque production and differ for both machine types. To define the inductances for the SPMSM type, Ampere's law is used, which is written for the machine as

$$\frac{B}{\mu_{PM}} 2h_m + \frac{B}{\mu_0} 2g + \frac{B}{\mu_{Fe}} l_{core} = N i_d \tag{4.9}$$

with the permeability of the permanent magnet μ_{PM}, magnet height h_m, air gap g, number of turns in d-axis N and the total length of the flux paths in the steel core l_{core}. Considering that $\mu_{PM} \approx \mu_0$ and neglecting $\frac{B}{\mu_{Fe}} l_{core}$ due to the high permittivity μ_{Fe} of

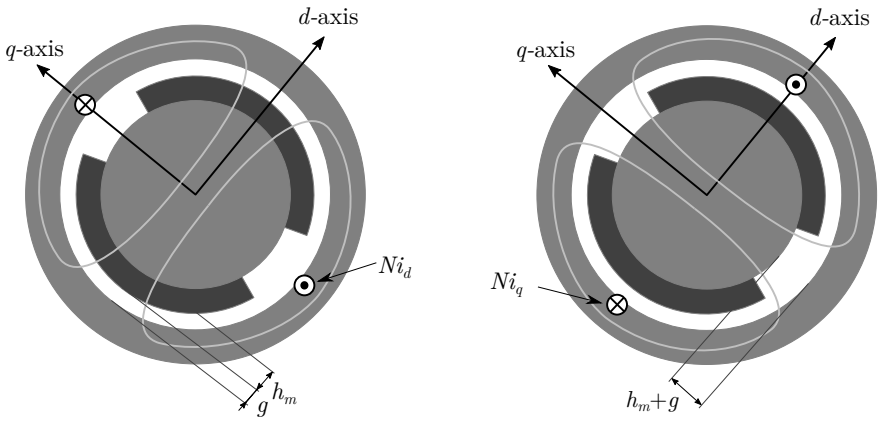

Figure 4.7.: Flux paths of SPMSM in d-axis (left) and q-axis (right) adapted from [3]

iron, follows

$$B = \frac{\mu_0 N}{2(g + h_m)} i_d$$

for the magnetic flux density B. Considering $N\Phi = NBA = L_d i_d$, the inductance in d-axis is given as

$$L_d = \frac{\mu_0 N^2 A}{2(g + h_m)}$$

with the air gap area A through which the flux crosses. Due to the fact, that the flux lines do not pass through the permanent magnets, the same result for the inductance in q-axis is obtained. This means, that for the SPMSM $L_d = L_q = L_s$ applies. This is not the case for the IPMSM machine type with buried magnets. Figure 4.8 shows a cross-section of IPMSM and the flux paths in d- and q-direction.

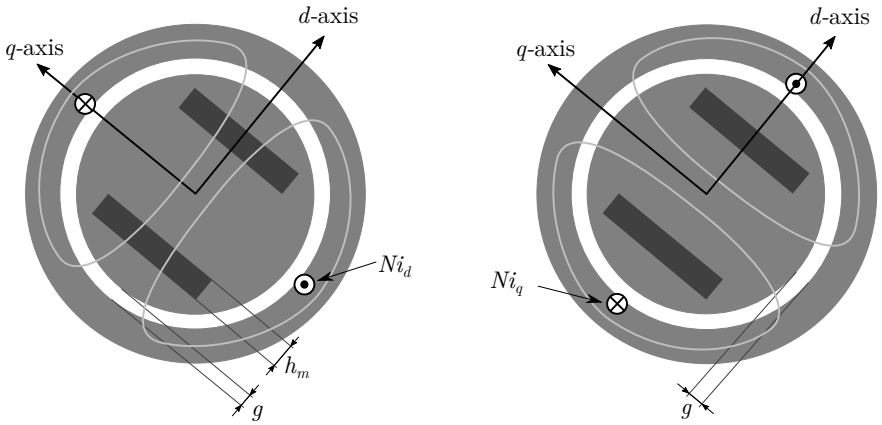

Figure 4.8.: Flux paths of IPMSM in d-axis (left) and q-axis (right) adapted from [3]

Performing the same approach with Ampere's law as in Equation 4.9 leads to different

values for the inductances in d- and q-direction. Due to the facts, that permanent magnets feature the same permeability as air and do not interfere the q-axis flux linkage, gives different reluctances for both directions. This yields to different values for L_d and L_q, which are calculated as

$$L_d = \frac{\mu_0 N^2 A}{2(g + h_m)}$$
$$L_q = \frac{\mu_0 N^2 A}{2g}$$

The magnetic asymmetry of $L_d < L_q$ for this type of IPMSM produces the additional reluctance torque, which can be utilized by a negative current in d-direction. In contrast to that, the torque in SPMSM's is only controlled via q-axis current and no reluctance torque can be exploited. Setting $L_d = L_q = L_s$ in Equation 4.1 shows, that the machine torque degenerates itself to Equation 4.2. Figure 4.9 shows a simplified cross-section view of an AC motor and according stator phase windings.

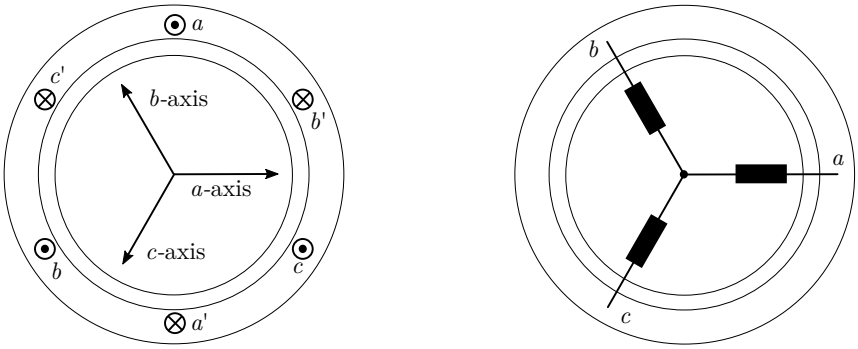

Figure 4.9.: Simplified cross-sectional view of AC motor with stator phase windings adapted from [3]

The axis of the a-phase current is aligned to the flux direction generated by the a-phase current flow, where the flux direction is determined by the right-hand rule [3]. This is also valid for the other two windings b and c, and the flux directions are symbolized by the coils direction on the right in Figure 4.9.

In a next step, the flux linkages of the stator windings as a function of the rotor position θ needs to be described. Considering different values of θ accords to a change of the effective air gap, which has its maximum value for $\theta = 0$. This occurs when flux linkage is considered in d-axis, whereas the minimum is present at $\theta = \pm\frac{\pi}{2}$. The inductances have at this points the values of L_d and L_q. In between, the inductance change its value according to a cosine-shaped characteristic with the periodicity of 2θ, caused by the none present polarity of reluctance. Figure 4.10 shows the rotor position dependent flux situation in more detail.

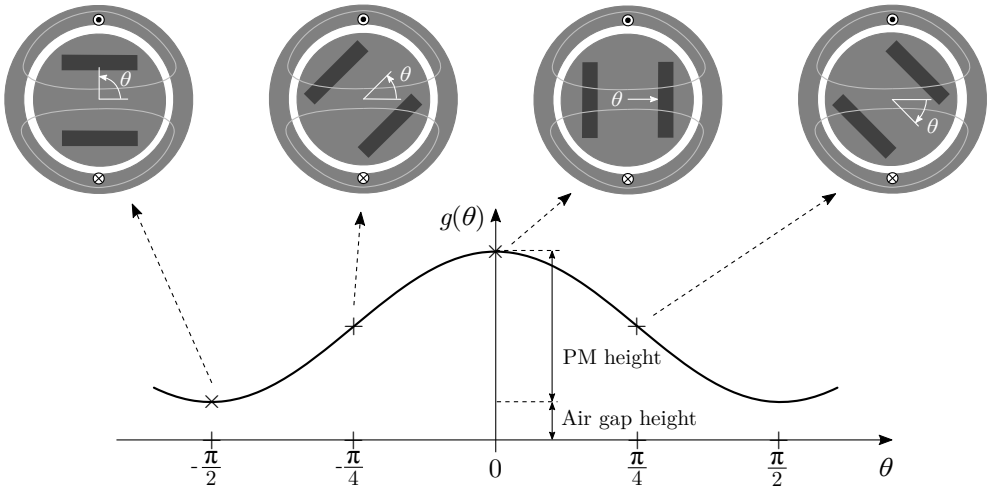

Figure 4.10.: Cosine-shaped effective airgap of phase a flux linkage depending on rotor position θ, adapted from [3].

The a-phase winding inductance is therefore determined as

$$L_a(\theta) = \frac{\mu_0 N^2 A}{2g(\theta)} = L_{ms} - L_\delta \cos 2\theta$$

with the static average air gap component L_{ms} and reluctance component L_δ. Extension of this result into a system of three-phase windings leads to an inductance matrix

$$\bar{\mathbf{L}}_{abc} = \mathbf{L}_{abc} - \mathbf{L}_{rlc}(\theta)$$

where the matrix $\mathbf{L}_{abc}$ describes the stator flux linkage for all three phases [3]

$$\mathbf{L}_{abc} = \begin{bmatrix} L_{ms} + L_{ls} & -\frac{1}{2}L_{ms} & -\frac{1}{2}L_{ms} \\ -\frac{1}{2}L_{ms} & L_{ms} + L_{ls} & -\frac{1}{2}L_{ms} \\ -\frac{1}{2}L_{ms} & -\frac{1}{2}L_{ms} & L_{ms} + L_{ls} \end{bmatrix}$$

and with the rotor angle dependent matrix $\mathbf{L}_{rlc}(\theta)$, the so-called reluctance matrix [3]

$$\mathbf{L}_{rlc}(\theta) = L_\delta \begin{bmatrix} \cos 2\theta & \cos(2\theta - 2\pi/3) & \cos(2\theta + 2\pi/3) \\ \cos(2\theta - 2\pi/3) & \cos(2\theta + 2\pi/3) & \cos 2\theta \\ \cos(2\theta + 2\pi/3) & \cos 2\theta & \cos(2\theta - 2\pi/3) \end{bmatrix}$$

The elements in the main diagonal are given by stator mutual and leak inductances L_{ms} and L_{ls} of phase a, b and c. The off-diagonal elements describe the mutual flux linkage from one phase to each other, where the factor $\cos(\frac{2\pi}{3}) = -\frac{1}{2}$ is determined through the 120° spatially separated stator coils. Calculation of the rotor dependent reluctance matrix $\mathbf{L}_{rlc}(\theta)$ is effortful and carried out in more detail in [65]. With these inductances,

the total flux linkage is then described as

$$\boldsymbol{\lambda}_{abc} = \begin{bmatrix} \lambda_a \\ \lambda_b \\ \lambda_c \end{bmatrix} = [\mathbf{L}_{abc} - \mathbf{L}_{rlc}(\theta)] \begin{bmatrix} i_a \\ i_b \\ i_c \end{bmatrix} + \Psi_{PM} \begin{bmatrix} \cos\theta \\ \cos(2\theta - 2\pi/3) \\ \cos(2\theta + 2\pi/3) \end{bmatrix} \tag{4.10}$$

by consideration of the angle θ dependency of the permanent magnet flux linkage concerning each phase. Equation 4.10 describes the flux linkage situation for an IPMSM completely and is also valid for the SPMSM type. This describes an easier case, since the matrix $\mathbf{L}_{rlc}(\theta)$ is a zero matrix because no reluctance influence has to be considered. When the flux linkage situation of the electric machine is determined, the electric differential equations can be formulated. The basic voltage equation

$$\mathbf{u}_{abc} = R_s \mathbf{i}_{abc} + \frac{d}{dt}\boldsymbol{\lambda}_{abc}$$

which is valid for any kind of three phase electric machine for the stator dynamics leads in this case to

$$\mathbf{u}_{abc} = R_s \mathbf{i}_{abc} + [\mathbf{L}_{abcs} - \mathbf{L}_{rlc}(\theta)] \frac{d}{dt}\mathbf{i}_{abc} - \omega \Psi_{PM} \begin{bmatrix} \sin\theta \\ \sin(2\theta - 2\pi/3) \\ \sin(2\theta + 2\pi/3) \end{bmatrix}$$

This differential equations describe the electric dynamics of the PMSM in a three-phase stationary reference frame. A significant disadvantage of this model is, that the parameters of the differential equations depend directly on the rotor position θ and are strongly coupled within the inductance matrices. A first simplification is reached by applying Clarke's transform as described in Section 4.2.1 to get an orthogonal two-phase representation of the machine instead of a three-phase system in the stationary reference frame.

Transformation of Flux Linkage into the Stationary Reference Frame

Above system of differential equations is now transformed into the stationary $\alpha\beta$-reference frame as described with Clarke's transformation in Equation 4.4. The transformation has to be applied to all parts of the stator flux linkage in Equation 4.10. This yields for $\mathbf{L}_{abc}\mathbf{i}_{abc}$ to

$$
\begin{aligned}
\boldsymbol{\lambda}^s_{\alpha\beta} &= \frac{2}{3}\Big[\lambda_a(t) + e^{j\frac{2\pi}{3}}\lambda_b(t) + e^{-j\frac{2\pi}{3}}\lambda_c(t)\Big] \\
&= \frac{2}{3}\Big[(L_{ms}+L_{ls})i_a - \frac{1}{2}L_{ms}i_b - \frac{1}{2}L_{ms}i_c \\
&\quad + e^{j\frac{2\pi}{3}}\big\{-\frac{1}{2}L_{ms}i_a + (L_{ms}+L_{ls})i_b - \frac{1}{2}L_{ms}i_c\big\} \\
&\quad + e^{j\frac{2\pi}{3}}\big\{-\frac{1}{2}L_{ms}i_a - \frac{1}{2}L_{ms}i_b + (L_{ms}+L_{ls})i_c\big\}\Big] \\
&= (\frac{3}{2}L_{ms}+L_{ls})\frac{2}{3}(i_a + e^{j\frac{2\pi}{3}}i_b + e^{-j\frac{2\pi}{3}}i_c) = L_s\mathbf{i}^s_{\alpha\beta}
\end{aligned} \tag{4.11}
$$

with the abbreviation $L_s = L_{ls} + \frac{3}{2}L_{ms}$. This result can also be obtained by using the transformation matrix $\mathbf{T}(\theta = 0)$ from Equation 4.7

$$
\boldsymbol{\lambda}^s_{\alpha\beta} = \mathbf{T}\boldsymbol{\lambda}_{abc} = \mathbf{T}\mathbf{L}_{abc}\mathbf{i}_{abc} = \mathbf{T}\mathbf{L}_{abc}\mathbf{T}^{-1}\mathbf{i}^s_{dq} = \mathbf{L}_{\alpha\beta}\mathbf{i}^s_{\alpha\beta}
$$

where $\mathbf{L}_{\alpha\beta} = \mathbf{T}\mathbf{L}_{abc}\mathbf{T}^{-1}$ is computed as

$$
\begin{aligned}
&= \frac{2}{3}\begin{bmatrix} 1 & -\frac{1}{2} & -\frac{1}{2} \\ 0 & \frac{\sqrt{3}}{2} & -\frac{\sqrt{3}}{2} \\ \frac{1}{\sqrt{2}} & \frac{1}{\sqrt{2}} & \frac{1}{\sqrt{2}} \end{bmatrix}\begin{bmatrix} L_{ms}+L_{ls} & -\frac{1}{2}L_{ms} & -\frac{1}{2}L_{ms} \\ -\frac{1}{2}L_{ms} & L_{ms}+L_{ls} & -\frac{1}{2}L_{ms} \\ -\frac{1}{2}L_{ms} & -\frac{1}{2}L_{ms} & L_{ms}+L_{ls} \end{bmatrix}\begin{bmatrix} 1 & 0 & \frac{1}{\sqrt{2}} \\ -\frac{1}{2} & \frac{\sqrt{3}}{2} & \frac{1}{\sqrt{2}} \\ -\frac{1}{2} & -\frac{\sqrt{3}}{2} & \frac{1}{\sqrt{2}} \end{bmatrix} \\
&= \begin{bmatrix} L_{ls}+\frac{3}{2}L_m & 0 & 0 \\ 0 & L_{ls}+\frac{3}{2}L_m & 0 \\ 0 & 0 & L_{ls} \end{bmatrix}
\end{aligned}
$$

by considering the $\alpha\beta$-parts of the matrix $\mathbf{L}_{\alpha\beta}$. In a next step, the transformation of the reluctance matrix $\mathbf{L}_{rlc}(\theta)$ in Equation 4.10 has to be carried out in the same manner as for the stator flux linkage. Defining $\Delta\boldsymbol{\lambda} = [\Delta\lambda_a, \Delta\lambda_b, \Delta\lambda_c]^T = \mathbf{L}_{rlc}(\theta)\mathbf{i}_{abc}$, utilizing the complex representation of $\cos 2\theta = \frac{1}{2}(e^{j2\theta} + e^{-j2\theta})$ and applying Clarke's transformation to map $\Delta\boldsymbol{\lambda}$ into the complex plane leads to

$$
\begin{aligned}
\Delta\boldsymbol{\lambda}^s_{\alpha\beta} &= \frac{2}{3}\Big[\Delta\lambda_a(t) + e^{j\frac{2\pi}{3}}\Delta\lambda_b(t) + e^{-j\frac{2\pi}{3}}\Delta\lambda_c(t)\Big] \\
&= \frac{2}{3}\frac{1}{2}L_\delta\Big[(e^{j2\theta}+e^{-j2\theta})i_a + (e^{j(2\theta-\frac{2\pi}{3})}+e^{-j(2\theta-\frac{2\pi}{3})})i_b + (e^{j(2\theta+\frac{2\pi}{3})}+e^{-j(2\theta+\frac{2\pi}{3})})i_c \\
&\quad + e^{j\frac{2\pi}{3}}(e^{j(2\theta-\frac{2\pi}{3})}+e^{-j(2\theta-\frac{2\pi}{3})})i_a + e^{j\frac{2\pi}{3}}(e^{j(2\theta+\frac{2\pi}{3})}+e^{-j(2\theta+\frac{2\pi}{3})})i_b \\
&\quad + e^{j\frac{2\pi}{3}}(e^{j2\theta}+e^{-j2\theta})i_c + e^{-j\frac{2\pi}{3}}(e^{j(2\theta+\frac{2\pi}{3})}+e^{-j(2\theta+\frac{2\pi}{3})})i_a + e^{-j\frac{2\pi}{3}}(e^{j2\theta}+e^{-j2\theta})i_b \\
&\quad + e^{-j\frac{2\pi}{3}}(e^{j(2\theta-\frac{2\pi}{3})}+e^{-j(2\theta-\frac{2\pi}{3})})i_c\Big] \\
&= \frac{2}{3}\frac{1}{2}L_\delta\Big[3e^{j2\theta}i_a + 3e^{j(2\theta-\frac{2\pi}{3})}i_b + 3e^{j(2\theta+\frac{2\pi}{3})}i_c\Big] = \frac{3}{2}L_\delta e^{j2\theta}(\mathbf{i}^s_{\alpha\beta})^*
\end{aligned} \tag{4.12}
$$

where $(\mathbf{i}^s_{\alpha\beta})^*$ denotes the complex conjugate vector of $\mathbf{i}^s_{\alpha\beta}$. In the last step, the rotor position dependent flux linkage of the permanent magnet in Equation 4.10 is mapped into the stationary $\alpha\beta$-frame too. This yields to

$$\begin{aligned}
\mathbf{\Psi}^s_{PM,\alpha\beta} &= \frac{2}{3}\Psi_{PM}\left[\cos\theta + e^{j\frac{2\pi}{3}}\cos(\theta - \frac{2\pi}{3}) + e^{-j\frac{2\pi}{3}}\cos(\theta + \frac{2\pi}{3})\right] \\
&= \frac{1}{3}\Psi_{PM}\Big[(e^{j\theta} + e^{-j\theta}) + (e^{j(\theta-\frac{2\pi}{3})} + e^{-j(\theta-\frac{2\pi}{3})})e^{j\frac{2\pi}{3}} \\
&\quad + (e^{j(\theta+\frac{2\pi}{3})}) + e^{-j(\theta+\frac{2\pi}{3})})e^{-j\frac{2\pi}{3}}\Big] \\
&= \frac{1}{3}\Psi_{PM}\left[e^{j\theta} + e^{-j\theta} + e^{j\theta} + e^{j(\theta-\frac{4\pi}{3})} + e^{j\theta} + e^{j(\theta+\frac{4\pi}{3})}\right] \\
&= \frac{1}{3}\Psi_{PM}3e^{j\theta} = \Psi_{PM}e^{j\theta}
\end{aligned} \tag{4.13}$$

which means, that the rotor flux vector represents a complex vector with magnitude Ψ_{PM} and angle θ. The total flux linkage from Equation 4.10 in the $\alpha\beta$-reference frame follows then by using Equations 4.11, 4.12 and 4.13 as

$$\boldsymbol{\lambda}^s_{\alpha\beta} = L_s\mathbf{i}^s_{\alpha\beta} - \frac{3}{2}L_\delta e^{j2\theta}(\mathbf{i}^s_{\alpha\beta})^* + \Psi_{PM}e^{j\theta} \tag{4.14}$$

Written in matrix formalism this results in

$$\begin{bmatrix}\lambda^s_\alpha \\ \lambda^s_\beta\end{bmatrix} = \begin{bmatrix}L_s - \frac{3}{2}L_\delta\cos 2\theta & -\frac{3}{2}L_\delta\sin 2\theta \\ -\frac{3}{2}L_\delta\sin 2\theta & L_s - \frac{3}{2}L_\delta\cos 2\theta\end{bmatrix}\begin{bmatrix}i^s_\alpha \\ i^s_\beta\end{bmatrix} + \Psi_{PM}\begin{bmatrix}\cos\theta \\ \sin\theta\end{bmatrix} \tag{4.15}$$

Due to the fact that for the SPMSM $L_\delta = 0$ applies, this result degenerates to

$$\begin{bmatrix}\lambda^s_\alpha \\ \lambda^s_\beta\end{bmatrix} = L_s\begin{bmatrix}i^s_\alpha \\ i^s_\beta\end{bmatrix} + \Psi_{PM}\begin{bmatrix}\cos\theta \\ \sin\theta\end{bmatrix}$$

PMSM Dynamics in the Stationary Reference Frame

With former results, the magnet flux situation is described in the stationary $\alpha\beta$-frame and common stator voltage equation

$$\mathbf{u}^s_{\alpha\beta} = R_s\mathbf{i}^s_{\alpha\beta} + \frac{d}{dt}\boldsymbol{\lambda}^s_{\alpha\beta} = R_s\mathbf{i}^s_{\alpha\beta} + \frac{d}{dt}\left(L_s\mathbf{i}^s_{\alpha\beta} - \frac{3}{2}L_\delta e^{j2\theta}(\mathbf{i}^s_{\alpha\beta})^*\right) + j\Psi_{PM}e^{j\theta}$$

is used to describe the IPMSM dynamics. In matrix form, the voltage equations are written as

$$\begin{bmatrix} u_\alpha^s \\ u_\beta^s \end{bmatrix} = R_s \begin{bmatrix} i_\alpha^s \\ i_\beta^s \end{bmatrix} + \begin{bmatrix} L_s - \frac{3}{2}L_\delta \cos 2\theta & -\frac{3}{2}L_\delta \sin 2\theta \\ -\frac{3}{2}L_\delta \sin 2\theta & L_s + \frac{3}{2}L_\delta \cos 2\theta \end{bmatrix} \frac{d}{dt} \begin{bmatrix} i_\alpha^s \\ i_\beta^s \end{bmatrix} - 3\omega L_\delta \begin{bmatrix} -\sin 2\theta & \cos 2\theta \\ \cos 2\theta & \sin 2\theta \end{bmatrix} \begin{bmatrix} i_\alpha^s \\ i_\beta^s \end{bmatrix} + \omega \Psi_{PM} \begin{bmatrix} -\sin\theta \\ \cos\theta \end{bmatrix} \tag{4.16}$$

and for the simpler SPMSM case

$$\begin{bmatrix} u_\alpha^s \\ u_\beta^s \end{bmatrix} = R_s \begin{bmatrix} i_\alpha^s \\ i_\beta^s \end{bmatrix} + L_s \frac{d}{dt} \begin{bmatrix} i_\alpha^s \\ i_\beta^s \end{bmatrix} + \omega \Psi_{PM} \begin{bmatrix} -\sin\theta \\ \cos\theta \end{bmatrix} \tag{4.17}$$

The transition from a three-phase into a two-phase systems description results in a more compact representation of the machine dynamics in the stationary reference frame, but the rotor angle dependency of the parameters is still present. This model structure plays an important role in the sensorless control algorithms for PMSM, where the information regarding the rotor position has to be reconstructed with different kinds of estimation algorithms. Since a lot of research effort is given to that specific topic already and the focus of this work lies on rotor position sensors itself, sensorless field-oriented control is not investigated any further.

PMSM Dynamics in the Synchronous Reference Frame

The field oriented control operates in an electric machine's rotor aligned reference frame with angle θ and rotates with speed ω. This means, an additional transformation from $\boldsymbol{\lambda}_{\alpha\beta}^s$ to $\boldsymbol{\lambda}_{dq}^r$ is necessary, which accords to a complex multiplication with $e^{-j\theta}$ formulated as $\boldsymbol{\lambda}_{dq}^r = e^{-j\theta}\boldsymbol{\lambda}_{\alpha\beta}^s$. Applying this transformation to Equation 4.14 gives for the flux linkage in the rotor oriented synchronous frame

$$\boldsymbol{\lambda}_{dq}^r = L_s e^{-j\theta}\mathbf{i}_{\alpha\beta}^s - \frac{3}{2}L_\delta e^{j\theta}(\mathbf{i}_{\alpha\beta}^s)^* + \Psi_{PM} = L_s \mathbf{i}_{dq}^r - \frac{3}{2}L_\delta(\mathbf{i}_{dq}^r)^* + \Psi_{PM} \tag{4.18}$$

These equations written in matrix formalisms lead to

$$\begin{bmatrix} \lambda_d^r \\ \lambda_q^r \end{bmatrix} = \begin{bmatrix} L_s - \frac{3}{2}L_\delta & 0 \\ 0 & L_s + \frac{3}{2}L_\delta \end{bmatrix} \begin{bmatrix} i_d^r \\ i_q^r \end{bmatrix} + \Psi_{PM} \begin{bmatrix} 1 \\ 0 \end{bmatrix} \tag{4.19}$$

and show compared to 4.15 a more simple diagonal structure and a vanished dependency of the rotor position θ. Recalling the voltage equations and their transformation into

the synchronous reference frame yields to

$$\begin{aligned}
\mathbf{u}^s_{\alpha\beta} &= R_s \mathbf{i}^s_{\alpha\beta} + \frac{d}{dt}\boldsymbol{\lambda}^s_{\alpha\beta} \\
e^{-j\theta}\mathbf{u}^s_{\alpha\beta} &= R_s e^{-j\theta}\mathbf{i}^s_{\alpha\beta} + e^{-j\theta}\frac{d}{dt}(e^{j\theta}e^{-j\theta}\boldsymbol{\lambda}^s_{\alpha\beta}) \\
\mathbf{u}^r_{dq} &= R_s \mathbf{i}^r_{dq} + e^{-j\theta}\frac{d}{dt}\left(e^{j\theta}\boldsymbol{\lambda}^r_{dq}\right) \\
&= R_s \mathbf{i}^r_{dq} + e^{-j\theta}\left(je^{j\theta}\frac{d\theta}{dt}\boldsymbol{\lambda}^r_{dq} + e^{j\theta}\frac{d}{dt}\boldsymbol{\lambda}^r_{dq}\right) \\
&= R_s \mathbf{i}^r_{dq} + j\omega\boldsymbol{\lambda}^r_{dq} + \frac{d}{dt}\boldsymbol{\lambda}^r_{dq}
\end{aligned} \tag{4.20}$$

Utilization of the flux linkage Equation 4.18 in the synchronous reference frame

$$\begin{aligned}
j\omega\boldsymbol{\lambda}^r_{dq} &= j\omega L_s \mathbf{i}^r_{dq} - j\omega\frac{3}{2}L_\delta(\mathbf{i}^r_{dq})^* + j\omega\Psi_{PM} \\
\frac{d}{dt}\boldsymbol{\lambda}^r_{dq} &= L_s\frac{d}{dt}\mathbf{i}^r_{dq} - \frac{3}{2}L_\delta\frac{d}{dt}(\mathbf{i}^r_{dq})^*
\end{aligned}$$

and insertion into 4.20 gives following voltage equations

$$\begin{aligned}
u^r_d &= R_s i^r_d + \omega\left(L_s + \frac{3}{2}L_\delta\right)i^r_q + \left(L_s - \frac{3}{2}L_\delta\right)\frac{di^r_d}{dt} \\
u^r_q &= R_s i^r_q + \omega\left(L_s - \frac{3}{2}L_\delta\right)i^r_d + \left(L_s + \frac{3}{2}L_\delta\right)\frac{di^r_q}{dt} + \omega\Psi_{PM}
\end{aligned}$$

Substituting

$$\begin{aligned}
L_d &= L_s - \frac{3}{2}L_\delta \\
L_q &= L_s + \frac{3}{2}L_\delta
\end{aligned}$$

leads to the final and well known voltage equations of an IPMSM in the synchronous dq-reference frame

$$u^r_d = R_s i^r_d + L_d\frac{di^r_d}{dt} - \omega L_q i^r_q \tag{4.21}$$

$$u^r_q = R_s i^r_q + L_q\frac{di^r_q}{dt} + \omega L_d i^r_d + \omega\Psi_{PM} \tag{4.22}$$

or in first order ordinary differential equation form as

$$\frac{d}{dt}\begin{bmatrix} i^r_d \\ i^r_q \end{bmatrix} = \begin{bmatrix} -\frac{R_s}{L_d} & \omega\frac{L_q}{L_d} \\ -\omega\frac{L_d}{L_q} & -\frac{R_s}{L_q} \end{bmatrix}\begin{bmatrix} i^r_d \\ i^r_q \end{bmatrix} - \frac{\omega\Psi_{PM}}{L_q}\begin{bmatrix} 0 \\ 1 \end{bmatrix} + \begin{bmatrix} \frac{1}{L_d}u^r_d \\ \frac{1}{L_q}u^r_q \end{bmatrix} \tag{4.23}$$

This result is also valid for the SPMSM, which degenerates by using $L_d = L_q = L_s$ into

$$u_d^r = R_s i_d^r + L_s \frac{di_d^r}{dt} - \omega L_s i_q^r \tag{4.24}$$

$$u_q^r = R_s i_q^r + L_s \frac{di_q^r}{dt} + \omega L_s i_d^r + \omega \Psi_{PM} \tag{4.25}$$

respectively in matrix notation

$$\frac{d}{dt}\begin{bmatrix} i_d^r \\ i_q^r \end{bmatrix} = \begin{bmatrix} -\frac{R_s}{L_s} & \omega \\ -\omega & -\frac{R_s}{L_s} \end{bmatrix} \begin{bmatrix} i_d^r \\ i_q^r \end{bmatrix} - \frac{\omega \Psi_{PM}}{L_s} \begin{bmatrix} 0 \\ 1 \end{bmatrix} + \frac{1}{L_s} \begin{bmatrix} u_d^r \\ u_q^r \end{bmatrix} \tag{4.26}$$

Note that these derivations are valid for a single pole-pair machine, where mechanical and electrical frequency are identical ($\omega = \omega_m$). Most common machines are built with higher pole-pair numbers p, which accords to p connected subsystems in series. This demands, that the machine parameters and electric frequency ω have to be scaled with the number of pole-pairs. The parameters of an electric machine are usually measured for all pole-pairs, which means that Equations 4.21 - 4.26 stay valid, except that the frequency ω has to be replaced by the electric frequency $\omega_e = \omega_m p$.

Power and Torque of a PMSM

The power of the electric machine P_e is given as the scalar product of voltages and currents of all three phases in the *abc*-frame [59]. The power relation is therefore given as

$$\begin{aligned} P_e = \mathbf{u}_{abc}^T \mathbf{i}_{abc} &= (\mathbf{T}(\theta)^{-1} \mathbf{u}_{dq}^r)^T \mathbf{T}(\theta)^{-1} \mathbf{i}_{dq}^r \\ &= \frac{3}{2} (\mathbf{T}(\theta)^T \mathbf{u}_{dq}^r)^T \mathbf{T}(\theta)^{-1} \mathbf{i}_{dq}^r \\ &= \frac{3}{2} \mathbf{u}_{dq}^{rT} \mathbf{i}_{dq}^r \end{aligned}$$

and shows that the power calculation is consistent in both reference frames, except the $\frac{3}{2}$ factor from the coordinate change. Neglecting the stator resistance in the steady state *dq*-voltage equations yields to

$$\begin{aligned} P_e &= \frac{3}{2}(u_d^r i_d^r + u_q^r i_q^r) \\ &= \frac{3}{2}\omega(\Psi_{PM} i_q^r + (L_d - L_q) i_d^r i_q^r) \\ &= \frac{3}{2} p \omega_m (\Psi_{PM} i_q^r + (L_d - L_q) i_d^r i_q^r) \end{aligned} \tag{4.27}$$

As mentioned in the introduction section, the torque of an electric machine is given as the vector product of stator flux linkage $\boldsymbol{\lambda}_{dq}^r$ and stator current $\mathbf{i}_{dq}^r$. With the factor $\frac{3}{2}$

from the transformation into the synchronous reference frame and the direct proportional scaling with the pole-pair number p, the torque M is given as

$$\begin{aligned} M_e &= \frac{3}{2}p(\boldsymbol{\lambda}^r_{dq} \times \mathbf{i}^r_{dq}) \\ &= \frac{3}{2}p\left(\begin{bmatrix}\lambda^r_d \\ \lambda^r_q \\ 0\end{bmatrix} \times \begin{bmatrix}i^r_d \\ i^r_q \\ 0\end{bmatrix}\right) \\ &= \frac{3}{2}p(\lambda^r_d i^r_q - \lambda^r_q i^r_d) \\ &= \frac{3}{2}p\left[(L_d i^r_d + \Psi_{PM})i^r_q - L_q i^r_q i^r_d\right] \\ &= \frac{3}{2}p\left[\Psi_{PM} i^r_q + (L_d - L_q)i^r_d i^r_q\right] \end{aligned} \tag{4.28}$$

which simplifies itself for the SPMSM type as

$$M_e = \frac{3}{2}p\Psi_{PM} i^r_q \tag{4.29}$$

The first part in Equation 4.28 represents the electro-magnetic torque based on the Lorentz force, whereas the second part belongs to the reluctance torque caused by the magnetic asymmetry of L_d and L_q. Due to the non-present magnetic saliency, the SPMSM can not develop such reluctance torque as Equation 4.29 shows. The torque equation is also obtained with Equation 4.27 by calculating $M_e = \frac{\partial P_e}{\partial \omega_m}$.

4.2.3. State of the Art Control Structure

With the PMSM voltage differential Equations 4.21 - 4.26, the machine dynamic is described in the rotating reference frame. The structure of these equations in this frame shows, that the complexity of the machine description is drastically reduced and the stator current is decomposed into two separate components similar as with the separately excited DC machine [61]. A big benefit of the field-oriented point of view is that all quantities in this frame can be handled as DC quantities, which is beneficial for the control design. Since all quantities are now considered in the synchronous rotating dq-reference frame, currents and voltages are not further superscripted with an additional index. Figure 4.11 shows the overview about a field-oriented control of a PMSM.

The idea is to control the machine in the rotating dq-frame. Therefore the current control values i_d and i_q have to be transformed from the accessible abc-frame into the dq-frame via Clarke and Park transformation as described in former subsections. A compensation block is usually used to nullify the non-linear couplings in the voltage equations of the electric machine and to simplify the plant for the current control design. The i_d and i_q current controllers operate in the dq-frame, which requires the inverse Park and Clarke transformations of the control voltages u_d and u_q. For performing these

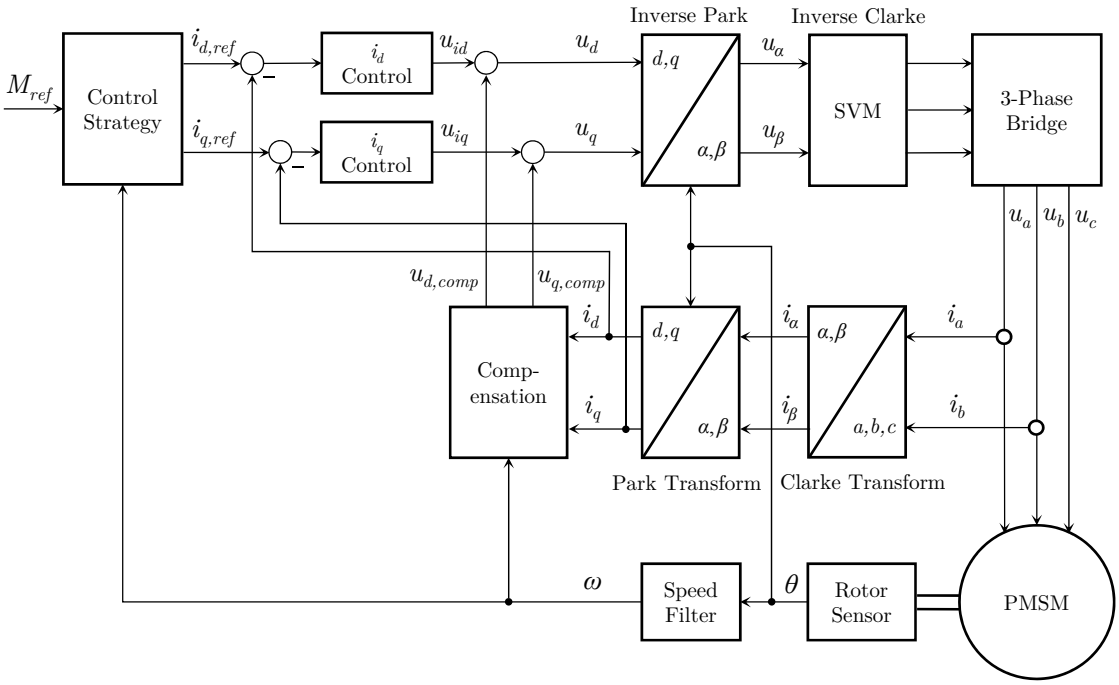

Figure 4.11.: Field-oriented control concept of a PMSM.

transformations, the rotor angle θ is needed and a present sensor error influences the accuracy of this transformations. Operating points of electric machines are determined by torque demand and electric frequency and therefore a control strategy block is needed, which calculates the necessary d- and q- current components for a given operating point determined by the machine's torque equation. Note that the electric frequency ω, which is usually derived in different ways from the rotor sensor position information, is assumed to be constant. Simulations showed, that this influence regarding the control strategy and torque ripple can be neglected. Regarding speed control mode this influence will be investigated in Section 4.12 in more detail. The aim of the following chapters is to describe this field-oriented system analytically and to investigate the consequences of a present rotor position error in terms of control quality.

4.2.4. Current Control Design with Modulus Optimum

To specify a certain operating point of the electric machine, a torque control functionality is demanded. Usually, the torque is not controlled directly, because this makes a torque sensor necessary, which is not applicable for most applications. Instead, the d- and q-current components are controlled, where two separated controllers are designed. Figure 4.12 shows the current control loops consisting of controller, power electronics and plant dynamics, where the modulus optimum control design method is used to specify the current PI-controller parameters [66].

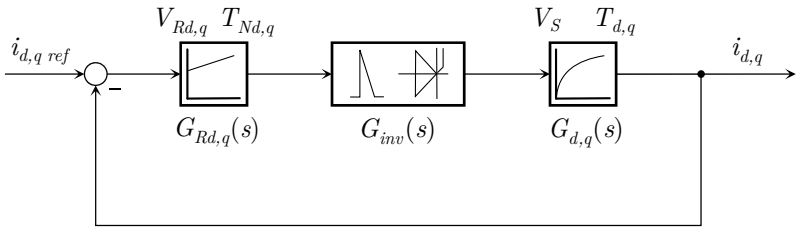

Figure 4.12.: Current control loop with controller, inverter and plant.

The plant dynamics are determined by the decoupled voltage differential equations and given as

$$u_d = R_s i_d + L_d \frac{di_d}{dt}$$
$$u_q = R_s i_q + L_q \frac{di_q}{dt}$$

or written as transfer functions in the Laplace domain

$$G_d(s) = \frac{i_d(s)}{u_d(s)} = \frac{1}{R_s} \frac{1}{1 + s\frac{L_d}{R_s}} = V_S \frac{1}{1 + sT_d}$$
$$G_q(s) = \frac{i_q(s)}{u_q(s)} = \frac{1}{R_s} \frac{1}{1 + s\frac{L_q}{R_s}} = V_S \frac{1}{1 + sT_q}$$

The control value of the controller is the input for the power electronics respectively power inverter, which is usually treated as a time delay from a system theorie point of view [66]. Dead time elements are described in time continuous domain as

$$G_{inv}(s) = V_{inv} e^{-sT_t}$$

To utilize linear system theory, the elements have to be written as fractional rational transfer functions, which is not possible for the above dead time system. Therefore, the common approximation

$$G_{inv}(s) = V_{inv} e^{-sT_t} \approx V_{inv} \frac{1}{1 + sT_t} \tag{4.30}$$

is used to describe the power electronics influence on the current control system. The controllers are realized as PI-controllers and written as following transfer functions

$$G_R(s) = V_R \frac{1 + sT_N}{sT_N} \tag{4.31}$$

respectively

$$G_{Rd,q}(s) = V_{Rd,q}\frac{1+sT_{Nd,q}}{sT_{Nd,q}} \tag{4.32}$$

with control gain V_R and reset time T_N computed by modulus optimum design and guarantees the condition $|T_{id,q}(j\omega)| = 1$ in the largest possible frequency range. Computation of the control parameters is discussed in more detail in [66]. Applying the modulus optimum rule leads to following control parameters for d- and q- loop

$$V_{Rd,q} = \frac{T_{d,q}}{2V_S T_t}$$
$$T_{Nd,q} = T_{d,q}$$

The SPMSM machine type has the same time constants in d- and q-direction, meaning that both current controllers are designed identical. Optimum modulus achieves a reduction of the transfer functions order due to the choice of $T_{Nd,q} = T_{d,q}$, which results in identical closed loop control dynamics for d- and q-direction. The closed loop dynamics follow as

$$T_{id,q}(s) = \frac{i_{d,q}(s)}{i_{d,qref}(s)} = \frac{G_{Rd,q}(s)G_{inv}(s)G_{d,q}(s)}{1+G_{Rd,q}G_{inv}(s)G_{d,q}(s)} = \frac{1}{1+s2T_t+s^2 2T_t^2} \approx \frac{1}{1+s2T_t} \tag{4.33}$$

where the approximation is useful for designing an outer speed control loop, which is used in Section 4.12.1. Figure 4.2.4 shows the bode plots and the step response for the designed current controller in d-direction.

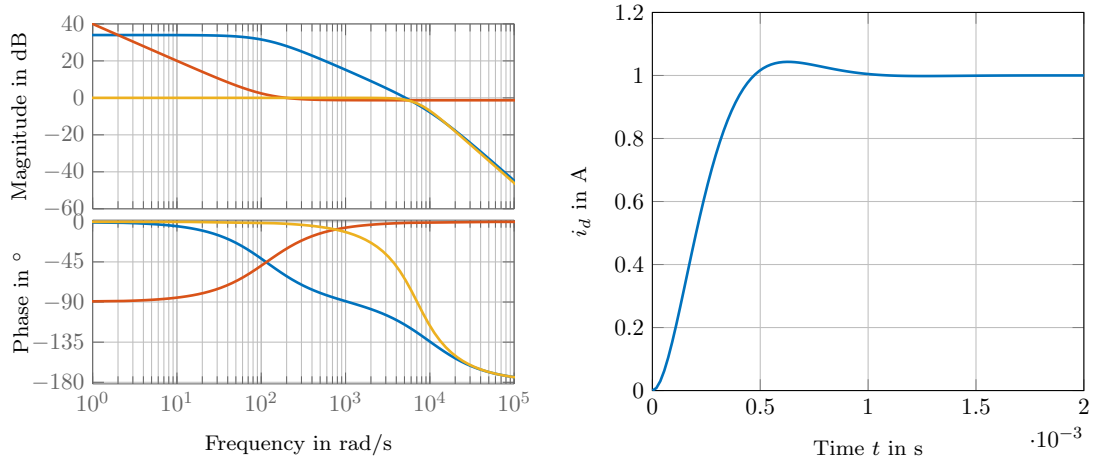

Figure 4.13.: Left: Bode plots of plant $G_{inv}(s)G_d(s)$ (blue), controller G_{Rd} (red) and closed loop transfer function $T_{id}(s)$ (yellow). Right: Step response with 4% overshoot specified by modulus optimum design.

Note that the current controllers are designed by considering the dead time delay of the power electronics; for the analytic mathematical description it is neglected at first. In Section 4.9, an approach is proposed to consider the inverter time delay approximation within the current control structure.

4.3. Rotor Position Measurement Error with PMSM in Rotating Reference Frame

With the mathematical description of electric machine, coordinate transformation and controller, a first approach for describing the whole field-oriented control dynamics is presented. The idea is to determine a disturbance transfer function, which describes the effect from a present rotor position error $\Delta\theta$ regarding the machine currents and output torque M_e. The computed machine torque can be utilized for example to analyze its impact on torsional oscillations within the powertrain of an electric vehicle as proposed in [67]. This chapter gives an overview about different approaches for a mathematical description of torque ripple induced by rotor position measurement errors.

4.3.1. Sworowski's Method

In [60], Sworowski investigates different perturbations, which influence the control quality of a SPMSM. One of the investigated distortions are rotor position errors and a method to calculate the resulting deviations in the machine currents is presented. This method assumes completely decoupled voltage equations and is only valid for the SPMSM machine type. Here, an extension for the IPMSM machines is presented and the results are examined for both machine types. Sworowski describes the rotor sensor error as a sum of harmonic functions

$$\Delta\theta(t) = \sum_k a_k \sin(k\omega_m t)$$

with order k, mechanical frequency ω_m and amplitude a_k of k^{th} order. Figure 4.14 shows the structure of the current control loop and the multiplicative distortions of the complex multiplication of $e^{j\theta}$ respectively $e^{-j\theta}$.

The signals in this approach are described as complex vectors consisting of real and imaginary part, which means that $\underline{i}_{dq} = i_d + j i_q$. The frequency response from the distorted output currents to the input reference current is written as

$$\begin{aligned}\frac{\underline{i}_{dq,ref}(j\omega) + \bar{\underline{i}}_{dq}(j\omega)}{\underline{i}_{dq,ref}(j\omega)} &= \frac{G_{Rd,q}(j\omega)e^{j\Delta\theta}G_{d,q}(j\omega)}{1 + G_{Rd,q}(j\omega)e^{j\Delta\theta}G_{d,q}(j\omega)e^{-j\Delta\theta}} = \frac{G_{Rd,q}(j\omega)G_{d,q}(j\omega)e^{j\Delta\theta}}{1 + G_{Rd,q}(j\omega)G_{d,q}(j\omega)} \\ &= T(j\omega)\mathfrak{F}\{e^{j\Delta\theta}\}\end{aligned}$$

with the closed loop frequency response $T(j\omega)$ and $\mathfrak{F}\{e^{j\Delta\theta}\}$ as the Fourier transform of

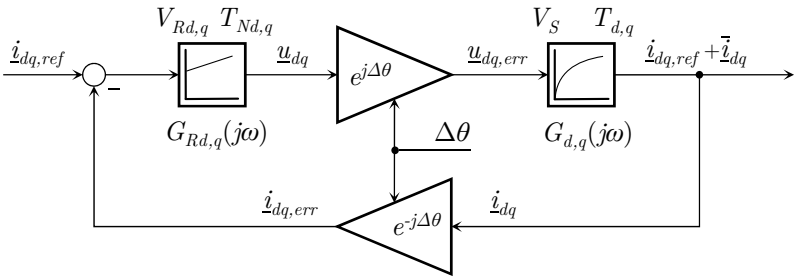

Figure 4.14.: Current control loop with rotor position sensor error adapted from [60].

$e^{j\Delta\theta}$. This Fourier transform can be approximated as

$$\mathfrak{F}\{e^{j\Delta\theta}\} \approx \mathfrak{F}\{1 + j\Delta\theta\} = 2\pi\delta(j\omega) + j\Delta\theta(j\omega)$$

with the Dirac delta distribution δ. Calculation of the frequency response leads to

$$\frac{\underline{i}_{dq,ref}(j\omega) + \bar{\underline{i}}_{dq}(j\omega)}{\underline{i}_{dq,ref}(j\omega)} = \underbrace{T(j\omega)2\pi\delta(j\omega)}_{=1} + T(j\omega)j\Delta\theta(j\omega)$$

and to the final distortion frequency response from the rotor sensor error $\Delta\theta$ to the complex current $\bar{\underline{i}}_{dq}$ as

$$\frac{\bar{\underline{i}}_{dq}(j\omega)}{\Delta\theta(j\omega)} = j\underline{i}_{dq,ref}(j\omega)T(j\omega) \tag{4.34}$$

Transformation of this result into the time domain gives

$$\bar{\underline{i}}_{dq}(t) = j\ \underline{i}_{dq,ref}(t) \sum_k |T(jk\omega_m)| a_k \sin\left(k\omega_m t + arg(T(jk\omega_m))\right)$$

The current distortion $\bar{\underline{i}}$ consists of a multiplication of $\underline{i}_{dq,ref}(t)$ with j, which results in a 90° rotation of the complex vector in mathematical positive sense. Additionally, the rotor sensor error $\Delta\theta$ is filtered with the closed loop frequency response $T(j\omega)$. This result can be applied to the SPMSM torque equation and leads to

$$\begin{aligned} M_e &= \frac{3}{2} p\Psi_{PM} \mathrm{Im}\{\underline{i}_{dq,ref} + \bar{\underline{i}}_{dq}\} \\ &= \frac{3}{2} p\Psi_{PM} \left[i_{q,ref} + i_{d,ref} \sum_k |T(jk\omega_m)| a_k \sin\left(k\omega_m t + arg\big(T(jk\omega_m)\big)\right) \right] \end{aligned}$$

Figure 4.15 depicts the results of Sworowski's method and static torque ripple calculations with exemplary eddy current sensor error at an operating point of $M_e = 72.37$ Nm and $n = 19099$ rpm. It shows, that the results of the torque ripple prediction matches the simulation results, due to the reliable calculation of the i_q-current. In contrast to that, the i_d-current results are not satisfactory, but this has no influence on torque dis-

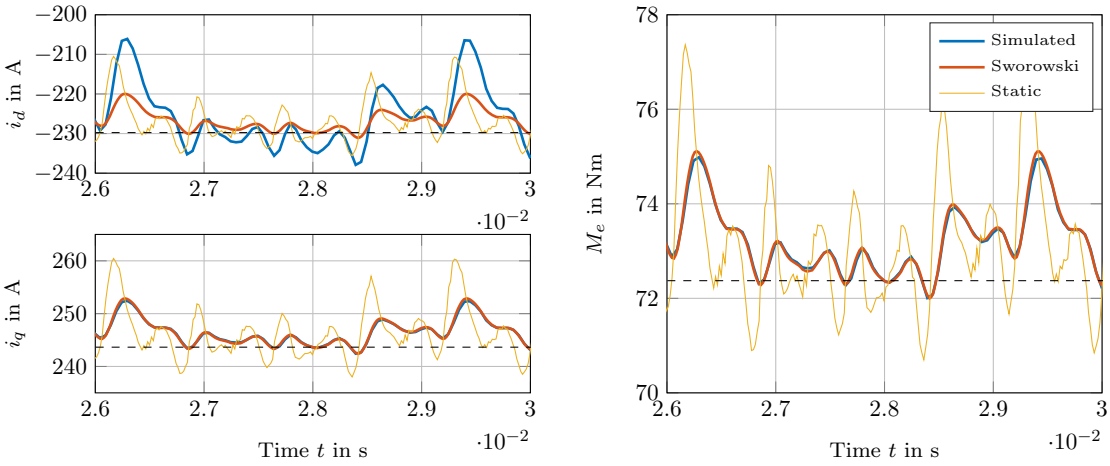

Figure 4.15.: Currents and torque ripple in operation point $M_e = 72.37$ Nm and $n = 19099$ rpm.

tortion of the SPMSM type. Additionally, the static results are plotted to show that this method does not provide usable results, overestimates the simulation results considerable and highlights that consideration of machine and controller dynamics is important for an accurate torque ripple calculation. Sworowski's approach is now consequently extended for the IPMSM type, which means that by consideration of Equation 4.34 the d-current distortion has also to be taken into account

$$\begin{aligned} \underline{i}_{dq} &= \underline{i}_{dq,ref} + \bar{\underline{i}}_{dq} = i_{d,ref} + j i_{q,ref} + j(i_{d,ref} + j i_{q,ref}) T(j\omega)\Delta\theta(j\omega) \\ &= i_{d,ref} - i_{q,ref} T(j\omega)\Delta\theta(j\omega) + j\big(i_{q,ref} + i_{d,ref} T(j\omega)\Delta\theta(j\omega)\big) \end{aligned}$$

Due to the optimum modulus control design, both current loops have the same closed loop dynamics. Utilization of

$$\begin{aligned} i_d &= \mathrm{Re}\{\underline{i}_{dq}\} = i_{d,ref} + \bar{i}_d = i_{d,ref} - i_{q,ref} T(j\omega)\Delta\theta(j\omega) \\ i_q &= \mathrm{Im}\{\underline{i}_{dq}\} = i_{q,ref} + \bar{i}_q = i_{q,ref} + i_{d,ref} T(j\omega)\Delta\theta(j\omega) \end{aligned}$$

and insertion into the IPMSM torque Equation 4.28 gives the torque ripple results for a consequent extension of Sworowoski's approach, which are depicted in Figure 4.16.

For this machine type the same sensor error and speed is used, but since the IPMSM provides more torque if current and voltage limits are present, the control strategy increases the torque from 72.37 up to 79.27 Nm. In the IPMSM case, the results are not satisfactory any more due to a significant overestimation of the torque ripple calculation compared to the simulation results. This shows, that Sworowski's method provides valid results for the SPMSM, but the generalization for the IPMSM has a certain lack of accuracy.

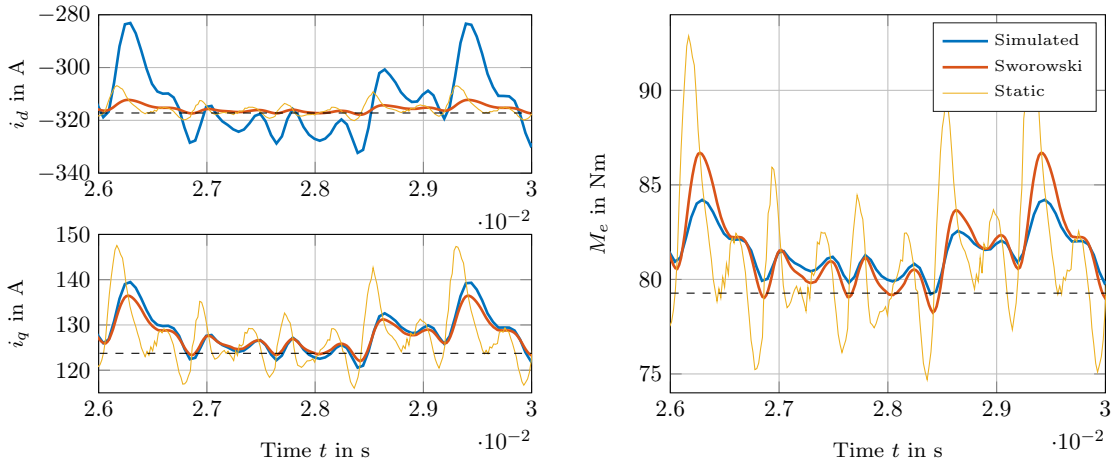

Figure 4.16.: Currents and torque ripple in operating point $M_e = 79.27$ Nm and $n = 19099$ rpm.

4.3.2. Linearization of the dq-Model

The field-oriented control system as shown in Figure 4.2 is non-linear due to the complex multiplications of $e^{j\Delta\theta}$, the non-linear voltage differential and IPMSM torque equations. As a first approach, the inverse Park transformation and rotor position error $\Delta\theta$ is considered with compensated voltage equations. This leads to

$$\begin{aligned} L_d \frac{di_d}{dt} &= -R_s i_d + \cos(\Delta\theta)\bar{u}_d - \sin(\Delta\theta)\bar{u}_q \\ L_q \frac{di_q}{dt} &= -R_s i_q + \sin(\Delta\theta)\bar{u}_d + \cos(\Delta\theta)\bar{u}_q \end{aligned}$$

The system outputs are defined as the misaligned machine currents, with which the current control loop is closed

$$\begin{aligned} \bar{i}_d &= \cos(\Delta\theta) i_d + \sin(\Delta\theta) i_q \\ \bar{i}_q &= -\sin(\Delta\theta) i_d + \cos(\Delta\theta) i_q \end{aligned}$$

This system of differential equations can be written in the general form as

$$\begin{aligned} \dot{\mathbf{x}} &= \mathbf{f}(\mathbf{x}, \mathbf{u}) \\ \mathbf{y} &= \mathbf{g}(\mathbf{x}, \mathbf{u}) \end{aligned}$$

With the state vector $\mathbf{x}$, input vector $\mathbf{u}$ and the general torque equation as third output in the output vector follows

$$\mathbf{f}(\mathbf{x},\mathbf{u}) = \begin{bmatrix} \frac{1}{L_d}\left[-R_s i_d + \cos(\Delta\theta)\bar{u}_d - \sin(\Delta\theta)\bar{u}_q\right] \\ \frac{1}{L_q}\left[-R_s i_q + \sin(\Delta\theta)\bar{u}_d + \cos(\Delta\theta)\bar{u}_q\right] \end{bmatrix}$$

$$\mathbf{g}(\mathbf{x},\mathbf{u}) = \begin{bmatrix} \cos(\Delta\theta) i_d + \sin(\Delta\theta) i_q \\ -\sin(\Delta\theta) i_d + \cos(\Delta\theta) i_q \\ \frac{3}{2} p\left[\Psi_{PM} i_q + (L_d - L_q) i_d i_q\right] \end{bmatrix}$$

For a holistic closed loop system description with current controller, the above non-linear system has to be linearized to apply linear system methods. The linearization at an equilibrium point $\mathbf{x}_R, \mathbf{u}_R$ results in a LTI (linear time invariant) system description in form of [68]

$$\boldsymbol{\Delta}\dot{\mathbf{x}} = \mathbf{A}\boldsymbol{\Delta}\mathbf{x} + \mathbf{B}\boldsymbol{\Delta}\mathbf{u}$$
$$\boldsymbol{\Delta}\mathbf{y} = \mathbf{C}\boldsymbol{\Delta}\mathbf{x} + \mathbf{D}\boldsymbol{\Delta}\mathbf{u}$$

which describes the dynamics of the non-linear system approximately in a close environment around the system's equilibrium point. The linear system matrices $\mathbf{A}$, $\mathbf{B}$, $\mathbf{C}$ and $\mathbf{D}$ are defined as the Jacobian matrices, which are computed as followed

$$\mathbf{A} = \left.\frac{\partial \mathbf{f}(\mathbf{x},\mathbf{u})}{\partial \mathbf{x}}\right|_{\mathbf{x}_R,\mathbf{u}_R} \qquad \mathbf{B} = \left.\frac{\partial \mathbf{f}(\mathbf{x},\mathbf{u})}{\partial \mathbf{u}}\right|_{\mathbf{x}_R,\mathbf{u}_R}$$
$$\mathbf{C} = \left.\frac{\partial \mathbf{g}(\mathbf{x},\mathbf{u})}{\partial \mathbf{x}}\right|_{\mathbf{x}_R,\mathbf{u}_R} \qquad \mathbf{D} = \left.\frac{\partial \mathbf{g}(\mathbf{x},\mathbf{u})}{\partial \mathbf{u}}\right|_{\mathbf{x}_R,\mathbf{u}_R}$$

and are leading for the equilibrium point $\mathbf{f}(\mathbf{x_R},\mathbf{u_R}) = \mathbf{0}$, determined by the the electric machine's operating point and control strategy i_{dR}, i_{qR}, ω_R and $\Delta\theta_R = 0$

$$\mathbf{x}_R = \begin{bmatrix} i_{dR} \\ i_{qR} \end{bmatrix}$$
$$\mathbf{u}_R = \begin{bmatrix} R_s i_{dR} \\ R_s i_{qR} \end{bmatrix} = \begin{bmatrix} u_{dR} \\ u_{qR} \end{bmatrix}$$

to following system matrices

$$\mathbf{A} = \begin{bmatrix} -\frac{R_s}{L_d} & 0 \\ 0 & -\frac{R_s}{L_q} \end{bmatrix} \qquad \mathbf{B} = \begin{bmatrix} \frac{1}{L_d} & 0 & -\frac{R_s i_{qR}}{L_d} \\ 0 & \frac{1}{L_q} & \frac{R_s i_{dR}}{L_q} \end{bmatrix}$$

$$\mathbf{C} = \begin{bmatrix} 1 & 0 \\ 0 & 1 \\ \frac{3}{2}p(L_d - L_q) i_{qR} & \frac{3}{2}p(\Psi_{PM} + (L_d - L_q) i_{dR}) \end{bmatrix} \qquad \mathbf{D} = \begin{bmatrix} 0 & 0 & i_{qR} \\ 0 & 0 & -i_{dR} \\ 0 & 0 & 0 \end{bmatrix}$$

This system consists of three inputs and three outputs and can therefore be represented as a 3×3 transfer matrix $\mathbf{G}(s)$, which describes the input-output relations from each input to each output. This transfer function matrix is calculated as [68]

$$\mathbf{G}(s) = \mathbf{C}(s\mathbf{E} - \mathbf{A})^{-1}\mathbf{B} = \begin{bmatrix} G_{11}(s) & G_{12}(s) & G_{13}(s) \\ G_{21}(s) & G_{22}(s) & G_{23}(s) \\ G_{31}(s) & G_{32}(s) & G_{33}(s) \end{bmatrix}$$

$$= \begin{bmatrix} \frac{1}{sL_d+R_s} & 0 & -\frac{R_s i_{qR}}{sL_d+R_s} \\ 0 & \frac{1}{sL_q+R_s} & \frac{R_s i_{dR}}{sL_q+R_s} \\ \frac{3}{2}p\frac{(L_d-L_q)i_{qR}}{sL_d+R_s} & \frac{3}{2}p\frac{\Psi_{PM}+(L_d-L_q)i_{qR}}{sL_q+R_s} & \frac{3}{2}p\frac{(L_d-L_q)R_s i_{qR}^2}{sL_d+R_s} + \frac{3}{2}p\frac{R_s i_{dR}(\Psi_{PM}+(L_d-L_q)i_{dR})}{sL_q+R_s} \end{bmatrix}$$

Due to the applied non-linear compensation of the voltage equations, the cross-coupling from d- and q-current is not existent and therefore $G_{12}(s) = G_{21}(s) = 0$ applies. Integration of the linearized substitute model into the current control loop gives the complete system description of electric machine and current controllers as depicted in Figure 4.17.

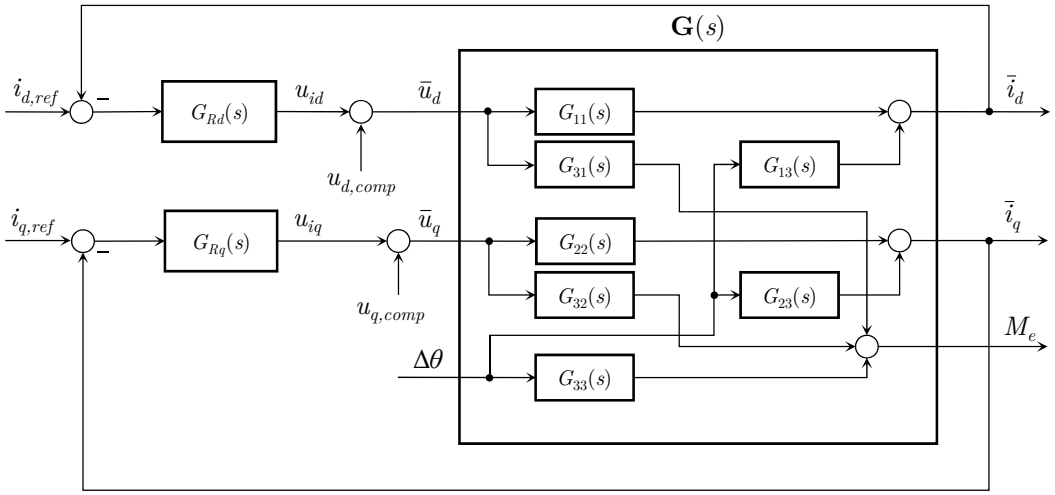

Figure 4.17.: Current control loop with linearized substitute multiple input multiple output (MIMO) system and torque as output.

It shows, that the sensor error $\Delta\theta$ influences torque and both current components. Additionally, the control transfer functions $G_{Rd}(s)$ and $G_{Rq}(s)$ are interfering the torque distortion too, which leads to following torque dynamics

$$M_e(s) = \left(G_{33}(s) - \frac{G_{13}(s)G_{Rd}(s)G_{31}(s)}{1 + G_{Rd}(s)G_{11}(s)} - \frac{G_{23}(s)G_{Rq}(s)G_{32}(s)}{1 + G_{Rq}(s)G_{22}(s)} \right) \Delta\theta(s)$$

Figure 4.18 shows the results of the compensated linear system with current control loop and machine torque as output signal. To obtain the machine currents i_d and i_q, an

additional inverse Park transformation has to be applied to the control currents $\bar{i}_d$ and $\bar{i}_q$.

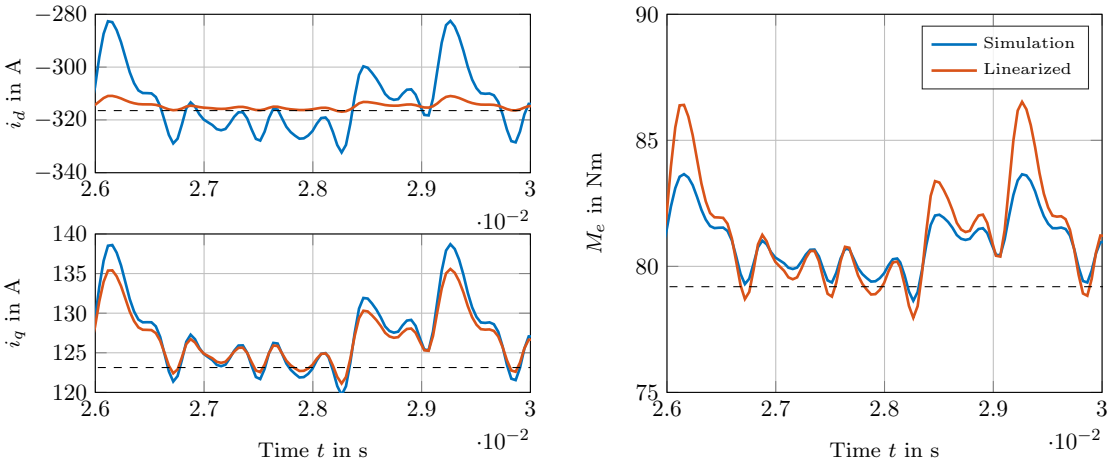

Figure 4.18.: Current and torque ripple at $M_e = 79.27$ Nm and $n = 19099$ rpm with consideration of torque equation within system dynamics.

The results show, that the characteristics of i_d and the torque M_e match the simulation unsatisfactory and the system $\mathbf{G}(s)$ has an inconveniently structure due to the strong coupling between currents and rotor position error and vice versa. Since linearization of the torque equation can be problematic and the machine's torque represents a static non-linear output relation, the torque equation is removed from the system description. Therefore it is sufficient to describe the dynamics of the control currents $\bar{i}_d$ and $\bar{i}_q$, transform them into machine currents i_d and i_q and calculate the resulting torque. The system parameters follow then with applied compensation voltages as

$$\mathbf{A} = \begin{bmatrix} -\frac{R_s}{L_d} & 0 \\ 0 & -\frac{R_s}{L_q} \end{bmatrix} \quad \mathbf{B} = \begin{bmatrix} \frac{1}{L_d} & 0 & -\frac{u_{qR}}{L_d} \\ 0 & \frac{1}{L_q} & \frac{u_{dR}}{L_q} \end{bmatrix}$$
$$\mathbf{C} = \begin{bmatrix} 1 & 0 \\ 0 & 1 \end{bmatrix} \qquad \mathbf{D} = \begin{bmatrix} 0 & 0 & i_{qR} \\ 0 & 0 & -i_{dR} \end{bmatrix}$$

with the transfer function matrix

$$\mathbf{G}(s) = \begin{bmatrix} \frac{1}{sL_d+R_s} & 0 & -\frac{u_{qR}}{sL_d+R_s} \\ 0 & \frac{1}{sL_q+R_s} & \frac{u_{dR}}{sL_q+R_s} \end{bmatrix} \tag{4.35}$$

in a simpler structure. This transfer matrix is used to describe the distortions of $\bar{i}_d$ and $\bar{i}_q$ due to the sensor error $\Delta\theta$ for the closed loop current control system. Afterwards, an additional inverse Park Transformation is used to calculate the machine currents i_d and i_q to compute the torque ripple via Equation 4.28, which is depicted in Figure 4.19.

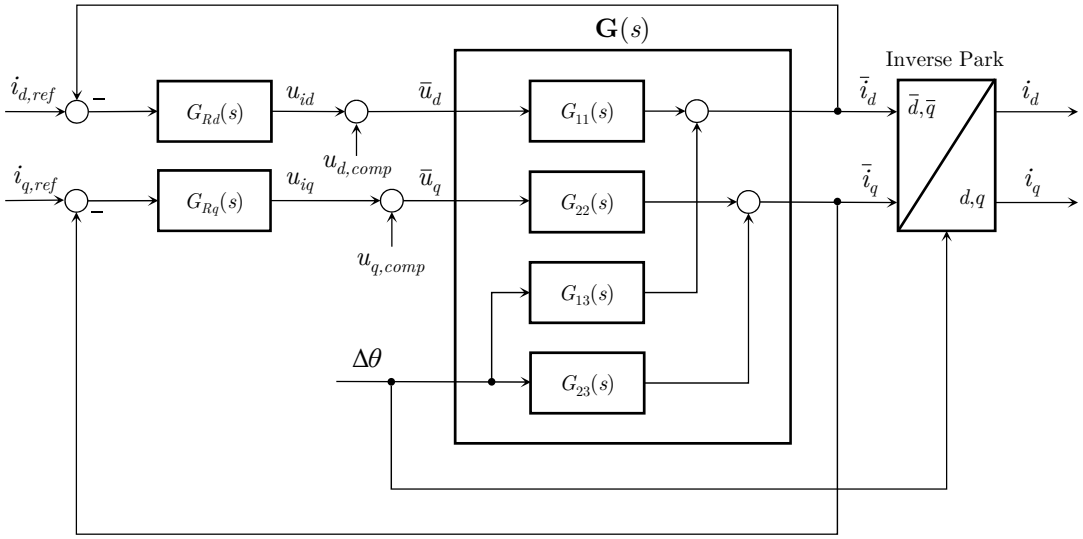

Figure 4.19.: Current control loop with linearized substitute MIMO system and controlled currents $\bar{i}_d$ and $\bar{i}_q$ as outputs. Machine currents i_d and i_q are calculated afterwards with inverse Park transformation.

This modification leads to the same machine currents as in Figure 4.18, because the description of the electric subsystem stays the same. The torque is calculated with the non-linear equation and not degenerated by the system linearization process, which is displayed in Figure 4.20.

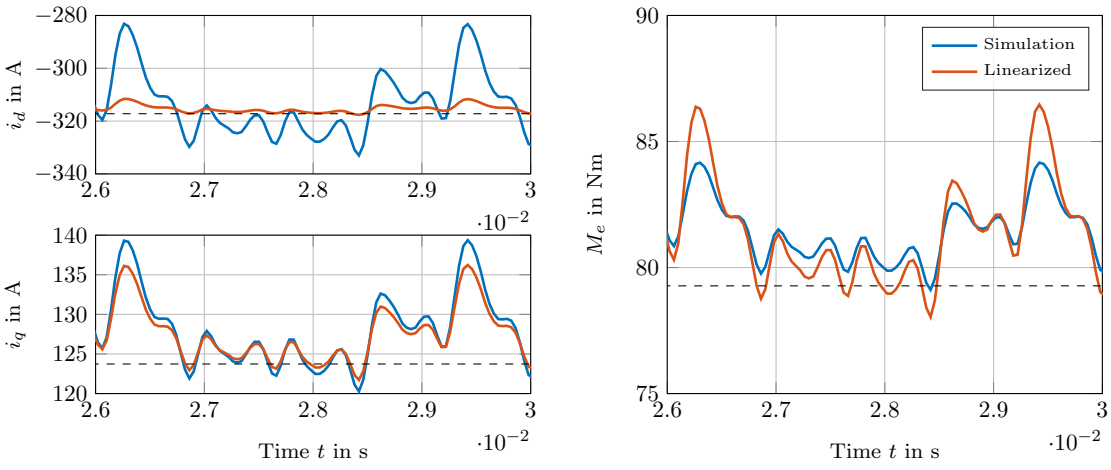

Figure 4.20.: Modified structure of torque ripple calculation without torque equation within system description at $M_e = 79.27$ Nm and $n = 19099$ rpm.

Due to the lack of accuracy, especially in the calculation of i_d, the torque ripple does

not fit the simulation results and is approximately twice times higher. One problem is the compensation, which applies voltages with distorted currents $\bar{i}_d$ and $\bar{i}_q$. This leads to incomplete decoupled voltage equations and therefore to poor estimations of the machine currents i_d and i_q. Further investigations on the simulation model show, that the general dq-model is not sufficient to describe the torque ripple caused by rotor position sensor errors with a satisfactory accuracy. This makes an enhancement of the voltage differential equations necessary, which is discussed in the next section.

4.4. Rotor Position Measurement Error with PMSM in Misaligned Reference Frame

Sworowski's method and the linearization of the general dq-model do not provide satisfying results regarding torque ripple calculation. Based on Kwang Hee Nam's approach [3], which describes a PMSM in a misaligned reference frame, an enhancement of the previous method of linearization is presented. This model description is used primary in sensorless control methods, with the aim to eliminate the direct measurement of the rotor position with a specific sensor. A misalignment of the synchronous dq-reference frame produces additional voltage and current terms within the electric differential equations, which are not considered by the ordinary dq-model. For developing the misaligned model, certain specific terms of the previous chapters are necessary, which explains the detailed derivation in Section 4.2.2. The deviation of these two involved coordinate systems is related with

$$\Delta\theta = \bar{\theta} - \theta$$
$$\Delta\omega = \bar{\omega} - \omega$$

Figure 4.21 shows the situation of the misaligned reference frame with real - but unknown - rotor angle θ and measured angle $\bar{\theta}$.

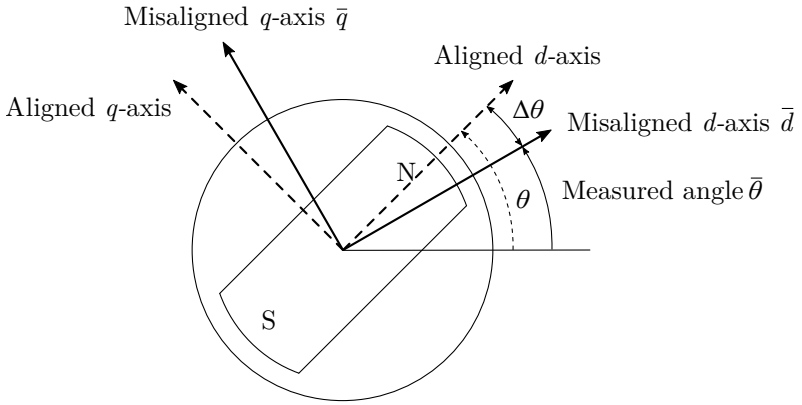

Figure 4.21.: Aligned and misaligned reference frame of PMSM adapted from [3].

Origin of the misaligned model is the flux linkage in the stationary $\alpha\beta$-frame from Equation 4.14

$$\boldsymbol{\lambda}^s_{\alpha\beta} = L_s \mathbf{i}^s_{\alpha\beta} - \frac{3}{2} L_\delta e^{j2\theta} (\mathbf{i}^s_{\alpha\beta})^* + \Psi_{PM} e^{j\theta}$$

But in contrast to previous considerations, the flux linkage is not transformed with the ideal angle θ into the rotating dq-frame. Instead, due to the additional rotor sensor error $\Delta\theta$, the transformation is applied with a different angle $\bar{\theta}$ into a misaligned rotating dq-reference frame. This gives for the flux linkage

$$\bar{\boldsymbol{\lambda}}^r_{dq} = e^{-j\bar{\theta}} \boldsymbol{\lambda}^s_{\alpha\beta} = L_s e^{-j\bar{\theta}} \mathbf{i}^s_{\alpha\beta} - \frac{3}{2} L_\delta e^{j(2\theta-\bar{\theta})} (\mathbf{i}^s_{\alpha\beta})^* + \Psi_{PM} e^{-j\Delta\theta}$$

and the appropriate currents $\bar{\mathbf{i}}^r_{dq} = e^{-j\bar{\theta}} \mathbf{i}^s_{\alpha\beta}$ for the flux linkage in a misaligned reference frame

$$\bar{\boldsymbol{\lambda}}^r_{dq} = L_s \bar{\mathbf{i}}^r_{dq} - \frac{3}{2} L_\delta (\bar{\mathbf{i}}^r_{dq})^* e^{-j2\Delta\theta} + \Psi_{PM} e^{-j\Delta\theta}$$

The common voltage equation

$$\bar{\mathbf{u}}^r_{dq} = R_s \bar{\mathbf{i}}^r_{dq} + j\bar{\omega} \bar{\boldsymbol{\lambda}}^r_{dq} + \frac{d}{dt} \bar{\boldsymbol{\lambda}}^r_{dq}$$

in the misaligned reference frame with utilization of

$$\begin{aligned}
j\bar{\omega} \bar{\boldsymbol{\lambda}}^r_{dq} &= j\bar{\omega} L_s \bar{\mathbf{i}}^r_{dq} - j\bar{\omega} \frac{3}{2} L_\delta (\bar{\mathbf{i}}^r_{dq})^* e^{-j2\Delta\theta} + j\bar{\omega} \Psi_{PM} e^{-j\Delta\theta} \\
\frac{d}{dt} \bar{\boldsymbol{\lambda}}^r_{dq} &= L_s \frac{d}{dt} \bar{\mathbf{i}}^r_{dq} - \frac{3}{2} L_\delta \frac{d}{dt} (\bar{\mathbf{i}}^r_{dq})^* e^{-j2\Delta\theta} + 3 L_\delta j\Delta\omega (\bar{\mathbf{i}}^r_{dq})^* e^{-j2\Delta\theta} - j\Delta\omega \Psi_{PM} e^{-j\Delta\theta}
\end{aligned}$$

gives the voltage equations for the PMSM in a misaligned reference frame as

$$\begin{aligned}
\begin{bmatrix} \bar{u}^r_d \\ \bar{u}^r_q \end{bmatrix} = R_s \begin{bmatrix} \bar{i}^r_d \\ \bar{i}^r_q \end{bmatrix} &+ \begin{bmatrix} L_s - \frac{3}{2} L_\delta \cos 2\Delta\theta & \frac{3}{2} L_\delta \sin 2\Delta\theta \\ \frac{3}{2} L_\delta \sin 2\Delta\theta & L_s + \frac{3}{2} L_\delta \cos 2\Delta\theta \end{bmatrix} \frac{d}{dt} \begin{bmatrix} \bar{i}^r_d \\ \bar{i}^r_q \end{bmatrix} \\
&+ (3\Delta\omega - \frac{3}{2}\bar{\omega}) L_\delta) \begin{bmatrix} \sin 2\Delta\theta & \cos 2\Delta\theta \\ \cos 2\Delta\theta & -\sin 2\Delta\theta \end{bmatrix} \begin{bmatrix} \bar{i}^r_d \\ \bar{i}^r_q \end{bmatrix} \\
&+ \bar{\omega} L_s \begin{bmatrix} -\bar{i}^r_q \\ \bar{i}^r_d \end{bmatrix} + \omega \Psi_{PM} \begin{bmatrix} \sin \Delta\theta \\ \cos \Delta\theta \end{bmatrix}
\end{aligned} \tag{4.36}$$

This model structure can be obtained as a generalization of the voltage equations in the stationary $\alpha\beta$-reference frame described in Equation 4.16. By setting $\Delta\theta = -\theta$, $\Delta\omega = -\omega$ and $\bar{\omega} = 0$, the misaligned model reduces itself to the model in the stationary $\alpha\beta$-reference frame. The structure of the misaligned model is quite elaborate, especially the interconnections of the misaligned current derivatives. The aim here is to describe the model as a system of first order ordinary differential equations; therefore some simplifications are necessary. The equations of the misaligned model can be separated rewritten

as

$$\begin{aligned}
\bar{u}_d^r &= \left(R_s - \frac{3}{2}\bar{\omega}L_\delta \sin 2\Delta\theta\right)\bar{i}_d^r + \left(L_s - \frac{3}{2}L_\delta \cos 2\Delta\theta\right)\frac{d\bar{i}_d^r}{dt} + \omega\Psi_{PM}\sin\Delta\theta \\
&\quad - \bar{\omega}\left(L_s + \frac{3}{2}L_\delta \cos 2\Delta\theta\right)\bar{i}_q^r + 3L_\delta\Delta\omega\bar{i}_q^r \cos 2\Delta\theta + E_D \\
\bar{u}_q^r &= \left(R_s + \frac{3}{2}\bar{\omega}L_\delta \sin 2\Delta\theta\right)\bar{i}_q^r + \left(L_s + \frac{3}{2}L_\delta \cos 2\Delta\theta\right)\frac{d\bar{i}_q^r}{dt} + \omega\Psi_{PM}\cos\Delta\theta \\
&\quad + \bar{\omega}\left(L_s - \frac{3}{2}L_\delta \cos 2\Delta\theta\right)\bar{i}_d^r + 3L_\delta\Delta\omega\bar{i}_d^r \cos 2\Delta\theta + E_Q
\end{aligned}$$

with the additional voltage terms E_D and E_Q given as

$$\begin{aligned}
E_D &= \frac{3}{2}L_\delta \sin 2\Delta\theta\frac{d\bar{i}_q^r}{dt} + 3L_\delta\Delta\omega\sin 2\Delta\theta\bar{i}_d^r \\
E_Q &= \frac{3}{2}L_\delta \sin 2\Delta\theta\frac{d\bar{i}_d^r}{dt} - 3L_\delta\Delta\omega\sin 2\Delta\theta\bar{i}_q^r
\end{aligned}$$

Now, a typical approximation for system linearization is done by assuming that $\Delta\omega$ and $\Delta\theta$ are small, which gives even more smaller values for $\Delta\omega\sin 2\Delta\theta$ and can therefore be neglected. With consideration of $\frac{d\bar{i}_d^r}{dt} \approx 0$ and $\frac{d\bar{i}_q^r}{dt} \approx 0$ in steady-state, the additional voltage terms E_D and E_Q are small enough to be omitted. Additional approximations of

$$\frac{3}{2}\bar{\omega}L_\delta \sin 2\Delta\theta = 3\bar{\omega}L_\delta \sin\Delta\theta\cos\Delta\theta \approx 3\bar{\omega}L_\delta \sin\Delta\theta$$

with

$$\begin{aligned}
L_s - \frac{3}{2}L_\delta \cos 2\Delta\theta &\approx L_s - \frac{3}{2}L_\delta = L_d \\
L_s + \frac{3}{2}L_\delta \cos 2\Delta\theta &\approx L_s + \frac{3}{2}L_\delta = L_q
\end{aligned}$$

and

$$\omega\Psi_{PM}\cos\Delta\theta \approx \bar{\omega}\Psi_{PM}\cos\Delta\theta - \Psi_{PM}\Delta\omega$$

lead to an approximated non-linear system of first order differential equations for the misaligned model

$$\frac{d\bar{i}_d^r}{dt} = -\frac{R_s}{L_d}\bar{i}_d^r - \bar{\omega}\frac{\Psi_{PM} - 3L_\delta\bar{i}_d^r}{L_d}\sin\Delta\theta + \bar{\omega}\frac{L_q}{L_d}\bar{i}_q^r - \frac{3L_\delta}{L_d}\Delta\omega\bar{i}_q^r + \frac{1}{L_d}\bar{u}_d^r \tag{4.37}$$

$$\begin{aligned}
\frac{d\bar{i}_q^r}{dt} &= -\frac{R_s}{L_q}\bar{i}_q^r - \bar{\omega}\frac{3L_\delta\bar{i}_q^r}{L_q}\sin\Delta\theta - \bar{\omega}\frac{L_d}{L_q}\bar{i}_d^r - \frac{\bar{\omega}\Psi_{PM}}{L_q}\cos\Delta\theta + \frac{\Psi_{PM}}{L_q}\Delta\omega \\
&\quad - \frac{3L_\delta}{L_q}\Delta\omega\bar{i}_d^r + \frac{1}{L_q}\bar{u}_q^r
\end{aligned} \tag{4.38}$$

Additionally, the relationship between position error $\Delta\theta$ and relative speed $\Delta\omega$

$$\frac{d\Delta\theta}{dt} = \Delta\omega \tag{4.39}$$

has to be considered. The assumption of small angle errors $\Delta\theta$, means utilization of $\sin\Delta\theta \approx \Delta\theta$, respectively $\cos\Delta\theta \approx 1$ and elimination of $L_\delta = \frac{L_q - L_d}{3}$ leads to the further simplified model

$$L_d\frac{d\bar{i}_d^r}{dt} = -R_s\bar{i}_d^r - \big((L_d - L_q)\bar{i}_d^r + \Psi_{PM}\big)(\omega + \Delta\omega)\Delta\theta + L_d\bar{i}_q^r\Delta\omega + L_q\bar{i}_q^r\omega + \bar{u}_d^r \tag{4.40}$$

$$L_q\frac{d\bar{i}_q^r}{dt} = -R_s\bar{i}_q^r + (L_d - L_q)\bar{i}_q^r(\omega + \Delta\omega)\Delta\theta - L_q\bar{i}_d^r\Delta\omega - (L_d\bar{i}_d^r + \Psi_{PM})\omega + \bar{u}_q^r \tag{4.41}$$

which is valid for the IPMSM and degenerates itself into

$$L_s\frac{d\bar{i}_d^r}{dt} = -R_s\bar{i}_d^r - \Psi_{PM}(\omega + \Delta\omega)\Delta\theta + L_s(\omega + \Delta\omega)\bar{i}_q^r + \bar{u}_d^r$$

$$L_s\frac{d\bar{i}_q^r}{dt} = -R_s\bar{i}_q^r - L_s(\omega + \Delta\omega)\bar{i}_d^r - \Psi_{PM}\omega + \bar{u}_q^r$$

for the simpler SPMSM machine type. Examination of the voltage differential equations show, that the complexity is increased compared to the general dq-model due to the consideration of the position error $\Delta\theta$. In addition, the speed deviation $\Delta\omega$ of the real dq- and misaligned reference frame plays an additional role and produces additive terms within the electric machine dynamics, which are not considered by application of the general dq-model.

4.4.1. Comparison of FOC with Rotor Position Error and PMSM in Misaligned Frame

In this subsection is shown that the previous derived misaligned model described by Equations 4.37 and 4.38 behaves like a field-oriented controlled machine with rotor position error. Figure 4.22 depicts the open loop machine model with coordinate transformations and sensor error, which is compared with the voltage equations of the misaligned model.

A mathematical derivation is more difficult and presented in the forthcoming subsection; therefore a simulation based result is used to show that both systems behave similar. For this purpose, both models are simulated and certain voltage levels for $\bar{u}_d$ and $\bar{u}_q$ are applied, according to the equilibrium voltages u_{dR} and u_{qR} from the chosen operating point at $M_e = 79.27$ Nm and $n = 19099$ rpm. Additionally, a measured sensor error from an eddy current sensor is applied as disturbance and the results of output currents $\bar{i}_d$, $\bar{i}_q$ and torque calculation of both models are compared with each other. In Figure 4.23, the model comparison and its results are depicted.

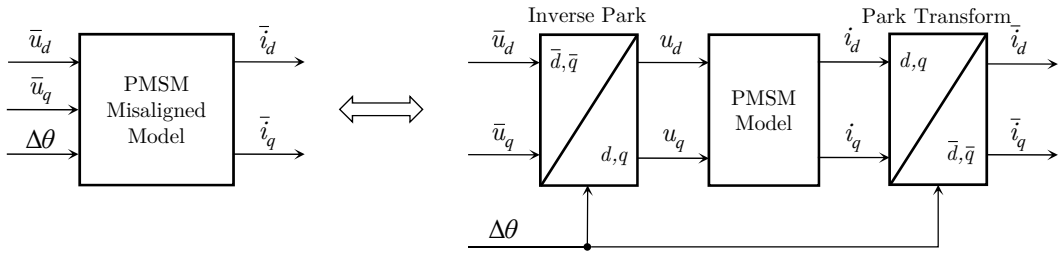

Figure 4.22.: Comparison of misaligned and simulation model for open loop field-oriented control with rotor position sensor error.

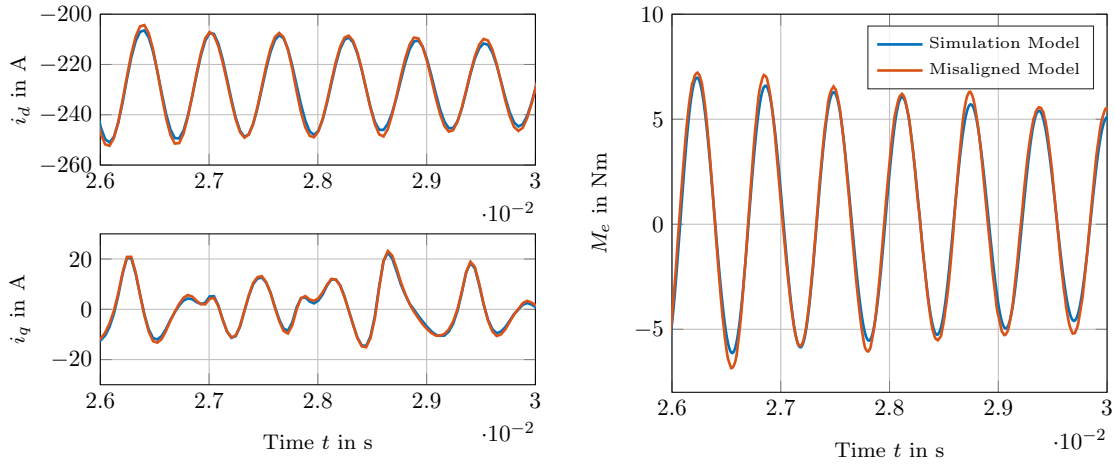

Figure 4.23.: Comparison of machine with transformation error and misaligned model by obtaining both current components and output torque with considered eddy current sensor error.

It shows, that the misaligned model has the capability to substitute the open loop field-oriented control with additional transformation error $\Delta\theta$. The current waveforms and calculated torque match the simulation results satisfactory; therefore the misaligned model can be used for further investigations on torque ripple caused by rotor position sensor errors.

4.5. System Description of Misaligned PMSM and Current Control with Compensation

As a next step, the misaligned system is integrated into the current control loop as done with the linearization of the general dq-model in Figure 4.19, which makes the

consideration of the compensation voltages

$$u_{d,comp} = -\omega L_q \bar{i}_q \tag{4.42}$$
$$u_{q,comp} = \omega(\Psi_{PM} + L_d \bar{i}_d) \tag{4.43}$$

necessary to model the machine with compensation from the current controller's point of view, where the superscripts for the rotating reference frame are omitted renewed. This leads to the slightly simpler structure of the voltage equations

$$L_d \frac{d\bar{i}_d}{dt} = -R_s \bar{i}_d - \big((L_d - L_q)\bar{i}_d + \Psi_{PM}\big)(\omega + \Delta\omega)\Delta\theta + L_d \bar{i}_q \Delta\omega + \bar{u}_d \tag{4.44}$$
$$L_q \frac{d\bar{i}_q}{dt} = -R_s \bar{i}_q + (L_d - L_q)\bar{i}_q(\omega + \Delta\omega)\Delta\theta - L_q \bar{i}_d \Delta\omega + \bar{u}_q \tag{4.45}$$
$$\frac{d\Delta\theta}{dt} = \Delta\omega \tag{4.46}$$

which are used for system linearization as performed in Section 4.3.2. The Jacobian matrices are used to compute a linearized LTI system with dynamic matrix $\mathbf{A}$ and input matrix $\mathbf{B}$

$$\mathbf{A} = \begin{bmatrix} -\frac{(\Delta\omega+\omega)(L_d-L_q)\Delta\theta - R_s}{L_d} & \Delta\omega & -\frac{(\Delta\omega+\omega)((L_d-L_q)i_{dR}+\Psi_{PM})}{L_d} \\ -\Delta\omega & \frac{(\Delta\omega+\omega)(L_d-L_q)\Delta\theta - R_s}{L_q} & \frac{(\Delta\omega+\omega)(L_d-L_q)i_{qR}}{L_q} \\ 0 & 0 & 0 \end{bmatrix}$$
$$\mathbf{B} = \begin{bmatrix} \frac{1}{L_d} & 0 & \frac{(L_q i_{dR} - L_d i_{dR} - \Psi_{PM})\Delta\theta + L_d i_{qR}}{L_d} \\ 0 & \frac{1}{L_q} & \frac{-(\Delta\theta i_{qR} + i_{dR})L_q + L_d \Delta\theta i_{qR}}{L_q} \\ 0 & 0 & 1 \end{bmatrix}$$

for i_{dR}, i_{dR} determined by the control strategy. With the choice of $\Delta\omega_R = 0$ and $\Delta\theta_R = 0$ as equilibrium points and the disturbed currents as outputs, the system matrices simplify themselves into

$$\mathbf{A} = \begin{bmatrix} -\frac{R_s}{L_d} & 0 & -\omega\frac{(Ld-Lq)i_{dR}+\Psi_{PM}}{L_d} \\ 0 & -\frac{R_s}{L_q} & -\omega\frac{(Ld-Lq)i_{qR}}{L_q} \\ 0 & 0 & 0 \end{bmatrix} \quad \mathbf{B} = \begin{bmatrix} \frac{1}{L_d} & 0 & i_{qR} \\ 0 & \frac{1}{L_q} & -i_{dR} \\ 0 & 0 & 1 \end{bmatrix}$$

and following output and feedforward system matrices

$$\mathbf{C} = \begin{bmatrix} 1 & 0 & 0 \\ 0 & 1 & 0 \end{bmatrix} \quad \mathbf{D} = \begin{bmatrix} 0 & 0 & 0 \\ 0 & 0 & 0 \end{bmatrix}$$

For obtaining the closed loop system with current control, the system representation with transfer functions is beneficial. This leads to the transfer function matrix

$$\mathbf{G}(s) = \begin{bmatrix} \frac{1}{sL_d+R_s} & 0 & \frac{sL_d i_{qR}+((L_q-L_d)i_{dR}-\Psi_{Pm})\omega}{s(L_d s+R_s)} \\ 0 & \frac{1}{sL_q+R_s} & \frac{sL_q i_{dR}-(L_q-L_d)i_{qR}\omega}{s(L_q s+R_s)} \end{bmatrix} \tag{4.47}$$

This matrix contains the electric machine's stator dynamics in the first diagonal and in the right column the influence from $\Delta\omega$ to control currents $\bar{i}_d$ and $\bar{i}_q$. In analogy to Figure 4.19, the complete current control system with sensor error as disturbance input is then substituted as shown in Figure 4.24.

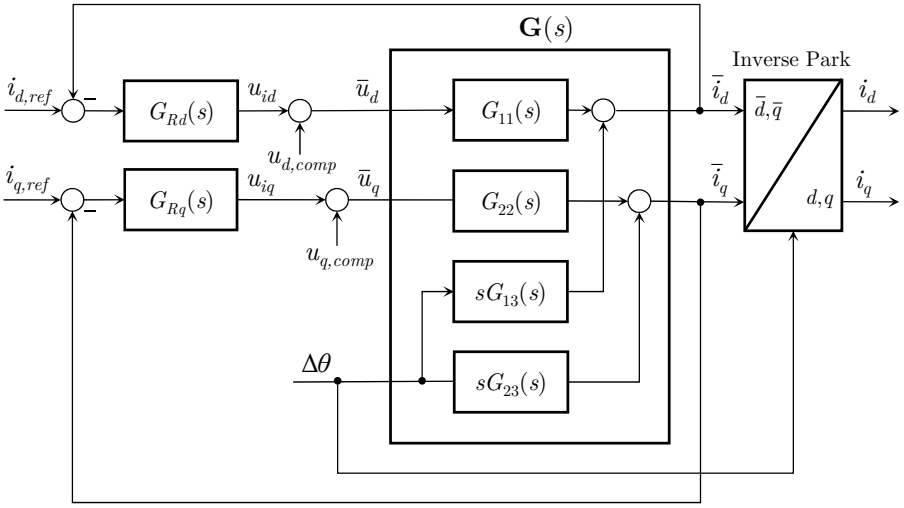

Figure 4.24.: Current control loop with linearized misaligned model and controlled currents $\bar{i}_d$ and $\bar{i}_q$ as outputs. Machine currents i_d and i_q are calculated afterwards with inverse Park transformation.

Maintaining the sensor error $\Delta\theta$ as input is considered by a multiplication of s within $G_{13}(s)$ and $G_{23}(s)$ and leads to following disturbance transfer functions

$$S_{\Delta\theta i_d}(s) = \frac{\bar{i}_d(s)}{\Delta\theta(s)} = \frac{sG_{13}(s)}{1+G_{Rd}(s)G_{11}(s)} \tag{4.48}$$

$$S_{\Delta\theta i_q}(s) = \frac{\bar{i}_q(s)}{\Delta\theta(s)} = \frac{sG_{23}(s)}{1+G_{Rq}(s)G_{22}(s)} \tag{4.49}$$

These disturbance transfer functions allow to calculate the current distortions of $\bar{i}_d$ and $\bar{i}_q$ caused by the rotor position error $\Delta\theta$ as shown in Figure 4.25.

Afterwards, an inverse Park transformation is performed to calculate the machine currents i_d respectively i_q and corresponding torque. It shows that the results of both current components match the simulation results better than the previous methods. Due to the

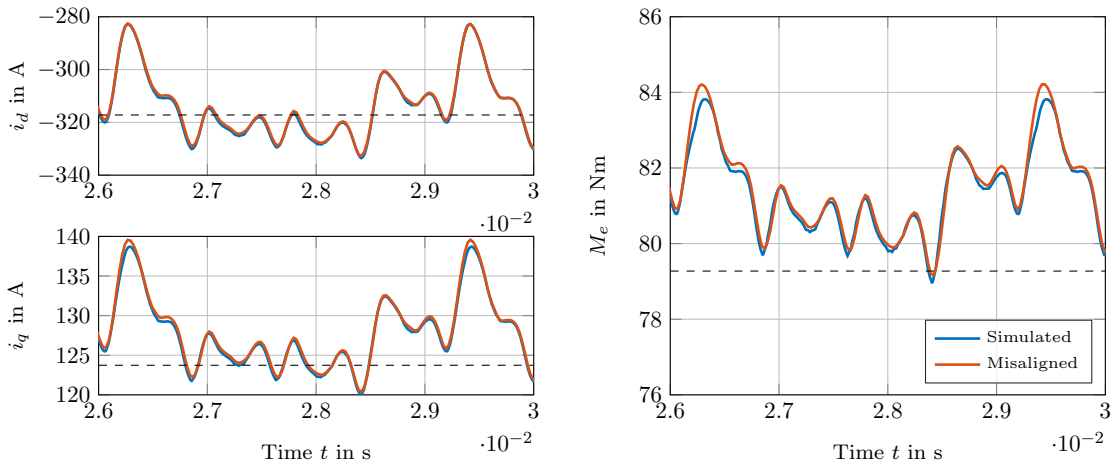

Figure 4.25.: Currents and torque situation in operation point $M_e = 79.27$ Nm and $n = 19099$ rpm and consideration of eddy current sensor error signal.

non-linearity of the torque equation it is mandatory that both current components are calculated satisfactory to receive accurate results regarding torque ripple calculations. Figure 4.26 shows the comparison of all investigated methods under consideration of a second eddy current sensor error behaviour at a different operating point.

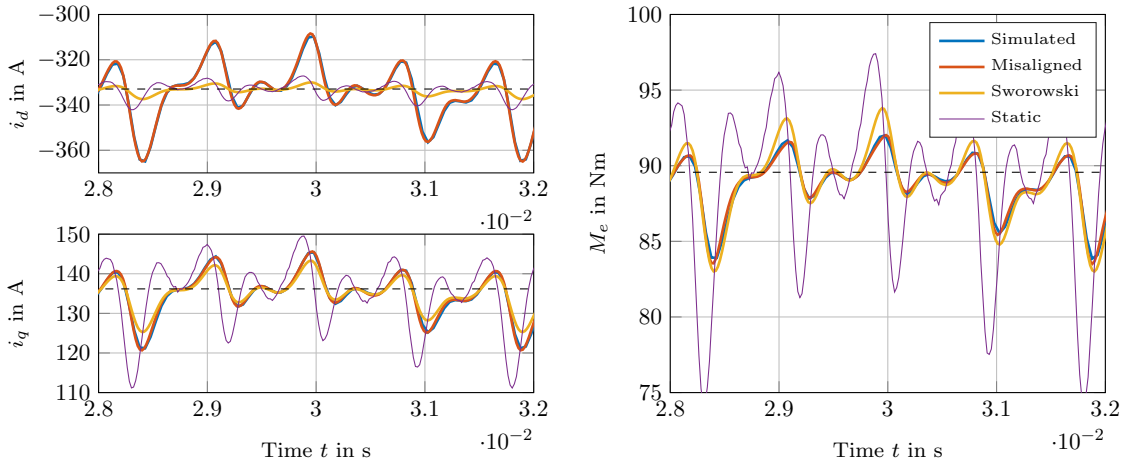

Figure 4.26.: Currents and torque in a different operating point $M_e = 89.57$ Nm and $n = 17189$ rpm with different eddy current sensor error signal.

It is visible, that the proposed method works for various error signals and different operating points of the electric machine and gives more accurate results compared to Sworowski's method. Figure 4.27 shows a comparison for the exemplary end-of-shaft, eddy current and resolver sensor error signals introduced in Figure 4.1.

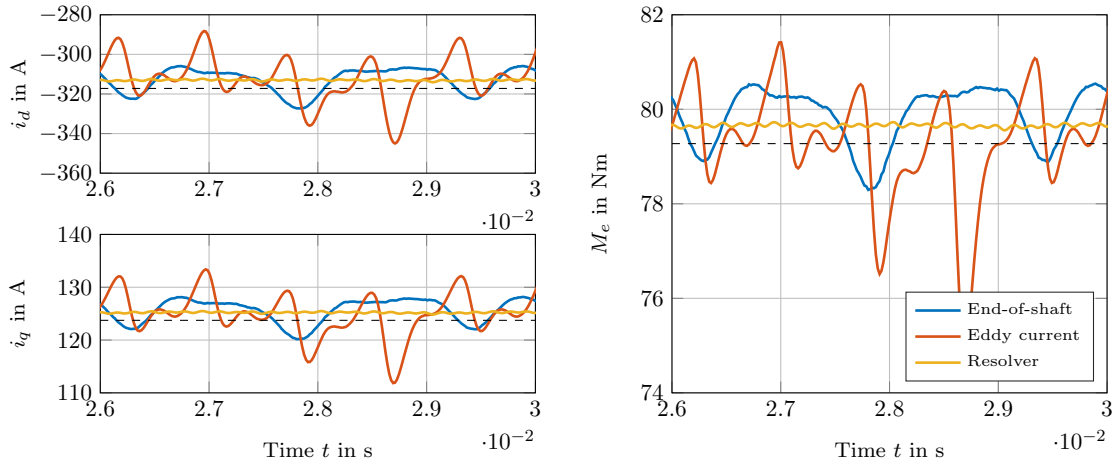

Figure 4.27.: Currents and torque situation in operation point $M_e = 79.27$ Nm and $n = 19099$ rpm for different sensor error signals.

Due to the precise rotor position measurement capability of the resolver, current and torque disturbances are very small and can be neglected in this specific case. But in contrast, the end-of-shaft and eddy current sensor types do produce a significant waviness in currents and torque.

4.6. Alternative Approach for Rotor Position Measurement Error and PMSM in Misaligned Reference Frame

This method represents the most general approach for describing the PMSM and Park transformations under consideration of a position sensor error signal and corresponds to a mathematical description of the substitute model depicted in Figure 4.22. The misaligned voltages $\bar{u}_{d,q}$ and currents $\bar{i}_{d,q}$ are related to the machine voltages $u_{d,q}$ and currents $i_{d,q}$ as followed

$$\bar{\mathbf{i}}_{d,q} = \begin{bmatrix} \bar{i}_d \\ \bar{i}_q \end{bmatrix} = \begin{bmatrix} \cos\Delta\theta & \sin\Delta\theta \\ -\sin\Delta\theta & \cos\Delta\theta \end{bmatrix} \begin{bmatrix} i_d \\ i_q \end{bmatrix} = \mathbf{R}^{-1}(\Delta\theta)\mathbf{i}_{d,q} \Rightarrow \mathbf{i}_{d,q} = \mathbf{R}(\Delta\theta)\bar{\mathbf{i}}_{d,q}$$

$$\mathbf{u}_{d,q} = \begin{bmatrix} u_d \\ u_q \end{bmatrix} = \begin{bmatrix} \cos\Delta\theta & -\sin\Delta\theta \\ \sin\Delta\theta & \cos\Delta\theta \end{bmatrix} \begin{bmatrix} \bar{u}_d \\ \bar{u}_q \end{bmatrix} = \mathbf{R}(\Delta\theta)\bar{\mathbf{u}}_{d,q}$$

Using this transformation within the voltage differential Equation 4.23 in matrix form and applying the transformation matrix $\mathbf{R}$ leads to

$$\frac{d}{dt}\left(\mathbf{R}\bar{\mathbf{i}}_{d,q}\right) = \begin{bmatrix} -\frac{R_s}{L_d} & \omega\frac{L_q}{L_d} \\ -\omega\frac{L_d}{L_q} & -\frac{R_s}{L_q} \end{bmatrix} \mathbf{R}\bar{\mathbf{i}}_{d,q} - \frac{\omega\Psi_{PM}}{L_q}\begin{bmatrix} 0 \\ 1 \end{bmatrix} + \begin{bmatrix} \frac{1}{L_d} & 0 \\ 0 & \frac{1}{L_q} \end{bmatrix} \mathbf{R}\bar{\mathbf{u}}_{d,q}$$

Consideration of

$$\mathbf{R}^{-1} = \begin{bmatrix} \cos\Delta\theta & \sin\Delta\theta \\ -\sin\Delta\theta & \cos\Delta\theta \end{bmatrix}$$
$$\frac{d}{dt}\mathbf{R} = \begin{bmatrix} -\sin\Delta\theta & -\cos\Delta\theta \\ \cos\Delta\theta & -\sin\Delta\theta \end{bmatrix} \underbrace{\frac{d\Delta\theta}{dt}}_{\Delta\omega}$$

gives

$$\frac{d}{dt}\mathbf{R}\bar{\mathbf{i}}_{d,q} + \mathbf{R}\frac{d}{dt}\bar{\mathbf{i}}_{d,q} = \begin{bmatrix} -\frac{R_s}{L_d} & \omega\frac{L_q}{L_d} \\ -\omega\frac{L_d}{L_q} & -\frac{R_s}{L_q} \end{bmatrix} \mathbf{R}\bar{\mathbf{i}}_{d,q} - \frac{\omega\Psi_{PM}}{L_q}\begin{bmatrix} 0 \\ 1 \end{bmatrix} + \begin{bmatrix} \frac{1}{L_d} & 0 \\ 0 & \frac{1}{L_q} \end{bmatrix} \mathbf{R}\bar{\mathbf{u}}_{d,q}$$

which can be expressed as a first order system of ordinary differential equations

$$\frac{d}{dt}\bar{\mathbf{i}}_{d,q} = \mathbf{R}^{-1}\begin{bmatrix} -\frac{R_s}{L_d} & \omega\frac{L_q}{L_d} \\ -\omega\frac{L_d}{L_q} & -\frac{R_s}{L_q} \end{bmatrix} \mathbf{R}\bar{\mathbf{i}}_{d,q} - \mathbf{R}^{-1}\frac{d}{dt}\mathbf{R}\bar{\mathbf{i}}_{d,q} - \mathbf{R}^{-1}\frac{\omega\Psi_{PM}}{L_q}\begin{bmatrix} 0 \\ 1 \end{bmatrix} + \mathbf{R}^{-1}\begin{bmatrix} \frac{1}{L_d} & 0 \\ 0 & \frac{1}{L_q} \end{bmatrix} \mathbf{R}\bar{\mathbf{u}}_{d,q}$$

This system leads to extensive equations for the IPMSM if separately written as

$$\begin{aligned} \frac{d\bar{i}_d}{dt} = \frac{1}{L_d L_q}\Big[& \left(R_s(L_d - L_q)\cos^2\Delta\theta - \omega(L_d^2 - L_q^2)\sin\Delta\theta\cos\Delta\theta - L_d R_s\right)\bar{i}_d \\ & + \left(\omega(L_q^2 - L_d^2)\cos^2\Delta\theta - R_s(L_d - L_q)\sin\Delta\theta\cos\Delta\theta + L_d^2\omega + L_d L_q\Delta\omega\right)\bar{i}_q \\ & + \left((L_q - L_d)\cos^2\Delta\theta + L_d\right)\bar{u}_d + (L_d - L_q)\cos\Delta\theta\sin\Delta\theta\bar{u}_q - \omega L_q\Psi_{PM}\sin\Delta\theta\Big] \end{aligned}$$

$$\begin{aligned} \frac{d\bar{i}_q}{dt} = \frac{1}{L_d L_q}\Big[& \left(\omega(L_q^2 - L_d^2)\cos^2\Delta\theta - R_s(L_d - L_q)\sin\Delta\theta\cos\Delta\theta - L_d L_q\Delta\omega - L_q^2\omega\right)\bar{i}_d \\ & + \left(\omega(L_d^2 - L_q^2)\sin\Delta\theta\cos\Delta\theta - R_s(L_d - L_q)\cos^2\Delta\theta - L_q R_s\right)\bar{i}_q \\ & + (L_d - L_q)\cos\Delta\theta\sin\Delta\theta\bar{u}_d + \left((L_d - L_q)\cos^2\Delta\theta + L_q\right)\bar{u}_q - \omega L_d\Psi_{PM}\cos\Delta\theta\Big] \end{aligned}$$

and to

$$\frac{d\bar{i}_d}{dt} = \frac{1}{L_s}\Big[- R_s\bar{i}_d + L_s(\omega + \Delta\omega)\bar{i}_q + \bar{u}_d + \omega\Psi_{PM}\sin\Delta\theta\Big]$$
$$\frac{d\bar{i}_q}{dt} = \frac{1}{L_s}\Big[- L_s(\omega + \Delta\omega)\bar{i}_d - R_s\bar{i}_q + \bar{u}_q + \omega\Psi_{PM}\cos\Delta\theta\Big]$$

for the simpler SPMSM case. Applying the compensation voltages, small angle error approximations and the relation between $\Delta\theta$ and $\Delta\omega$ as in the former section gives

$$\begin{aligned}
\frac{d\bar{i}_d}{dt} &= \frac{1}{L_d L_q}\Big[\big(-L_q(\Delta\theta(L_d-L_q)\omega+R_s)\big)\bar{i}_d+\big(\Delta\omega L_q L_d-\Delta\theta R_s(L_d-L_q)\big)\bar{i}_q \\
&\quad + L_q\bar{u}_d+(L_d-L_q)\Delta\theta\bar{u}_q-\omega L_d\Psi_{PM}\Delta\theta \\
\frac{d\bar{i}_q}{dt} &= \frac{1}{L_d L_q}\Big[\big(-\Delta\theta R_s(L_d-L_q)-\Delta\omega L_q L_d\big)\bar{i}_d+\big(L_d(\Delta\theta(L_d-L_q)\omega-R_s)\big)\bar{i}_q \\
&\quad + (L_d-L_q)\Delta\theta\bar{u}_d+L_d\bar{u}_q \\
\frac{d\Delta\theta}{dt} &= \Delta\omega
\end{aligned}$$

This system of differential equations in the form of $\dot{\mathbf{x}}=\mathbf{f}(\mathbf{x},\mathbf{u})$ is linearized for the same operating points as in the previous misaligned example, namely i_{dR}, i_{qR} determined by the control strategy. This leads, with calculation of the Jacobian matrices, to following system parameters $\mathbf{A}$ and $\mathbf{B}$

$$\mathbf{A}=\begin{bmatrix} -\frac{\Delta\theta(L_d-L_q)\omega+R_s}{L_d} & \frac{\Delta\omega L_q L_d-\Delta\theta R_s(L_d-L_q)}{L_d L_q} & -\omega\frac{(Ld-Lq)i_{dR}+\Psi_{PM}}{L_d} \\ -\frac{\Delta\omega L_q L_d+\Delta\theta R_s(L_d-L_q)}{L_d L_q} & \frac{\Delta\theta(L_d-L_q)\omega-R_s}{L_q} & \omega\frac{(Ld-Lq)i_{qR}}{L_q} \\ 0 & 0 & 0 \end{bmatrix}$$

$$\mathbf{B}=\begin{bmatrix} \frac{1}{L_d} & \frac{(L_d-L_q)\Delta\theta}{L_d L_q} & i_{qR} \\ \frac{(L_d-L_q)\Delta\theta}{L_d L_q} & \frac{1}{L_q} & -i_{dR} \\ 0 & 0 & 1 \end{bmatrix}$$

With the same choice of $\Delta\omega_R=0$, $\Delta\theta_R=0$ as equilibrium points and disturbed currents as outputs, the system matrices simplify themselves into

$$\mathbf{A}=\begin{bmatrix} -\frac{R_s}{L_d} & 0 & -\omega\frac{(Ld-Lq)i_{dR}+\Psi_{PM}}{L_d} \\ 0 & -\frac{R_s}{L_q} & \omega\frac{(Ld-Lq)i_{qR}}{L_q} \\ 0 & 0 & 0 \end{bmatrix} \quad \mathbf{B}=\begin{bmatrix} \frac{1}{L_d} & 0 & i_{qR} \\ 0 & \frac{1}{L_q} & -i_{dR} \\ 0 & 0 & 1 \end{bmatrix}$$

$$\mathbf{C}=\begin{bmatrix} 1 & 0 & 0 \\ 0 & 1 & 0 \end{bmatrix} \qquad \mathbf{D}=\begin{bmatrix} 0 & 0 & 0 \\ 0 & 0 & 0 \end{bmatrix}$$

which are exactly the same as by linearizing the misaligned model in the former chapter. Note that this does not mean, that the misaligned model and the alternative approach have the same voltage equations, but applying the linearization method on both models leads to the same substitute LTI system description. Therefore, it makes no difference by obtaining the control system within linear system theory, if the misaligned model or the complete alternative formulation with transformation error within the electric dynamics is used as origin of the linearization process.

4.7. Control Parameter Sensitivity

As mentioned in Section 4.2.4, current controllers are usually designed with the modulus optimum rule. This rule is applied to determine the control parameters V_R and T_N for the d- and q-axis current loop. The time constant T_N is used to cancel out the pole of the plant dynamics, therefore this parameter is kept constant for this parameter sensitivity study. Writing the disturbance transfer functions from Equations 4.48 and 4.49, which describe the impact from rotor sensor errors to d- and q-currents, parametrized by the controller gains leads to

$$S_{\Delta\theta i_d}(s) = \frac{\bar{i}_d(s)}{\Delta\theta(s)} = \frac{sG_{13}(s)}{1 + G_{Rd}(s)G_{11}(s)} = \frac{s^2 L_d^2 i_{qR} + s\omega L_d\big((L_q - L_d)i_{dR} - \Psi_{PM}\big)}{(sL_d + R_s)(sL_d + V_{Rd})}$$

$$S_{\Delta\theta i_q}(s) = \frac{\bar{i}_q(s)}{\Delta\theta(s)} = \frac{sG_{23}(s)}{1 + G_{Rq}(s)G_{22}(s)} = \frac{s^2 L_q^2 i_{dR} + s\omega L_q i_{qR}(L_q - L_d)}{(sL_q + R_s)(sL_q + V_{Rq})}$$

Three parameter variations are performed regarding the control gains V_{Rd} and V_{Rq}, where both parameters are scaled simultaneously and the effect on current and torque ripple is investigated. Figure 4.28 shows the results for the default operating point, eddy current sensor error and varied current controller gains $V_{Rd,q}$.

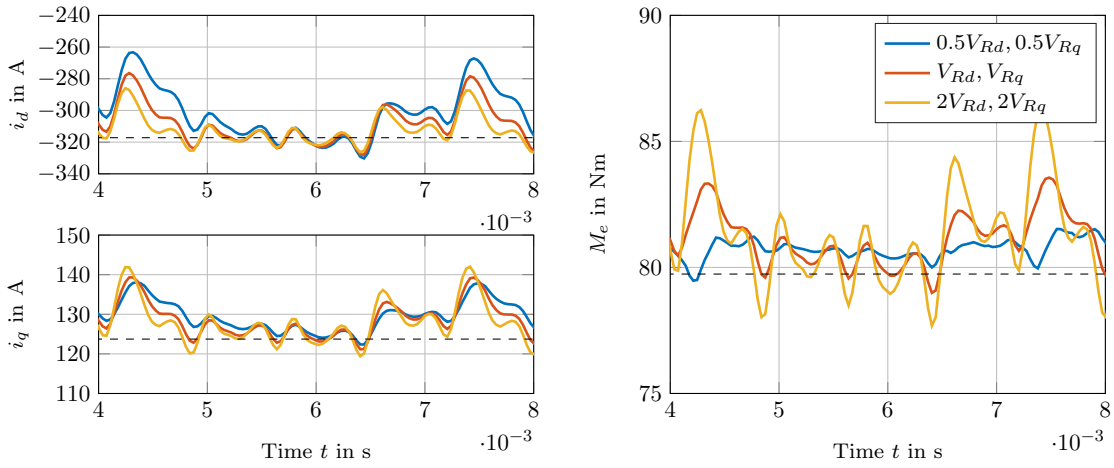

Figure 4.28.: Stationary currents and torque at operating point M_e = 79.27 Nm and n = 19099 rpm for different current control gains.

Although the current oscillations on the left do not seem to decrease with smaller controller gain, the resulting torque ripple on the right is significantly reduced. This is caused by the non-linear relationship of the torque equations and machine currents. It shows, that reducing the current controller gain V_{Rd} and V_{Rq} provides an effective possibility to reduce the remaining stationary torque ripple. One drawback of this restriction is - as expected - that the dynamics of the current control loop and therefore of the

torque build-up gets decreased simultaneously. Figure 4.29 shows the torque command step responses for both current loops and the transient torque behaviour for different control gains.

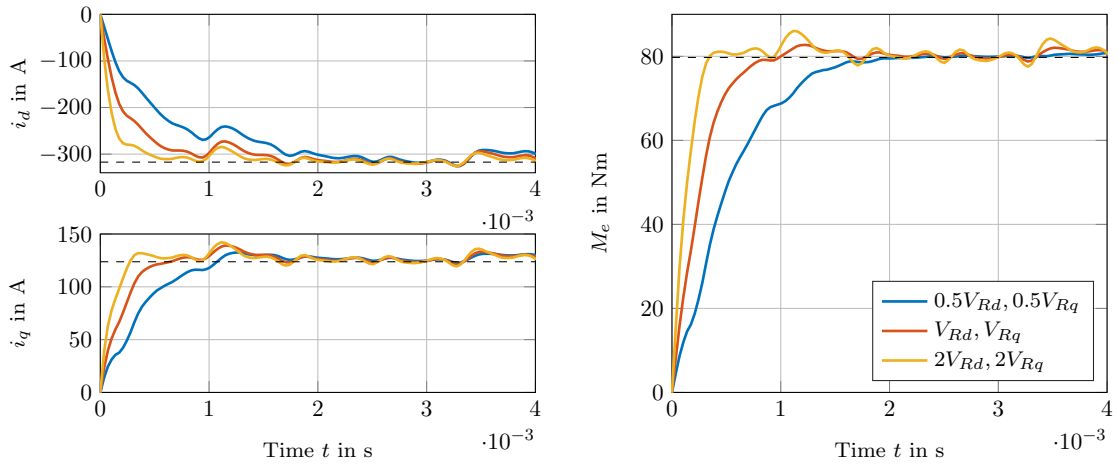

Figure 4.29.: Step responses of currents and torque at operating point $M_e = 79.27$ Nm and $n = 19099$ rpm for different current control gains.

This investigations can be summarized: if the high torque dynamics recoverable with the modulus optimum are not necessary to fulfill within the application, reduction of the current control gain can be an effective mechanism to reduce torque ripple induced by rotor position sensor errors.

4.8. Influence of Sensor Parameter Variations

In Section 3.7 at the end of Chapter 3, parametrizable look-up tables were introduced to map the sensor error characteristic over one mechanical period as a function of the varied parameters on the test bench. These multidimensional matrices are used now in this section to obtain the impact of sensor parameter variations on the currents and torque of the electric machine. To demonstrate the applicability, ten randomly distributed validation points are used and the disturbance transfer functions of the former subsection are utilized. Figure 4.30 shows, how different sensor parameter variations of an end-of-shaft sensor influence the controlled torque and currents.

In this particular case only mechanical parameter variations are considered, whereas temperature, speed and supply voltage are kept constant. The black solid torque line in the torque results represents the sensor error impact in its origin, if no mechanical misalignment is present. By applying mechanical parameter variations, additional sensor errors occur and the impact of the investigated parameter set is depicted in various colors. Although this specific end-of-shaft sensor measures the rotor position quite accurate

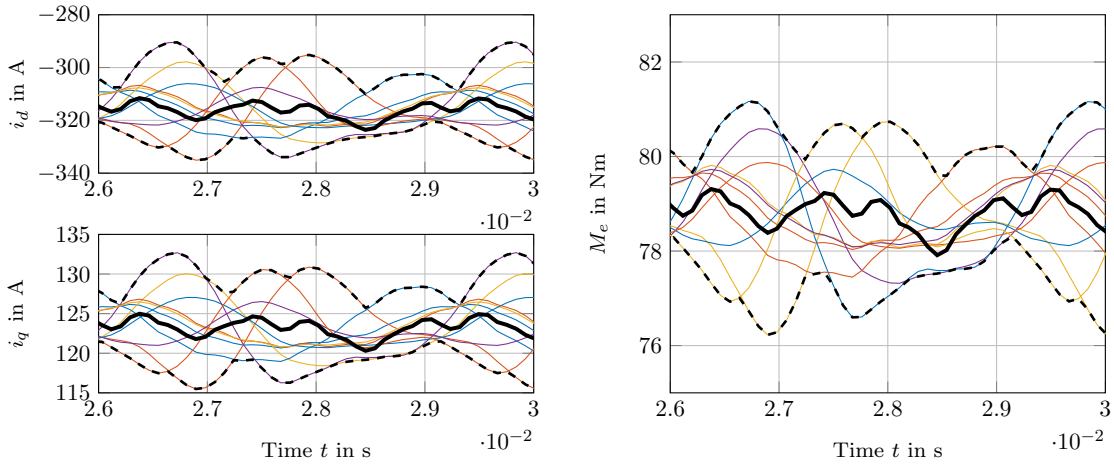

Figure 4.30.: End-of-shaft sensor parameter variation and its influence on currents and torque at operating point $M_e = 79.27$ Nm and $n = 19099$ rpm.

($|\Delta\theta| < 1°$), it has a certain sensitive regarding mechanical displacement. The dashed black lines provide a graphical limit to rate the range of current and torque disturbances for the investigated parameter variations. Figure 4.31 shows the same investigations for a different end-of-shaft sensor type, which has a stronger dependency on mechanical misalignment and produces therefore a significant higher current and torque waviness.

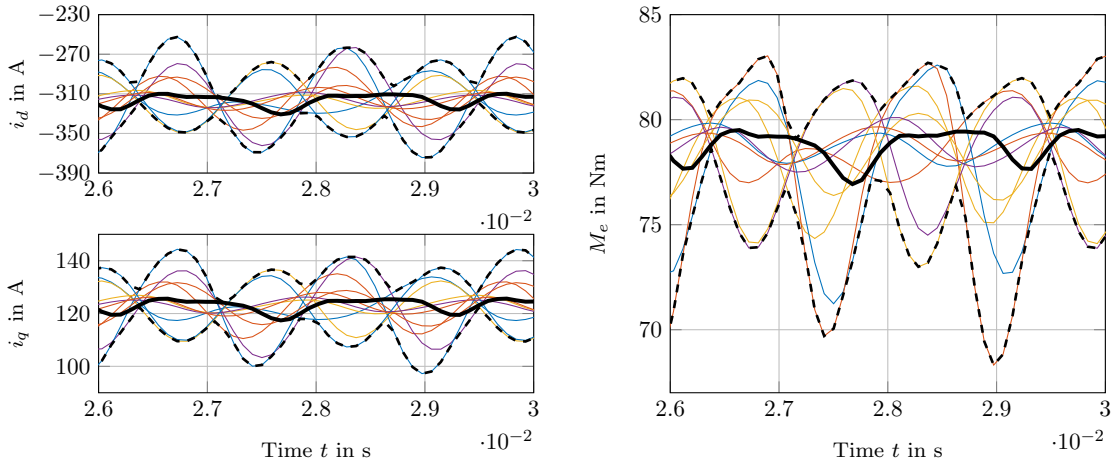

Figure 4.31.: Different end-of-shaft sensor parameter variation and its influence on currents and torque at operating point $M_e = 79.27$ Nm and $n = 19099$ rpm.

The presented method allows to combine the test bench measurements with the mathematical description of the sensor error regarding the field-oriented controlled PMSM to rate its impact on currents and torque. With this approach, critical operating points of

the electric machine can be investigated in more detail and the necessary sensor parameter accuracy to maintain specified torque requirements can be defined.

4.9. Consideration of Power Electronics Delay Time

As introduced in Section 4.2.4, the time delay of the power electronics is considered in the current control design, but neglected for investigations regarding torque quality. Figure 4.24 shows the substitute model with the linearized MIMO system of the PMSM, current control and inverse park transformation for computation of machine currents. Applying constant compensation voltages leads to voltage differential equations as in Equations 4.44 and 4.45 and provide decoupled current control loops. This means, that the cross-coupling transfer functions $G_{12}(s)$ and $G_{21}(s)$ are zero, which simplifies the calculation of the disturbance transfer functions $S_{\Delta\theta i_d}(s)$ and $S_{\Delta\theta i_q}(s)$ significantly. A first approach for considering the approximated inverter transfer function $G_{inv}(s)$ from Equation 4.30 is, to add it directly after the current control transfer functions $G_{Rd,q}(s)$. But this is not sufficient, as the compensation voltages $u_{dq,comp}$ are also influenced by the delay time. In this way, these voltage terms have to be described as dynamic systems and complete decoupling of the current control loops is not fulfilled any more. Therefore, Equations 4.39 - 4.41 have to be extended with the compensation voltage dynamics from Equations 4.42 and 4.43

$$T_t \frac{du_{d,comp}}{dt} = -u_{d,comp} - \omega L_q i_q$$
$$T_t \frac{du_{q,comp}}{dt} = -u_{q,comp} + \omega (L_d i_d + \Psi_{PM})$$

determined by the inverter transfer function $G_{inv}(s)$. Afterwards, the procedure remains the same by linearizing the system of ordinary differential equations for the same equilibrium points, which leads to following 5^{th} order system

$$\mathbf{A} = \begin{bmatrix} -\frac{R_s}{L_d} & \omega\frac{L_q}{L_d} & \frac{1}{L_d} & 0 & -\omega\frac{(L_d-L_q)i_{dR}+\Psi_{PM}}{L_d} \\ -\omega\frac{L_d}{L_q} & -\frac{R_s}{L_q} & 0 & \frac{1}{L_q} & -\omega\frac{(L_d-L_q)i_{qR}}{L_q} \\ 0 & -\omega\frac{L_q}{T_t} & -\frac{1}{T_t} & 0 & 0 \\ \omega\frac{L_d}{T_t} & 0 & 0 & -\frac{1}{T_t} & 0 \\ 0 & 0 & 0 & 0 & 0 \end{bmatrix} \quad \mathbf{B} = \begin{bmatrix} \frac{1}{L_d} & 0 & i_{qR} \\ 0 & \frac{1}{L_q} & -i_{dR} \\ 0 & 0 & 0 \\ 0 & 0 & 0 \\ 0 & 0 & 1 \end{bmatrix}$$

$$\mathbf{C} = \begin{bmatrix} 1 & 0 & 0 & 0 & 0 \\ 0 & 1 & 0 & 0 & 0 \end{bmatrix} \qquad \mathbf{D} = \begin{bmatrix} 0 & 0 & 0 \\ 0 & 0 & 0 \end{bmatrix}$$

with input and output signals as in the former chapter. Computation of the transfer matrix of this system via

$$\mathbf{G}(s) = \mathbf{C}(s\mathbf{E} - \mathbf{A})^{-1}\mathbf{B}$$

shows, that the cross coupling transfer functions $G_{12}(s)$ and $G_{21}(s)$ do not vanish. This means, that the compensation is only fulfilled for stationary scenarios, which is not the case if arbitrary shaped rotor position sensor errors are present. Generally, the system order gets drastically extended by considering the inverter dynamics in the transfer function matrix $\mathbf{G}(s)$, where the specific result of its elements are not displayed. Setting the inverter delay time T_t to zero degenerates the model into the same form as in Equation 4.47. Figure 4.32 shows the substitute model with current control and approximated inverter transfer function. The necessary derivative of the sensor error is considered in the disturbance transfer functions $G_{13}(s)$ and $G_{23}(s)$.

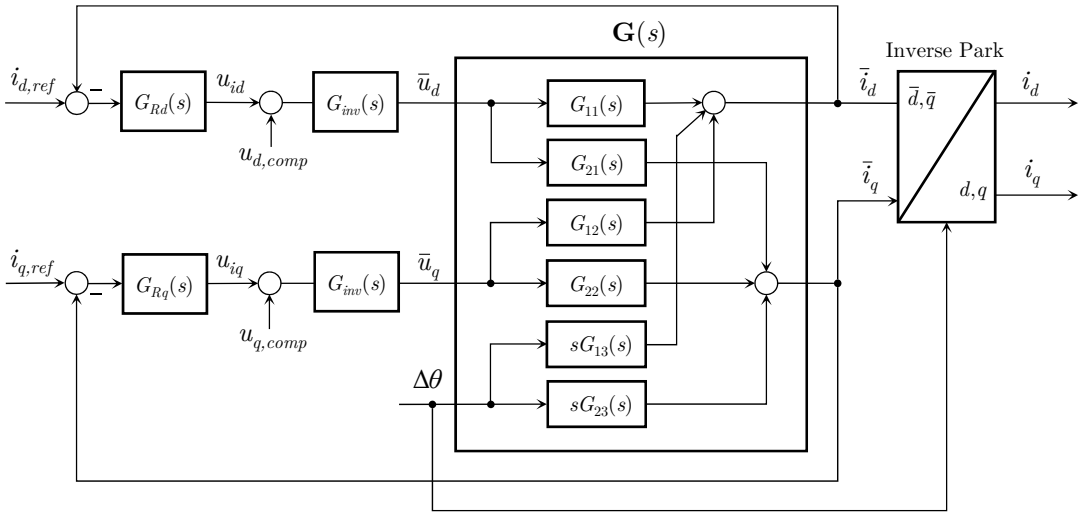

Figure 4.32.: Substitute model with non-ideal decoupling of current loops due to present inverter delay transfer function.

Computation of the disturbance transfer functions from sensor error to d and q- current components is also more elaborated in this case due to the meshed structure of above MIMO system. Introducing the abbreviations for the d-current loop

$$\bar{G}_{21}(s) = -\frac{G_{21}(s)G_{Rq}(s)G_{inv}(s)G_{12}(s)}{1 + G_{Rq}(s)G_{inv}(s)G_{22}(s)}$$
$$\bar{G}_{23}(s) = -\frac{G_{23}(s)G_{Rq}(s)G_{inv}(s)G_{12}(s)}{1 + G_{Rq}(s)G_{inv}(s)G_{22}(s)}$$

and analogous in q-direction

$$\bar{G}_{12}(s) = -\frac{G_{12}(s)G_{Rd}(s)G_{inv}(s)G_{21}(s)}{1 + G_{Rd}(s)G_{inv}(s)G_{11}(s)}$$
$$\bar{G}_{13}(s) = -\frac{G_{13}(s)G_{Rd}(s)G_{inv}(s)G_{21}(s)}{1 + G_{Rd}(s)G_{inv}(s)G_{11}(s)}$$

leads to following disturbance transfer functions

$$S_{\Delta\theta i_d}(s) = \frac{s\big(G_{13}(s) + \bar{G}_{23}(s)\big)}{1 + G_{Rd}(s)G_{inv}(s)\big(G_{11}(s) + \bar{G}_{21}(s)\big)} \tag{4.50}$$

$$S_{\Delta\theta i_q}(s) = \frac{s\big(G_{23}(s) + \bar{G}_{13}(s)\big)}{1 + G_{Rq}(s)G_{inv}(s)\big(G_{22}(s) + \bar{G}_{12}(s)\big)} \tag{4.51}$$

Note that the complexity and order of this transfer functions is significantly higher than without consideration of the power electronics delay time. As mentioned before, neglecting the delay implies $G_{12}(s)$ and $G_{21}(s) = 0$, which simplifies this disturbance transfer functions into the same form as in Equations 4.48 and 4.49. Figure 4.33 shows the results of current and torque ripple by considering the approximated inverter transfer function, where a delay time of $T_t = 100\ \mu s$ was used, which represents a common value for actual power electronics.

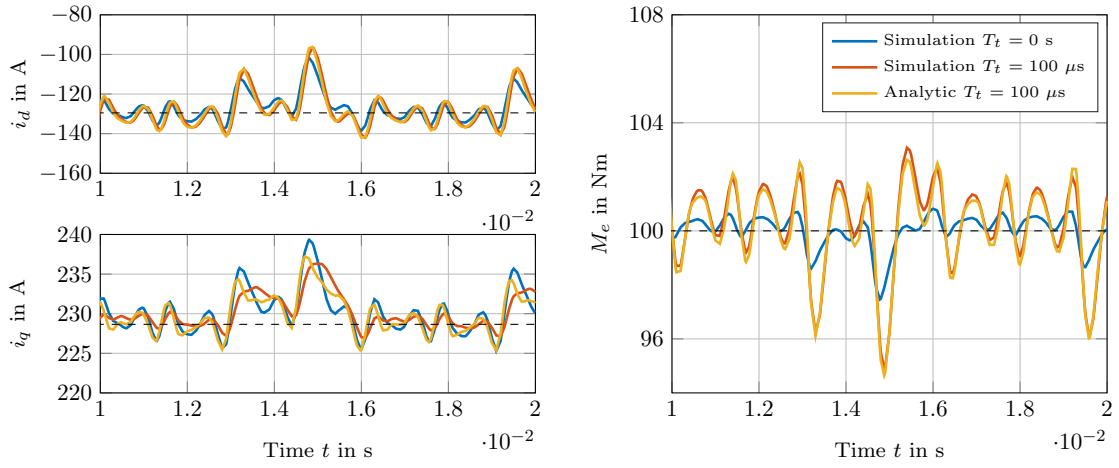

Figure 4.33.: Currents and torque in a different operating point $M_e = 100$ Nm and $n = 9549$ rpm with eddy current sensor.

It shows, that the inverter delay has a negative impact on the produced torque ripple, which gets considerably enlarged in this scenario. But the presented modified approach allows to consider the additional torque ripple caused by the power electronics delay time. Note that for higher speeds the deviations between simulation and analytic system description increases; therefore this method has a limited applicability. Additionally, the difference between approximated and real inverter transfer function simulation results increases with higher speed. A better approach would be to use a time discrete represenation of current controller [69] and electric machine [59], which allows an exact consideration of the inverter delay and investigations on its impact on control quality. Due to the additional complexity, this approach is not carried out in more detail here.

4.10. Control Strategies

This chapter has the aim to introduce the most common operating strategies for PMSM's and to investigate their torque ripple sensitivity caused by rotor position errors. For this purpose, the previous developed linearized system consisting of machine, current controller and rotor sensor error is utilized. Operating points of electric machines are determined by torque M_e and electrical speed ω_e. Obtaining the SPMSM torque equation

$$M_e = \frac{3}{2} p \Psi_{PM} i_q$$

shows, that the torque demand of the machine is directly controlled via i_q. As the d-component is not involved in this equation, the machine is usually controlled via $i_{d,ref} = 0$ in the base speed operating range. This method is called "Zero D-Axis Current" (ZDAC) or "$i_d = 0$" - control and provides the property of giving maximum torque with given stator current described by $I_s^2 = i_d^2 + i_q^2$. In contrast, for the IPMSM the torque equation

$$M_e = \frac{3}{2} p \big(\Psi_{PM} i_q + (L_d - L_q) i_d i_q \big)$$

is a function of both current components. The ZDAC method can also be applied, but then the additional reluctance torque of the IPMSM is not utilized. The basic idea for the IPMSM is to get the desired torque with the smallest stator current possible, which means that the stator current vector I_s has to be directed perpendicular to the iso-torque lines of the machine as shown in Figure 4.3. In this work, control strategies such as Maximum Torque per Ampere (MTPA), Maximum Torque per Voltage (MTPA), Maximum Power Control (MPC) and Loss Minimizing Control (LMC) are analyzed in terms of their sensitivity to rotor position sensor errors. In [70] and [71] additional control strategies are introduced, such as Unity Power Factor (UPF) and Constant Mutual Flux Linkage (CMFL) control, but they are not further considered in this work.

4.10.1. Maximum Torque per Ampere (MTPA) Control

Especially in vehicle traction motor applications, it is important to use the additional reluctance torque of IPMSM's. Therefore, both current components have to be controlled in such way, that the sum of electro-magnetic and reluctance torque is maximized. This strategy is called Maximum Torque per Ampere, which accords to the ZDAC-control for the SPMSM type. There are different approaches for calculating the corresponding d- and q- currents. One possibilty includes the formulation as an optimization problem with an objective function $f(i_d, i_q)$ [66]

$$\begin{aligned} \text{minimize } f(i_d, i_q) &= -\frac{3}{2} p \big(\Psi_{PM} i_q + (L_d - L_q) i_d i_q \big) \\ \text{subject to } c(i_d, i_q) &= \sqrt{I_s^2 - i_d^2 - i_q^2} \end{aligned}$$

which is minimized under consideration of an equality constraint $c(i_d, i_q)$. This can be formulated as a Lagrangian L in the form

$$L = -\frac{3}{2}p\big(\Psi_{PM} i_q + (L_d - L_q) i_d i_q\big) + \lambda\sqrt{I_s^2 - i_d^2 - i_q^2}$$

To find the minimum of the Lagrangian, the partial derivatives regarding i_d, i_q and λ

$$\frac{\partial L}{\partial i_d} = -\frac{3}{2}p(L_d - L_q) i_q - 2\lambda i_d \tag{4.52}$$

$$\frac{\partial L}{\partial i_q} = -\frac{3}{2}p\big(\Psi_{PM} + (L_d - L_q) i_d\big) - 2\lambda i_q \tag{4.53}$$

$$\frac{\partial L}{\partial \lambda} = I_s^2 - i_d^2 - i_q^2 \tag{4.54}$$

are set to zero, which gives for the Lagrangian multiplier λ from Equations 4.52 and 4.53

$$\lambda = -\frac{3p(L_d - L_q) i_q}{4 i_d}$$

$$\lambda = -\frac{3p(\Psi_{PM} + (L_d - L_q) i_d)}{4 i_q}$$

Elimination of the Lagrangian multiplier leads to the searched relation between i_d and i_q

$$i_{d\ 1,2} = -\frac{\Psi_{PM}}{2(L_d - L_q)} \pm \sqrt{\frac{\Psi_{PM}^2}{4(L_d - L_q)^2} + i_q^2}$$

where the proof of which solution represents a minimum is not carried out here. The meaningful solution solving this problem is the second one, which reads

$$i_d = -\frac{\Psi_{PM}}{2(L_d - L_q)} - \sqrt{\frac{\Psi_{PM}^2}{4(L_d - L_q)^2} + i_q^2} \tag{4.55}$$

An alternative expression is possible via current angle β and length of stator current I_s, where β is defined as the angle between the stator current vector I_s and the q-axis in the dq-plane. With $i_d = I_s \sin\beta$, the expression for the current angle as a function of stator current I_S can be written as [66]

$$\beta = \arcsin\left(\frac{\Psi_{PM} - \sqrt{\Psi_{PM}^2 + 8(L_d - L_q)^2 I_s^2}}{4(L_d - Lq) I_s}\right) \tag{4.56}$$

The sensor error influences directly the applied current angle β, which results in a disturbed current angle $\beta + \Delta\theta$ and therefore in a deviation of the desired iso torque line as depicted in Figure 4.3. This causes the investigated torque ripples, but due to the perpendicularity of current vector and iso torque lines, the resulting torque deviation is

usually not that significant in base speed operating range. Figure 4.34 shows the trajectory of the MTPA strategy within constant torque range and current distortions caused by rotor position errors for a torque-speed ramp scenario.

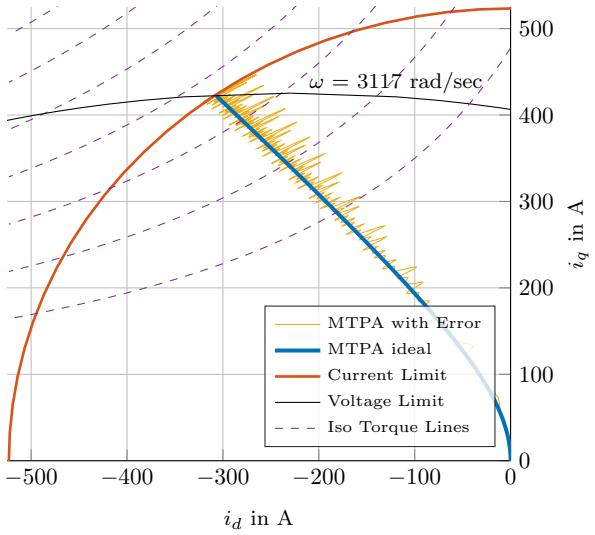

Figure 4.34.: MTPA strategy within base speed operating range and current trajectories influenced by position sensor error $\Delta\theta$.

The output torque is always restrained by the present current limit, which is determined by the maximum stator current I_{max}. No stationary operating points are possible outside the current limit circle. The exemplary electric machine has a rated operating point of $M_{max} = 260$ Nm at $\omega_1 = 3117$ rad/s (5950 rpm), which defines the electric speed where the voltage limit hits the intersection of current limit and MTPA trajectory. If the torque demand is lower than the maximum torque, the voltage limit occurs at higher speeds. The electric frequency ω_1, where the voltage limit is active for the first time, is calculated as

$$\omega_1 = \frac{U_{max}}{\sqrt{(L_d i_d + \Psi_{PM})^2 + (L_q i_q)^2}} \tag{4.57}$$

and follows from the stationary voltage equations with omitted stator resistance. Typically, an operating point is defined by torque and mechanical speed. Therefore it is beneficial to express the stator current distribution with torque demand M_{ref}. Insertion of Equation 4.55 into the IPMSM torque equation leads to

$$M_{ref} = \frac{3}{2} p \left(\Psi_{PM} i_q + \frac{1}{2} \big(- \Psi_{PM} - \sqrt{\Psi_{PM}^2 + 4(L_d - L_q)^2 i_q^2} \big) \right)$$

which results in a forth order polynomial in i_q

$$i_q^4 + \frac{2M_{ref}\Psi_{Pm}}{3p(L_d - L_q)^2} i_q - \frac{4M_{ref}^2}{9p^2(L_d - L_q)^2} = 0 \tag{4.58}$$

Roots computation of above polynomial gives the optimal q-current component i_q in the sense of MTPA and utilization of Equation 4.55 leads to the corresponding d-component i_d. In the next subsection it is discussed, how the speed of the electric drive can be increased above the rated speed.

4.10.2. Maximum Power Control (MPC)

If the electric machine reaches its rated speed, voltage and possibly current limits are present. To increase the mechanical speed of the electric drive, the induced voltage, respectively back-electromotive force (back-EMF) has to be reduced, which is done by applying a larger negative d-current i_d to decrease the stator flux linkage [66]. This operating strategy is called lower field weakening range or maximum power control. It can be formulated for active voltage limit by neglecting the stator resistance voltage drop as

$$\Psi_0^2 = \left(\frac{U_{max}}{\omega}\right)^2 = (L_d i_d + \Psi_{PM})^2 + (L_q i_q)^2 \tag{4.59}$$

which leads to following restriction for the d-current

$$i_d = \frac{\Psi_{PM}}{L_d} \pm \frac{1}{L_d}\sqrt{\left(\frac{U_{max}}{\omega}\right)^2 - (L_q i_q)^2} \tag{4.60}$$

Applying a more negative d-current ensures the whereabouts on the iso torque lines, which is only possible as long as the stator current restriction $i_d^2 + i_q^2 \leq I_{max}^2$ is fulfilled. The voltage limit restriction describes elliptic shaped permissible areas of i_d and i_q current combinations and shrinks with increasing speed. Inserting Equation 4.60 into the torque equation gives the dependency of q-current i_q as a function of torque demand and electrical speed

$$M_{ref} = \frac{3}{2}p\left(\Psi_{PM} i_q + \frac{(L_d - L_q)}{L_d}\Big(- \Psi_{PM} \pm \sqrt{\left(\frac{U_{max}}{\omega}\right)^2 - (L_q i_q)^2}\Big) i_q\right)$$

Solving this equations regarding the searched q-current component leads to following quartic polynomial

$$i_q^4 + p_2 i_q^2 + p_1 i_q + p_0 = 0$$

with coefficients

$$p_2 = \frac{\Psi_{PM}^2 L_q^2 - (L_d - L_q)^2 \frac{U_{max}^2}{\omega^2}}{L_q^2 (L_d - L_q)^2}$$
$$p_1 = -\frac{4 L_d \Psi_{PM} M_{ref}}{3 L_q p (L_d - L_q)^2}$$
$$p_0 = \frac{4 L_d^2 M_{ref}^2}{9 L_q^2 p^2 (L_d - L_q)^2}$$

Figure 4.35 shows the transition from the MTPA strategy into the lower field weakening region by increasing the negative d-current component.

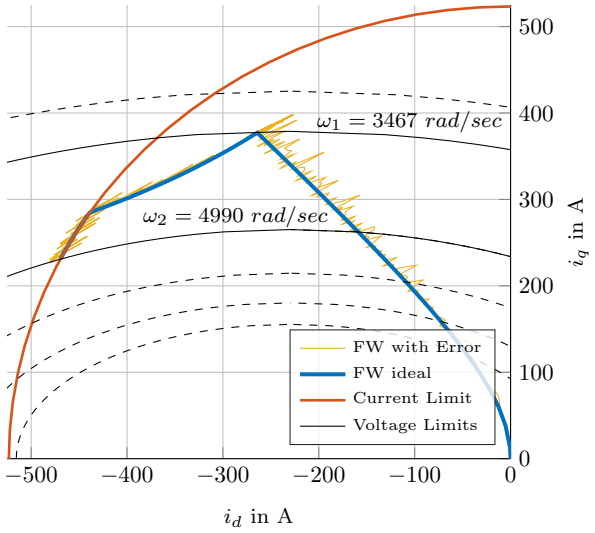

Figure 4.35.: MTPA and MPC field weakening strategy along the iso torque lines with present voltage limits within allowable current limit.

In this scenario, the machine is not operated with the maximum torque at rated speed, instead a torque demand of 220 Nm is applied, which results with an active voltage limit at a higher speed $\omega_1 = 3467$ rad/s (6621 rpm). Therefore, an additional d-current is applied to move further along the iso torque lines to maintain the desired torque. Note that the application of this method is limited by the still present current limit I_{max}, meaning that after the intersection of the trajectory with the current limit only movement along the current limit circle is possible. The shrinking area of the voltage ellipses by increased speed further restricts the continued existence on the current limit circle, until the electric speed reaches $\omega_2 = 4990$ rad/s (9530 rpm). Therefore in a last step, the strategy has to be changed once more to stay within the ellipses defined by the active voltage limit to reach the maximum speed of the electric machine.

4.10.3. Maximum Torque per Voltage (MTPV) Control

This control strategy is applied as a last step in high-speed operation to reach the maximum speed of the electric drive. The voltage limit ellipses are shrinking into the point $(i_f = -\frac{\Psi_{PM}}{L_d}, 0)$ for $\omega \to \infty$, which claims for the current trajectory to stay within these areas. The maximum torque for a given flux level is obtained, when the iso torque lines and voltage limit curves intersect tangentially. This can be formulated as following optimization problem [66]

$$\begin{aligned} \text{minimize } f(i_d, i_q) &= -\frac{3}{2}p\big(\Psi_{PM} i_q + (L_d - L_q) i_d i_q\big) \\ \text{subject to } c(i_d, i_q) &= \frac{U_{max}^2}{\omega^2} - (\Psi_{PM} + L_d i_d)^2 - (L_q i_q)^2 \end{aligned}$$

By computation of the corresponding Lagrangian

$$L = -\frac{3}{2}p\big(\Psi_{PM} i_q + (L_d - L_q) i_d i_q\big) + \lambda \frac{U_{max}^2}{\omega^2} - (\Psi_{PM} + L_d i_d)^2 - (L_q i_q)^2$$

and elimination of the Lagrangian multipliers, the solution for the so-called Maximum Torque per Voltage (MTPV) control mode is given as

$$i_d = -\frac{\Psi_{PM} + \Delta\Psi_d}{L_d} \tag{4.61}$$

$$i_q = -\frac{\sqrt{\frac{U_{max}^2}{\omega^2} - \Delta\Psi_d^2}}{L_q} \tag{4.62}$$

with the abbreviation

$$\Delta\Psi_d = \frac{L_q \Psi_{PM} - \sqrt{(L_q \Psi_{PM})^2 + 8(L_d - L_q)^2 \frac{U_{max}^2}{\omega^2}}}{4(L_d - L_q)}$$

The MTPV strategy is usually combined with the previous two strategies to operate the electric drive within the complete speed range. Figure 4.36 shows the complete control strategy of the electric drive for a reference torque of 220 Nm and maximum electric speed of $\omega = 10000$ rad/s, which is equivalent to 19099 rpm for a five pole machine. In [72] the transition from the different regions and current control strategies are explained in more detail. Note that the current i_f represents the necessary d-current component for a complete field weakening of the permanent magnet stator flux linkage Ψ_{PM}. Three different cases occur and have to be distinguished:

i) $\Psi_{PM} > L_d I_{max}$

ii) $\Psi_{PM} = L_d I_{max}$

iii) $\Psi_{PM} < L_d I_{max}$

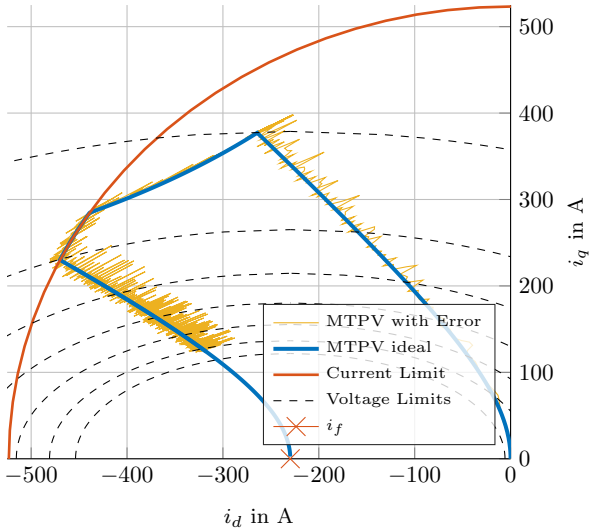

Figure 4.36.: MTPA, MPC and MTPV strategy for high speed operation. The trajectory moves along where the voltage limit ellipses hit the iso torque lines tangentially.

For the first machine type, i_f lies outside the current limit circle and therefore the maximum speed is limited electrically. The second type implies $i_f = -I_{max}$ and provides theoretically a infinite constant power region. In this work, the considered machine is an example of the third case, which has the possibility to increase the speed theoretically up to infinity, but the power is decreasing with increasing mechanical speed. In [73], these circumstance and relations are explained in more detail. Figure 4.37 on the left shows the control strategy concerning i_d and i_q for maximum reference torque of 260 Nm with the three presented control modes and distortions caused by an eddy current sensor error.

On the right, the typical torque-speed and power characteristics can be obtained as well as the present torque ripple due to the disturbed current components. The power of the electric machine is increasing after the rated speed, which is typical for machines with $\Psi_{PM} < L_d I_{max}$ property.

For the SPMSM, the same concept is applied, but in the constant torque operating range ZDAC is used, which corresponds to the MTPA condition. This means that the necessary q-component is simply given as

$$i_q = \frac{2M_{ref}}{3p\Psi_{PM}}$$

The base speed operating range for maximum torque ends by considering Equation 4.59

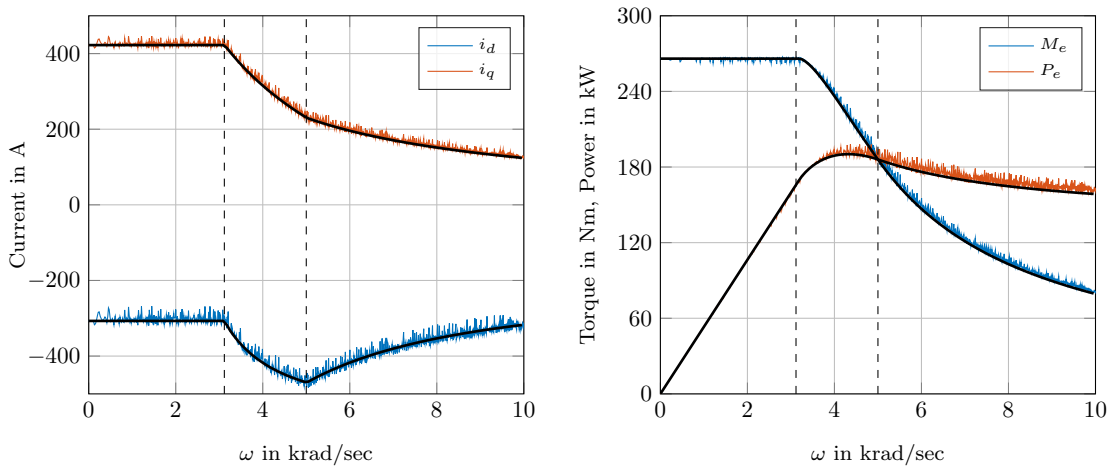

Figure 4.37.: Currents in d and q-direction (left) and torque with power characteristics (right) with eddy current sensor error and maximum torque. Dashed lines show the transition from MTPA to MPC and from MPC to MTPV.

for $i_d = 0$ and $i_q = I_{max}$

$$\omega_1 = \frac{U_{max}}{\sqrt{(L_s i_d + \Psi_{PM})^2 + (L_s i_q)^2}} = \frac{U_{max}}{\sqrt{L_s^2 I_{max}^2 + \Psi_{PM}^2}}$$

In the lower field weakening range a negative d-current is applied as in Equation 4.60 for the IPMSM, which is limited to a value of $i_f = -\frac{\Psi_{PM}}{L_s}$ within the available current limits. With further increased speed the current trajectory hits the voltage limit again at

$$\omega_2 = \frac{U_{max}}{\sqrt{L_s^2 I_{max}^2 - \Psi_{PM}^2}}$$

With further increased speed, the d-current is kept at i_f and the q-component is limited through the voltage circles and determined by obtaining Equation 4.59 as

$$i_q = \frac{U_{max}}{\omega L_s}$$

Figure 4.38 shows the combination of these three operating modes for the SPMSM type and maximum torque speed characteristic.

The iso torque lines, which are straight lines parallel to the d-axis, are not shown for better clarity. The first two voltage limit circles represent the speed where switching of the strategy is necessary. The scenario is simulated for a maximum torque of 155 Nm up to an electrical speed of 10000 rad/s (19099 rpm), and gives following values for $\omega_1 = 4263$ rad/s (8142 rpm) and $\omega_2 = 5183$ rad/s (9898 rpm).

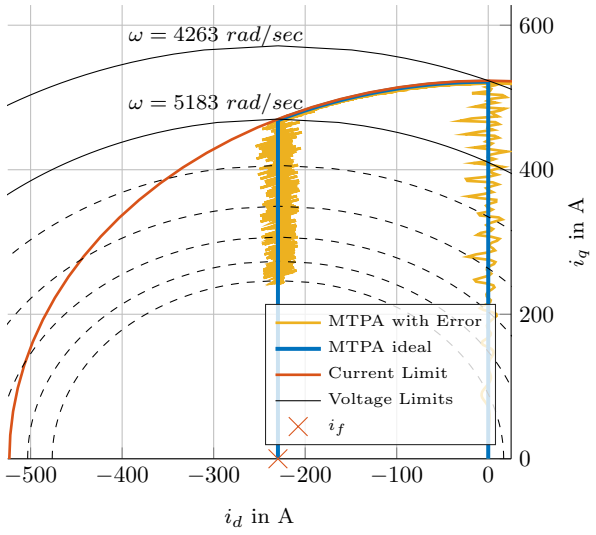

Figure 4.38.: MTPA, MPC and MTPV current control strategy combination for the SPMSM machine type

4.10.4. Loss Minimizing Control (LMC)

Different kinds of losses occur in electric machines and only ohmic losses were considered by the stator resistance R_s so far. These losses are indicated as P_{cu} and determined as

$$P_{cu} = \frac{3}{2} R_s (i_d^2 + i_q^2)$$

But additional losses are present in the machine, such as iron and stray losses. In [74], a listing of different kind of losses, which occur in an electric drive system, is presented. Iron losses are usually indicated as the combination of eddy current and hysteresis losses. One common possibility to model the iron losses is [3],[75]

$$P_{fe} = c_{fe} \omega^{\gamma} \Psi_0^2$$

with $\gamma \approx 1.5$ - 1.6 and $c_{fe} \approx 1.5$ - 1.6. In this work a quite similar approach is used, but the iron losses are modelled similar as in [66] with an additional frequency dependent iron resistance R_c

$$\frac{1}{R_c} = \frac{1}{R_{c0}} + \frac{1}{\omega R_{c1}} \tag{4.63}$$

The iron losses can then be written with the main field voltage U_H as

$$P_{fe} = \frac{U_H^2}{R_c} = \frac{\omega^2 \Psi_0^2}{R_c} = \frac{3}{2} \frac{u_{d0}^2 + u_{q0}^2}{R_c}$$

Note that the flux linkage Ψ_0, as defined in Equation 4.59, depends on d- and q-current component. This means, that with applying a negative d-current i_d the flux linkage Ψ_0 can be decreased and therefore the iron resistance R_c, respectively iron losses are decreased. This is the basic idea of Loss Minimization Control. Figure 4.39 shows the equivalent circuit diagram of the PMSM with additional parallel iron resistance R_c, which is representative for the iron losses within the electric machine.

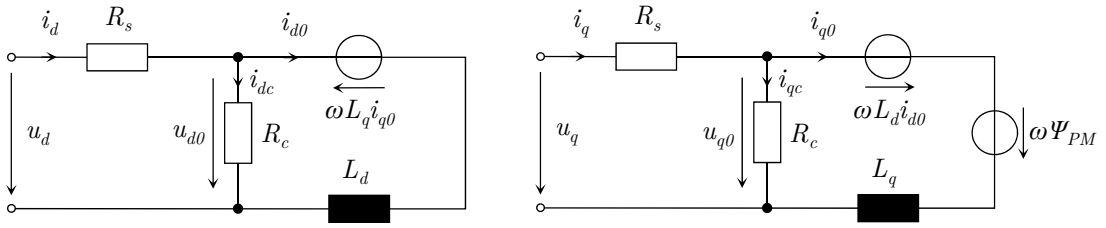

Figure 4.39.: Equivalent circuit diagram of PMSM in d- and q-axis with additional parallel iron resistance R_c adapted from [66].

Adding an iron resistance produces an additional node within the electric circuit and the residual currents i_{d0} and i_{q0} expressed via control currents gives

$$i_{d0} = \frac{R_c^2 i_d + \omega L_q (R_c i_q - \omega \Psi_{PM})}{L_d L_q \omega^2 + R_c^2} \tag{4.64}$$

$$i_{q0} = \frac{R_c^2 i_q - \omega R_c (L_d i_d + \Psi_{PM})}{L_d L_q \omega^2 + R_c^2} \tag{4.65}$$

and corresponding voltage drops on the iron resistance as

$$u_{d0} = -\omega L_q i_{q0} \tag{4.66}$$

$$u_{q0} = \omega (L_d i_{d0} + \Psi_{PM}) \tag{4.67}$$

by omitting the dynamic voltage drops regarding L_d and L_q. Stray losses are also possible to be considered with this approach. Usually they are modelled in form of [3]

$$P_{stray} = c_{str} \omega^2 (i_d^2 + i_q^2)$$

with a stray coefficient c_{str}, but in this work these type of losses is not further taken into account due to their insignificant impact on rotor position error investigations.

As in the former sections, searching of the optimal current trajectory in the dq-plane is formulated as an optimization problem as

$$\text{minimize } f(i_d, i_q) = P_{cu} + P_{fe} = \frac{3}{2} R_s (i_d^2 + i_q^2) + \omega^2 \frac{(L_d i_d + \Psi_{PM})^2 + (L_d i_d)^2}{R_c}$$

$$\text{subject to } c(i_d, i_q) = M_{ref} - \frac{3}{2} p \big(\Psi_{PM} i_q + (L_d - L_q) i_d i_q \big)$$

with the following Lagrangian

$$L = P_{cu} + P_{fe} + \lambda \left(M_{ref} - \frac{3}{2} p\big(\Psi_{PM} i_q + (L_d - L_q) i_d i_q\big) \right)$$

This means, that the LMC strategy minimizes the sum of electric and iron losses with respect to the desired operating torque. Solving the optimization problem leads to the following solution for the d-current

$$i_d = \frac{1}{2} \Bigg[\frac{(L_d L_q - 2L_d^2)\Psi_{PM}\omega^2 - \Psi_{PM} R_c R_s}{(L_d^2\omega^2 + R_c R_s)(L_d - L_q)} + \frac{\sqrt{4(L_q^2\omega^2 + R_c R_s)(L_d^2\omega^2 + R_c R_s)(L_d - L_q)^2 i_q^2 + \Psi_{PM}^2 (L_d L_q \omega^2 + R_c R_s)^2}}{(L_d^2\omega^2 + R_c R_s)(L_d - L_q)} \Bigg] \tag{4.68}$$

As in the previous chapter, an expression with torque demand M_{ref} instead of the unknown q-current component is beneficial. Inserting Equation 4.68 into the IPMSM torque relation leads also to an quartic polynomial in the form of

$$i_q^4 + p_1 i_q + p_0 = 0$$

with following coefficients

$$p_1 = \frac{2}{3} \frac{(L_d L_q \omega^2 + R_c R_s)\Psi_{PM} M_{ref}}{p(L_d - L_q)^2 (L_q^2\omega^2 + R_c R_s)}$$

$$p_0 = -\frac{4}{9} \frac{(L_d^2\omega^2 + R_c R_s) M_{ref}^2}{p^2 (L_d - L_q)^2 (L_q^2\omega^2 + R_c R_s)}$$

Noteworthy is that with $R_c \to \infty$, which accords that no iron losses are considered, the solution of the above LMC optimization problem converges into the MTPA solution from Equation 4.58. That makes sense, because MTPA can also be formulated as an optimization problem, which minimizes the ohmic losses. By increasing the electrical frequency $\omega \to \infty$, which means that the iron losses are the dominating losses compared to the ohmic losses, the LMC trajectory converges into the MTPV solution. This means, that the LMC trajectory is always bounded between these two special cases. For the SPMSM type, the LMC strategy leads to the simpler solution for the d-current

$$i_d = -\frac{L_s \Psi_{PM} \omega^2}{L_s^2\omega^2 + R_s R_c} \tag{4.69}$$

if the same optimization problem as for the IPMSM with $L_d = L_q = L_s$ is applied. In this case, the optimization problem can be directly formulated for the residual current

i_{d0}, which leads to the more general solution

$$i_{d0} = -\frac{L_s \Psi_{PM} \omega^2 (R_s + R_c)}{L_s^2 (R_s + R_c)\omega^2 + R_s R_c^2} \tag{4.70}$$

where both solutions converge towards zero for $R_c \to \infty$, according to the ZDAC solution. Considering for this machine that $R_c \gg R_s$ applies, the solution from Equation 4.70 converges into Equation 4.69. Solving the optimization problem for i_{d0} and the IPMSM case is possible too, but leads to unmanageably and extensive terms and is therefore not carried out here. Since the torque is independent from the d-current for the SPMSM, the q-current follows directly from Equation 4.29

$$i_q = \frac{2M_{ref}}{3p\Psi_{PM}} \tag{4.71}$$

Figure 4.40 shows the different loss distribution for LMC and IPMSM in more detail.

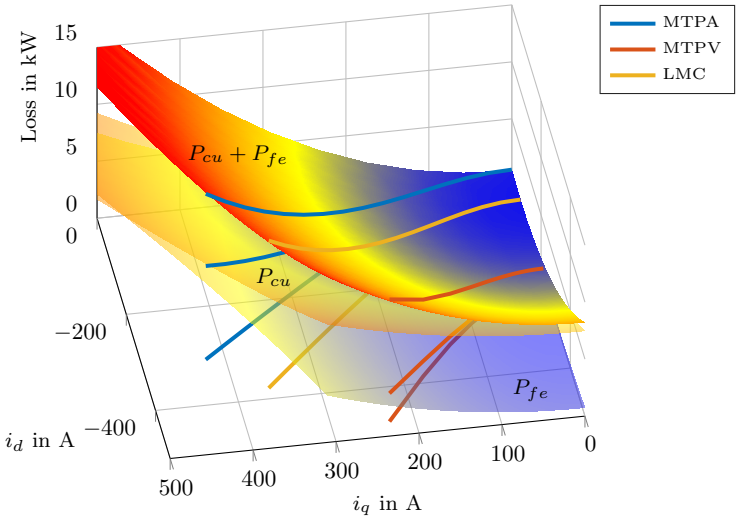

Figure 4.40.: Loss properties of different current control strategies.

It shows the different loss surfaces for an IPMSM at a constant speed of 4000 rpm with varying torque from 0 up to 260 Nm. The MTPA, MTPV and LMC trajectories are displayed on the bottom of the dq-current plane and show, that the solution for the LMC for this specific mechanical speed lies between the MTPA and MTPV trajectory. The lowest transparent surface represents the iron losses depending on the operating point, which are minimized by the red MTPV solution projected into the iron loss surface. The second transparent plane features the ohmic losses, which are minimized by the MTPA solution in blue. The solid surface on top represents the sum of ohmic and iron losses and has its minimum somewhere in between, which is exactly where the yellow LMC trajectory goes along the total loss surface for different torque variations. LMC uses

more negative d-current, which certainly increases the ohmic losses, but it can result in a better total loss trade off by considering the iron losses too. The strategy can also be obtained as a function of the electric drive's speed regarding the control currents, output torque and power. Figure 4.41, left, shows that the strategy uses more negative d-current and has to reduce the q-component due to present current limitation of $i_d^2 + i_q^2 \leq I_{max}^2$. Additionally, a comparison of MTPA and LMC strategy under the influence of an eddy current sensor error is depicted on the right. However, the characteristic curve of torque and power over speed is not influenced by applying LMC instead of MTPA (in comparison with Figure 4.37).

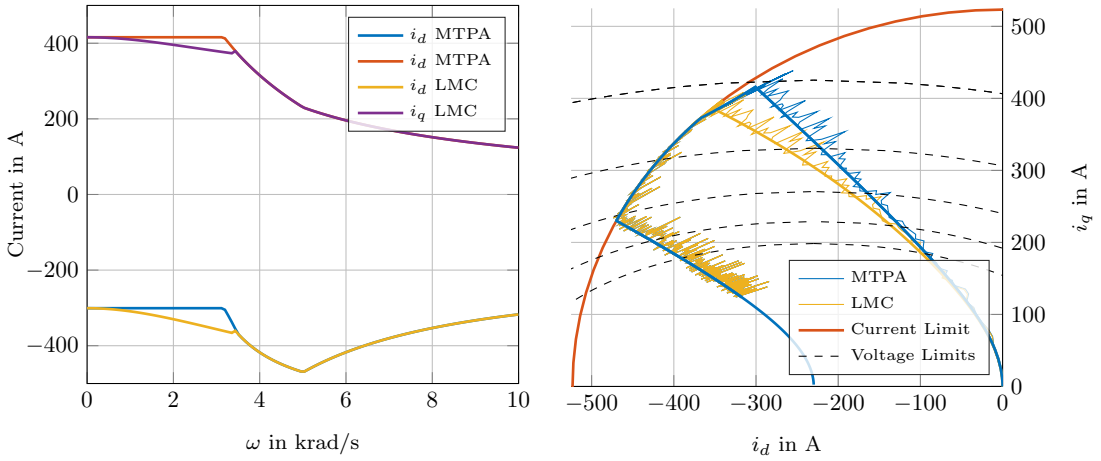

Figure 4.41.: Currents in d and q-direction (left) and and comparison of MTPA and LMC trajectory for maximum reference torque of 260 Nm.

Modelling of Iron Losses

As mentioned in the previous subsection, modelling of iron losses can be challenging and different approaches have been developed for this purpose. Computation results of a FEM simulation were obtained, where iron losses of the machine are calculated for different operating points. In this work, iron losses are modelled as proposed in [66], but in contrast the iron resistance is modelled as a serial resistor

$$R_c = R_{c0} + \omega R_{c1}$$

consisting of a constant value R_{c0} and speed dependent term R_{c1}, because it provided better results compared to the parallel approach. Subsequently an optimizer is used by considering Equations 4.64 - 4.67 to determine the coefficients of the iron resistance and

to

$$\text{minimize } f(i_d, i_q, \omega) = \left(P_{fe,meas} - \frac{3}{2} \frac{u_{d0}^2 + u_{q0}^2}{R_c} \right)^2 \tag{4.72}$$

where the residual currents i_{d0} and i_{q0} decoupled and expressed via complete stator current components i_d and i_q for stationary conditions. This parameter fitting problems leads to $R_{c0} = 48.479\ \Omega$ and $R_{c1} = 4.634 \cdot 10^{-3}\ \Omega\text{s/rad}$. Figure 4.42 shows the results of the coefficient fitting regarding the iron losses resistance compared with the FEM simulation.

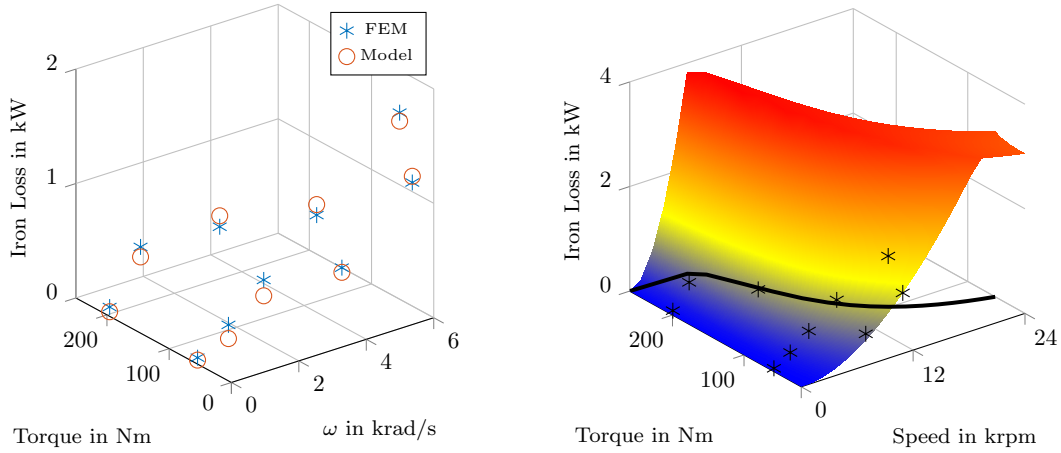

Figure 4.42.: Comparison of FEM results and iron resistance model (left). Iron losses with fitted iron resistance R_c within complete operating range of electric machine (right).

Note that there are lots of different and more accurate approaches for modelling iron losses [76], but the basic idea here is to consider these losses sufficiently accurate enough to evaluate LMC strategy and efficiency properties. It is important to take iron losses into account, because neglecting these losses would lead to unrealistic high machine efficiency values.

4.10.5. Influence of Rotor Position Errors on Different Control Strategies

Former considerations are now applied to analyze the resulting torque ripple induced by rotor position errors. The disturbance transfer functions from Equations 4.48 and 4.49 are used to calculate the controlled current values $\bar{i}_d$ and $\bar{i}_q$. As this values do not represent the real machine currents i_d and i_q, an inverse park transform with the sensor error is applied and the output torque is computed. As objective criterion, the torque ripple behaviour - as defined in Equation 4.3 - is used in all operating points of the electric machine. A comparison of the resulting torque ripple map by applying MTPA and LMC strategy is depicted in Figure 4.43.

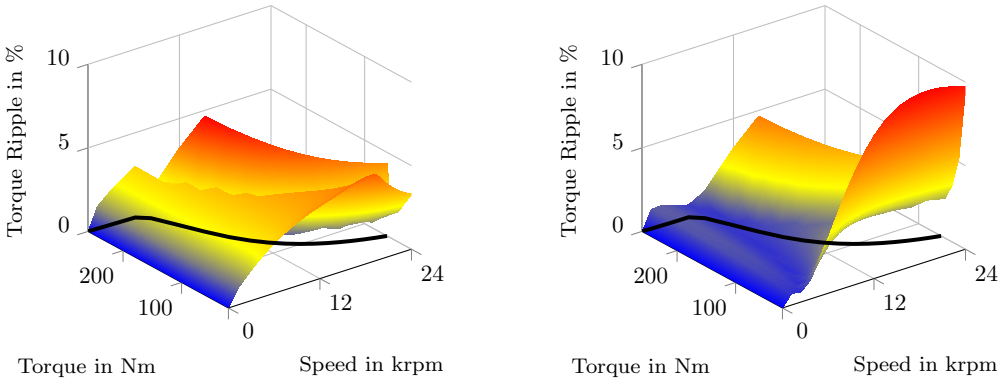

Figure 4.43.: IPMSM torque ripple maps for MTPA (left) and LMC strategy (right).

The picture on the left shows the resulting torque ripple over meaningful operating points of the IPMSM indicated by the solid black line for MTPA strategy and eddy current sensor error. The torque ripple map corresponds well with the simulation results from Figure 4.5 on the top left by considering the different z-axis scaling. The scaling is changed here for a better comparison with the torque ripple on the right, which represents the results of the LMC strategy. It shows, that the LMC produces less torque ripple for high torque and low speed operating points, but significantly higher torque ripple for high speed and low torque conditions. In this operating points, the torque values are nearly twice as big as for the MTPA strategy. For field weakening operating range is no difference apparent, because both strategies operate in the same manner in this region. This means, that the choice of the IPMSM operating strategy takes impact onto the resulting torque ripples induced by rotor position measurement errors. As mentioned in Section 4.10, other control strategies like UPF and CMFL were developed, which are not implemented in this work. The method itself stays valid, which means that if these control strategies are implemented, torque ripple analysis with the presented method is possible for any given control strategy.

For the SPMSM machine type, mainly the disturbance in the q-current component deter-

mines the torque, because no reluctance torque, which is influenced by a multiplication of both current components, is present. Therefore, the induced torque distortions are smaller for this machine type by tendency, which is depicted in Figure 4.44 for MTPA on the left and LMC on the right.

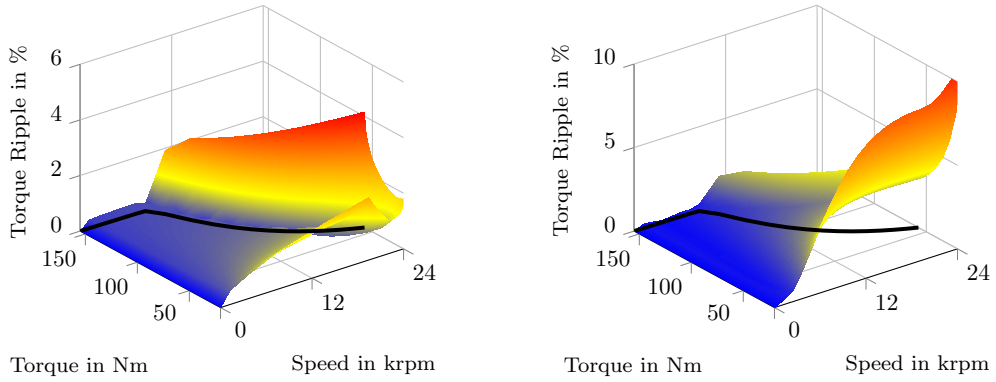

Figure 4.44.: SPMSM torque ripple maps for MTPA (left) and LMC strategy (right).

Other investigated sensors as the resolver and end-of-shaft type may provide more accurate rotor position measurement. Therefore their impact on the torque ripple is lower compared to the eddy current sensor. But the characteristic shape and hot spots are located in the same regions, as shown in Figure 4.45.

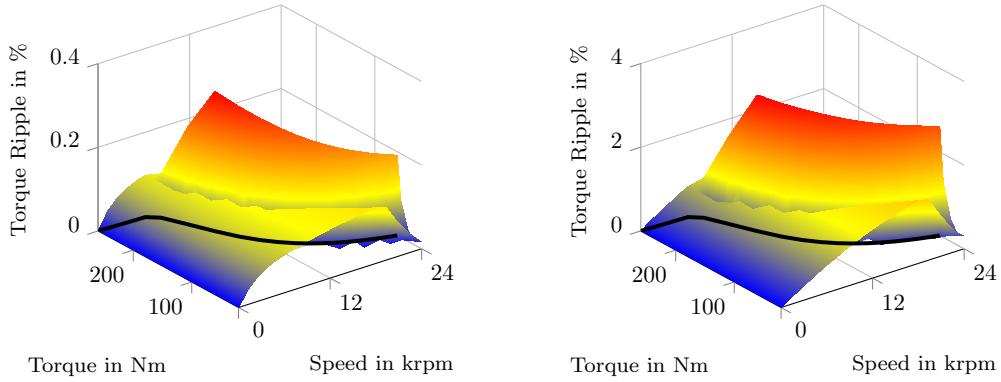

Figure 4.45.: Torque ripple maps with resolver (left) and end-of-shaft sensor (right).

4.11. Additional Losses and Efficiency

In this section, the effect of rotor position errors regarding the efficiency of a PMSM is investigated in more detail. Due to the sensor error, harmonic distortions in d- and q-currents occur, which produces additional ohmic and iron losses. Additionally, the average output torque can decrease for bigger sensor errors, which reduces the mechanical output power P_{mech} of the electric machine. A parameter study shows, that following loss and power considerations are only possible, if the sensor error can be considered as small. This is the case for sensor errors in the range of $|\Delta\theta| < 5°$. If bigger sensor errors are applied to the simulation model, the mechanical output power lowers drastically and makes loss comparison and efficiency calculations difficult.

4.11.1. Calculation of Power and Losses

Considering the equivalent circuit diagram in 4.39, adding an iron resistance leads to an enhancement of the dynamic voltage Equations 4.21 and 4.22. This gives [77]

$$\frac{di_{d0}}{dt} = \frac{1}{L_d}(u_d - R_s i_d + \omega L_q i_{q0})$$
$$\frac{di_{q0}}{dt} = \frac{1}{L_q}(u_d - R_s i_d - \omega L_q i_{q0} - \omega \Psi_{PM})$$

and applying Kirchhoff's law gives for the controlled currents i_d and i_q

$$i_d = \frac{1}{R_c}\big(L_d \frac{di_{d0}}{dt} - \omega L_q i_{qc} + R_c i_{dc}\big)$$
$$i_q = \frac{1}{R_c}\big(L_q \frac{di_{q0}}{dt} + \omega L_d i_{dc} + \omega \Psi_{PM} + R_c i_{qc}\big)$$

with

$$i_{dc} = i_d - i_{d0}$$
$$i_{qc} = i_q - i_{q0}$$

The output torque of the electric machine has then consequently been adapted to

$$M_e = \frac{3}{2} p\big(\Psi_{PM} i_{q0} + (L_d - L_q) i_{d0} i_{q0}\big)$$

Simulations show, that consideration of the additional dynamics from i_{d0} and i_{d0} is not necessary for this investigations. Therefore the stationary equivalent circuit diagram is used, where the residual currents are calculated afterwards by utilizing the general dq-model as in the minimization problem of the iron resistance parameters in Equation 4.72. Obtaining the stationary dq-voltages and separation of the searched currents leads

to

$$i_{d0} = \frac{R_c^2 i_d + \omega L_q (R_c i_q - \omega \Psi_{PM})}{L_d L_q \omega^2 + R_c^2}$$
$$i_{q0} = \frac{R_c^2 i_q - \omega R_c (L_d i_d + \Psi_{PM})}{L_d L_q \omega^2 + R_c^2}$$

with following voltages

$$u_{d0} = -\omega L_q i_{q0}$$
$$u_{q0} = \omega (L_d i_{d0} + \Psi_{PM})$$

The disturbance transfer functions for $S_{\Delta\theta i_d}(s)$ and $S_{\Delta\theta i_q}(s)$ from Equations 4.48 and 4.49 are used to compute the distorted currents $i_{d,q}$, with which the residual currents $i_{d,q0}$, the output torque and power are calculated. Additionally, the electric input power p_{el}, copper losses p_{cu} and iron losses p_{fe} are computed as followed

$$p_{cu}(t) = \frac{3}{2} R_s \big(i_d^2(t) + i_q^2(t)\big)$$
$$p_{fe}(t) = \frac{3}{2} R_c \big(i_{dc}^2(t) + i_{qc}^2(t)\big)$$
$$p_{mech}(t) = M_e(t) \frac{\omega}{p}$$
$$p_{el}(t) = \frac{3}{2} \big(u_d(t) i_d(t) + u_q(t) i_q(t)\big)$$

In this case, the power values are time dependent quantities and for the purpose of loss and efficiency considerations, the arithmetic mean value

$$\bar{P} = \frac{1}{T} \int_{t_0}^{t_0+T} p(t) dt$$

has to be used to rate the power conditions, if rotor sensor errors are present. Above power equations are used to compute different power and loss values with and without rotor position sensor error to rate its impact on these quantities.

4.11.2. Results of Power and Loss Considerations

To rate the additional losses induced by sensor errors, power balance is calculated with and without sensor error for the same operating points as in the former chapters and the difference of this four power quantities is computed afterwards. Figure 4.46 shows the additional copper and iron losses caused by an eddy current sensor error by applying MTPA as current control strategy.

Considering the high waviness of d- and q- current signals as for example in Figure 4.25 and several former results suggests itself to produce quite additional copper and iron loss.

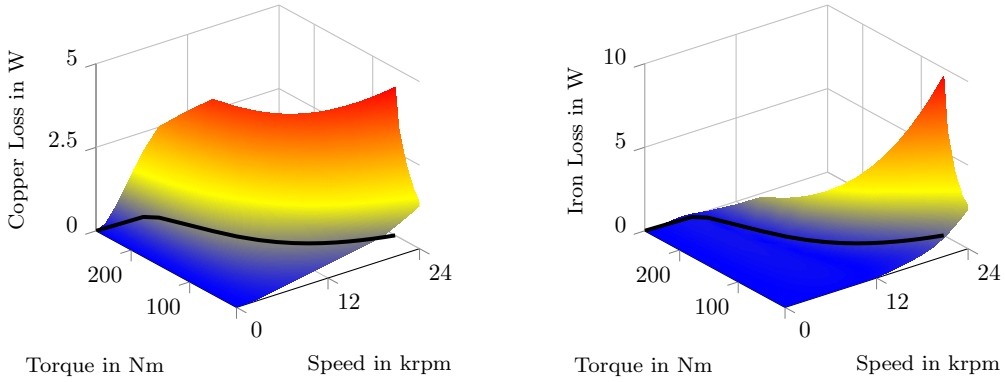

Figure 4.46.: Copper (left) and iron (right) losses for different operating points with MTPA strategy and eddy current sensor error behaviour.

Obtaining this surfaces shows that the additional losses caused by disturbed currents are very small compared to the maximum power of this specific electric machine of 160 kW and can therefore be neglected. This statement can not be generalized, because this specific machine type has a very small stator resistance R_s and low iron losses represented by R_c. For example, increasing the stator resistance to a value of 1 Ω leads to additional ohmic losses of about 100 W, which means that for smaller machines with higher ohmic stator and lower iron resistances noticeable additional losses may occur. For the SPMSM type the additional losses have a similar shape, but are even smaller caused by lower current disturbances compared to the IPMSM. A comparison between MTPA and LMC gives nearly the same characteristics for both kinds of losses. Computation of the efficiency η is implemented by calculation of

$$\eta = \frac{\bar{P}_{mech}}{\bar{P}_{el}}$$

for all different operating points and compared with the efficiency map of the electric machine without sensor error. The difference is therefore the efficiency loss contributed by the sensor error. Note that for this investigations the mean value of the sensor error $\Delta\theta$ is removed. Reason for that is, that for MTPA a static offset can cause an additional negative d-current similar to the LMC approach, which has beneficial properties regarding the efficiency (see Figure 4.41). This can lead to the result, that the efficiency of the electric drive is higher with rotor position error as without. Figure 4.47 shows the result of the efficiency loss from the analytic model compared with the simulation results for MTPA.

It can be obtained, that analytic and simulation model match each other and therefore the analytic approach is suitable for power and efficiency considerations. Due to machine parameters and the low impact from the rotor sensor error regarding additional losses, the efficiency loss of the electric drive can be neglected in this case. But as for the

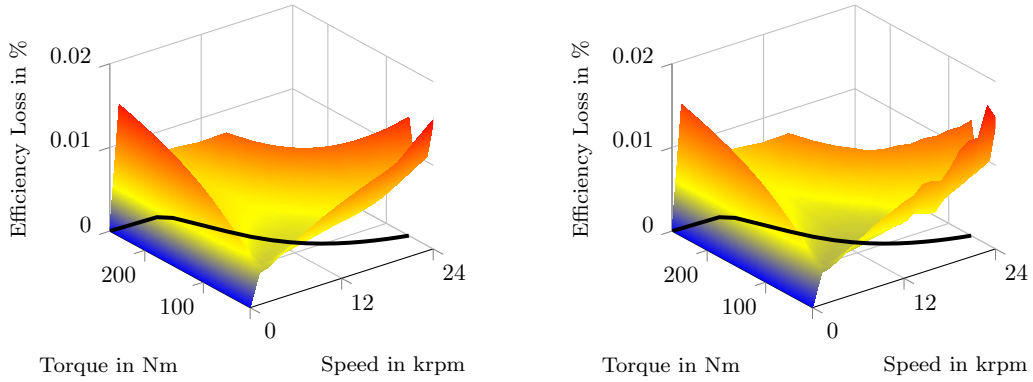

Figure 4.47.: Analytic and simulation results of efficiency loss with eddy current sensor error behaviour and MTPA strategy.

additional losses, efficiency degradation can play a role for other machine parameter sets. For the SPMSM case, the efficieny loss is even smaller and the difference of LMC compared to MTPA is depicted in Figure 4.48.

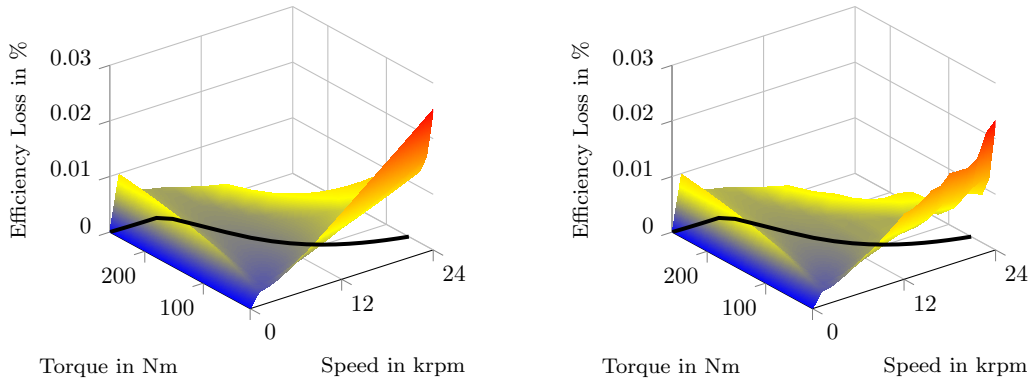

Figure 4.48.: Analytic and simulation results of efficiency loss with eddy current sensor error behaviour and LMC strategy

Finally it should be mentioned, that these considerations are only valid for small angle errors, which is the case for the investigated sensor errors. Higher values of sensor errors change the operating point and therefore the electric and mechanical output power of the electric machine significantly, which makes an efficiency comparison difficult. Additionally, the analytic approach would not provide usable results for current distortion calculation in this case any more.

4.12. Effect on Speed Control

Speed control is an important control mode for electric drives in general and also interesting within vehicle applications such as cruise control for example. Usually, the driver activates or releases the acceleration pedal to maintain the vehicle's speed, which correlates to a torque controlled operation as discussed in the previous section. Driving without the need of frequently controlling the speed provides safety, comfort and easiness for the driver. Therefore, cruise control systems were developed for constant speed driving and are implemented as speed-tracking controllers, which autonomously follow a pre-set vehicle speed [78]. The typical speed control structure consists of an inner current, respectively torque control loop and overlaid speed control loop. Since a rotor position sensor is used for the field-oriented current control, this position sensor will be used to generate a motor speed information signal for the speed control loop to avoid the necessity of an additional speed sensor or encoder. Calculation of the rotor speed can be done in the easiest way by differentiating the rotor position signal or by a tracking loop similar to a resolver-to-digital conversion [18]. Different observer-based structures for velocity estimation are presented in [79], which can provide better results in terms of accuracy and quantization. But these models are not considered further, because the focus in this section lies on a straightforward velocity signal generation. Caused by the rotor position sensor error, the generated speed signal will also contain an additional error and the speed control loop will produce a certain speed ripple. This section has the aim to analyze and describe the impact of rotor position errors regarding speed control applications.

4.12.1. Control Structure and Controller Design

As mentioned before, the control structure consists of an inner torque, respectively current control loop and an outer speed control loop. As the electric time constants of the current controlled electric machine are significant lower than from the involved mechanics within the speed loop, the field-oriented controlled machine can be substituted by the approximated transfer function introduced in Equation 4.33

$$T_M(s) = \frac{M_e(s)}{M_{ref}(s)} \approx \frac{1}{1 + s2T_t} = \frac{1}{1 + sT_\sigma}$$

This means, that the torque build-up of the field-oriented PMSM is treated as a first-order lag (PT1) element. The plant for the speed controller therefore consists of the approximated closed loop torque transfer function $T_M(s)$ and a mechanical subsystem. Note, that in this work the mechanics are only considered by the inertia J of the electric machine. For vehicle applications a total inertia has to be taken into account, which contains wheels, transmission and vehicle mass. Additionally, the load torque M_L, which contains the inertia force, aerodynamic drag, rolling resistance and road grade force, depends on the vehicle speed. The following result should not be restricted for vehicle

applications, therefore the analysis does not consider a typical vehicle powertrain as load. In [78] these specific application is discussed in more detail. The mechanics are described via principle of angular momentum with a constant inertia J, machine torque M_e, load torque M_L and speed proportional friction coefficient B

$$J\frac{d\omega_m}{dt} = M_e - B\omega_m - M_L$$

which can be written with $M_L = 0$ as following transfer function

$$G_{mech}(s) = \frac{\omega_m(s)}{M_e(s)} = \frac{1}{B + sJ}$$

Frictional losses are neglected for following considerations, which simplifies above mechanical transfer function to an integrator with time constant $T_{mech} = J$

$$G_{mech}(s) = \frac{1}{sT_{mech}}$$

Figure 4.49 shows the common structure of a speed control loop, consisting of current control transfer function $T_M(s)$, mechanics and speed controller $G_{R\omega}(s)$.

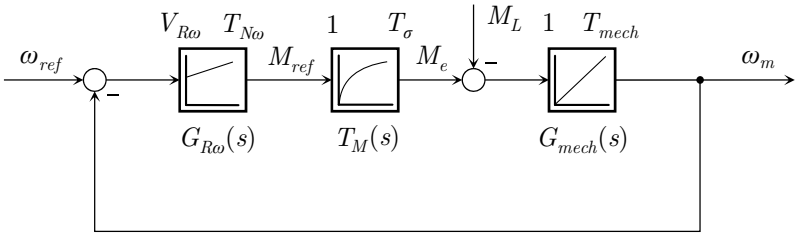

Figure 4.49.: Speed control loop with substitute current control transfer function and mechanics.

Control value is the mechanical frequency ω_m, which is related to the speed n in rpm as

$$n = \omega_m \frac{60}{2\pi} = \omega_m \frac{30}{\pi}$$

The speed controller is usually also implemented as PI-controller, but the modulus optimum design is not applicable due to the additional integrator within the plant. Instead the symmetric optimum method is applied to determine the controller coefficients, which has the aim to maximize the phase margin of the open loop transfer function. This leads to following control parameters [66]

$$V_{R\omega} = \frac{T_{mech}}{2V_S T_\sigma} = \frac{J}{2T_\sigma}$$
$$T_{N\omega} = 4T_\sigma$$

with plant gain $V_S = 1$ and the according PI speed controller transfer function from Equation 4.31. Utilization of this control parameters leads to following closed loop speed transfer function

$$T_\omega(s) = \frac{1 + s4T_\sigma}{1 + s4T_\sigma + s^2 8T_\sigma^2 + s^3 8T_\sigma^3} \tag{4.73}$$

The zero in the numerator of $T_\omega(s)$ causes significant overshoots in the step response and can be compensated by filtering the reference speed ω_{ref} with an additional first-order lag element $G_G(s)$, which is consequently dimensioned as

$$G_G(s) = \frac{\omega^*_{ref}(s)}{\omega_{ref}(s)} = \frac{1}{1 + sT_G} = \frac{1}{1 + s4T_\sigma}$$

This considerations are only valid, if the mechanical rotor speed is known respectively measured with a separate speed sensor. Using a rotor position sensor for speed control leads to an extension of the speed control loop as depicted in Figure 4.50.

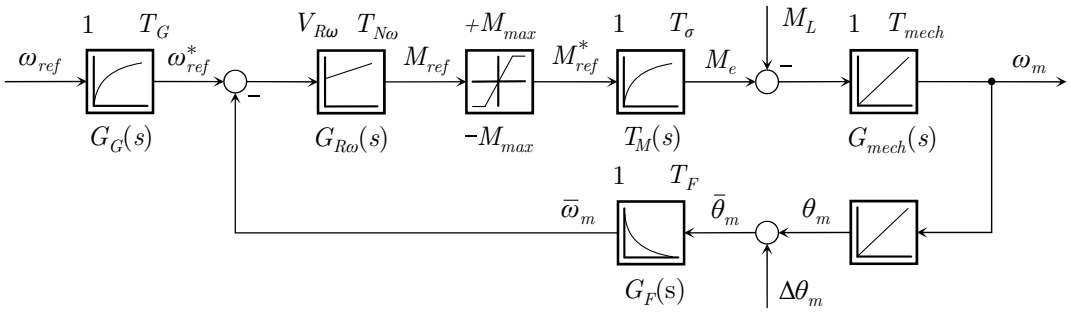

Figure 4.50.: Speed control loop with speed filter $G_F(s)$ for generating speed information from rotor position sensor and input reference filter $G_G(s)$.

To consider the additional error contributed from the rotor position sensor, the mechanical speed ω_m is integrated over time to compute the mechanical rotor position θ_m. Afterwards, the measured rotor sensor error $\Delta\theta_m$ is added to calculate a rotor position signal, which correlates to a real sensor measurement signal. Note that this additional rotor sensor error relates to a mechanical and not an electrical angle. Therefore the measurements have to be downscaled by the motor pole number p. A speed filter $G_F(s)$ is utilized to reconstruct a speed signal, which is basically a differentiator, but due to its non-proper transfer function it has to be extended with an additional pole determined by the time constant T_F

$$G_F(s) = \frac{s}{1 + sT_F}$$

Adding this element leads to an extension of the substitute sum of time constants within

the speed control loop and has to be considered within the control design as [80]

$$T_\Sigma = T_\sigma + T_F$$

where the symmetric optimum rule is applied for T_Σ, which gives following closed loop speed transfer function

$$\begin{aligned} T_\omega(s) = \frac{\omega_m(s)}{\omega_{ref}(s)} &= \frac{\frac{1}{sJ} G_{R\omega}(s) T_M(s)}{1 + \frac{1}{s^2 J} G_{R\omega}(s) T_M(s) G_F(s)} \\ &= \frac{(1 + sT_F)(1 + s4T_\Sigma)}{1 + s4T_\Sigma + s^2 8T_\Sigma^2 + s^3 8T_\Sigma^3 + s^4 8T_F T_\sigma T_\Sigma^2} \end{aligned} \tag{4.74}$$

This transfer function reduces itself for $T_F = 0$ and $T_\sigma = T_\Sigma$ into the same as in Equation 4.73. The pre-filtering of ω_{ref} has to be extended in this case into

$$G_G(s) = \frac{1}{(1 + sT_F)(1 + s4T_\Sigma)}$$

The disturbance transfer function $S_{\Delta\theta\omega}(s)$, which has the same denominator polynomial as the closed loop transfer function, describes the impact from the rotor position error $\Delta\theta_m$ to the mechanical speed

$$\begin{aligned} S_{\Delta\theta\omega}(s) = \frac{\omega_m(s)}{\Delta\theta_m(s)} &= \frac{-\frac{1}{sJ} G_{R\omega}(s) T_M(s) G_F(s)}{1 + \frac{1}{s^2 J} G_{R\omega}(s) T_M(s) G_F(s)} \\ &= -\frac{s(1 + s4T_\Sigma)}{1 + s4T_\Sigma + s^2 8T_\Sigma^2 + s^3 8T_\Sigma^3 + s^4 8T_F T_\sigma T_\Sigma^2} \end{aligned} \tag{4.75}$$

To valid these models, the field-oriented control simulation in Figure 4.2 is extended with a symmetric optimum speed control loop. This means, that the speed controller produces torque commands, which are acting as inputs for the control strategy and setting the desired torque with the current control dynamics determined by $T_M(s)$. Note that the sensor error $\Delta\theta_m$ affects in the simulation the field-oriented control and the speed control loop, whereas the torque ripple induced by the sensor error is not considered by the linear system representation in Equation 4.75. The value for the speed filter time constant T_F is usually calculated with bandwidth requirements regarding the speed control loop, but in this case no such requirements are given and a default value of $T_F = 1$ ms is used. Figure 4.51 depicts a step response comparison of simulation and analytic model results and remaining stationary speed ripple.

It shows, that both step responses produce a significant overshoot caused by the zero in the closed loop transfer function $T_\omega(s)$. The reason for the deviation between simulation and analytic model in the transient phase lies in the fact, that the speed controller hits the output torque limit M_{max}, which is implemented within the control strategy. This leads to a bigger overshoot and slower speed command response compared to the analytic model. This is not a relevant restriction, because this method has the aim to

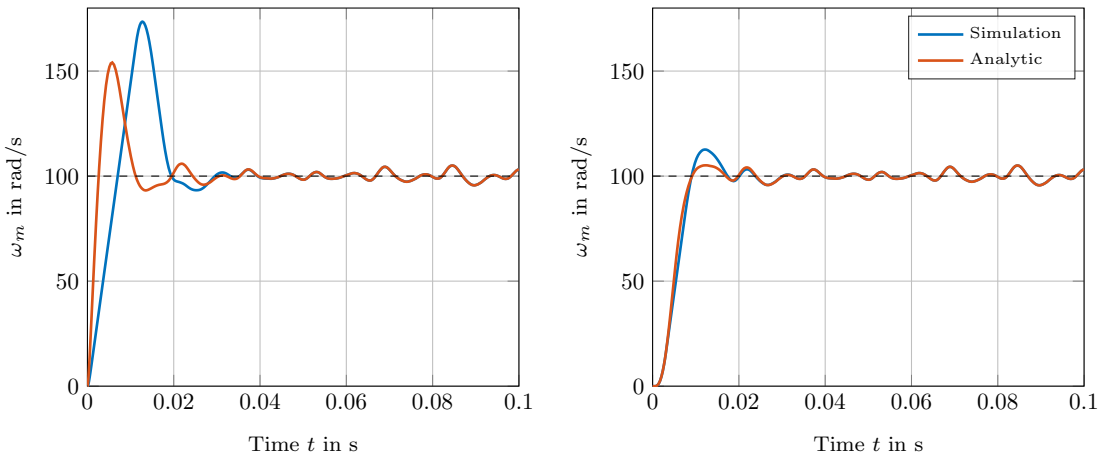

Figure 4.51.: Speed control step response with no load torque, eddy current sensor error, $T_F = 1$ ms and $\omega_{ref} = 100$ rad/s (955 rpm). Results without compensation on the left and with pre-filtering transfer function $G_G(s)$ on the right.

evaluate speed ripples induced by rotor position error in stationary operating points and the comparison shows, that after the step response decays, the results match each other. The linear system representation can therefore be used to calculate the stationary speed ripples for any kind shaped rotor position error, as long the speed controller does not saturates by hitting the maximum torque output $\pm M_{max}$. This should not be the case in general for reasonable values of rotor position errors.

It is also noteworthy, that the additional torque ripple induced within the field-oriented control does not affect the speed control results, and therefore it is justifiable to neglect this additional disturbance torque in speed control considerations. Figure 4.51 on the right shows the step responses with the pre-filter transfer function $G_G(s)$, which reduces the overshoot and provides better transient speed behaviour. However, the pre-filter has no impact on the disturbance transfer function $S_{\Delta\theta\omega}(s)$ and therefore no influence regarding speed ripples induced by rotor position errors. Figure 4.52 shows the speed ripple and consistency of simulation and analytic model for this example in more detail. In this scenario, an eddy current sensor error was used, which results in a speed ripple of about 9.44 % for a given speed command of $\omega_m = 100$ rad/s (955 rpm).

Another issue is the consideration of the output control torque produced by the speed controller, which is depicted on the right. The controller produces oscillating torque commands for the current controller within the range of $\Delta M_e \approx \pm$ 50 Nm. This means, the sensor error has the same effect as an oscillating load torque, which can rise into significant values like in this scenario. This kind of stationary behaviour is usually undesirable in speed control, because it produces additional losses and should therefore be avoided. The disturbance transfer function from the rotor position error to the torque

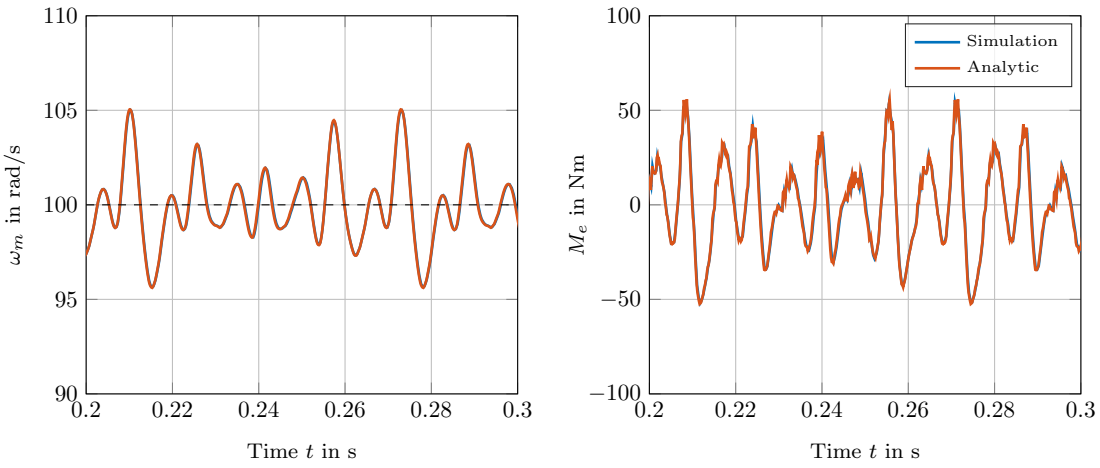

Figure 4.52.: Speed ripple in more detail (left) and control torque on the right.

command of the speed control is given as

$$\begin{aligned} S_{\Delta\theta M}(s) &= \frac{M_{ref}(s)}{\Delta\theta_m(s)} = \frac{-G_{R\omega}(s)G_F(s)}{1+\frac{1}{s^2J}G_{R\omega}(s)T_M(s)G_F(s)} \\ &= -\frac{s^2(1+s4T_\Sigma)(1+sT_\sigma)T_{mech}}{1+s4T_\Sigma+s^28T_\Sigma^2+s^38T_\Sigma^3+s^48T_FT_\sigma T_\Sigma^2} \end{aligned} \tag{4.76}$$

As shown in the previous results, rotor position errors can cause significant speed ripples and oscillations in the speed control torque values. Due to their higher accuracy, end-of-shaft and resolver results are not depicted explicitly and their effects on speed ripple can be more or less neglected. There are two present degrees of freedom: one possibility is to vary the speed controller gain $V_{R\omega}$ and the other is the speed filter time constant T_F. The impact of these parameters regarding speed control quality are discussed in the next subsections.

4.12.2. Speed Filter Parameter Sensitivity

Rotor sensor errors can produce significant speed ripples and control torque oscillations, if a speed filter is used as depicted in Figure 4.50. One possibility is to tune the filter time constant T_F and to obtain its influence regarding the speed control loop. The disturbance transfer function $S_{\Delta\theta\omega}(s)$ in Equation 4.75 depends mainly on the sum time constant T_Σ, determined by T_σ and T_F. Therefore, the value of the filter parameter T_F has a strong influence on the denominator polynomial of the disturbance transfer function $S_{\Delta\theta\omega}(s)$, but also - due to the single degree of freedom control architecture - on the closed loop speed transfer function $T_\omega(s)$ with the same denominator polynomial. The disturbance and closed loop transfer functions parametrized by the filter time constant T_F are given

as

$$S_{\Delta\theta\omega}(s) = -\frac{s\big(1 + s4(T_F + T_\sigma)\big)}{1 + s4(T_F + T_\sigma) + s^2 8(T_F + T_\sigma)^2 + s^3 8(T_F + T_\sigma)^3 + s^4 8 T_F T_\sigma (T_F + T_\sigma)^2}$$

$$T_\omega(s) = \frac{(1 + sT_F)\big(1 + s4(T_F + T_\sigma)\big)}{1 + s4(T_F + T_\sigma) + s^2 8(T_F + T_\sigma)^2 + s^3 8(T_F + T_\sigma)^3 + s^4 8 T_F T_\sigma (T_F + T_\sigma)^2}$$

The pre-filtering with $G_G(s)$ is applied to the closed loop transfer function $T_\omega(s)$ to cancel out the zeros in the numerator polynomial, but this has no impact on the disturbance transfer function $S_{\Delta\theta\omega}(s)$. These transfer functions can be used for time and frequency domain analysis and to investigate the impact of the filter time constant on the stationary and dynamic behaviour of the speed control loop. Note that changing the time constant T_F also changes the sum time constant T_Σ, which makes a renewed calculation of speed control parameters necessary. Figure 4.53 shows a parameter study for $T_F = 1$, 2 and 3 ms.

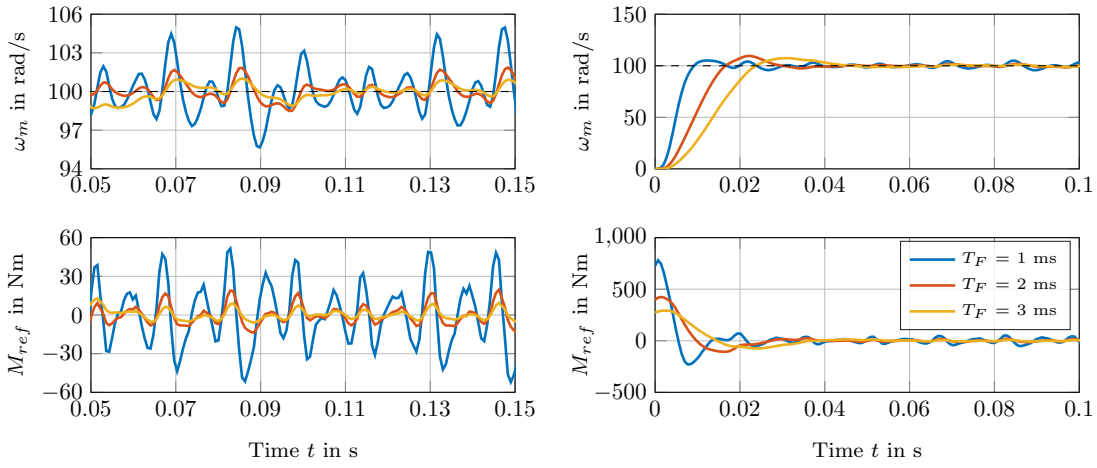

Figure 4.53.: Speed ripple and control torque for stationary and dynamic speed control with different speed filter time constants.

On the left, the stationary results regarding the speed ripple and control torque are depicted for the same reference speed command of $\omega_m = 100$ rad/s. It shows, that an increased filter time constant not only decreases the stationary speed ripple, it also softens the control activity caused by the speed controller. Therefore, higher values for the filter time constant are an important leverage to improve the stationary behaviour regarding speed ripples and torque oscillations. Disadvantage is, that the transient dynamic behaviour of the speed control loop declines, which is depicted on the right. Figure 4.54 shows this analysis in the frequency domain by obtaining the amplitude frequency responses.

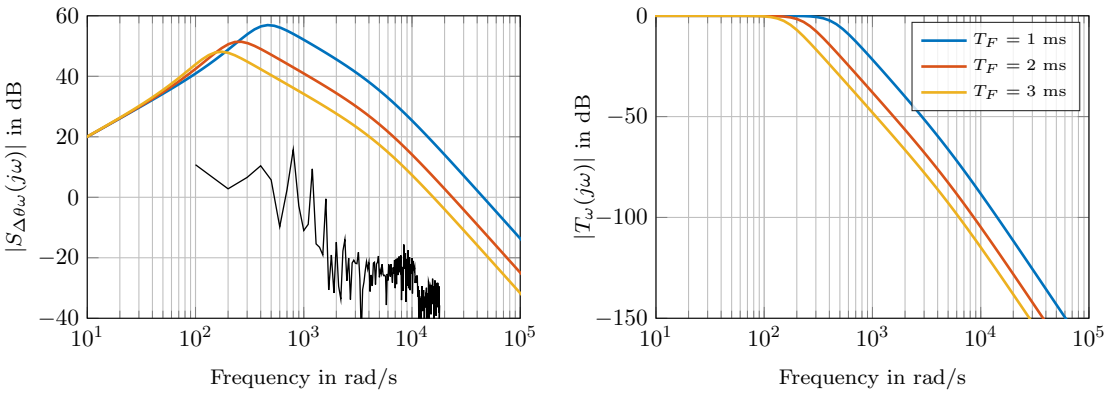

Figure 4.54.: Amplitude frequency response for different speed filter time constants.

On the left it shows the disturbance transfer functions for all three parameter variations and the arbitrarily scaled Fourier transform $\Delta\theta_m(j\omega)$ of the eddy current sensor error $\Delta\theta_m(t)$. As depicted in Figure 4.1, this specific sensor error contains a dominant 4^{th}, 8^{th} and 12^{th} harmonic, which occur in this scenario at $\omega_m = 400$, 800 and 1200 rad/s. For smaller filter time constants, these harmonics are getting more amplified by the disturbance transfer function as for higher values. Therefore the resulting speed ripple is significantly higher in this case. In contrast to the torque ripple considerations in Section 4.5, these transfer functions do not depend on the operating point of the electric machine and therefore the resulting torque ripple is strongly influenced by the harmonic composition of the present sensor error. On the right the closed loop transfer functions are depicted, which shows that for smaller values of T_F the bandwidth is higher, which ensures a faster dynamic speed control response as shown in Figure 4.53 on the right.

4.12.3. Speed Control Parameter Sensitivity

Another degree of freedom to influence speed ripples and control torque activity induced by rotor position sensor errors is to vary the parameters $V_{R\omega}$ and $T_{N\omega}$ of the speed controller, which are usually determined by the symmetric optimum rule. Changes in the time constant $T_{N\omega}$ are not very intuitive and do not provide the desired effect. Therefore, the influence of the controller gain $V_{R\omega}$ is considered, which leads to

$$S_{\Delta\theta\omega}(s) = -\frac{s(1+s4T_\Sigma)V_{R\omega}}{V_{R\omega} + s4T_\Sigma V_{R\omega} + s^2 4T_\Sigma T_{mech} + s^3 4T_\Sigma^2 T_{mech} + s^4 4T_F T_\sigma T_\Sigma T_{mech}}$$

$$T_\omega(s) = \frac{(1+sT_F)(1+s4T_\Sigma)V_{R\omega}}{V_{R\omega} + s4T_\Sigma V_{R\omega} + s^2 4T_\Sigma T_{mech} + s^3 4T_\Sigma^2 T_{mech} + s^4 4T_F T_\sigma T_\Sigma T_{mech}}$$

Figure 4.55 shows the results of a parameter study regarding the speed control gain $V_{R\omega}$.

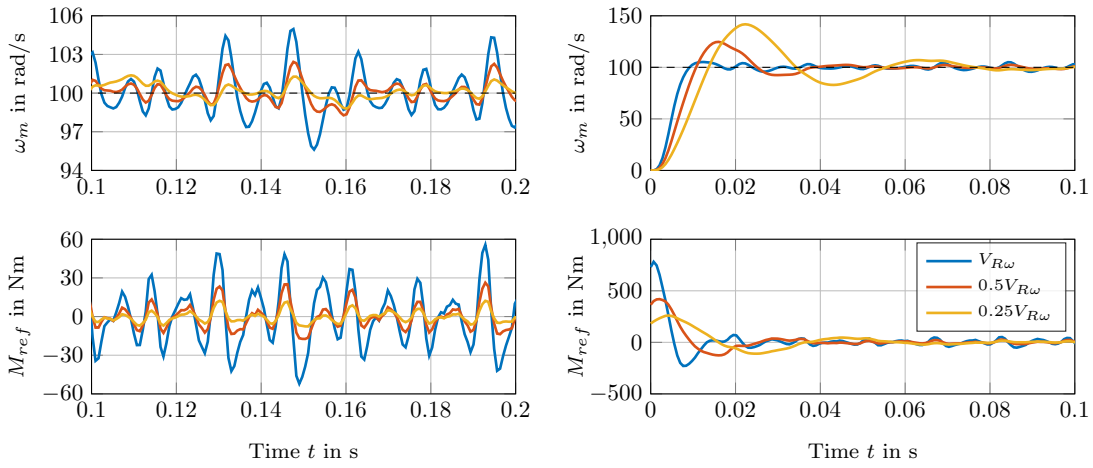

Figure 4.55.: Speed ripple and control torque for stationary and dynamic speed control with different control parameter values.

It shows on the left, that decreasing the controller gain also decreases the stationary speed ripple, similar as for the speed filter time constant. By viewing at the step responses on the right, it can be seen that decreasing the controller gain leads to a less damped system, which takes a severe time to get stationary. This is caused by the influence of the control gain regarding the polynomial coefficients and the incomplete zero compensation of the speed command pre-filter $G_G(s)$. Therefore, it is recommended to affect the stationary speed ripples with the speed filter time constant T_F and keep the speed control gain $V_{R\omega}$ calculated by the symmetric optimum method.

4.12.4. Speed Control with Tracking Loop

As mentioned in the begin of this section, velocity information calculation is often performed with a tracking loop [18], [81], which is similar to the resolver-to-digital conversion introduced in Section 2.2.2. The idea involves forming a closed loop tracking system that forces the estimation of the rotor position $\hat{\theta}_m$ to converge to the actual position θ_m. Figure 4.56 shows the structure of the tracking loop, which consists basically of a PI-controller and integrator within a feedback loop.

The transfer function from the input, which is represented by the rotor sensor information $\bar{\theta}_m$ to the rotor position estimation $\hat{\theta}_m$ is given as

$$G_{T\theta}(s) = \frac{\hat{\theta}_m(s)}{\bar{\theta}_m(s)} = \frac{1 + s\frac{2\delta}{\omega_0}}{1 + s\frac{2\delta}{\omega_0} + s^2\frac{1}{\omega_0^2}} \tag{4.77}$$

and is used in resolver-to-digital conversion to track the rotor angle $\bar{\theta}_m(s)$. The output signal $\hat{\theta}_m(s)$ is computed by an integration over time of a former signal, which has

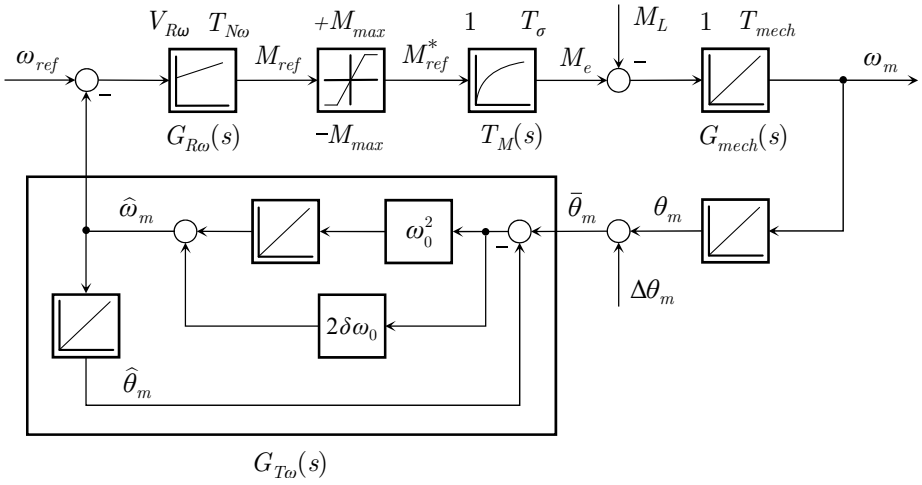

Figure 4.56.: Speed control with tracking loop transfer function for generating speed information signal

to be in this case the derivative of the rotor position estimation and represents the speed estimation $\hat{\omega}_m$. The transfer function of the measured rotor position to the speed estimation is consequently

$$G_{T\omega}(s) = \frac{\hat{\omega}_m(s)}{\bar{\theta}_m(s)} = \frac{s(1 + s\frac{2\delta}{\omega_0})}{1 + s\frac{2\delta}{\omega_0} + s^2\frac{1}{\omega_0^2}} \tag{4.78}$$

These transfer functions contain the parameters δ and ω_0, which are designed in such way, that the tracking loop bandwidth is comparable with the speed filter $G_F(s)$ and that both systems provide the same gain for $s \to \infty$. This leads for $T_F = 1$ ms and $\delta = 1$ to

$$\omega_0 = \frac{1}{2\delta T_F} \tag{4.79}$$

Figure 4.57 shows the comparison of a speed control manoeuvre simulation between speed filter and tracking loop method.

The scenario consists of step, ramp and sinusoidal speed responses to determine the difference between both methods. The overshoot in the beginning is reasoned through the non-present pre-filtering of both methods. But the simulation shows, that especially in transient domains the tracking loop provides a significant better behaviour compared to the ordinary speed filter. Applying the final value theorem of the Laplace transform [68]

$$\lim_{t\to\infty} \left(\omega_{ref}(t) - \hat{\omega}_m(t)\right) = \lim_{s\to 0} s\mathscr{L}\left\{\omega_{ref}(t) - \hat{\omega}_m(t)\right\}$$

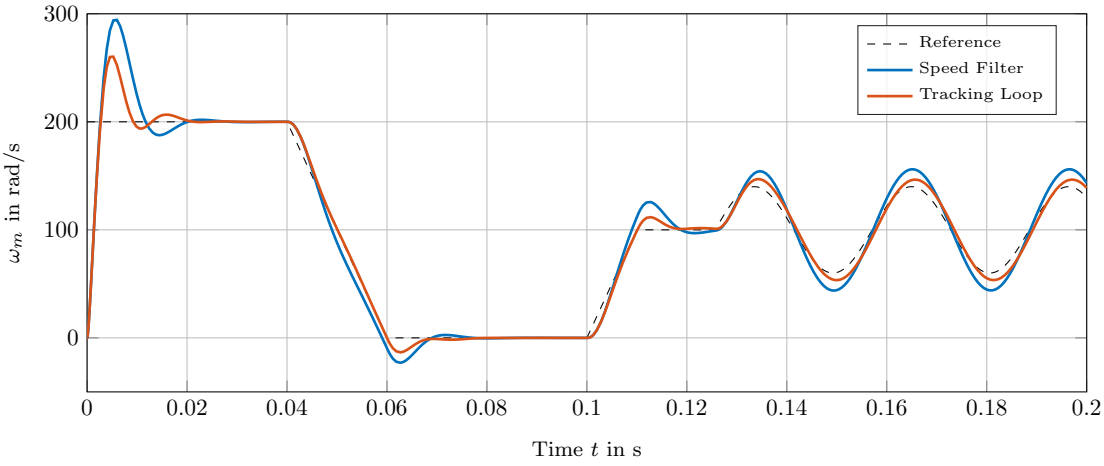

Figure 4.57.: Comparison of speed filter and tracking loop method in speed control.

with a ramp signal as input for the speed filter

$$\lim_{s\to 0} s\left(\frac{1}{s^2} - \frac{1}{s^2}\frac{1}{s}\frac{s}{1+sT_F}\right) = \lim_{s\to 0}\frac{1}{s}\frac{sT_F}{1+sT_F} = T_F$$

and for the tracking loop

$$\lim_{s\to 0} s\left(\frac{1}{s^2} - \frac{1}{s^2}\frac{1}{s}\frac{s(1+s\frac{2\delta}{\omega_0})}{1+s\frac{2\delta}{\omega_0}+s^2\frac{1}{\omega_0}}\right) = \lim_{s\to 0}\frac{1}{s}\frac{s^2\frac{1}{\omega_0^2}}{1+s\frac{2\delta}{\omega_0}+s^2\frac{1}{\omega_0}} = 0$$

shows, that the tracking loop has no stationary control error compared to the speed filter. This leads to lower speed deviations in general and control torque activity by the speed controller is reduced additionally. Utilization of Equation 4.74 and 4.75 with $G_{T\omega}(s)$ gives for the closed loop

$$T_\omega(s) = \frac{\omega_m(s)}{\omega_{ref}(s)} = \frac{s(1+s4T_\Sigma)(\omega_0^2+s2\delta\omega_0+s^2)}{s(\omega_0^2+s4T_\Sigma\omega_0^2)(1+s\frac{2\delta}{\omega_0})+s^3 8T_\Sigma^2(\omega_0^2+s2\delta\omega_0+s^2)(1+sT_\sigma)}$$

and disturbance transfer function

$$S_{\Delta\theta\omega}(s) = \frac{\omega_m(s)}{\Delta\theta_m(s)} = -\frac{s^2\omega_0^2(1+s4T_\Sigma)(1+s\frac{2\delta}{\omega_0})}{s(\omega_0^2+s4T_\Sigma\omega_0^2)(1+s\frac{2\delta}{\omega_0})+s^3 8T_\Sigma^2(\omega_0^2+s2\delta\omega_0+s^2)(1+sT_\sigma)}$$

Variation of the tracking loop parameter ω_0 regarding sensitivity of speed ripples induced by rotor position errors leads to similar results as in Figure 4.53, because it correlates with varying the speed filter parameter T_F as defined in Equation 4.79 and is therefore not carried out in more detail. Instead, T_F is kept constant at 1 ms and the damping factor δ is varied to investigate its impact on speed ripple. Figure 4.58 depicts this

parameter variations regarding the tracking loop transfer function $G_{T\omega}$ in frequency domain and step response behaviour in time domain with eddy current sensor error.

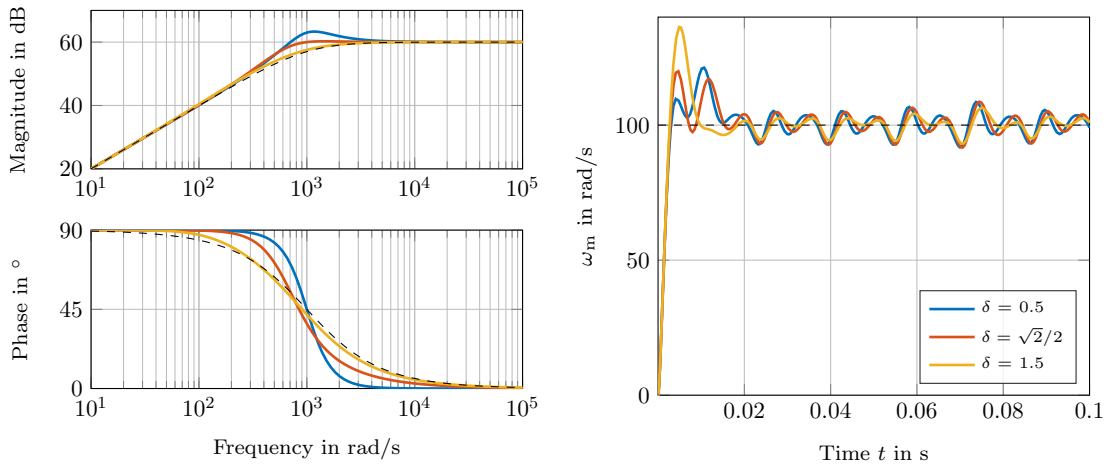

Figure 4.58.: Damping factor variation of tracking loop and speed ripple results.

On the left, the different frequency responses of $G_{T\omega}(j\omega)$ are depicted with $G_F(j\omega)$ in dashed lines as comparison. Obtaining the results in time domain shows, that variation of the damping factor has influence on the step response dynamics, but the impact on the stationary speed ripple is marginal. The bode plots indicate, that for increasing values for the damping factor $G_{T\omega}(j\omega)$ converges into $G_F(j\omega)$. Inserting Equation 4.79 into the tracking loop transfer function $G_{T\omega}$ from Equation 4.78 leads to

$$G_{T\omega}(s) = \frac{s(1 + s4\delta^2 T_F)}{1 + s4\delta^2 T_F + s^2 4\delta^2 T_F^2}$$

and considering large values for δ gives

$$\lim_{\delta\to\infty} \frac{s(1 + s4\delta^2 T_F)}{1 + s4\delta^2 T_F + s^2 4\delta^2 T_F^2} = \lim_{\delta\to\infty} \frac{\frac{s}{\delta^2} + s^2 4T_F}{\frac{1}{\delta^2} + s4T_F + s^2 4T_F^2} = \frac{s}{1 + sT_F}$$

which shows, that for increasing damping factors δ tracking loop and speed filter transfer functions match each other. It can be summarized, that both speed calculation methods can be applied in the purpose of speed control. Speed ripples caused by inaccurate position measurement can be decreased and damped via bandwidth of the speed filter, respectively tracking loop. Disadvantage of this method is, that the dynamic of the speed control loop gets decreased for both speed filter types and the additional degree of freedom represented by the damping factor has no beneficial influence on suppressing rotor position measurement disturbances.

4.13. Conclusion

In this chapter, a method is introduced to analyze the impact of rotor position sensor errors on control quality aspects of a field-oriented controlled PMSM. The measured sensor error signals from the test bench are used and a mathematical description is presented, how these error signals disturb currents and torque of the electric machine. This description can be utilized for any kind of reasonable error signal and provides valid results for the SPMSM and IPMSM type. The influence of control parameters, power electronic delay times and different control strategies are investigated, too. Additionally, the impact of rotor position measurement errors regarding additional losses, efficiency and their influence on speed controlled applications is considered.

If a precise rotor position measurement sensor is applied - like the exemplary resolver - no notable disturbances of above mentioned control quality aspects should occur. In contrast to that, less accurate sensor types - like the eddy current sensor examples - can contribute a significant impact on the control quality regarding torque and speed control applications. Therefore, this sensor type is mainly used in this chapter for demonstration purposes. The impact of measurement errors on efficiency is weak in general, but it does depend strongly on the machine parameters and has therefore to be analyzed separately for a given machine-sensor combination. The investigations also shows that the implemented control strategy determines in which operating regions significant torque disturbances occur and that rotor position sensor errors do contribute mostly in the high speed field-weakening range. If the electric machine is operated in constant torque mode and field-weakening is not necessary (or not possible), the requirements on the rotor position measurement accuracy can therefore be lowered considerable. Utilizing a rotor position sensor for speed signal generation within speed controlled applications produces additional speed disturbances. At the end of this chapter is showed, that decreasing the bandwidth of a speed filter or tracking loop is the most effective way to suppress rotor position sensor induced perturbations for speed control.

5. Summary

This work deals with investigations of rotor position measurement of electric machines, especially of permanent magnet synchronous machines within automotive applications. Since these applications usually operate within harsh environment, e.g. in terms of temperature, mechanical misalignment, supply voltage, the applied sensors need to be robust in terms of different parameter variations. The present thesis suggests a method to examine different sensor technologies regarding their parameter stability and their influence on the control of a permanent magnet synchronous machine.

In the first chapter, a motivation for the necessity of rotor position measurement within automotive applications is presented. Measurement of the rotor shaft position plays an important role in electric vehicle powertrains, hybridization concepts and electrification of ancillary units.

The next section gives an overview about different sensor technologies, which are suitable for automotive purposes. In this survey, resolver, magneto-resistive and eddy current sensor types are considered. It is elaborated, how these different sensor technologies are evaluated for computation of the rotor position information. Several error mechanisms e.g. DC offset errors, amplitude mismatch, additional harmonic content or quadrature phase shift errors are discussed and summarized to provide a better insight, how manipulation of sensor signals produce additional errors in rotor position measurement. Description of these different error sources is performed analytically and presented for analogue sensor signals and resolvers. Several preliminary work dealing with this topic is available; therefore this chapter represents a summary of different sensor error mechanisms. It is shown, that an analytic description of these errors is possible by varying signal parameters, but manipulating sensor parameters produces a complex superimposition of different error sensor influences. Describing the sensor error as a function of the manipulated sensor parameter is difficult, because deep knowledge about the sensor structure is necessary and it is utterly possible to link the varied parameters to the sensor signals and resulting measurement error. Therefore, instead of a mathematical-physical approach an experimental method is considered for further investigations.

Chapter three introduces a method to evaluate the sensor error characteristics as a function of different parameter variations. A test bench is used, which provides the possibility to vary mechanical positioning, temperature, speed and supply voltage of the investigated sensor technology. This test bench is completely automated and allows to perform a big amount of measurement in different operating points in a short period of time. The sensor's peak-to-peak error over one mechanical revolution is used as performance index and a quadratic regression model is computed to describe the sensi-

tivity regarding different parameter variations. Different statistical tests are performed to show the explanatory power and usefulness of this introduced method. The Design of Experiment approach can be carried out with different design types, which are discussed and a method to rate these designs regarding their response surface model capability is introduced. This experimental approach in combination with the automated test bench allows to characterize different sensor technologies and configurations in a short period of time to benchmark several sensor candidates to find the best solution for a specific application. An adaptation of this method for other sensor systems (such as speed sensors) is possible, if an adequate performance criterion is defined. An interesting outlook and extension of this approach includes a strategy to get regression models with confidence bounds and prediction intervals for a sample of same sensor realizations. This could provide the information, how a specific sensor behaves for a large number of realizations. In the end of this chapter, multidimensional look-up-tables are introduced to map the sensor's error behaviour as a function of different parameter variations. This allows to reproduce the complete error characteristics over one mechanical period as measured on the test bench.

In chapter four, sensor error measurements are applied within the simulation of a field-oriented motor control. These simulations show a mismatch between simulation results and proposed methods of different publications, because most of the literature does not consider the dynamics of machine and current control in terms of sensor errors. Sworowski's method - which is designed and valid for the surface permanent magnet synchronous machine type - is extended and analyzed regarding its applicability on the interior machine type. Since the results are not satisfactory, a new description of the permanent magnet synchronous machine in a misaligned reference frame is presented. This allows to compute resulting current and torque disturbances in the control system from standstill up to high speed field-weakening regions with appropriate disturbance transfer functions. Current control parameter influence on the control quality is discussed and a method for an approximated consideration of power electronics delay time is presented. Sensor error measurements from the test bench are combined with the proposed description to evaluate the impact of sensor parameter variations regarding machine currents and torque. Different control strategies are introduced and their sensitivity regarding rotor position measurement errors are analyzed. Additionally, the impact of sensor errors on different losses and efficiency degradation in permanent magnet synchronous machines is evaluated. A time discrete description of current control, electric machine and sensor error would be an interesting extension of the presented method and results, since most controllers are implemented digitally. But investigations of high speed operating points - where rotor position errors are more significant - can cause difficulties with discrete time systems; therefore only continuous-time models are considered. Rotor position sensors are suitable for generating speed information, which makes it interesting to use this sensor type for speed control applications, since adding an additional speed sensor increases costs, complexity and fault liability. Errors in rotor position measurement do also occur in the generated speed signal and therefore a certain speed ripple is present in speed control applications. Two methods of speed signal generation via speed

filter and tracking loop are presented and their parameter sensitivity regarding produced speed ripple and control activity is discussed.

This work introduces an experimental method based on a DOE strategy to evaluate different rotor position sensors regarding parameter robustness and to assess their automotive usability under use of a specific test bench. Additionally, existent mathematical descriptions to investigate how different kinds of measured rotor position signals do interfere a field-orientated control of PMSM are enhanced and utilized regarding selected control quality related aspects. In this way, the present thesis provides a contribution to the improvement of rotor position sensor specifications and their impact on the control quality of electric motors.

A. Test Bench for Sensor Evaluation

In this section, specifications and design of the sensor test bench is discussed. As introduced in the beginning of Chapter 3 in Figure 3.1, a specific test bench was designed to evaluate the sensor's robustness regarding several parameter variations. The test bench provides the possibility to vary several mechanical, electrical and thermal parameters of the DUT, such as:

- Mechanical misalignment in Δx-, Δy- and Δz-direction
- Tilt angle $\Delta\varphi$ between sensor rotor and stator plane
- Speed variations Δn
- Temperature changes ΔT within the typical automotive range
- Supply voltage variations ΔV

A.1. Test Bench Concept

Figure A.1 shows a cross-sectional view of the test bench concept and involved components for variation of above itemized parameters and sensor evaluation.

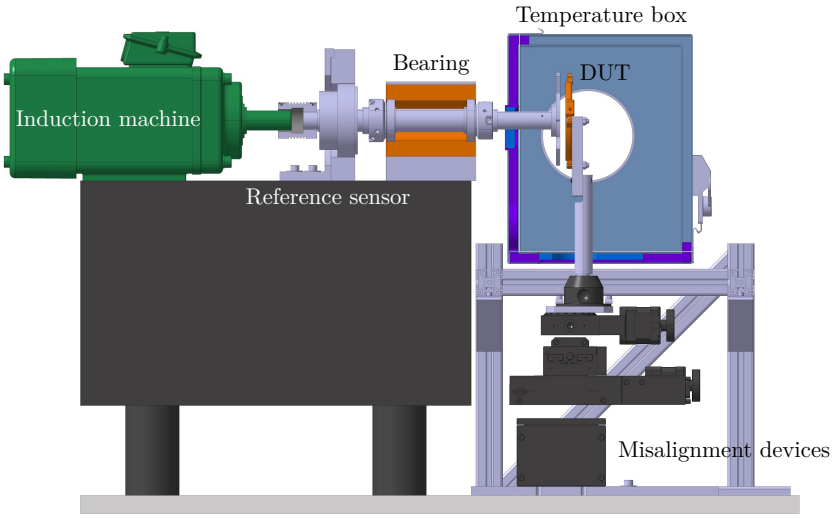

Figure A.1.: Cross-sectional view of the test bench concept [82].

The test bench utilizes an induction machine manufactured by Perske [83] to cover up a speed range from 0 up to 24000 rpm and is controlled via field-oriented control concept, which is implemented within a Siemens S120 drive system [84]. This machine drives the shaft for the DUT and the reference sensor system, which is carried out as a high-precise Hall-based rotor position measurement system built by Baumer Hübner [85] and is simultaneously used for controlling the induction machine. The mechanical misalignment is realized by the stationary part of the investigated sensor. Four independently controlled stepper slide units from OWIS [86],[87],[88] are combined to establish the necessary position misalignment. The DUT is integrated into a temperature box to cover up the typical automotive temperature range and is externally tempered by a temperature chamber from ESPEC [89]. Dimensioning and mechanical design of the test bench and all of its components is discussed in [82]. Figure A.2 shows the realization of the test bench concept with focus on electric drive, reference sensor and DUT within the temperature box.

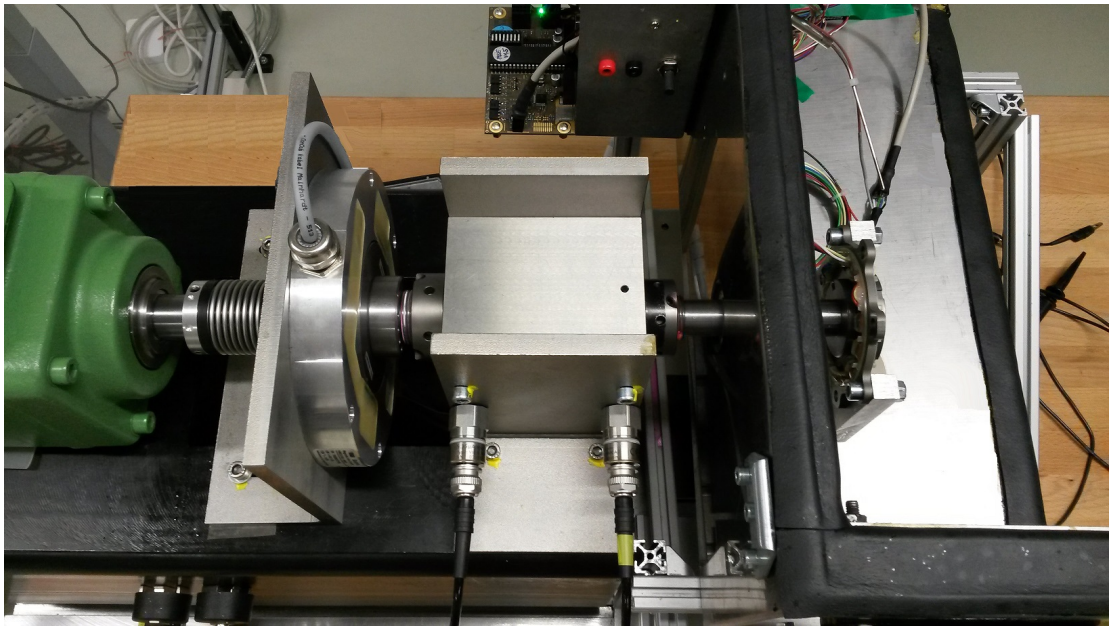

Figure A.2.: Test bench realization with resolver as DUT.

It shows a configuration, where a resolver is integrated into the test bench with the additional necessary signal processing hardware for the resolver-to-digital conversion. Figure A.3 shows the complete test bench room and all involved components, which are necessary to perform the specified measurements and experiments.

The temperature chamber on the right is repurposed to change the temperature within the external temperature box, where the DUT is integrated. On the left, the power electronic hardware for the electric drive is placed within a switch cabinet to shield the measured sensor signals from electromagnetic distortions. The additional signal

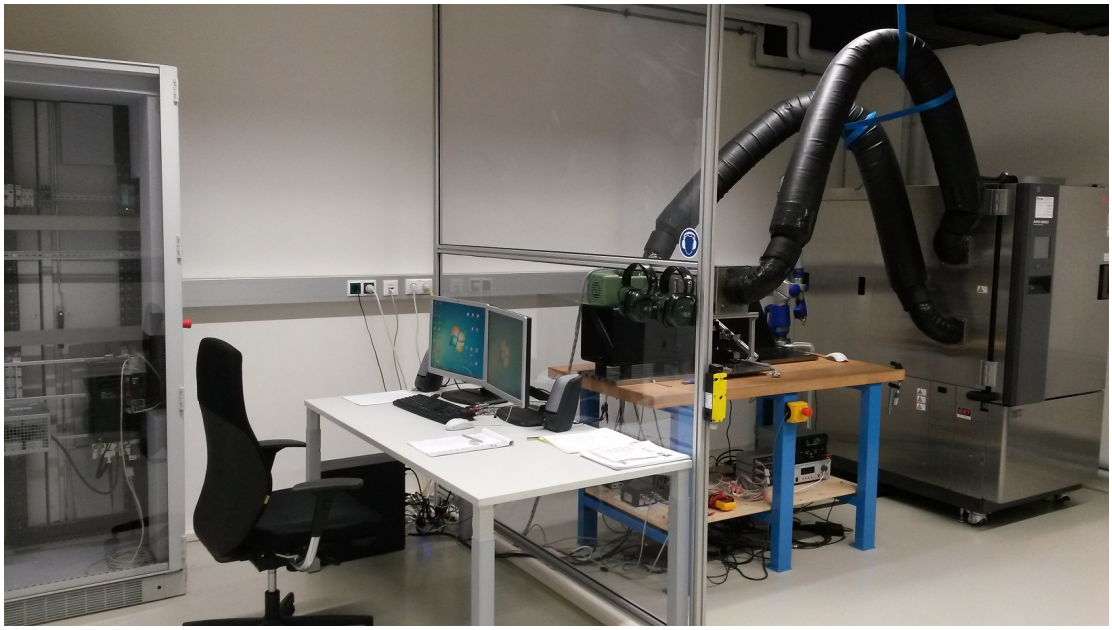

Figure A.3.: Test bench room overview and all involved components.

processing box from reference sensor and data acquisition unit is attached under the test bench table. The test bench PC is used to control all sub-modules and to store, display and process the measured data. Table A.1 summarizes the specifications and design goals of the sensor test bench.

Table A.1.: Test bench specifications.

Parameter	**Min**	**Max**	**Tolerance**	**Unit**
Tilt angle $\Delta\varphi$	-45	+45	$< 10^{-5}$	°
Misalignment Δx, Δy	-15	+15	0.01	mm
Misalignment Δz	0	+15	0.01	mm
Mechanical speed	-24000	+24000	$< 1\%$	rpm
Temperature	-40	+160	< 1	°C
Supply voltage	0	+40	0.01	V
Sample rate	-	5	-	MS/Sec
Reference angle resolution	< 0.1	-	-	°
Acceleration	-	>10000	-	rpm/sec

A.2. Test Bench Automation

In a first design step, all test bench elements had to be parametrized by hand for every measurement point of the experimental design. This lead to time consuming test plan executions and a high possibility of wrong defined settings. Therefore, an automation concept was developed with the aim to integrate all present test bench elements holistically. This allows to operate all involved test bench sub-modules directly via test bench PC in combination with a specific designed LabVIEW surface. Additionally, complete test plans and extensive experiments can be performed with the automated test bench autonomously, which increases safety, reproducibility and decreases experiment execution times significantly. Figure A.4 shows the basic automation concept, integrated modules and utilized interfaces of the different test bench elements, where thick lines indicate a bus and arrowed lines a point-to-point connection. In [90], the implemented test bench automation and graphical user interface development is carried out in more detail.

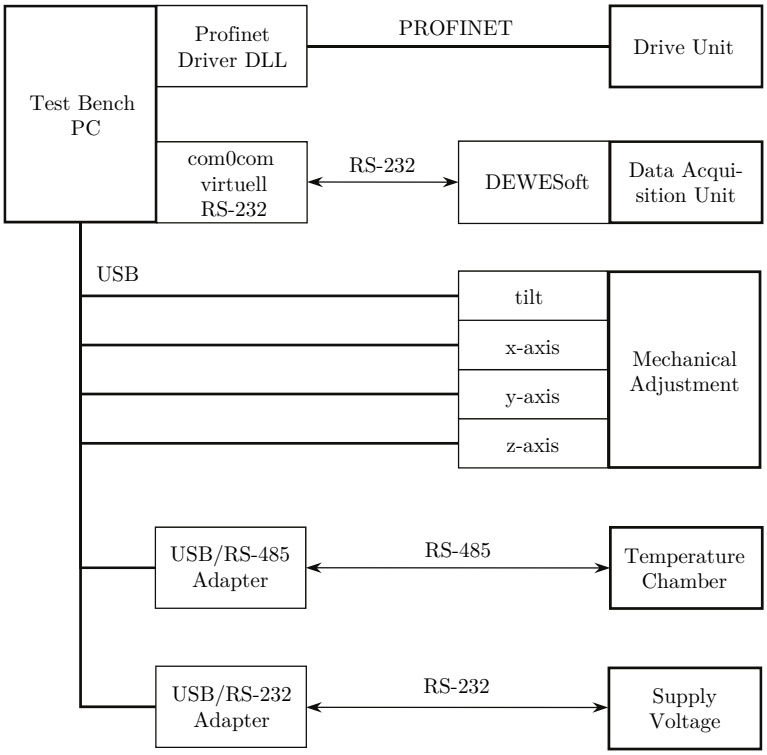

Figure A.4.: Test bench automation concept, adapted from [90].

In a first step, an appropriate experimental space and design must be defined, which is computed in MATLAB or directly in the LabVIEW environment. Afterwards the test plan is integrated into the LabVIEW surface, which starts the execution of the defined experiment. The test bench PC controls all participating modules and triggers

the data acquisition unit. After finishing all necessary measurements, the measured data is converted into a MATLAB compatible format, where the evaluation and sensor characterization - as introduced in Chapter 3 - is implemented. The automated test bench is used for designing the parametrizable look-up-tables mentioned in Chapter 3.7 too, which are further used for control quality investigations as described in Chapter 4. Figure A.5 shows exemplary pictures of the developed graphical user interface (GUI) for the implemented manual and automated test bench operating modes.

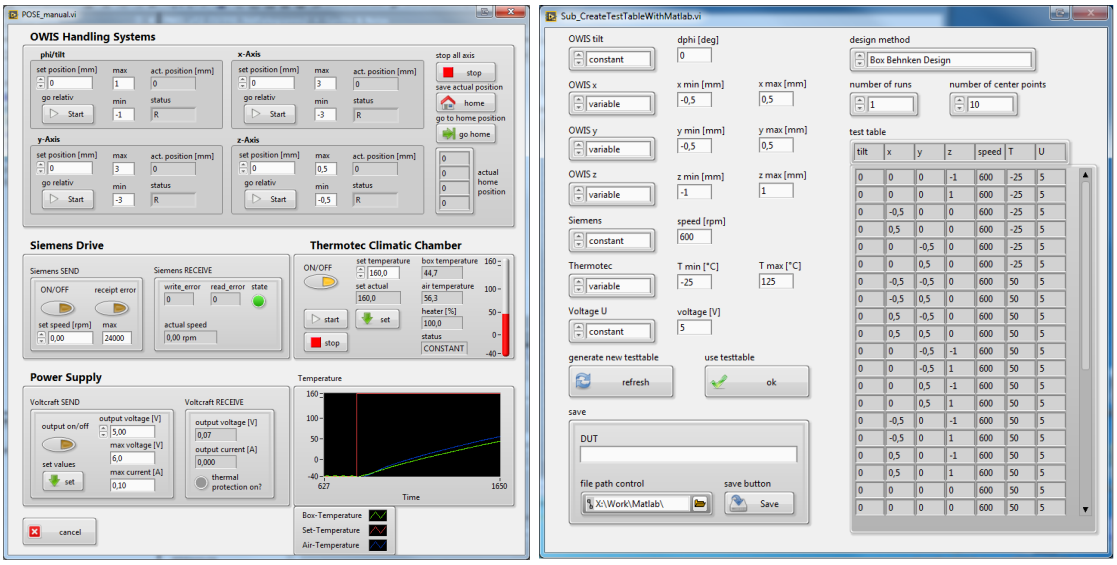

Figure A.5.: Developed test bench GUI for manual operation mode (left) and automated test procedure (right) [90].

On the left, the main GUI is depicted, where all test bench components are controlled independently. This allows to change the sensor operating points and to define a representative origin for further measurements and experiments. The figure on the right displays the automated test mode, where the executed design with an appropriate design space is configured. Afterwards, the test bench automation processes the defined test plan and stores the measurement results autonomously.

The implemented data acquisition unit from Dewetron [91] allows to measure and process different sensor interfaces online. If sensor parameters are varied via test bench GUI, the impact on the measured rotor position information of the DUT is observed directly. Figure A.6 shows an exemplary online measurement scenario of a four pole sensor. The two diagonal and almost identical lines represent the measured reference sensor and DUT position signals. The difference of these two signals defines the sensor error $\Delta\theta$, where the four poles periodicity of the investigated sensor within a mechanical revolution is apparent. Additionally, the data acquisition unit allows an online computation of several sensor error quantities, such as maximum, minimum, mean average or peak-to-

peak values and to monitor several process values as speed and test bench component temperatures.

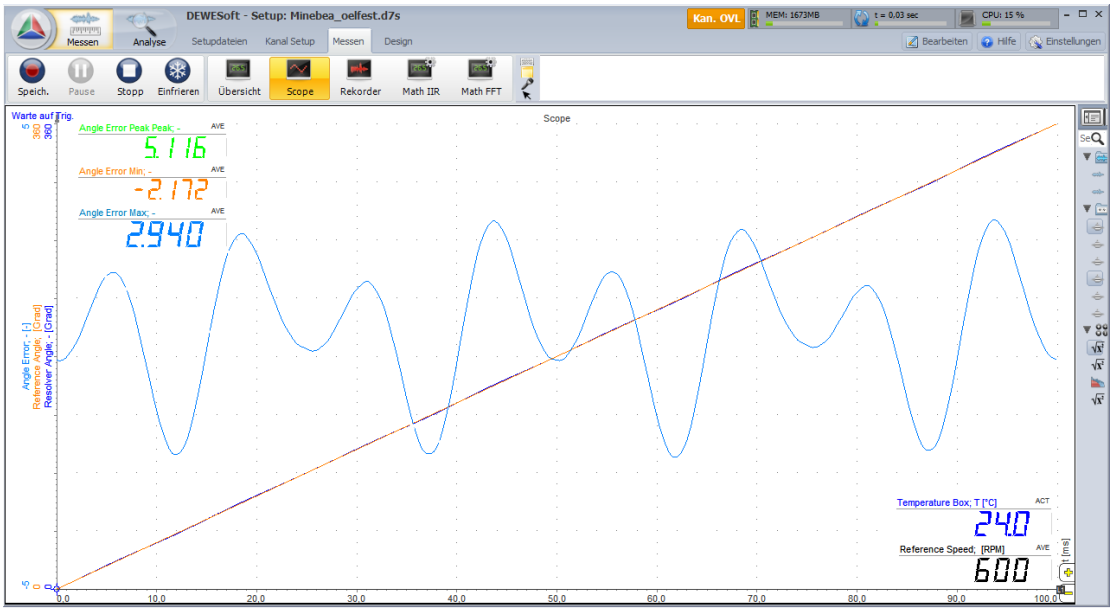

Figure A.6.: Online measurement of a four pole sensor with reference angle, sensor angle and sensor error over one mechanical period.

Bibliography

[1] G. Babiel. *Elektrische Antriebe in der Fahrzeugtechnik: Lehr- und Arbeitsbuch.* Studium : Elektrotechnik. Vieweg+Teubner Verlag, 2009. ISBN: 9783834805638.

[2] A. Binder. *Elektrische Antriebe für Zero Emission Vehicles ZEV - Vorlesungsskript*, 2016. Institut für Elektrische Energiewandlung, Technische Universität Darmstadt.

[3] K. H. Nam. *AC Motor Control and Electric Vehicle Applications.* CRC Press, 2013. ISBN: 9781439819630.

[4] IPMSM cross-sectional view. *www.linkedin.com/pulse/global-permanent-magnet-motor-market-research-report-saurabh-sinha.* Date of access: 2017.06.16.

[5] J. Gächter and M. Hirz. *Evaluation and Modeling of Rotor Position Sensor Characteristics for Electric Traction Motors.* SAE 2016 World Congress and Exhibition, April 2016.

[6] T. Tille. *Automobil-Sensorik.* Springer Berlin Heidelberg, 2016. ISBN: 9783662489437.

[7] O.C. Kivanc, S.B. Ozturk, R.N. Tuncay, E. Kesici, and C. Yazi. *Electro-hydraulic power steering system modelling for parameter fault detection based on model reference adaptive frame.* IECON 2016 - 42nd Annual Conference of the IEEE Industrial Electronics Society, pages 1808–1814, Oct 2016.

[8] X. Ge, Z. Q. Zhu, R. Ren, and J. T. Chen. *Analysis of Windings in Variable Reluctance Resolver.* IEEE Transactions on Magnetics, 51(5):1–10, May 2015. ISSN: 0018-9464.

[9] Cumatix Smartsyn Resolver. *www.cumatix.com/en/sensors/resolversmartsyn.* Date of access: 2017.06.16.

[10] Cumatix VR Resolver. *www.cumatix.com/en/sensors/vr-resolvers.* Date of access: 2017.06.16.

[11] M. Ludwig, M. Rieder, and M. Wolf. *Introduction of a MR Rotor-Position Sensor for Off-Axis Application and Comparison to Competitive Technologies.* SAE 2016 World Congress and Exhibition, 9:219–230, April 2016.

[12] J. Marek, H.-P. Trah, Y. Suzuki, and I. Yokomori. *Sensors Applications, Volume 4, Sensors for Automotive Applications.* Wiley-VCH, July 2003. ISBN: 3527295534.

[13] L. Ye, M. Yang, and L. Xu. *Rotor study of inductive angle sensor.* 2012 IEEE

International Conference on Mechatronics and Automation, pages 697–701, Aug 2012. ISSN: 2152-7431.

[14] EFI Eddy Current Sensor. *www.efiautomotive.com/technologie*. Date of access: 2017.06.16.

[15] S. Balemi. *Automatic Calibration of Sinusoidal Encoder Signals*. Proceedings of the 16th IFAC World Congress, July 2005.

[16] J. Lara and A. Chandra. *Position error compensation in quadrature analog magnetic encoders through an iterative optimization algorithm*. IECON 2014 - 40th Annual Conference of the IEEE Industrial Electronics Society, pages 3043–3048, Oct 2014. ISSN: 1553-572X.

[17] M. Mienkina, P. Pekarek, and F. Dobes. *56F80x Resolver Driver and Hardware Interface*. Application Note, pages 1–13, August 2005.

[18] J. Krah, H. Schmirgel, and M. Albers. *FPGA Based Resolver to Digital Converter Using Delta-Sigma Technology*. International PCIM Europe Conference, Proceedings, Nürnberg, pages 931–936, June 2006.

[19] R. Ramakrishnan, A. Gebregergis, M. Islam, and T. Sebastian. *Effect of position sensor error on the performance of PMSM drives for low torque ripple applications*. Electric Machines Drives Conference, 2013 IEEE International, pages 1166–1173, May 2013.

[20] J. Hu, J. Zou, F. Xu, Y. Li, and Y. Fu. *An Improved PMSM Rotor Position Sensor Based on Linear Hall Sensors*. IEEE Transactions on Magnetics, 48(11):3591–3594, Nov 2012. ISSN: 0018-9464.

[21] D.C. Hanselman. *Resolver Signal Requirements for High Accuracy Resolver-to-Digital Conversion*. IEEE Transactions on Industrial Electronics, 37(6):556–561, Dec 1990.

[22] S. Jung, B. Lee, and K. Nam. *PMSM control based on edge field measurements by Hall sensors*. Applied Power Electronics Conference and Exposition (APEC), 2010 Twenty-Fifth Annual IEEE, pages 2002–2006, Feb 2010. ISSN: 1048-2334.

[23] U. Ausserlechner. *A Theory of Magnetic Angle Sensors with Hall Plates and without Fluxguides*. Progress In Electromagnetics Research B, 49:77–106, 2013.

[24] U. Ausserlechner. *Closed Analytical Formulae for Multi-Pole Magnetic Rings*. Progress In Electromagnetics Research B, 38:71–105, 2012.

[25] M. Metz, A. Haberli, M. Schneider, R. Steiner, C. Maier, and H. Baltes. *Contactless angle measurement using four Hall devices on single chip*. Solid State Sensors and Actuators, International Conference on Transducers, 1:385–388, Jun 1997.

[26] K.C. Kim. *Optimal Angle Error Reduction of Magnetic Position Sensor by 3D Finite Element Method*. Journal of Magnetics, 18:454–459, Oct 2013.

[27] S. Jing, Z. Meng, and J. Shanlin. *The Principle of Reluctance Resolver and EMF Waveform Optimization Based on FEM.* 2011 First International Conference on Instrumentation, Measurement, Computer, Communication and Control, pages 615–618, Oct 2011.

[28] H. Rohling. *Stochastische Prozesse - Vorlesungsskript*, 2006. Institut für Nachrichtentechnik, Technische Universität Hamburg-Harburg.

[29] R.M. Feldman and V. Ciriaco. *Applied Probability and Stochastic Processes.* Springer Publishing Company, Incorporated, 2nd edition, 2010. ISBN: 9783642051555.

[30] J. Gächter, J. Fabian, M. Hirz, A. Schmidhofer, and H. Lanzenberger. *Evaluation of Angular Sensor Systems for Rotor Position Sensing of Automotive Electric Drives*, pages 277–286. Springer International Publishing, 2014. ISBN: 9783319080871.

[31] R.H. Myers, D.C. Montgomery, and C.M. Anderson-Cook. *Response Surface Methodology: Process and Product Optimization Using Designed Experiments.* Wiley Series in Probability and Statistics. Wiley, 2009. ISBN: 9780470174463.

[32] K. Siebertz, D. van Bebber, and T. Hochkirchen. *Statistische Versuchsplanung - Design of Experiments (DoE).* Springer Berlin Heidelberg, 2010. ISBN: 9780470174463.

[33] W.K. Wong. *Comparing robust properties of A, D, E and G-optimal designs.* Computational Statistics and Data Analysis 18, pages 441–448, June 1993.

[34] P.F. de Aguiar, B. Bourguignon, M.S. Khots, D.L. Massart, and R. Phan-Than-Luu. *D-optimal designs.* Chemometrics and Intelligent Laboratory Systems, 30(2):199 – 210, 1995. ISSN: 0169-7439.

[35] Mathworks MATLAB: Statistics and Machine Learning Toolbox User's Guide. *https://iasbs.ac.ir/computer/tutorials/matlab/stats_tb.pdf.* Date of access: 2017.06.23.

[36] Analog Devices ADA4571: Integrated AMR Angle Sensor and Signal Conditioner. *www.analog.com/media/en/technical-documentation/data-sheets/ADA4571.pdf.* Date of access: 2017.06.19.

[37] Schramberg Magnet- und Kunststofftechnik. *www.magnete.de/uploads/tx_fbmagneticfieldcalc/NdFeB_46_80_p_E.pdf.* Date of access: 2017.06.19.

[38] L. Fahrmeir, T. Kneib, and S. Lang. *Regression: Modelle, Methoden und Anwendungen.* Statistik und ihre Anwendungen. Springer Berlin Heidelberg, 2009. ISBN: 9783642018374.

[39] StatsDirect Statistical Software. *www.statsdirect.com/help/basics/p_values.htm.* Date of access: 2017.06.19.

[40] N.R. Draper and H. Smith. *Applied regression analysis.* Number Bd. 1 in Wiley series in probability and statistics: Texts and references section. Wiley, 1998. ISBN: 9780471170822.

[41] H. Stocker. *Methoden der Empirischen Wirtschaftsforschung, Einführung in die angewandte Ökonometrie - Vorlesungsskript*, 2015. Universität Innsbruck.

[42] J. Bortz. *Statistik für Human- und Sozialwissenschaftler.* Springer-Lehrbuch. Springer, 2005. ISBN: 9783540212713.

[43] H. Büning. *Robuste und adaptive Tests.* De Gruyter, 1991. ISBN: 9783110128277.

[44] J.J. Borkowski, B. Chomtee, and K. Panishkan. *Componentwise Variance Dispersion Graphs for Mixture Experiments.* Proceedings of the American Statistical Association - Section on Quality and Productivity, pages 1773–1782, Jan 2008.

[45] Analog Devices AD2S1210: Variable Resolution 10-Bit to 16-Bit R/D Converter with Reference Oscillator. *www.analog.com/media/en/technical-documentation/data-sheets/AD2S1210.pdf.* Date of access: 2017.06.20.

[46] Arnold Magnetics Technologies: Injection Molded Magnet Plastiform 2051. *www.arnoldmagnetics.com/en-us/Products/Injection-Molded-Magnets.* Date of access: 2017.06.20.

[47] Mathworks MATLAB: Optimization Toolbox User's Guide. *www.mathworks.com/help/pdf_doc/optim/optim_tb.pdf.* Date of access: 2017.06.20.

[48] A. Hertzmann, D. Fleet, and M. Brubaker. *Machine Learning and Data Mining Lecture Notes*, 2015. Department of Computer and Mathematical Sciences, University of Toronto Scarborough.

[49] Mathworks MATLAB: Neural Network Toolbox User's Guide. *www.mathworks.com/help/pdf_doc/nnet/nnet_ug.pdf.* Date of access: 2017.06.20.

[50] J. Prakash Maran, V. Sivakumar, K. Thirugnanasambandham, and R. Sridhar. *Artificial neural network and response surface methodology modeling in mass transfer parameters predictions during osmotic dehydration of Carica papaya L.* Alexandria Engineering Journal, 52(3):507 – 516, 2013. ISSN: 1110-0168.

[51] M. Mourabet, A. El Rhilassi, M.Bennani-Ziatni, and A. Taitai. *Comparative Study of Artificial Neural Network and Response Surface Methodology for Modelling and Optimization the Adsorption Capacity of Fluoride onto Apatitic Tricalcium Phosphate.* Universal Journal of Applied Mathematics, 2(2):84–91, 2014.

[52] Mathworks MATLAB: Simulink Methods for Estimating Missing Points. *www.de.mathworks.com/help/simulink/ug/methods-for-estimating-missing-points.html.* Date of access: 2017.06.20.

[53] J. Lara, J. Xu, and A. Chandra. *Effects of Rotor Position Error in the Performance of Field-Oriented-Controlled PMSM Drives for Electric Vehicle Traction Applications.* IEEE Transactions on Industrial Electronics, 63(8):4738–4751, Aug 2016. ISSN: 0278-0046.

[54] K. Cho, Y. Lee, H. Mok, H. Kim, K. Jun, and Y. Cho. *Torque Ripple Reduction*

of a PM Synchronous Motor for Electric Power Steering using a Low Resolution Position Sensor. Journal of Power Electronic, 10(6):709–716, 2010.

[55] S. Gradev, P. Brockerhoff, K. Kapser, D. Nugraha, and R. Vuletic. *Analysis of sensor parameter characteristics and digital control on the electric drive's performance.* Electric Drives Production Conference (EDPC), 2013 3rd International, pages 1–6, Oct 2013.

[56] W. Sibo, Z. Huichao, L. Zhiyu, and W. Xiaoxu. *A new torque ripple test method base on PMSM torque ripple analysis for electric vehicles.* EVS28 Internation Electric Vehicle Symposium and Exhibtion, pages 1–10, 2015.

[57] Y. Wang, H. Jing, W. Chen, and X. Wang. *The analysis and simulation of motor's torque ripple in electric vehicle.* 2011 International Conference on Consumer Electronics, Communications and Networks (CECNet), pages 5328–5331, April 2011.

[58] L. Hao, S. Gopalakrishnan, C. Namuduri, and K. Rahman. *Impact of position sensor accuracy on the performance of IPM drives.* 2013 IEEE Energy Conversion Congress and Exposition, pages 196–201, Sept 2013. ISSN: 2329-3721.

[59] N.P. Quang and J.A. Dittrich. *Vector Control of Three-Phase AC Machines: System Development in the Practice.* Power Systems. Springer Berlin Heidelberg, 2008. ISBN: 9783540790297.

[60] E. Sworowski. *Ganzheitliche Methodik zur Analyse und Kompensation von ansteuerungsbedingten Störungen im Regelkreis permanenterregter Synchronmaschinen.* Wissenschaftliche Reihe Fahrzeugtechnik Universität Stuttgart. Springer Fachmedien Wiesbaden, 2014. ISBN: 9783658074500.

[61] W. Leonhard. *Regelung elektrischer Antriebe.* Springer Verlag, 2000. ISBN: 354067179X.

[62] F. Blaschke. *Das Verfahren der Feldorientierung zur Regelung der Drehfeldmaschine (The Method of Field Orientation For Control of Three Phase Machines).* PhD thesis, University of Braunschweig, 1973.

[63] K. Hasse. *Zur Dynamik drehzahlgeregelter Antriebe mit stromrichter-gespeisten Asynchron-Kurzschlusslüfermaschinen.* PhD thesis, Technische Hochschule Darmstadt, 1969.

[64] D. Schröder. *Elektrische Antriebe Grundlagen.* Springer-Lehrbuch. Springer Berlin Heidelberg, 2009. ISBN: 9783642029905.

[65] P.C. Krause, O. Wasynczuk, S.D. Sudhoff, and IEEE Power Engineering Society. *Analysis of electric machinery and drive systems.* IEEE Press series on power engineering. IEEE Press, 2002. ISBN: 9780471143260.

[66] D. Schröder. *Elektrische Antriebe - Regelung von Antriebssystemen.* Number Bd. 10 in Elektrische Antriebe - Regelung von Antriebssystemen. Springer Berlin Heidelberg, 2009. ISBN: 9783540896128.

[67] G. Götting. *Dynamische Antriebsregelung von Elektrostraßenfahrzeugen unter Berücksichtigung eines schwingungsfähigen Antriebsstrangs.* PhD thesis, Institut für Leistungselektronik und Elektrische Antriebe, RWTH Aachen University, 2004. ISBN: 9783832228040.

[68] M. Horn and N. Dourdoumas. *Regelungstechnik: rechnerunterstützter Entwurf zeitkontinuierlicher und zeitdiskreter Regelkreise.* Elektrotechnik : Regelungstechnik. Pearson Studium, 2004. ISBN: 9783827372604.

[69] H. Moon, H. Kim, and M. Youn. *A discrete-time predictive current control for PMSM.* IEEE Transactions on Power Electronics, 18(1):464–472, Jan 2003. ISSN: 0885-8993.

[70] J. Agrawal and B. Sanjay. *Steady-state Analysis and Comparison of Control Strategies for PMSM.* Modelling and Simulation in Engineering, 2015(6):13:13–13:13, January 2015.

[71] R. Monajemy and R. Krishnan. *Control and dynamics of constant-power-loss-based operation of permanent-magnet synchronous motor drive system.* IEEE Transactions on Industrial Electronics, 48(4):839–844, Aug 2001. ISSN: 0278-0046.

[72] G. Gallegos-Lopez, F. S. Gunawan, and J. E. Walters. *Optimum torque control of permanent-magnet AC Machines in the field-weakened region.* IEEE Transactions on Industry Applications, 41(4):1020–1028, July 2005. ISSN: 0093-9994.

[73] D.W. Novotny and T.A. Lipo. *Vector Control and Dynamics of AC Drives.* Monographs in electrical and electronic engineering. Clarendon Press, 1996. ISBN: 9780198564393.

[74] W. Hassan and B. Wang. *Efficiency optimization of PMSM based drive system.* Proceedings of The 7th International Power Electronics and Motion Control Conference, 2:1027–1033, June 2012.

[75] C. Mademlis, I. Kioskeridis, and N. Margaris. *Optimal efficiency control strategy for interior permanent-magnet synchronous motor drives.* IEEE Transactions on Energy Conversion, 19(4):715–723, Dec 2004. ISSN: 0885-8969.

[76] A. Krings. *Iron Losses in Electrical Machines - Influence of Material Properties, Manufacturing Processes and Inverter Operation.* PhD thesis, Electrical Energy Conversion, KTH School of Electrical Engineering, 2014. ISBN: 9789175950990.

[77] N. Urasaki, T. Senjyu, and K. Uezato. *Relationship of parallel model and series model for permanent magnet synchronous motors taking iron loss into account.* IEEE Transactions on Energy Conversion, 19(2):265–270, June 2004. ISSN: 0885-8969.

[78] F. Diba, A. Arora, and E. Esmailzadeh. *Optimized robust cruise control system for an electric vehicle.* Systems Science & Control Engineering, 2(1):175–182, 2014.

[79] R. D. Lorenz and K. W. Van Patten. *High-resolution velocity estimation for all-*

digital, AC servo drives. IEEE Transactions on Industry Applications, 27(4):701–705, July 1991. ISSN: 0093-9994.

[80] B. Heimann, W. Gerth, and K. Popp. *Mechatronik*. Fachbuchverl. Leipzig im Carl-Hanser-Verlag, 2007. ISBN: 9783446405998.

[81] D. Y. Han, Y. Cho, and K. B. Lee. *Simple rotor position estimation for sensorless control of IPMSM using PLL based on EEMF*. 2016 IEEE Transportation Electrification Conference and Expo, ITEC Asia-Pacific, pages 656–660, June 2016.

[82] S. Walch. *Development of a testbench for evaluation of high rotational speed sensors of powertrains*. Master's thesis, Graz University of Technology, 2015.

[83] Perske Special Electric Motors V60.11-2: 5 kW / 400 Hz Induction Machine. *www.perske.de/images/pdf/perske_katalog_en.pdf*. Date of access: 2017.06.21.

[84] Siemens Sinamics S120 Drive System. *https://mall.industry.siemens.com/mall/de/-ww/catalog/products/10030361*. Date of access: 2017.06.21.

[85] Baumer Hüebner HMC 16 (M) + HEAG 158 V (M) Incremental Encoder. *www.baumerhuebner.com/uploads/media/hmc16_heag158.pdf*. Date of access: 2017.06.21.

[86] OWIS Elevator Stage HV 100. *www.owis.eu/fileadmin/user_upload/owis.eu/products/pdf/pi_hv_100.pdf*. Date of access: 2017.06.21.

[87] OWIS Precision Linear Stage LT 60. *www.owis.eu/fileadmin/user_upload/owis.eu/-products/pdf/pi_lt_60.pdf*. Date of access: 2017.06.21.

[88] OWIS Angular Adjustment Stage WV 60. *www.owis.eu/fileadmin/user_upload/owis-.eu/products/pdf/pi_wv_60.pdf*. Date of access: 2017.06.21.

[89] Espec Environmental Stress and Temperature Chamber ARG-0220. *www.espec.de/fileadmin/espec/PDF/Reach-in/AR_Series.pdf*. Date of access: 2017.06.21.

[90] D. Mähr. *Development of a Testbed Control and Visualization Software for the Evaluation of Automotive Sensors*. Master's thesis, Graz University of Technology, 2015.

[91] Dewetron DEWE-ORION-0816-5Mx Integrated Data Acquisition AD Board. *www.dewetron.com/product/dewe-orion-0816-5mx*. Date of access: 2017.06.21.